Computational fluid dynamics indicators to improve cardiovascular pathologies

Eduardo Soudah Prieto

SUPERVISORS:
Prof. Eugenio Oñate Ibañez de Navarra
Prof. Luis Miguel Cervera Ruiz
Prof. Raimon Jané Campos

PhD Thesis
Biomedical Engineering Doctoral Programme
Universitat Politècnica de Catalunya - BarcelonaTech

Barcelona, November 2015

UNIVERSITAT POLITÈCNICA DE CATALUNYA
BARCELONATECH
Escola de Doctorat

Acta de calificación de tesis doctoral

Curso académico:

Nombre y apellidos

Programa de doctorado

Unidad estructural responsable del programa

Resolución del Tribunal

Reunido el Tribunal designado a tal efecto, el doctorando / la doctoranda expone el tema de la su tesis doctoral titulada _____

_____.

Acabada la lectura y después de dar respuesta a las cuestiones formuladas por los miembros titulares del tribunal, éste otorga la calificación:

☐ NO APTO ☐ APROBADO ☐ NOTABLE ☐ SOBRESALIENTE

(Nombre, apellidos y firma) Presidente/a		(Nombre, apellidos y firma) Secretario/a
(Nombre, apellidos y firma) Vocal	(Nombre, apellidos y firma) Vocal	(Nombre, apellidos y firma) Vocal

_____, _____ de _____ de _____

El resultado del escrutinio de los votos emitidos por los miembros titulares del tribunal, efectuado por la Escuela de Doctorado, a instancia de la Comisión de Doctorado de la UPC, otorga la MENCIÓN CUM LAUDE:

☐ SÍ ☐ NO

(Nombre, apellidos y firma) Presidente de la Comisión Permanente de la Escuela de Doctorado	(Nombre, apellidos y firma) Secretario de la Comisión Permanente de la Escuela de Doctorado

Barcelona a _____ de _____ de _____

Dedicated to
my father...

Acknowledgments

First I would like to deeply thank Anne-Béatrice, Victoria and 'baby 2' (on her way) for their patience, encouragement and support throughout my PhD. I would like also to express my gratitude to my parents, brother, sister and my family for their constant moral support. From the start they always trust in me.

I would like also to express my sincere gratitude to my supervisor, Eugenio Oñate for giving me the opportunity to join the International Center for Numerical Methods in Engineering (CIMNE) and work under his supervision. He has strongly supported my work with deep enthusiasm and worthy ideas. His aptitude to go straight to the point together with his talent in studying and solving problems have made a crucial contribution to the outcome of this work. I wish also to thank Miguel Cervera and Raimon Jané for their continuous interest, support and guidance during this thesis.

I would like to warmly thank all of the former and present members of CIMNE who made the work place a friendly environment and who are now, more friends than colleagues: to Jorge S.Ronda with whom we had a great collaboration and interesting technical, for his continuous support in my research (Jorge, eres un crack y lo sabes); to Carlos Labra, Enrique Ortega, Ariel Eijo, Temo and Maurizio Bordone with whom I shared the office during years for his endless good mood, kindness and all of the discussions we had; to Riccardo Rossi, Pooyan Dadvand, Carlos Roig and Jordi Cotela for their support in the integration of the 1D implementation and reduced model into KRATOS and for their kindness and all of the interesting technical discussions we had; to Joaquin (Cartagena) for his endless confidence, friendship and 'salad-shared'; Adrian Silisque, Elke Pahl and Steffen Mohr who made Barcelona a place to enjoy; to GID Department for always being so nice, ready to help and supportive; to Miguel Angel y Lucia for your really good mood, to Alberto for listen and support me during his stage at Barcelona, you showed me a new way of living and Joaquin Arteaga, thanks to you I am writing this. Further thanks to all of the people who work at CIMNE. It was great working with you all. Thank you for your work and your motivation.

Sincere thanks to CIMNE-TIC department: Jordi Jimenez who is always positive and always enthusiastic and motivated by new projects, to Sergio Valero, maestro Sensei, maestro programador, Angel Priegue (Alias Cruchi) 'tranquilo Edu no pasa nada', Cruchi thanks for your patience and thank for the 'Cafe-relaxing time in plaza mayor' on Friday evening, Aleki who always bring a great atmosphere to the office; Claudio Zinggerling for your professionalism and all of

the discussions we had on different subjects and his friendly support; Andy for his friendliness; Francesc Campá for his good mood and friendship and Alberto Tena for his kindness....por cierto, la undécima ESTA DADA!!!

Many great collaborations in the clinical setting were possible during the project. To those who contributed, thank you. Special thanks go to Dr.Francesc Carreras, Dr.Xavier Alomar and Dr.Pedro Hion-Li. at the Hospital Sant Pau i Creu Blanca, all of whom gave me the chance to discover the clinical environment and freely shared with me their inestimable knowledge.

Further thanks to all of co-authors have contributed to the achievement of this thesis, thank you very much. This work would not be possible without your support.

Most of all, I would like to warmly thank all the friends from PALENCIA and VALLADOLID. You always have been there.

Eduardo Soudah Prieto
Barcelona, 4 Noviembre.

Presentation

This thesis has been structured following the normative for PhD Thesis as a compendium of publications to obtain the degree of International Doctor in Biomedical Engineer. It was approved by 'Comissió de programa de Doctorat en Enginyeria Biomedica' on 15^{th} December 2015. The studies included in the Thesis belong to the same research line, leading to four papers already published in international journals.

Paper 1.
Title: A Reduced Order Model based on Coupled 1D/3D Finite Element Simulations for an Efficient Analysis of Hemodynamics Problems.
Authors: E.Soudah, R.Rossi, S.Idelsohn, E.Oñate.
Journal: Journal of Computational Mechanics. (2014) 54:1013-1022.
DOI: 10.1007/s00466-014-1040-2

Paper 2.
Title: CFD Modelling of Abdominal Aortic Aneurysm on Hemodynamic Loads using a Realistic Geometry with CT.
Authors: E.Soudah, E.Y.K. Ng, T.H Loong, M.Bordone, P. Uei and N.Sriram.
Journal: Computational and Mathematical Methods in Medicine. Volume 2013 - 472564, 01/06/2013.
DOI: 10.1155/2013/472564

Paper 3.
Title: Modelling human tissues an efficient integrated methodology.
Authors: M.Cerrolaza, G.Gavidia, E.Soudah, M. Martín-Landrove.
Journal: Biomedical Engineering: Applications, Basis and Communications. (2014) Vol. 26, No 1. 1450012.
DOI: 10.4015/S1016237214500124

Paper 4.

Title: Mechanical stress in abdominal aortic aneurysms using artificial neural networks.
Authors: Eduardo Soudah, José F. Rodríguez, Roberto López
Journal of Mechanics in Medicine and Biology. Vol. 15, No. 3 (2015) 1550029
DOI: 10.1142/S0219519415500293

Articles are reprinted with permission, and have been reformatted to fit the layout of the thesis. In addition, the 'Comissió de programa de Doctorat en Enginyeria Biomedica' confirm that none of the co-authors has used, or is going to use, any of the articles here presented in another PhD Thesis.

Contents

List of Figures

List of Tables

Abstract

In recent years, the study of computational hemodynamics within anatomically complex vascular regions has generated great interest among clinicians. The progress in computational fluid dynamics, image processing and high-performance computing have allowed us to identify the candidate vascular regions for the appearance of cardiovascular diseases and to predict how this disease may evolve. Medicine currently uses a paradigm called diagnosis. In this thesis we attempt to introduce into medicine the predictive paradigm that has been used in engineering for many years. The objective of this thesis is therefore to develop predictive models based on diagnostic indicators for cardiovascular pathologies.

We try to predict the evolution of aortic abdominal aneurysm, aortic coarctation and coronary artery disease in a personalized way for each patient. To understand how the cardiovascular pathology will evolve and when it will become a health risk, it is necessary to develop new technologies by merging medical imaging and computational science. We propose diagnostic indicators that can improve the diagnosis and predict the evolution of the disease more efficiently than the methods used until now. In particular, a new methodology for computing diagnostic indicators based on computational hemodynamics and medical imaging is proposed. We have worked with data of anonymous patients to create real predictive technology that will allow us to continue advancing in personalized medicine and generate more sustainable health systems. However, our final aim is to achieve an impact at a clinical level. Several groups have tried to create predictive models for cardiovascular pathologies, but they have not yet begun to use them in clinical practice. Our objective is to go further and obtain predictive variables to be used practically in the clinical field.

It is to be hoped that in the future extremely precise databases of all of our anatomy and physiology will be available to doctors. These data can be used for predictive models to improve diagnosis or to improve therapies or personalized treatments.

Resumen

Durante los últimos años, el estudio de las enfermedades cardiovasculares mediante el uso técnicas computacionales ha generado muchas expectativas en el campo de la medicina. Los avances realizados en técnicas de procesamiento de imágenes, métodos computacionales y el uso de grandes procesadores de cálculo han permitido identificar y correlacionar variables hemodinámicas con los estados incipientes o de desarrollo de patologías cardiovasculares. Hoy en día la medicina se basa en el diagnóstico, pero en esta tesis queremos tratar de introducir el concepto de medicina computacional preventiva. El objetivo principal es desarrollar modelos preventivos basados en indicadores de diagnóstico para patologías car-diovasculares combinando procesamiento de imágenes y técnicas computacionales.

En esta tesis, tratamos de predecir la evolución de aneurismas abdominales o la formación del trombo intraluminal en el interior del saco aneurismático, estudio de la ateroesclerosis y de la coartación de aorta, así como, posibles problemas derivados de la válvula aórtica de manera personalizada a cada paciente. Para entender cómo una patología cardiovascular evolucionará y cuándo va a convertirse en un riesgo para la salud, es necesario desarrollar una metodología eficiente que permita calcular indicadores de diagnóstico. En esta tesis, hemos propuesto indicadores de diagnóstico basados en técnicas computacionales e imágenes médicas que pueden mejorar el diagnóstico y a la vez podrían predecir la evolución de una patología de manera más eficiente que los métodos utilizados hasta ahora. Sin embargo, el objetivo final es llevar dichos indicadores a la práctica clínica. Actualmente estamos trabajando con datos de pacientes anónimos para crear una gran base de datos que nos permita avanzar en la medicina personalizada y en la generación de sistemas de salud más sostenibles. Es de esperar que en el futuro existan estas bases de datos a disposición de los médicos, y que estos datos se puedan utilizar para mejorar el diagnóstico o para mejorar terapias o tratamientos personalizados.

Resum

En els últims anys, l'estudi de l'hemodinàmica computacional en regions vasculars anatòmicament complexes ha generat un gran interès entre els clínics. El progrés obtingut en la dinàmica de fluids computacional, en el processament d'imatges i en la computació d'alt rendiment ha permès identificar regions vasculars on poden aparèixer malalties cardiovasculars, així com predir-ne l'evolució. Actualment, la medicina utilitza un paradigma anomenat diagnòstic. En aquesta tesi s'intenta introduir en la medicina el paradigma predictiu utilitzat des de fa molts anys en l'enginyeria. Per tant, aquesta tesi té com a objectiu desenvolupar models predictius basats en indicadors de diagnòstic de patologies cardiovasculars.

Tractem de predir l'evolució de l'aneurisma d'aorta abdominal, la coartació aòrtica i la malaltia coronària de forma personalitzada per a cada pacient. Per entendre com la patologia cardiovascular evolucionarà i quan suposarà un risc per a la salut, cal desenvolupar noves tecnologies mitjançant la combinació de les imatges mèdiques i la ciència computacional. Proposem uns indicadors que poden millorar el diagnòstic i predir l'evolució de la malaltia de manera més eficient que els mètodes utilitzats fins ara. En particular, es proposa una nova metodologia per al càlcul dels indicadors de diagnòstic basada en l'hemodinàmica computacional i les imatges mèdiques. Hem treballat amb dades de pacients anònims per crear una tecnologia predictiva real que ens permetrà seguir avançant en la medicina personalitzada i generar sistemes de salut més sostenibles. Però el nostre objectiu final és aconseguir un impacte en lŠàmbit clínic. Diversos grups han tractat de crear models predictius per a les patologies cardiovasculars, però encara no han començat a utilitzar-les en la pràctica clínica. El nostre objectiu és anar més enllà i obtenir variables predictives que es puguin utilitzar de forma pràctica en el camp clínic.

Es pot preveure que en el futur tots els metges disposaran de bases de dades molt precises de tota la nostra anatomia i fisiologia. Aquestes dades es poden utilitzar en els models predictius per millorar el diagnòstic o per millorar teràpies o tractaments personalitzats.

Chapter 1

Introduction

Clinical evidences have always allowed us to identify the candidate vascular regions for the appearance of cardiovascular diseases and to predict how these diseases may evolve. These clinical evidences are usually based on biological markers or anatomical indicators. However, over the last few years, thanks to the progress in computational hemodynamics, imaging processing, geometry reconstruction techniques and the increase in high-performance computing, variables such as, wall shear stress, wall elasticity, vorticity, turbulent kinetic energy, flow patterns or pressure drop, among others, have become new clinical evidences or diagnostic indicators (DIs), especially for cardiovascular diseases (CVD). Previously, patient-specific simulations were typically applied in advanced stages of disease progression, and consequently, from a medical point of view were a diagnosis-costly ineffective. In that sense, computational hemodynamics has emerged as a promising tool to estimate these new DIs and it's playing a key role in the understanding of CVD hemodynamics. The correlation of these new DIs with patient-specific data is needed to predict the development of cardiovascular pathologies and to improve the surgical strategies. In fact, these DIs are increasingly becoming a clinical reference standard for early diagnosis, treatment and prognosis allowing a better stratification of patients with disease stage adapted therapy instead of escalating to the most aggressive and costly therapy. Therefore, the precise knowledge and understanding of computational hemodynamics has become a necessity of the medical community, which includes the cardiovascular physiology, medical imaging and Computational Fluid Dynamics (CFD).

The purpose of this chapter is to give an outline of the most common diagnostic indicators used in cardiovascular diseases, as well as, the objectives and the methodology used in this thesis.

1.1 Biomechanical forces

It is well-known that the interactions of pulsatile blood flow with arterial geometries generate complex biomechanical forces on the vessel wall with spatial and temporal variations. Those biomechanical forces act over the internal layer of the arteries, endothelium. The endothelium produces a wide array of biochemical signals (homeostatic mediators) under physiological con-

ditions [102][21] keeping the artery healthy. A key stimulus to maintain the protective status of the endothelial lining at the inner vessel wall is the tangential force that blood flow exerts on it; this tangential force is known as wall shear stress (WSS) (figure 1.1). Fluctuations of the wall shear stress provoke changes in the biochemical signals[104], may arise the initiation and progression some cardiovascular diseases. For example, the growth or possibly rupture of the aneurysm wall[40], plaque instability in the carotid bifurcation[16][15] or in the coronaries [35][103], thrombus formation[41][22] or playing an important role in atherogenesis[3][10]. From a clinical stand point, the assessment of hemodynamic forces within the cardiovascular system circulation is still a challenge for the medical community, due to the three dimensional blood flow patterns close to the arterial wall needs to be measured in vivo. For that reason, computational hemodynamics has emerged as important tool for the clinician, allowing to quantify those hemodynamic forces and to correlate with the progression of cardiovascular pathologies.

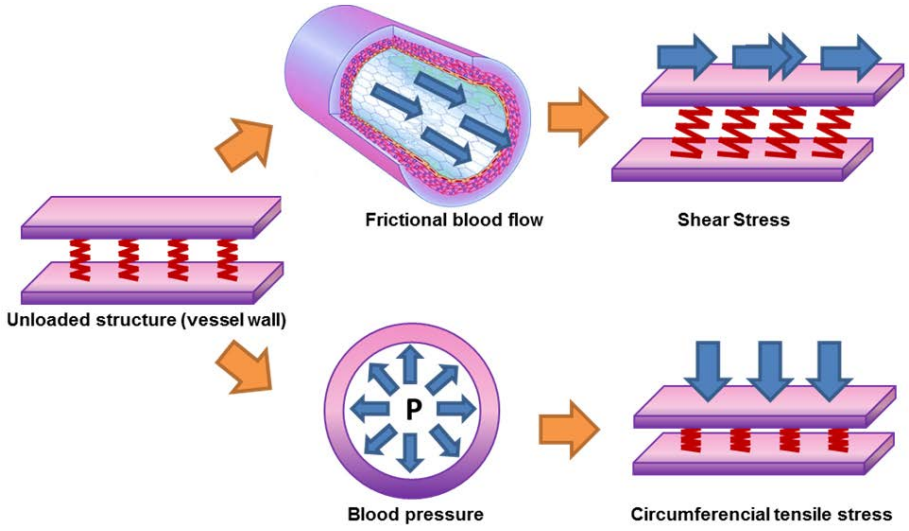

Figure 1.1: Biomechanical forces acting on the arterial wall. Blood pressure and blood flow induce forces in the vascular system that lead the initiation or progression of some cardiovascular diseases. Blood pressure produces a force directed perpendicular to the vessel wall. As a consequence, the cylindrical structure will be stretched circumferentially, resulting in a circumferential stress. In contrast, the force induced by a difference in movement of blood and the non-moving vessel wall leads to stress and strain parallel to the surface of endothelial cells. Due to its shearing deformation, this is called a shear stress. This shear stress exerts its main effects through the activation of mechanosensitive receptors and signalling pathways.

1.2 Diagnostic Indicators

As pointed out, blood flow induces a reaction force Fμ over vessel wall. The reaction force depends of the contact surface, blood-surface interface and velocity gradient between the vessel wall and blood adjacent layers[70]. For a viscous isotropic incompressible fluid, the constitutive relation between τ_{ij} and the strain rate tensor $d_{ij} = 1/2 \cdot (u_{i,j} + u_{j,i})$ is:

$$\tau_{ij} = 2 \cdot \mu \cdot d_{ij} = \mu \left(\frac{\delta u_i}{\delta x_j} + \frac{\delta u_j}{\delta x_i} \right) \tag{1.1}$$

where μ is fluid dynamic viscosity, where $\mathbf{u}$ the fluid velocity, $\delta / x_{i,j}$ is the distance to the vessel wall and τ_{ij} is the wall shear stress. If τ_{ij} is proportional to the deviatoric stress tensor (relation between the shear stress and the strain rate is linear), the fluid is known as Newtonian fluid. And when the relation between the deviatoric shear stress and the strain rate tensor is nonlinear, the fluid is known as Non-Newtonian fluid. Therefore, the relationship between the deviatoric stress tensor and the strain rate tensor models defined the rheological behavior of a fluid. Perktold et al.[70] pointed out how the errors deriving from employing a Newtonian model for blood yield non-essential differences in flow characteristics and wall shear stress distributions. In this thesis, a rigid wall (no slippage is allowed) and blood (see appendix A) as Newtonian fluid are considered, therefore WSS can be defined as:

$$\tau_{ij} = \mathbf{WSS} = \mu \cdot \dot{\gamma} = \mu \cdot \frac{\delta u_j}{\delta x_i} \tag{1.2}$$

where $\dot{\gamma}(\text{sec}^{-}1)$ is the shear rate $(\delta u_j / \delta x_i)$, where $\mathbf{u}_j$ is the parallel blood fluid velocity to the wall and x_i the normal distance to the arterial wall. Figure 1.2 shows the blood flood hemodynamic forces acting on vessel wall. When analyzing a cardiac flow (pulsating flow), it may be of

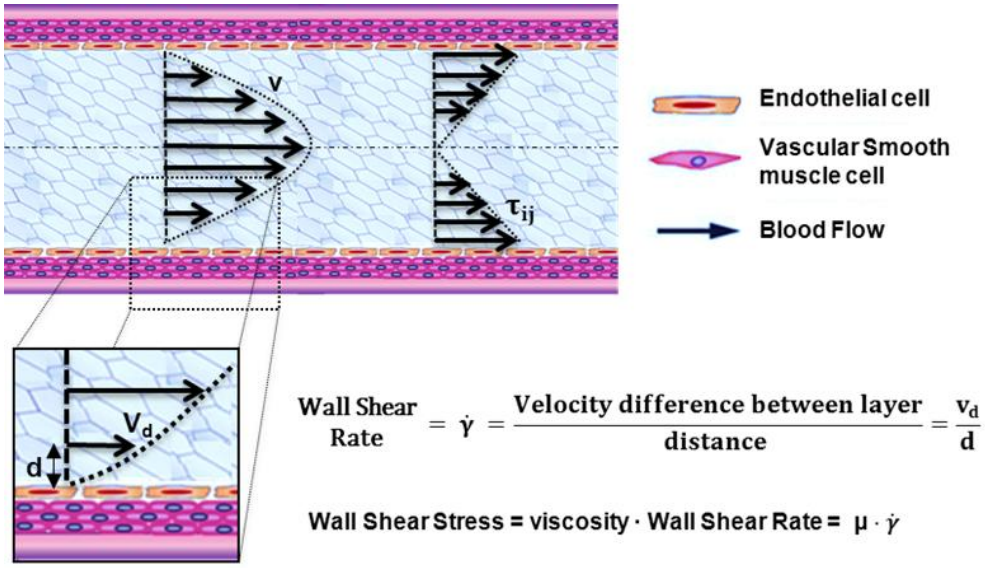

Figure 1.2: Hemodynamic forces that act on blood vessels. Wall shear stress (WSS) is proportional to the product of the blood viscosity (μ) and the spatial gradient of blood velocity at the wall (dv/dy).

interest to quantify the average load at a certain instant of the cardiac cycle, as time averaged WSS (TAWSS). Usually, WSS distributions is normalized by the average parent vessel WSS in the same

patient to allow comparison among different patients[87][108]

$$TAWSS = \frac{1}{T} \cdot \left| \int_0^T \mathbf{WSS} \cdot dt \right| \tag{1.3}$$

where WSS is the instantaneous shear stress vector and T is the duration of the cycle. Another parameter related to WSS oscillations is the oscillatory shear index (OSI)[16]:

$$OSI = \frac{1}{2} \left[1 - \frac{\left| \int_0^T \mathbf{WSS} \cdot dt \right|}{\int_0^T |\mathbf{WSS}| \cdot dt} \right] \tag{1.4}$$

Oscillatory shear index is used to identify regions on the vessels wall subjected to highly oscillating WSS values during the cardiac cycle. For example, a purely oscillatory flow with equal forward and backward contributions will produce an OSI of 0.5; however, in unidirectional flows the OSI will be identically zero. High OSI induces region with perturbed endothelial alignment. These regions are usually associated with bifurcations flows and vortex formation that are strictly related to atherosclerotic plaque formation and fibrointimal hyperplasia.

Based on wall shear stress, and its temporal and spatial variations, other indices have been proposed to capture the mechanobiological effects over the endothelium[53], such us, relative residence time(RRT)[37], particle residence time(PRT)[91] or endothelial cell activation potential (ECAP)[22]. Relative Residence Time (RRT) is defined as the state of disturbed flow. The residence time of the blood near the wall is reflected by combination of WSS and OSI. Mathematically, RRT is inversely proportional to the magnitude of the time-averaged WSS vector:

$$RRT = \frac{1}{(1 - 2 \cdot OSI) \cdot TAWSS} \tag{1.5}$$

The particle residence time describes flow stagnation or recirculation, for example in the abdominal aneurysm [22] or cerebral aneurysm [90]. ECAP is defined the endothelial susceptibility, and correlate the TAWSS with the OSI:

$$ECAP = \frac{OSI}{TAWSS} \tag{1.6}$$

The main purpose of this index is to identify local regions of the wall that can be exposed to prothrombotic WSS stimuli. Higher values of the ECAP index will thereby correspond to situations of large OSI and small TAWSS, that is, i.e. in abdominal aneurysm, intraluminal thrombus (ILT) development.

Nowadays, the combination of these WSS based-indicators are employed as promising hemodynamic predictors of the cardiovascular pathologies (figure 1.3). Although, computational methods, medical imaging resolution and acquisition speed have increased over the past decades, assessment

of WSS is still challenging in complex flow geometries [74][58][7][65]. For that reason, a good modelization combined with a numerical simulation is still needed.

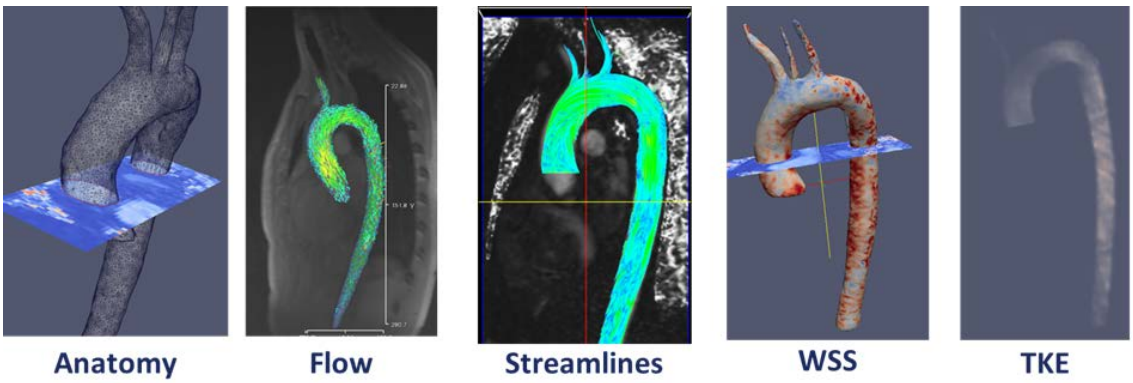

Figure 1.3: Diagnostic Indicators in a patient-specific model

Other importance feature in many cardiovascular diseases is the helical flow patterns and turbulent blood flow, characterized by fast random temporal and spatial velocities fluctuations[64]. These irregular and rapid fluctuations are not present in healthy situations, and play also a key role in some cardiovascular pathologies. The helical flow patterns show a measure(index) of blood flow complexity, and therefore, is an important factor in the development of cardiovascular disease, as shown in figure 1.4. Given the fluid flow velocity vector field **u**, the vorticity vector field **w** is the curl of the velocity field:

$$\mathbf{w} = \nabla \times \mathbf{u} \tag{1.7}$$

Basically, the vorticity vector points along the axis of spin, and the magnitude of the vorticity vector encodes the rate of spin. Given the vorticity vector field, mathematicians introduce several useful additional concepts: vortex lines, vortex sheets and vortex tubes. Technically speaking, vortex lines are the integral curves of the vorticity vector field; this simply means that vortex lines are curves which are tangent to the vorticity field at each point. Vortex sheets, meanwhile, are surfaces which are tangent to the vorticity field at all points. Vortex tubes are three-dimensional regions obtained by taking a 2 dimensional area orthogonal to the vorticity field, and then taking all the vortex lines through that area. Now, the **helicity (h)** is defined as the inner product of the velocity and the vorticity:

$$\mathbf{h} = \mathbf{u} \ \ \mathbf{w} \tag{1.8}$$

Thus, if the streamlines of the fluid are orthogonal to the vorticity, then the helicity is zero. This is the case with a transverse vortex. In the case of a longitudinal vortex, the helicity is non-zero, and measures how tightly the streamlines corkscrew along a vortex tube. In fact, the helicity of a

vortex tube can be defined by integrating the helicity field:

$$\mathbf{H} = \int \mathbf{u} \cdot (\nabla \, x \, \mathbf{u}) \cdot d^3 r \tag{1.9}$$

It is a theorem of inviscid fluid mechanics that the helicity of a vortex tube is preserved over time. However, if a vortex tube is stretched, then its cross sectional area decreases, and the magnitude of the vorticity w increases, lowering the pressure at the center of the vortex. So, from a blood flow dynamics, the stretching of longitudinal vortex tubes could be a indicators of a cardiovascular pathology [4]. These effects are directly correlated with the oscillatory shear index [16].

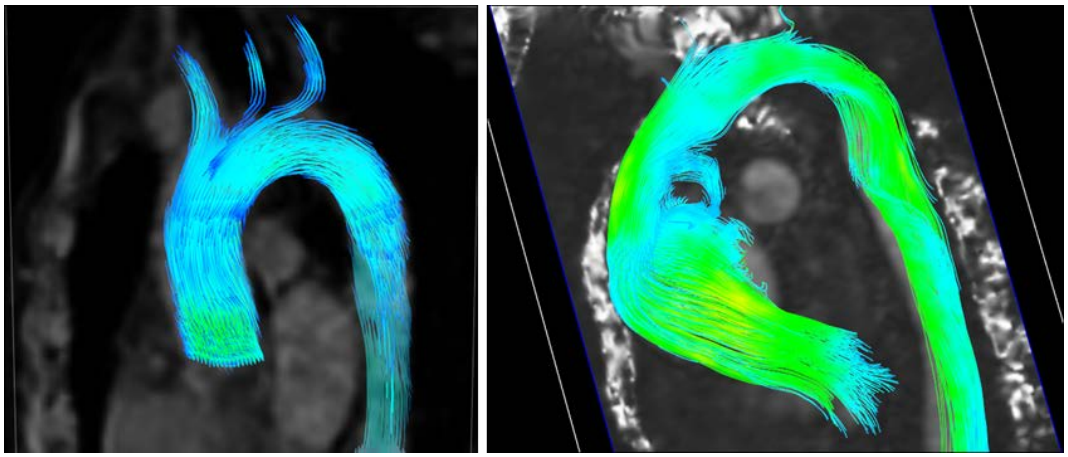

Figure 1.4: Left: Streamlines in a healthy aorta. Right: Streamlines in unhealthy aorta

Another index to evaluate blood complexity is to measure the Turbulent Kinetic Energy (TKE). The velocity and the turbulent kinetic energy combined can give a visualization of disturbed flow. Increased level of TKE indicates more turbulent flow, and it is undesirable for the cardiovascular system. For this reason, analyzing and understanding energy transfer and dissipation in some cardiovascular pathologies is important for the clinician. From mathematical point of view, the turbulent kinetic energy is calculated and defined as half sum of the variance of the velocity fluctuations:

$$TKE = \frac{1}{2} \cdot (\overline{u'^2} + \overline{v'^2} + \overline{w'^2}) \tag{1.10}$$

The pressure is also an important indicator about the arteries status, due to represents the hemodynamic forces within the cardiovascular system circulation. Nowadays, the pressure drop (or gradient) has been evaluated as powerful predictors of epicardial coronary disease or aortic Coarctation. From a clinical standpoint, the assessment of hemodynamic forces within the coronaries circulation (or Aorta) is still difficult, because pressure can be only measured invasively and flow cannot be measured directly with Doppler ultrasound in small deep coronary vessels, as the coronaries.

For that reason, computational hemodynamic becomes a promising tool to estimate the pressure non-invasively. For example, pressure-derived myocardial Fractional Flow Reserve index(FFR) is the standard goal for determining the physiological significance of a coronary stenosis[73]. FFR index is calculated as the ratio of the distal pressure to the stenosis/coartaction by the proximal pressure to the lesion in a non-rest situation (or maximum effort). Furthermore, the clinicians are able to reproduce several patient-conditions modifying the boundary conditions of computational model, based only on a medical image. The clinicians should simulate a non-inducing stress situation to the patient reducing the intervention costs. The capability of computing the pressure drop without pressure-wire has gained wide acceptance in the clinical community in the recent years[94][100].

1.2.1 Clinical practice & Diagnostic Indicators

The purpose of this section is doing a review of how the Diagnostic Indicators (above mentioned) can be applied into a clinical practice.

1.2.1.1 Atherosclerosis

Atherosclerosis is a disease in which plaque builds up inside your arteries. Plaque is made up of fat, cholesterol, calcium, and other substances found in the blood. Over time, plaque hardens and narrows your arteries, and in advanced phases of atherosclerosis, plaque becomes vulnerable. This limits the flow of oxygen-rich blood to your organs and other parts of your body and a possible rupture of vulnerable (or unstable) plaque exposes thrombogenic material, such as collagen to the circulation and eventually induces thrombus formation in the lumen. Plaque rupture can occur whenever plaque stress exceeds the plaque strength and thus the prediction of plaque rupture may be augmented by accurate assessment of hemodynamic forces [11]. Atherosclerosis can affect any artery in the body, including arteries in the heart, brain, arms, legs, pelvis, and kidneys, and mainly affects middle and large sized arteries near side branches and at the inner bend of curved segments. At these locations, the average normalized drag force of the flowing blood acting on the vessel wall, the wall shear stress (WSS), is low and/or turbulent leading to endothelial dysfunction and ingress of lipids into the vessel wall, initiating an inflammatory response. Thus in the early phases of the disease WSS can predict locations of plaque initiation and progression[86]. In more advanced stages of disease, when plaque growth results in lumen narrowing, the local WSS patterns will change such that certain plaque regions to mainly located upstream- are exposed to elevated WSS[32]. Evidence is accumulating that the elevated WSS influences plaque composition in such a way that it induces local weakening of the plaque, making plaque regions exposed to high WSS prone to rupture[34][30] [31]. Clinical studies confirmed these findings: plaque rupture, both in coronary arteries and carotid arteries are observed more frequently in the upstream of the plaque[55][19][110]. Shear stress with a low mean or maximum value and varying direction (oscillating shear stress) has been associated with development of plaque vulnerability. As a result, different diseases may develop based on which arteries are affected, for example, acute myocardial infarction is mainly triggered by rupture of so-called vulnerable plaques in the

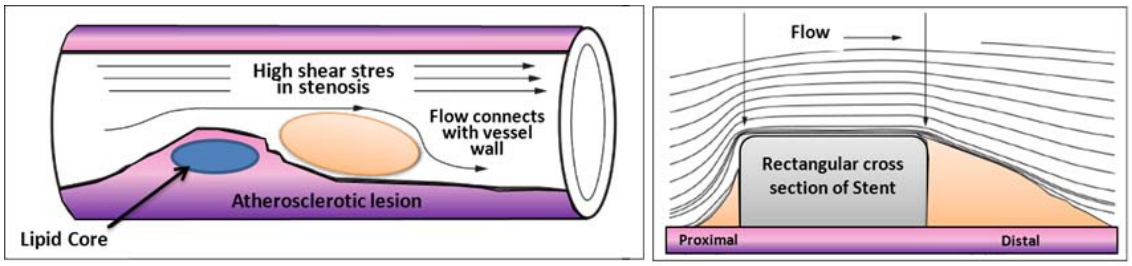

Figure 1.5: Left, Atherosclerosis lesion. Right, Flow around rectangular section of stent

coronary arteries linked with the coronary stenosis. In [69] there is a review comparing the localization of atherosclerotic lesions with the distribution of haemodynamic indicators calculated using computational fluid dynamics.

1.2.2 Coronary Artery Disease

Coronary artery disease(CAD) is the most common type of heart disease and cause of heart attacks. CAD is caused by abnormal narrowing of the coronary arteries (coronary stenosis) resulting in reduction of blood flow to the heart. The stenosis impedes to deliver oxygen to the heart muscle, which provoking heart attack. This disease is directly related with the atherosclerosis plaque. When stenosis occurs, the common clinical practice for decision taking related to the need (or not) of implanting a stent in a obstructed coronary artery requires the measurement of the Fractional Flow Reserve (FFR). FFR is derived from measuring the ratio of aortic pressure and pressure beyond a stenosis. Stenting is a specialized treatment for coronary arteries that are narrowed or blocked by plaques. It involves placing a balloon into the narrowed portion of the coronary artery with a surrounding wire mesh (stent). When the balloon is expanded, the stent remains in the vessel keeping the plaque pushed outwards, to let blood flow to the heart pass by.

From the technical point of view, invasive FFR measurement is often flawed by submaximal hyperemia (underestimating the stenosis severity) and by issues related to the guiding catheter[73]. A large guiding catheter may interfere with maximum blood flow and a guiding catheter with side holes may influence proximal coronary pressure and interfere with intracoronary administration of adenosine. Animal studies have suggested that a significant portion of subjects undergoing invasive FFR with adenosine do not achieve maximal hyperemia[43]. This suggests that the physiologic significance of some lesions may be underestimated when using standard current vasodilator doses and that higher, potentially toxic doses, may be needed in order to achieve maximal hyperemia. From clinical point of view, invasive FFR is unable to depict the coronary culprit lesion in cases of serial coronary lesions or in case of lesions in side branches of bifurcations[48], [18].For this reason less than 10% of European patients are subject to an invasive FFR measurement. In recent years, several alternative methods based on Computational Fluid Dynamics (CFD) have been proposed for non-invasive estimation of coronary blood flow circulation [85]. CFD has been applied to coronary computed tomography angiography for computation of FFR. However, accuracy of method[47],[63] and diagnostic accuracy remains suboptimal[105]. The main challenges

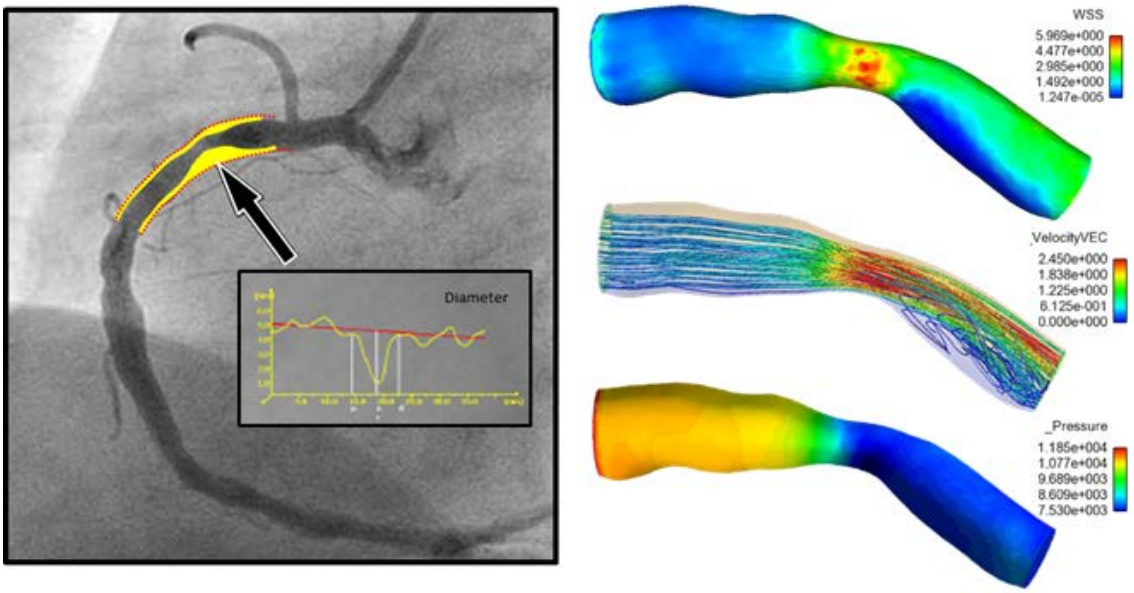

Figure 1.6: Streamline and wall shear stress in a coronary artery

for such methods are the lack of patient-specific data including anatomy, patient-specific boundary conditions, the condition of the microvasculature of the myocardium, and the large-scale computational resources required for the complex calculations. In [92] pressure gradients are computed using CFD in which the geometry of the aorta is extracted from MRA. Additional MR Phase contrast imaging is performed to measure the velocity which is used as boundary conditions. In [94], lumped parameter models of the heart, systemic circulation and coronary microcirculation are coupled to a patient specific 3D model of the aortic root and epicardial coronary arteries extracted from CTA. Disadvantages of these approaches are that all calculations are performed exclusively in 3D as well as the fact that the calculations cannot be performed during intervention because of the need for CT. Moreover, one vital piece of information is still missing in CFD, namely the condition of the coronary circulatory auto-regulation, also known as the patients cardiac flow reserve. This results in a method that is of high computational complexity. A recent study applied CFD to three dimensional X-ray angiography for the computation of the FFR incorporating the coronary flow reserve[98] . However, this method requires X-ray angiographic imaging during hyperemia which is a burden to the patient. Placing known side effects of adenosine into perspective; reduced blood flow to the heart which might worsen symptoms in patients with coronary heart diseases or even cause a heart attack, this is clearly an undesired situation especially during diagnostic coronary angiography.

1.2.2.1 Aortic Aneurysms

The aortic dilatation is an asymptomatic disease with complicated and lethal sharp pains that can occur anywhere in the human aorta. By definition, if the aorta diameter at least is 50% greater than the normal size of the aorta produces what is called "aneurysm". And if this occurs in the thoracic

aorta is termed a Thoracic Aortic Aneurysm(TAA), in the abdominal aorta is named Abdominal Aortic Aneurysm(AAA). However, the aneurysm pathogenesis is still unknown. It is thought that

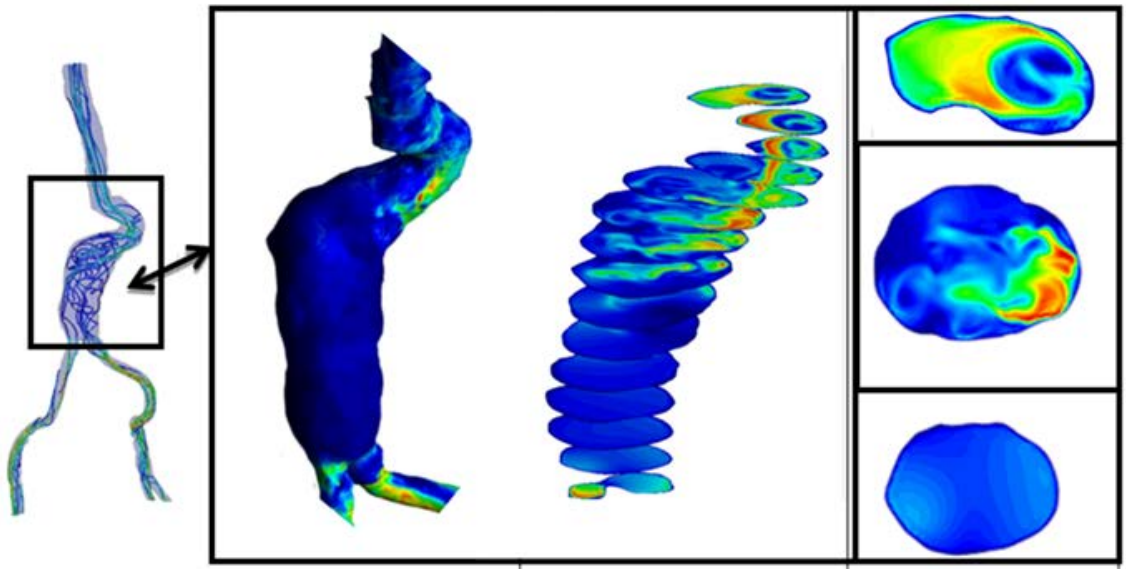

Figure 1.7: Diagnostic Indicators in Aortic Abdominal Aneurysm. Streamlines, wall shear stress and velocity profiles at different section of the aneurismatic sac.[87]

the initial dilatation is caused partly by degeneration of the medial elastin and smooth muscles in the arterial wall or by the effect of the wall shear stress. Vessel wall remodelling as a result of shear stress alteration is accompanied by synthesis and secretion of *NO*, growth factors and metalloproteins, which contribute to aneurysm pathogenesis. Genetics and risk factors like smoking, hypertension, chronic obstructive pulmonary disease(COPD), inflammation and atherosclerosis play key roles in aneurysms genesis and progression[12]. In this context, there are few predictors of the aorta dilatation available in the clinical practice. Mainly, they are based on the aortic diameter and increasing aortic size. Currently, the accepted values have been changing over time and they are actually being discussed by the groups with experience, for example, [81][66] in TAA patients or [82][79] in AAA patients. There is also a hemodynamic factor of parietal stress in the aortic dilatation, which is currently a little-known factor. Prior works, related TAA, have confirmed the presence of different flux in bicuspid aortic valve without aortic dilation compared to tricuspid aortic valves patterns by using cardiac magnetic resonance imaging (cardiac MRI). Abnormal flow patterns have been also detected in aneurysms located in the ascending aorta which confirms flow jets to the anterolateral wall of the aorta [20]. It is also known that shear stresses play an important role in the initiation, progression and rupture of aneurysms[9][95]. Vorticity inside the aneurysm is connected to aneurysm plaque or thrombus formation [40][22]. Figure 1.7 shows some DI's in an Aortic Abdominal Aneurysm(AAA).

1.2.2.2 Aortic Coarctation

Aortic coarctation(CoA) occurs approximately in 10% of patients with congenital heart defects and represents a narrowing of the descending aorta (see paper 1). Due to the reduction in the aorta descending diameter, high pressure gradients can appear across the CoA, resulting in an increased cardiac workload in the left ventricle during systole [44]. The narrowing of the aorta creates a flow jet with high velocity, inducing a very complex turbulent flow field. Recently, researchers has characterized changes of hemodynamic parameters such as pulse blood pressure, aortic capacitance, and wall shear stress due to the presence of an aortic coarctation [44][49][51]. Hemodynamic changes caused by the coarctation can result in endothelial dysfunction [62], provoking non normal values of TAWSS or elevated OSI for CoA patients.

1.3 Objectives

The general objective in this thesis is improving computational hemodynamics to develop patient specific diagnostic indicators for an early identification of cardiovascular incumbent physiopathological state (and its progress). To reach this goal, this thesis attempts to improve the prior mathematical models used for cardiovascular system for a deeper understanding on the response of the cardiovascular system to:

- improve diagnostics and therapeutical procedures for Aorta Coarctation (paper 1 in Chapter 2),
- study the mechanical factors that may be important in triggering the onset of aneurysms (paper 2 in Chapter 3 and paper 4 in Chapter 5),
- combine medical images with computational hemodynamic to estimate DI's (Chapter 6) and
- use medical images data to generate computational model (paper 3 in Chapter 4).

Other applications studied based on the methodology developed in this work were, (i) a new method to estimate the fractional flow reserve (FFR) using CFD data, (ii) study of new mechanical factor related to the AAA and (iii) studied the effect of vorticity and the eccentricity of the aortic bicuspid valve (in Chapter 7).

From the methodology point of view, a new methodology to compute diagnostic indicators based on computational hemodynamics has been proposed. In order to compute the pressure drop under different patient-specific situations, a reduced-order model has been developed in paper 1. The reduced-order method was implemented as part of the C++ finite element library KRATOS[17]. KRATOS is a multiphysics simulation open source (LGPL licence) framework based on the stabilized Finite Element Method for analysis of the Navier-Stokes equations in viscous flows. Efficient and parallel solvers for 3D fluid problems have been implemented in KRATOS that allow tackling large problems using supercomputers if available. The 1D model developed in this thesis was also implemented as new elements inside KRATOS. Blood was modeled as a Newtonian fluid with constant density and different outlet conditions were implemented. In Appendix B a detail description of the implementation is shown.

Additionally, the diagnostic indicators have been correlated with the patient-specific geometry (paper 2). Once a 3D model of a vascular tree is obtained, the geometry is meshed having special attention in the near-wall region(boundary layer) using the tetrahedral (3D) elements. A good boundary layer mesh allows to properly capturing the sharp velocity gradients. The Navier-Stokes equations (see section 1.4.2) were solved with TDYN [14] to model blood flow in the normal and aneurysmatic abdominal aortas. For the 3D model, rigid wall was assumed and no-slip boundary condition was applied at the luminal wall. A volumetric/mass flow rate was applied at the inlet and a pressure wave was applied at the outlets. A python script implemented to compute WSS-based diagnostic indicator is shown in Appendix C. A new procedure to segment the aorta using 4D flow CMR data has been also proposed. Beyond this, 4D flow CMR visualization offer a qualitative and

comprehensive descriptions of the flow fields than any other in-vivo imaging technique (in chapter 7). The velocity data provided by 4D flow CMR has been complementary to the higher resolution velocity fields computed by the CFD in order to estimate the WSS. We have also developed an algorithm to compute WSS based on the 4D flow CMR data. To compute vorticity and helicity from a velocity field a Vascular Modeling Toolkit (VMTK) [4] was used. In spite of this, a new diagnostic indicator to estimate coronary artery disease based on computational hemodynamics has been also proposed (in chapter 7).

In this thesis, blood has been considered as incompressible and Newtonian fluid, and we will focus on the systemic arterial system and coronary circulation. Further information about Cardiovascular Physiology can be found in Appendix A. In the following, a brief summary of the methods employed to reach the objectives of this thesis is given below. For a complete description of the methodology used in this thesis see papers 1-4 in chapter 2-6, respectively.

1.4 Methodology

1.4.1 Patient-specific modelling

Patient-specific modeling is the development of computational models of human physiology that are individualized to patient-specific data. Imaging data can be stored in the Digital Imaging and Communication in Medicine (DICOM) format [6]. The DICOM format file contains two parts: the header which stores detailed information about the patient such as name, type of scan, ages, dimension of the image and the voxel, image position, and so forth. The second data set contains information of each scanned image. Segmentation of medical image was required to extract the geometry of the region of interest (or analysis). The segmentation process can include several procedures as threshold, region growing, centerline, among others, followed by 3D anatomical reconstruction to obtain a coarse solid model. During threshold, a range of gray scale values are selected such that the region to be selected is of the best contrast. After the regions of interest are extracted, the voxels are labelling together with an identificator to create the 3D geometry.

In paper 3 an efficient methodology for preprocessing and postprocessing medical images to generate computational meshes for numerical simulation is explained. A schematic flowchart for creating and validating a 3D patient-specific model is shown in Figure 5 of paper 3. Aneurysm models (patient-specific geometries) of paper 2 were reconstructed from computer tomography-angiography (CTA) scans using the diagnostic software ITK-SNAP[109] and DIPPO[13].

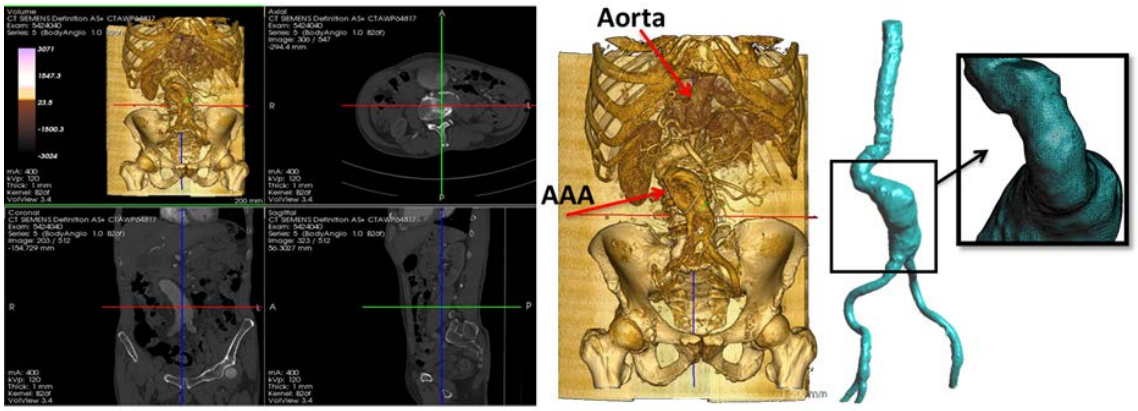

Figure 1.8: Left CT DICOM (sagital, coronal and axial images) of patient with Aortic Abdominal Aneurysm. Center CT volume render of Aortic Abdominal Aneurysm illustrating the Abdominal sac. Right computational patient-specific model and computational mesh

Both image processing programs employ active contour (deformable models) which move under the action of external forces according to the image intensity and first and second spatial image gradients. A schematic diagram depicting the segmentation of medical image at various locations of the Abdominal Aneurysm is shown in figure 1.8. Coronary models of chapter 7 were reconstructed from X-ray coronary angiography (XA). At the moment, X-ray coronary angiography is the standard technique for anatomical assessment of the coronary arteries and the diagnosis of

coronary artery disease. The 3D model reconstructed was based on two bi-dimensional images taken from different perspectives. Then the reconstruction of abdominal aneurysm anatomy or coronary into a computational mesh (computer model) is performed based on the segmentation information. To generate the computational mesh GiD Pre and Postprocessor [13] and the open source Vascular Modeling Toolkit (VMTK) [4] were used.

Next, a list of freely available tools for medical image processing and mesh generation using in the appended papers is outlined; VTK[83] is an open-source software toolkit for visualization, computer graphics and image processing with a great online community and numerous examples. VTK is cross platform with implementations for Windows, Mac Os and Linux. Users can code in C++, Java, Phyton or TCL. Knowlegde of VTK means that developers can take advantage of other tools sush as ITK, ITK-SANP or IGSTK[25], to name a few. ITK[38] is an open-source, cross-platform system that sits on top of VTK. It provides developers with an extensive suite of software tools for image analysis. ITK-SNAP[109] is a freely available tool built on ITK and VTK for image manipulation. The source code for ITK-SNAP is part of ITK Applications, so developers can add their own modifications. DCMTK[1] is a collection of libraries and applications for reading, writing and otherwise manipulating DICOM images. It works with multiple operating systems. VMTK[4] is collection of applications for pre and postprocessing medical images.

1.4.1.1 4D flow cardiovascular magnetic resonance imaging

At present, 4D flow cardiovascular magnetic resonance imaging (4D CMRI) sequences are being a promising tool to visualize and quantify 4D (3D+t) blood flow. From these sequences the raw data can be obtained and conveniently processed, allowing visualization of the blood flow patterns in any segment of the cardiovascular tree[59][50][72]. Nevertheless, the visualization of these images entails an important manual work, becoming a very time-dependent task and then turning out to be not useful in the current clinical practice. Therefore, it is important to improve the technology and the methods of automatic representation of the 4D blood flows, in particular for the WSS analysis. In chapter 6, it is demonstrated that 4D flow CMRI technique is a reliable tool to provide the boundary conditions for the Computational Fluid Dynamics(CFD) in order to estimate the WSS within the entire thoracic aorta in a short computation time. Our image-based CFD methodology exploits the morphological MRI for geometry modelling and 4D flow CMRI for setting the boundary conditions for the fluid dynamics modelling. The aim is to evaluate visualization of well-defined aortic blood flow features and the associated wall shear stress by the combination of both techniques. In that sense, CIMNE has developed a home-made ad-hoc software (Aorta4D) oriented to make progress in this field of work [50][89][72]. Aorta4D will afford analysis and spatially visualization of the registered 3-directional blood flow velocities, and perform a 3D semi-automatic segmentation based on the 4D flow CMRI data.

1.4.2 Computational hemodynamics

In this section we will limit to the essential description of mathematical equations that govern the blood flow and the most important dimensionless parameters characterizing the blood flow[29].

In this thesis, we consider blood as an homogeneous, incompressible, constant-density (ρ =1050 kg/m^3) and newtonian fluid with constant viscosity (μ =0.0035 Pa.s). Vascular walls are modeled as non-permeable, rigid walls (see section A). Under these assumptions, the conservation of mass and momentum in the compact form are described by the following system of partial differential equations (1.11):

$$\begin{aligned} \rho \cdot \left(\frac{\partial \mathbf{u}}{\partial \mathbf{t}} + (\mathbf{u} \cdot \bigtriangledown \mathbf{u}) \right) + \nabla\, p - \nabla \cdot (\mu \bigtriangleup \mathbf{u}) &= \rho \cdot \mathbf{f} \qquad \text{in } \Omega(0,t) \\ \nabla u &= 0 \qquad \text{in } \Omega(0,t) \end{aligned} \tag{1.11}$$

where Ω is a three-dimensional domain, **u** denotes the blood velocity, **p** is the pressure field, ρ density, μ the dynamic viscosity of the fluid and **f** the volumetric acceleration. Volumetric forces(ρ· **f**) and thermal effects are not considered in this thesis. The spatial discretization of the Navier-Stokes equations has been done by means of the finite element method (FEM), while for the time discretization an iterative algorithm that can be considered as an implicit fractional step method has been used [14][17]. Blood flow can be characterized by the Reynolds and Womersley [107] dimensionless number. These numbers correlate the inertial and viscous forces of the previous equation 1.11. The Womersley number is a dimensionless parameter that represents the ratio between oscillatory inertial forces and viscous forces. Physically, the Womersley number can be interpret as the ratio of artery diameter to the laminar boundary layer growth over the pulse period (characteristic frequency).

$$\alpha = \frac{D}{2} \cdot \sqrt{\frac{w\rho}{\mu}} \tag{1.12}$$

where **w** the characteristic frequency and D is the characteristic diameter. If α is high, the fluid is nonviscous, and If α is low, the viscosity of the fluid is high. Womersley number characterizes the unsteady of the blood flow. The ratio of the inertial force to the viscous forces is the dimensionless parameter called **Reynolds number**

$$RE = \frac{U^2 \rho}{\frac{\mu u}{D}} = \frac{LU\rho}{\mu} \tag{1.13}$$

When we have a large Reynolds number inertial forces are dominant over viscous forces and viceversa. This naturally leads us to the role of Reynolds number as the key parameter which identifies the transition of the flow to turbulence. Usually, Reynolds number suggests that in most arteries of the cardiovascular system the flow is laminar. The exceptions are the flow in severely stenotic vessels, where the flow regime can be become transitional or turbulent. Turbulence blood flow implies fluctuating pressure acting on the arterial wall, and fluctuating, increased shear stress, which can be provoke post-stenotic dilation or atherogenesis. In this thesis, blood flow has being considering laminar. Next image 1.9 shows the full process, from the medical image to the numerical simulation (Aortic Abdominal Aneurism imaging, geometry modelling, finite elements meshing and mechanical and hemodynamics numerical simulation)

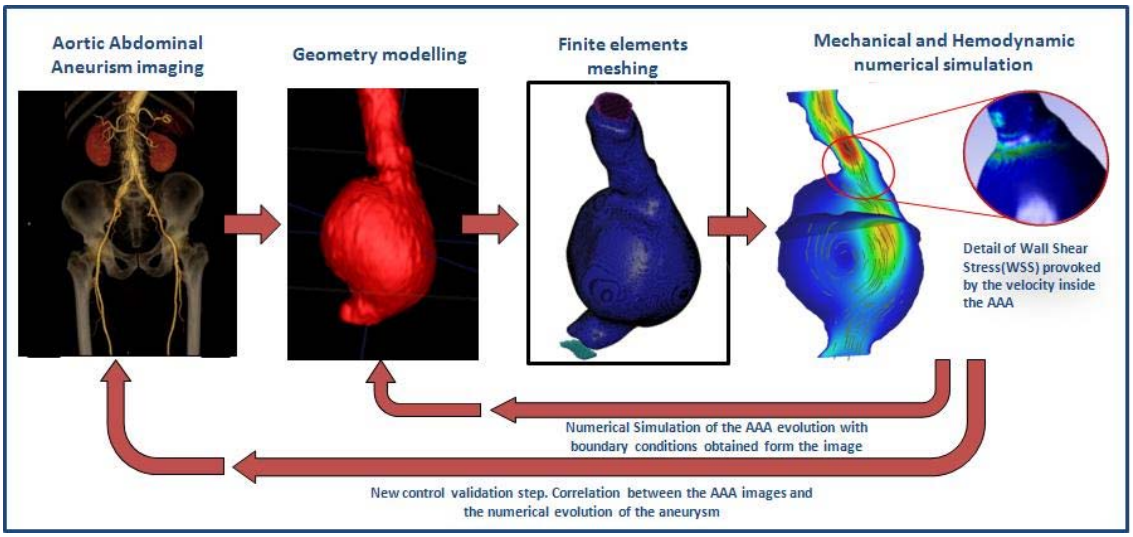

Figure 1.9: From the medical image to the simulation

1.4.2.1 Patient-specific boundary conditions

It is well known that to estimate properly the DI's, the specific patient-specific boundary conditions are needed. Several authors [42][76][93] have noted how inlet velocity profiles and flow waveform shapes play an non-negligible role on wall shear stress or pressure distributions. Nowadays, there are several medical techniques to perform velocity measurements inside large arteries in vivo and non-invasively, as Doppler Utrasound or phase-contrast magnetic resonance. Using this acquired data into the computational hemodynamical model will provide us enough information to perform our computational simulation. It should be pointed out that the conditions measured depend on physical activity and posture of the patient [52]. In chapter 2 and chapter 7 the technique uses to acquire the velocity information for the prescription of patient-specific boundary conditions was phase-contrast magnetic resonance.

Acquisition of boundary conditions by phase-contrast magnetic resonance: At present Cardiac Magnetic Resonance Imaging (MRI) image is the only non-invasive imaging modality that can measure 3D blood velocity in a 3D representation, and that allows visualization of spatial distribution of velocity in a two-dimensional plane (2D). This technique is valuable non-invasively tool for evaluation of the cardiovascular flow patterns owing to its unique possibility to simultaneously acquire sectional imaging without restriction, anatomy (magnitude image) and blood flow velocities(phase image) with a single scan. The majority of the commercial systems offer the bi-dimensional phase-contrast sequence to quantify blood velocity and derivative cardiac flow. These sequences are reliable and precise methods to calculate stroke volume for pulmonary/systemic flow ratios estimation (Qp:Qs) and to calculate volume regurgitation in valvular insufficiencies [54][88]. At present, the phase-contrast sequences are being developed to allow obtaining information of the 4D flow (see 1.4.1.1).

Boundary conditions from multiscale modeling of circulation: Another approach to impose

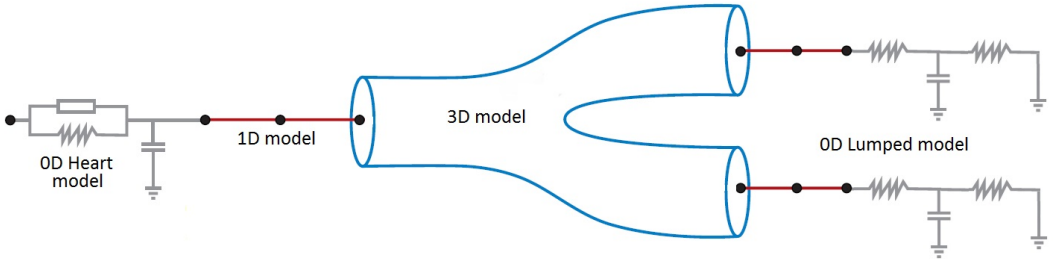

Figure 1.10: Coupling of 0D heart model, with 1D model (Systemic Circulation), 3D model (patient-specific geometry) and 0D lumped models (terminal resistance) to perform a computational analysis

the boundary conditions is to use reduced models, as 1D model or 0D (lumped) models. 1D and 0D models are mathematical models able to reproduce the systemic and pulmonary circulation by an 1D approach of the Navier-Stokes equations (see Appendix B) or by electrical analogy, respectively. Next figure 1.10 shows a standard approach to provide realistic local boundary conditions for 3D CFD simulations at the specific arterial domain using 1D models of the entire arterial tree, terminated with 0D models at the distal ends[99]. The values of the components (usually Resistance, Inductance and Capacitor) of the lumped model can be estimated from physical data of the subject [68][56]. This approach is quite used because it is capable to account for the effect of local pathological conditions on the whole circulatory system, providing realistic boundary conditions for the 3D problem [29][93][57].

1.4.3 Postprocessing

Output data were imported into GiD for post-processing[13]. A python script to compute WSS-based indicators was performed into EnSight[2] (Appendix C).

Chapter 2

A Reduced Order Model based on Coupled 1D/3D Finite Element Simulations for an Efficient Analysis of Hemodynamics Problems.

Title: A Reduced Order Model based on Coupled 1D/3D Finite Element Simulations for an Efficient Analysis of Hemodynamics Problems.
Authors: E.Soudah, R.Rossi, S.Idelsohn, E.Oñate.
Journal: Journal of Computational Mechanics. (2014) 54:1013-1022.
Received: 18 February 2014 / Accepted: 30 April 2014 / Published online: 23 May 2014
DOI: 10.1007/s00466-014-1040-2

Scientific contribution: Design of a new methodology to estimate the pressure drop in aortic coarctation under different scenarios. The methodology is based on the integration a 1D numerical model (see appendix B) into a reduced order model based on 3D CFD formulation.

Contribution to the paper:The principal author developed and implemented the 1D model and the reduced order model into the KRATOS Multi-Physics software (www.cimne.com/kratos)([17]).

Comput Mech (2014) 54:1013–1022
DOI 10.1007/s00466-014-1040-2

ORIGINAL PAPER

A reduced-order model based on the coupled 1D-3D finite element simulations for an efficient analysis of hemodynamics problems

Eduardo Soudah · Riccardo Rossi · Sergio Idelsohn · Eugenio Oñate

Received: 18 February 2014 / Accepted: 30 April 2014 / Published online: 23 May 2014

Abstract A reduced-order model for an efficient analysis of cardiovascular hemodynamics problems using multiscale approach is presented in this work. Starting from a patient-specific computational mesh obtained by medical imaging techniques, an analysis methodology based on a two-step automatic procedure is proposed. First a coupled 1D-3D Finite Element Simulation is performed and the results are used to adjust a reduced-order model of the 3D patient-specific area of interest. Then, this reduced-order model is coupled with the 1D model. In this way, three-dimensional effects are accounted for in the 1D model in a cost effective manner, allowing fast computation under different scenarios. The methodology proposed is validated using a patient-specific aortic coarctation model under rest and non-rest conditions.

Keywords Blood flow · Boundary conditions · Reduced-order models and Aortic coarctation

1 Introduction

The simulation of blood flow problems assumes a large importance in biomechanics due to the many potential fields of application. The use of realistic boundary conditions is essential to guarantee the performance and the accuracy of numerical simulations, especially in cardiovascular problems. In particular, the flow in arteries depends strongly on the outflow boundary conditions which model the downstream domain. The application of constant tractions as outlet boundary conditions for 3D domains represents the simplest possibility. Unfortunately, such conditions are not realistic and cause spurious pressure waves to become in the solution. Such waves travel along the artery network and distort the numerical solution. An efficient technique is thus needed to minimize these effects. Sophisticated outlet boundary conditions [29,30] aimed to minimizing such problem can be found in the literature. Others authors address the problem by applying geometrical multiscale modeling [4,7,9,17,34,36]. These approaches typically consist in the combination of models with different levels of approximation (3D, 1D and 0D models) each aimed at capturing particular features of the solution. 3D models are applied in regions where details of the local flow are needed. This is typically the case when the flow is strongly three dimensional or it tends to be turbulent. 1D models are typically used in the up-downstream domain of the 3D models, so that the whole arterial network can be described efficiently taking into account flow propagation effects. Zero dimensional models (or lumped models) are generally used to describe the lower level of the cardiovascular system or to model the heart. A typical problem that rises at the interface between the 1D and 3D domains is the mapping of the parabolic velocity distribution (assumed in the 1D model) to an "equivalent" distribution on the 3D inlet. Such mapping is not trivial since the discretized 3D model is generally not exactly circular. A proposal to solve the impasse can be found in [2]. In current work we opted for the simpler (but less accurate) option of applying a spatially uniform inlet velocity, with a total flow corresponding to the one of the 1D. This is only acceptable since our aim is not to compute the Wall Shear Stress (WSS) but rather to estimate the dissipation induced by the non-standard topol-

E. Soudah · R. Rossi · S. Idelsohn · E. Oñate
International Center for Numerical Methods in Engineering (CIMNE), Technical University of Catalonia, 08034 Barcelona, Spain
e-mail: esoudah@cimne.upc.edu

S. Idelsohn (✉)
Institució Catalana de Recerca i Estudis Avançats (ICREA), Barcelona, Spain
e-mail: sergio@cimne.upc.edu

ogy of the artery or area of interest. We also observe that the method we propose works under the assumption that the 3D inlet and outlet boundaries are approximately perpendicular to the centerline of the artery and positioned at points in which the flow can be reasonably approximated as 1D. It is interesting to remark that, as observed in the extensive review paper [18,31], the reliable computation of WSS, which is often the target of CFD simulations, depends on the availability of a sufficiently fine discretization of the boundary layer and is sensibly affected by the Fluid-Structure Interaction of the flow with the artery boundaries. The idea we leverage in the current work is that the extra dissipation induced by severe variations of the geometry is dominated by the appearance of turbulent effects within the volume. The evaluation of such effect requires a sufficiently fine discretization of the volume but does not put the extra requirements on the boundary layer mesh, and shall not be severely affected by the deformability of the walls, hence allowing the assumptions of considering the walls rigid which greatly simplifies the simulation and reduces the runtime. In [25] an extensive review of the most popular 1D models can be found. Recently, new models have been proposed [1,20,22,28] improving the viscoelastic behavior of the walls. However, the 1D models alone are not capable to capture in an effective way the energy losses due to the 3D geometrical shapes of the arteries, e.g, in stenotic arteries, aneurysms or other cardiovascular pathologies, such as aorta coarctation. Nevertheless, to discretize the whole 3D cardiovascular domain or coupled fluid-structure interaction (FSI) modeling is computational expensive and unfeasible in practical applications due to the numerical challenges involved. Despite its modeling shortcomings, geometrical multiscale models combined with patient-specific geometries remains the predominant approach for vascular blood flow. Such models allow quantifying the hemodynamics variables such as, flow reversal, flow separation and wall shear stress areas over the arterial wall in a non-invasive way useful for clinicians. Notable exceptions include the work of [29,32,33] on cerebral aneurysms.

In this paper, we propose a reduced-order Computational Fluid Dynamics (CFD) model specifically aimed to the estimation of the pressure gradient and the energy losses induced by stenosis in cardiovascular scenarios. The key features of our approach are: (1) a patient-specific anatomy and a computational mesh obtained during a routine clinical imaging session; (2) a coupled multiscale 0D-1D-3D model to approximate the energy losses induced by a narrowing of the artery lumen. The solution of the 3D model is used to train a reduced-order model which is aimed to capturing the pressure drop within two sections located upstream and downstream of the stenosis. Then the reduced-order model is integrated within the 1D model to create a 1D reduced-order model. Such model is able to simulate the energy losses and the flow distribution taking into account the patient-specific anatomy in real time under different scenarios. The ultimate goal is to validate the CFD framework with the energy losses through an aortic coarctation (CoA) under resting and non-resting conditions of the patient. CoA of the aorta occurs approximately in 10 % of patients with congenital heart defects and represents a narrowing of the descending aorta. Due to the reduction in the aorta descending diameter, high pressure gradients can appear across the CoA, resulting in an increased cardiac workload in the left ventricle during systole [14]. Investigation into the hemodynamics and bio-mechanical basis of the morbidity in CoA shows that the pressure gradient is dependent on the aorta area reduction, the flow rate and the physiological state of the patient: during non-rest conditions the pressure gradient can increase considerably and can provoke heart failure [13]. To measure the pressure gradient under these non-rest conditions, that are difficult to replicate in a clinic environment, is a biomedical challenge [3]. For is reason, a procedure that combines patient-specific image data and numerical tools to further understand the hemodynamics alterations, under resting and non-resting situations will allow clinicians to improve the diagnosis and define which should be the CoA treatment for the patient [14,23]. Some authors have used CFD models to study the hemodynamics in the CoA [12,13]. However, different numerical approaches might lead to different pressure predictions. The reduced-order methodology described in this paper has been implemented as part of the C++ finite element library KRATOS (www.cimne.com/kratos) [5]. KRATOS is a multi-physics simulation open source (LGPL licence) framework based on the stabilized Finite Element Method for analysis of the Navier-Stokes equations in viscous flows. Efficient and parallel solvers for 3-D fluid-structure interaction (FSI) [6] problems have been implemented in KRATOS that allow tackling large problems using supercomputers if available.

2 Computational framework

As previously stated, realistic boundary conditions are essential for simulating a appropriately behavior of the blood flow propagation. In this section we define a 1D FSI model coupled to a reduced-order model for cardiovascular analysis. The methodology used consists on a two step process. The first step (training phase) consists in estimating correctly the pressure drop between two sections of a 3D model by solving a geometrical multiscale problem. From the numerical point of view, we embed a 3D domain into a 1D network in order to perform 3D simulations within a consistent hemodynamics conditions provided by a 1D FSI model. A lumped model is used to simulate the peripheral vascular beds of the cardiovascular system. Once the first simulation is completed, the pressure drop predicted by the 3D model is used to train the 1D reduced-order model via a least square fitting procedure.

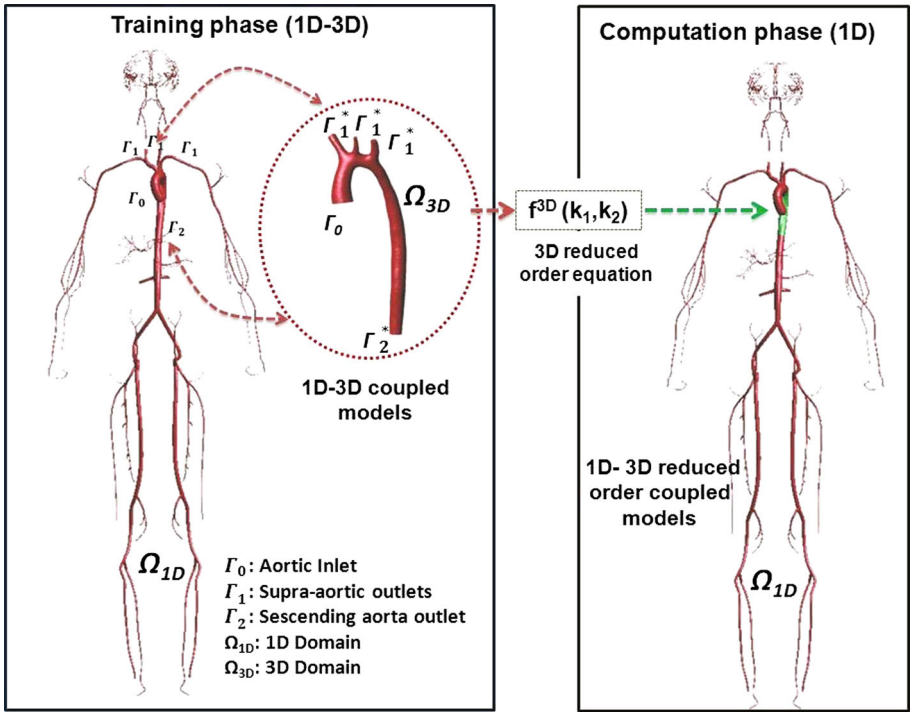

Fig. 1 3D-1D coupled approach schematics. Γ_i are the interface surfaces

The trained model is thus able to estimate the energy losses between the two areas selected in the 3D model. Once the reduced-order model is defined, a coupled 1D FSI-reduced-order model will be capable of estimating the patient-specific pressure drop under different rest or non-rest situations. The second step (computing phase) consists in setting different boundary conditions for the coupled 1D FSI-reduced-order model to estimate the pressure drop (at any point) taking in account the 3D anatomical model. This will enable us to simulate different pathological situations taking into account the energy losses produced by the 3D model. Besides, this reduced-order approach brings down the computational costs significantly. The flow diagram of this scheme is shown in Fig. 1.

2.1 Mathematical model for the 1D reduced-order model

In this section we describe a non-linear 1D formulation and the reduced-order model proposed to account for the 3D effects caused by the patient-specific area of interest. In absence of branching, an artery may be considered as a cylindrical compliant tube which extends from z = 0 to z = L, where L is the the artery length. The artery takes into account the assumptions of axial symmetry, radial displacements, constant pressure on each section, no body forces and dominance of axial velocity. The governing system of equations for an incompressible newtonian fluid are derived by applying conservation of mass and momentum in a 1-D impermeable and deformable tubular control volume. These equations are:

$$\left(\frac{\partial \mathbf{A}}{\partial \mathbf{t}} + \frac{\partial \mathbf{Q}}{\partial \mathbf{z}}\right) = 0 \tag{1a}$$

$$\left(\frac{\partial \mathrm{Q}}{\partial t}\right) + \frac{\partial}{\partial z}\left(\alpha \frac{Q^2}{A}\right) + \frac{\mathbf{A}}{\rho}\frac{\partial \mathrm{P}}{\partial z} + \mathbf{K_R}\left(\frac{Q}{A}\right) = 0 \tag{1b}$$

$$P_{ext} + \frac{Eh_o\sqrt{\Pi}}{1-\mu^2}\frac{\sqrt{A}-\sqrt{A_o}}{A_o} = P \tag{1c}$$

where A(z,t) is the cross-sectional area of the vessel, Q(z,t) is the mean blood flow, P is the average internal pressure over the cross-section, α is the momentum-flux correction coefficient, z is the axial coordinate along the vessel, t is the time, ρ is the density of the blood taken as 1,050 Kg/m^3 and K_R is the friction force per unit length, which is modeled as $K_R = 2\pi \cdot \nu(\gamma + 2)$ [8], with ν being the viscosity of the blood taken here as 4.5 m·Pa·s. The vessel wall is modeled as a thin, homogeneous and elastic material. Parameters A_0 and h_0 in Eq. 1(c) are the sectional area and the wall thickness, respectively, at the reference state (P_0,U_0), with P_0 and U_0 assumed to be zero, E is the Young modulus and μ is the Poisson's ratio, typically taken as $\mu \approx 0.5$, which implies that the biological tissue is practically incompressible. In absence of detailed of patient-specific data, the wall elasticity and the thickness of the 55 largest arteries are based on data published by Wang and Parker [35]. At each domain decomposition, whether corresponding to a discontinuity in the mechanical or geometrical vessel properties, or to a cardiovascular branching, continuity of flow and of total pressure is enforced as follows:

$$Q_i = \sum_d (Q_j)_d \tag{2}$$

$$P_i + \frac{1}{2}\rho \frac{{Q_i}^2}{{A_i}^2} = (P_j)_d + \frac{1}{2}\rho \frac{({Q_j}^2)_d}{({A_j}^2)_d} + ({f^{3D}}_j(k_1, k_2))_d \tag{3}$$

where indexes i and j denote the parent and the daughter vessels respectively, and d indicates the number of system domains. Function $f^{3D}(k_1, k_2)$ denotes the energy losses of the 3D model, where k_1 and k_2 are obtained by fitting the pressure drop between the two planes defined in the 3D model. k_1 and k_2 are the viscous and turbulent coefficients that should be adjusted according to the pressure drop between the two planes defined in the 3D model. In this work we do not consider the inertial term. The system obtained is solved by a Newton iteration scheme, taking as the starting point the reference section area and flow, i.e:

$${f^{3D}}_j(k_1, k_2) = k_1 Q_j + k_2 \mid Q_j \mid Q_j \tag{4}$$

With simple manipulations of the differential Eq. (1) it is possible to obtain the conservative form for the temporal evolution of the flow and the vessels area and discretize the system obtained using a second order Taylor-Galerkin scheme. This scheme is appropriate for this problem as it can propagate waves of different frequencies without suffering from excessive dispersion and diffusion errors. A derivation of the 1D-FSI models can be found in [8] and [27]. The Taylor-Galerkin scheme requires a time step limitation in order to keep the solution stable. In this work the stabilization technique adopted has been the Courant Friedrichs Lewy condition (CFL condition) [21].

$$\Delta t \leq CFL \min_{0 \leq i \leq N} \left(\frac{h_i}{max(\lambda_{1,i}, \lambda_{1,i+1})} \right) \tag{5}$$

where N is the number of the elements, h_i is the local element size and $\lambda_{1,i}$ indicates the value of the eigenvalue evaluated at the mesh i^{th} node of the matrix of the conservative form obtained from the derivation of the 1D-FSI model [8]. The CFL value adopted is 0.57 [21]. The 3D computational analysis is performed assuming that the arterial wall is rigid. Blood is considered as an homogeneous laminar Newtonian fluid modelled by the incompressible Navier-Stokes equations using the same density and dynamic viscosity as for the 1D model. Although these are important limitations, they make the simulation effort simpler. Furthermore, the knowledge of the patient-specific mechanical properties is quite difficult, consequently the objective of this work is to determine the pressure gradient in the anatomical domain using a reduced-order model based on multiscale modeling. Recent studies [15] use turbulence models to predict the kinetic energy due to the narrowing of the coarctation.

2.2 3D-1D Coupling interfaces

In order to keep the continuity in the area sections between the 3D and the 1D geometrical models, the diameters of the 1D geometrical model were firstly scaled taking into account a proportional diameter factor between the 3D and 1D geometrical models. The properties of the 1D geometrical models were taken from [35]. For the training phase, at each coupling 1D-3D interface we enforce the continuity of the flow and the total pressure (Eqs. 2, 3). This means that at every time step t_n we compute the velocity and the pressure using the 1D approach over the whole domain Ω_{1D}. Then, the variables over the interface sections (Γ_1, Γ_2) of the Ω_{1D}-Ω_{3D} domain are determined (Fig. 1). Following that, the 3D problem is solved in Ω_{3D} using the boundary conditions obtained in the Γ_1, Γ_2 sections from the 1D model. For the next time step $(t_n + 1)$ the process is repeated until the final simulation time is reached. This coupling procedure is justified by the fact that the 1D domain can be considered as a passive element which absorbs the flow generated by the 3-D domain. During the training phase, pressure values at Γ_1 and Γ_2 interfaces are stored for each time step with the objective of estimating the coefficients k_1 and k_2 of Eq. 4 by the least squares method. We choose the value of f^{3D} (k_1,k_2) that minimizes the sum of the squared pressure drop from the 1D flow values compared to the 3D values. In Sect. 3.1.3 we show a pressure drop of the 3D computational values versus the predictions of the reduced-order model (Fig. 3). For the computation phase, the coupled 1D coupled FSI—reduced-order model is solved by using the coefficients k_1 and k_2 estimated previously.

3 Study case: aorta coarctation

3.1 Training phase

3.1.1 Model anatomy, geometry and mesh

The physiological and geometrical data used in this work was obtained from [3].The patient was a 71 kg, 177 cm tall, 17-year old male with a mild thoracic aortic coarctation. Image data come from a 1.5-T Phillips scanner using a gadolinium-enhanced MR angiography (MRA) with the patient in the supine position. The 3D model (Fig. 2) includes the ascending aorta, aortic arch, descending aorta, left subclavii, brachiocephalic and finally left common carotid arteries in Stereo Lithography (STL) file format. To generate the 3D volume we used the pre and post-processor GiD [10]. GiD can be efficiently used for mesh generation in CFD analysis. For generating the 3D volume mesh from the STL file, we have used an isosurface stuffing procedure. This algorithm generates tetrahedral element form a small set of precomputed stencils. The boundary mesh is guaranteed to be a geo-

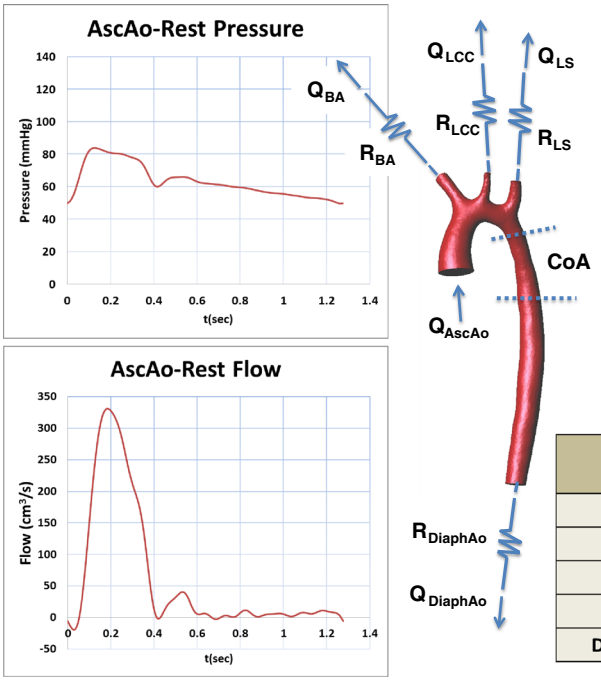

	Total Flow (L/min)	% AscAo
AscAo	3.71	100
BA	0.624	17
LCC	0.312	8
LC	0.364	10
DiaphAo	2.41	65

Fig. 2 Patient-specific anatomical model with a mild thoracic aortic coarctation (CoA). Ascending aortic flow waveforms (in cm^3/s) under rest conditions measured by the (PC)-MRI sequence and ascending aortic pressure (in mmHg) measured with a pressure catheter under rest conditions. The table shows the total flow (in L/min) and percentage of ascending aortic flow through the various branches of the aortic model under rest conditions

metrically and topologically accurate approximation of the isosurface [16]. This technique ensures tetrahedral volume elements with optimal angle and volume for the simulations. Using this method we have obtained smooth elements and an aspect radio for the whole mesh greater than 0.9 (the ideal ratio is one for an equilateral triangle). In this work we dont need a refined boundary layer mesh, due to the we have focused on the energy dissipation induced by the turbulence effects. In [18] other authors propose how to build a patient-specific models from medical images taking into account a fine discretization of the boundary layer in order to capture the WSS and OSI effects over the arterial wall. The result of the isostuffing procedure is a volume mesh of 4,322,556 four-noded tetrahedral elements and 206,880 three-noded triangles with 777,235 nodes. The original surface mesh has 138,532 linear triangles and 69,268 nodes. Figure 2 shows a rendering image of the 3D volume mesh. The 1D computational mesh contains 551 linear two-noded elements and 586 nodes.

3.1.2 Boundary conditions: inlet and outlet conditions at rest

Blood flow information [3] was acquired using a cardiac-gated, 2D, respiratory compensated, phase-contrast (PC) sequence with through-plane velocity encoding. The cardiac output of the patient was 3.71 L/min, the heart rate was 47 beats per minute (cardiac cycle T = 1.277 s). Figure 2 shows the blood flow and pressure waveforms at the ascending aorta (AscAo). The inlet velocity profile is prescribed as uniform and flat at the inlet surface. The quality of the waveforms to the supra-aortic vessels (the Brachiocephalic artery (BA), the left common carotid artery (LCC) and the left subclavian artery (LS) arteries) was deemed too noisy to be used in the computations. Figure 2 and the related table show the total flow through each branch given as a percentage of the ascending aortic flow.

Invasive pressure wire measurements were acquired in a catheterization laboratory-equipped XMR suite [3]. Pressure was obtained in the ascending aorta (proximal to the coarctation). The proximal systolic, diastolic, and mean pressures were 83.92, 49.68, and 63.35 mmHg, respectively. These values were used to set the parameters for the lumped model. These lumped models are usually composed of a set of resistances and compliances to model the microvascular beds. The compliance influences the transient flow waveform, while the mean value is affected by the resistance only. Due to the assumption that only the mean flow over the cardiac cycle in the BA, LCC , LS and DiaphAo arteries is known, the boundary condition estimation is limited to correctly determining the resistance values at each of these outlets. For estimating the terminal resistance parameter, we use Ohm's law taking into account the flow distribution at the rest state(see the Table in Fig. 2);

$$Q_i * R_i = P_i - P_{out} \tag{6}$$

where Q_i is the flow at the BA, LCC , LS and DiaphAo arteries, P_i is the mean systolic pressure at the aortic root, P_{out} is the venous pressure for the cardiovascular system and R_i is the flow resistance for each branch-domain. Since the circulation system is not closed, a constant venous pressure

of 5 mmHg is prescribed at the output of each artery [24]. Solving the set of differential-algebraic equations we obtain the following flow resistance for each branch as: $R_{BA} = 7.48 \cdot 10^{11}$Pa · s/m^3, $R_{LCC} = 1.50 \cdot 10^{12}$Pa · s/m^3, $R_{LS} = 1.28 \cdot 10^{12}$Pa · s/m^3 and $R_{DiaphAo} = 1.94 \cdot 10^{11}$Pa · s/m^3. Once the total resistances are estimated at these branches, the next step is to distribute the total resistances to the lumped models for all outlets of the 1D cardiovascular domain. To do that we have used a technique based on scaling laws for estimating the blood resistance. This method assumes that the radii and the lengths can be approximated as $R_1 = \varphi R_0$ and $L_1 = \lambda L_0$, being R_0 and L_0 is the radii and the length of the artery at a further distance and φ and λ are constant scaling factors. Therefore for any artery the radii and the length are $R_n = \varphi R_{n-1}$ and $L_n = \lambda L_{n-1}$, respectively. Under the Poiseuille law and assuming that we have 2^n arteries, then the flow distribution is $Q_0/2^n$, and the resistances in the terminal branches can be estimated as follows:

$$\Delta p_n = Q_n \frac{8_n \mu}{\pi R_n^4} \Rightarrow \Delta p_n = \left\{\frac{\lambda}{2\varphi^4}\right\}^n Q_0 \frac{8 L_0 \mu}{\pi R_0^4} = \left\{\frac{\lambda}{2\varphi^4}\right\}^n \Delta p_0$$

$$\Delta p_T = \sum_{n=1}^{N} \Delta p_n = \Delta p_0 \sum_{n=1}^{N} \left\{\frac{\lambda}{2\varphi^4}\right\}^n \tag{7}$$

where Δp_T is the sum of the pressure gradients after each bifurcation through the network, Δp_n is the starting point from the outlet of the terminal artery and N is the number of bifurcations. Dividing Δp_T by Q_0, the resistance $R_\mu T$ can be estimated as:

$$R_{\mu T} = R_{\mu 0} \sum_{n=1}^{N} \left\{\frac{\lambda}{2\varphi^4}\right\}^n \tag{8}$$

The flow can be approximated using Murray's law [19] as $Q \simeq kr^3$. Therefore $\lambda = \sqrt{0.6}$. Murray's law determines the vessel radius that requires a minimum of energy the vascular system. A relation between φ and λ can be estimated as [26]:

$$\lambda = \frac{N}{N+1} \frac{1}{2\varphi^2} \tag{9}$$

On the other hand, considering the main 55 arteries of the 1D arterial model [35], the R_{BA}, R_{LCC}, R_{LS} and $R_{DiaphAo}$ parameters and taking in account the vessels that arise from BA, LCC, LS and DiaphAo arteries the resistance values for all the terminal branches at the rest condition are finally estimated (see Table 1).

3.1.3 Reduced-order model

In order to settle Eq. 4, we have to define two planes in the 3D geometrical model. The planes chosen were in the ascending aorta (proximal to the coarctation) and in the descending aorta (distal to the coarctation); see Fig. 2. Once these two planes and the inlet and boundary conditions for rest situations are defined, we solve the coupled 3D-1D model. We use an adaptative time step based on the 1D simulation. For each time step, we calculate and store the mean values of the pressure and blood flow for the two planes. These values are then used to estimate the k_1 and k_2 coefficients in (Eq. 4) using a least squares method. The coefficients values found are $k_1 = 3.08 \cdot 10^{-3}$ and $k_2 = 5 \cdot 10^{-4}$, so that function $f^{3D}(k_1,k_2)$ minimizes the sum of the squared pressure drop from the flow values versus the 3D values. Figure 3 (left) shows the pressure drop obtained with the 3D computational values and the reduced-order model. The mean error between the CFD pressure drop and the 3D reduced-order model is 3 %. Figure 3 (right) shows the dependence between the pressure drop and the flow. The area below the hysteresis loop is the energy dissipated. If it is low we can estimate the pressure drop by function $f^{3D}(k_1,k_2)$. Thus, the reduced-order model is capable to capture the energy losses provoked by the geometry of the 3D model. The total computation time for the training phase in a standard PC with Linux environment, 32 bit, 4 GB RAM and dual core 2.83 GHz CPU was about 10 h.

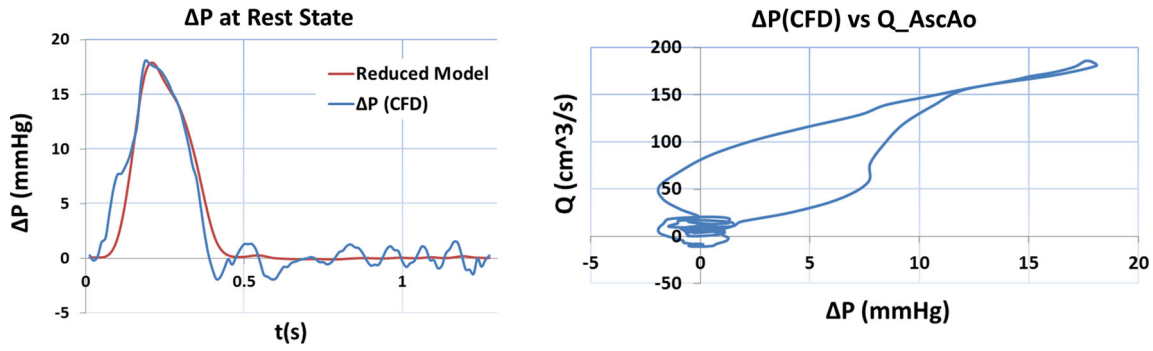

Fig. 3 *Left*: pressure drop between the 3D computational values versus the reduced-order model. *Right*: dependence between the pressure drop and the flow (hysteric loop)

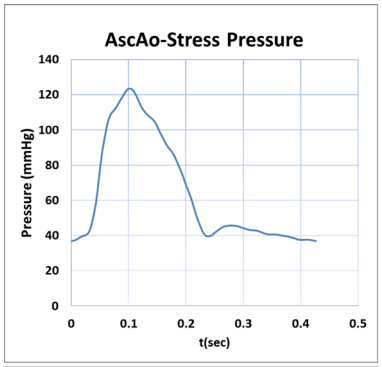

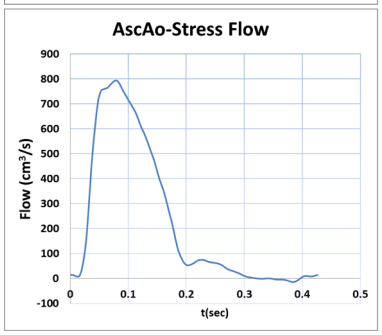

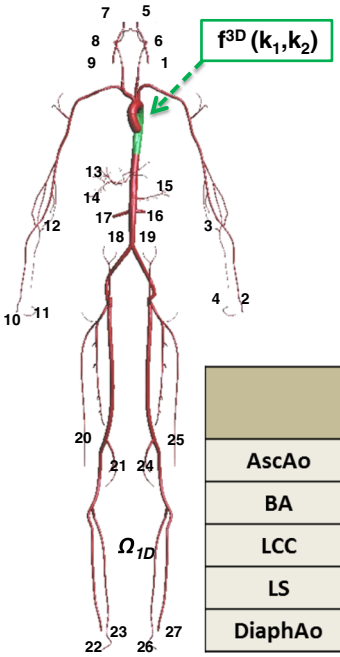

	Total Flow (L/min)	% AscAo
AscAo	13.53	100
BA	3.355	25
LCC	0.6875	5
LS	1.4575	11
DiaphAo	8.03	59

Fig. 4 1D anatomical model based on [35]. Ascending aortic flow waveforms (in cm^3/s) under non-rest conditions as measured by the PC-MRI sequence and ascending aortic pressure (in mmHg) measured with a pressure catheter under non-rest conditions. Table shows the total flow (in L/min) and percentage of ascending aortic flow through the various branches of the aortic model under non-rest conditions. Numbers indicate the terminal branches. Table 1 shows the name and resistance values

3.2 Computation phase

3.2.1 Non-rest situation

Stress (or non-rest) conditions were induced by administering isoprenaline to the patient. Flow and pressure data waveforms were acquired using the same protocol as in rest conditions [3]. The cardiac output of the patient increased to 13.53 L/min and the heart rate to 141 beats per minute (cardiac cycle T = 0.425 s). Figure 4 shows the flow waveform at AscAo. Similar as for a rest situation, the quality of the waveforms at the BA, LCC, and LS arteries was deemed too noisy to be used for the computations. Figure 4 shows the total flow through each branch given as a percentage of the ascending aortic flow. Pressure was obtained in the ascending aorta (proximal to the coarctation). The proximal systolic, diastolic, and mean pressures were 123.35, 36.77, and 64.30 mmHg, respectively (Fig. 4). For estimating the terminal resistance parameters under non-rest situations we have used the same procedure as in rest situations (3.1.2). The results are $R_{BA} = 1.41 \cdot 10^{11}\text{Pa} \cdot \text{s/m}^3$, $R_{LCC} = 6.90 \cdot 10^{11}\text{Pa} \cdot \text{s/m}^3$, $R_{LS} = 3.25 \cdot 10^{11}\text{Pa} \cdot \text{s/m}^3$ and $R_{DiaphAo} = 5.91 \cdot 10^{10}\text{Pa} \cdot \text{s/m}^3$. Table 1 shows the terminal resistance values for the terminal vessels for rest and non-rest situations.

Once the terminal resistances for the non-rest condition are set and the parameters k_1 and k_2 of the 3D reduced-order model are fitted (see Sect. 3.1.3). We are able to estimate the pressure drop under non-rest conditions. For this purpose, we impose the flow profile (Fig. 4) in the ascending aorta of the 1D model. In Fig. 5 the pressure drop under non-rest conditions is shown. The table below shows the mean, systolic and diastolic pressure for the rest and non-rest situations obtained with the reduced-order model. Experimental results are also shown for comparison purposes. The 1D reduced-order model can be also used to simulate other pathological conditions without the necessity to perform the 3D simulation.

4 Results

From a qualitative point of view, the numerical results shows that the pressure is correctly captured by the reduced-order model (Fig. 3). For the rest situation, the mean (2.83 mmHg) and maximum (18.07 mmHg) pressure drops are estimated using the 3D-1D coupling model. For the non-rest situation, the mean and maximum pressure drops of 13.68 and 44.06 mmHg are estimated using the 1D-reduced-order model. These values are in agreement with previous studies [3,13]. In the rest situation, the reduced model is able to capture the pressure drop with an error under 3 %. Note that the methodology used for parameter estimation can be improved

Table 1 Resistance values for the cardiovascular model in Fig. 4

	Artery name	R_{Rest}	$R_{Non\text{-}rest}$		Artery name	R_{Rest}	$R_{Non\text{-}rest}$
1	Right vertebral	29.6	7.52	15	Intercostals	4.47	1.36
2	Right radius	0.68	0.14	16	Renal	0.68	2.02
3	Right interosseous	4.5	1.14	17	Inferior mesenteric	0.68	2.02
4	Right ulnar	4.5	1.14	18	Superior mesenteric	0.68	2.02
5	Right int. carotid	34.6	15.9	19	Splenic	0.68	2.02
6	Right ext. carotid	34.6	15.9	20	Left ext. iliac	0.10	0.0315
7	Left int. carotid	29.6	7.52	21	Left deep femoral	0.10	0.0315
8	Left ext. carotid	29.6	7.52	22	Left posterior tibial	0.0157	0.00479
9	Left vertebral	17.3	3.27	23	Left anterior tibial	0.0157	0.00479
10	Left radius	0.4	0.075	24	Right ext. iliac	0.10	0.0315
11	Left interosseous	2.63	0.49	25	Right deep femoral	0.0157	0.00479
12	Left ulnar	2.63	0.49	26	Right posterior tibial	0.0157	0.00479
13	Hepatic superior	4.47	1.36	27	Right anterior tibial	0.10	0.0315
14	Gastric	4.47	1.36				

R is the terminal resistance (10^9Pa s/m^3) for the rest and non-rest situations based on the experimental measurements from [35]

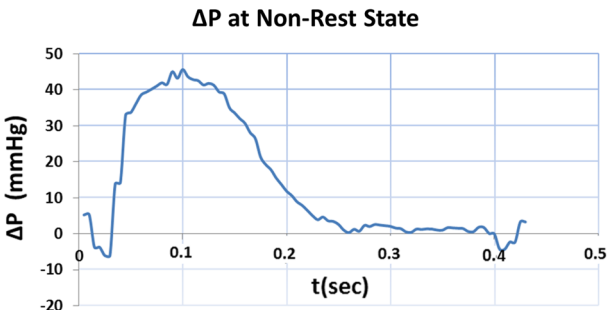

	Rest (CFD)	Rest (Exp)	Non-Rest (CFD)	Non-Rest (Exp)
Mean Pressure	60.61	63.35	61	64.30
Max Pressure	97.99	83.917	136.71	123.35
Min Pressure	46.37	49.68	31.59	36.77
Mean ΔP CoA	2.83	-	13.86	-
Max ΔP CoA	18.07	-	45.66	-

Fig. 5 Pressure drop for non-rest situation and CFD results versus experimental results. Pressures are in mmHg. CoA represents the coarctation and ΔP the pressure drop

with the objective of avoiding the oscillatory behavior of the pressure in the descending aorta. Some authors [11,36] use the three-element Windkessel model for improving the fitting of the lumped model. The approach used in this work is however much simpler in the mathematical treatment, while still being able to match the systolic, diastolic and mean pressure values.

5 Conclusion

We have presented a CFD framework which combines patient-specific model and a reduced-order model to estimate the energy losses in cardiovascular problems. The framework has been evaluated with a patient-specific aortic coarctation(CoA) under non-rest and rest situations with satisfactory results. The procedure consists of a two step process. First a reduced-order model is trained using a coupled 1D-3D FEM analysis and then is used together with a 1D solver under different pathological conditions. The reduced-order model is expressed as a sum of the viscous and turbulent terms, and it is capable to capture the energy losses provoked by the anatomy shape. The error of the reduced-order model is acceptable to capture the pressure drop over two sections of the 3D FEM model. We have modified the 1D formulation in order to integrate the reduced-order model into the framework developed. Results demonstrate that the reduced model is robust with respect to changes in the pathological conditions for patient-specific cases. In order to apply the procedure for a new patient, the framework developed requires a patient-specific model and knowledge of the pathological conditions in a rest situation. In terms of clinical diagnosis the most important feature to be captured is the pressure drop which can be estimated under non-rest situations. The main advantage of the proposed framework is that it relies only on measurements acquired during a rest situation. Then, it can be used under non-rest or rest conditions in a small computation time. The most important numerical approximation intro-

duced in this work is that the training of the reduced-order model is performed using the 3D patient-specific anatomical data considering the boundary conditions taken from the 1D model. The advantage is a great reduction of the computational time versus the fully coupled analysis. The numerical results show that the 1D model retrofitted by using the trained reduced model correctly captures the pressure gradient and the energy losses in cardiovascular diseases.

Acknowledgments This research was supported by the HFLUIDS project of the National RTD Plan of the Spanish Ministry of Science and Innovation I+D BIA2010-15880 and by the ERC Advanced Grant projects "REALTIME"(AdG-2009325) and "SAFECON"(AdG-267521). We also thank Dr.Pooyan Dadvand for his support on the implementation of the reduced-order model in KRATOS and Mr.Maurizio Bordone for his help during the fitting of the terminal resistances during training and computation phases.

References

1. Alastruey J, Khir AW, Matthys KS, Segers P, Sherwin SJ, Verdonck PR, Parker KH, Peiró J (2011) Pulse wave propagation in a model human arterial network: assessment of 1-D visco-elastic simulations against in vitro measurements. J Biomech 44(12):2250–2258
2. Bazilevs Y, Takizawa K, Tezduyar TE (2013) Computational fluid-structure interaction: methods and applications. ISBN: 978-0-470-97877-1. p 404
3. CFD Challange: Patient-Specific Hemodynamics at Rest and Stress through an Aortic Coarctation. 2013. http://www.vascularmodel.org/miccai2013/
4. Cristiano A, Malossi I, Blanco PJ, Crosetto P, Deparis S, Quarteroni A (2013) Implicit coupling of one-dimensional and three-dimensional blood flow models with compliant vessels. Multiscale Model Simul 11(2):474–506
5. Dadvand P, Rossi R, Oñate E (2010) An object-oriented environment for developing finite element codes for multi-disciplinary applications. Arch Comput Methods Eng 17:253–297
6. Dadvand P, Rossi R, Gil M, Martorell X, Cotela J, Juanpere E, Idelsohn SR, Oñate E (2013) Migration of a generic multi-physics framework to HPC environments. Comput Fluids 80(10):301–309
7. Formaggia L, Nobile F, Quarteroni A, Veneziani A (1999) Multiscale modelling of the circulatory system: a preliminary analysis. Comput Vis Sci 2:75–83
8. Formaggia L, Lamponi D, Quarteroni A (2003) One dimensional model for blood flow in arteries. J Eng Math 47:251–276
9. Formaggia L, Gerbeau JF, Nobile F, Quarteroni A (2001) On the coupling of 3D and 1D Navier-Stokes equations for flow problems in compliant vessels. Comput Methods Appl Mech Eng 191:561–582
10. GiD (2011) The personal pre and postprocessor, http://www.gidhome.com CIMNE
11. Ismail M, Wall WA, Gee MG (2013) Adoint-based inverse analysis of windkessel parameters for patient-specific. Vasc Models J Comput Phys 244:113170
12. Itu L, Sharma P, Ralovich K, Mihalef V, Ionasec R, Everett A, Ringel R, Kamen A, Comaniciu D (2013) Non-invasive hemodynamic assessment of aortic coarctation: validation with in vivo measurements. Ann Biomed Eng 41:669–681
13. LaDisa JJ et al (2011) Computational simulations for aortic coarctation: representative results from a sampling of patients. J Biomech Eng 133(9):091008–091017
14. LaDisa JJ, Dholakia RJ, Figueroa CA, Vignon-Clementel IE, Chan FP, Samyn MM, Cava JR, Taylor CA, Feinstein JA (2011) Computational simulations demonstrate altered wall shear stress in aortic coarctation patients treated by resection with end-to-end anastomosis. Congenit Heart Dis 6:432–443
15. Lantz J, Ebbers T, Engvall J, Karlsson M (2013) Numerical and experimental assessment of turbulent kinetic energy in an aortic coarctation. J Biomech 46(11):1851–1858
16. Lorensen WE, Cline HE (1987) Marching cubes: a high reso-lution 3d surface construction algorithm. In: Proceedings of SIGGRAPH, pp 163–169
17. Malossi A, Blanco PJ, Crosetto P, Deparis S, Quarteroni A (2013) Implicit coupling of one-dimensional and three-dimensional blood flow models with compliant vessels multiscale modeling. Simulation 11(2):474–506
18. Manguoglu M, Takizawa K, Sameh AH, Tezduyar TE (2010) Solution of linear systems in arterial fluid mechanics computations with boundary layer mesh refinement. Comput Mech 46:83–89
19. Murray CD (1926) The physiological principle of minimum work: I. The vascular system and the cost of blood volume. Proc Natl Acad Sci USA 12(3):207–214
20. Perdikaris P, Karniadakis GE (2014) Fractional-order viscoelasticity in one-dimensional blood flow models. Ann Biomed Eng, pp 0090–6964
21. Quartapelle L (1993) Numerical solution of the incompressible Navier-Stokes equations. Birkhauser Verlag, Basel
22. Raghu R, Vignon-Clementel IE, Figueroa CA, Taylor CA (2011) Comparative study of viscoelastic arterial wall models in nonlinear one-dimensional finite element simulations of blood flow. J Biomech Eng 133:081003–081011
23. Ralovich K et al (2012) Hemodynamic assessment of pre-and post-operative aortic coarctation from MRI. In: Ayache N, Delingette H, Golland P, Mori K (eds) MICCAI 2012, Part II, vol 7511., LNCSSpringer, Heidelberg, pp 486–493
24. Reymond P (2011) Pressure and flow wave propagation in patient-specific models of the arterial tree. PhD Thesis, École Polytechnique Fédérale de Lausanne
25. Reymond P, Merenda F, Perren F, Rafenacht D, Stergiopulos N (2009) Validation of a one-dimensional model of the systemic arterial tree. Am J Physiol Heart Circ Physiol 297(1):H208–H222
26. Sherman TF (1981) On connecting large vessels to small. The meaning of Murray's law. J Gen Physiol 78(4):431–453
27. Sherwin SJ, Franke V, Peiró J, Parker KH (2003) One-dimensional modelling of a vascular network in space-time variables. J Eng Math 47:217–250
28. Steele BN, Valdez-Jasso D, Haider MA, Olufsen MS (2011) Predicting arterial flow and pressure dynamics using a 1D fluid dynamics model with a viscoelastic wall SIAM. J Appl Math 71(4):1123–1143
29. Takizawa K, Christopher J, Tezduyar TE, Sathe S (2010) Space-time finite element computation of arterial fluid-structure interactions with patient-specific data. Int J Numer Methods Biomed Eng 26:101–116
30. Takizawa K, Moorman C, Wright S, Purdue J, McPhail T, Chen PR, Warren J, Tezduyar TE (2011) Patient-specific arterial fluid-structure interaction modeling of cerebral aneurysms. Int J Numer Methods Fluids 65:308–323
31. Takizawa K, Moorman C, Wright S, Christopher J, Tezduyar TE (2011) Wall shear stress calculations in space-time finite element computation of arterial fluid-structure interactions. Comput Mech 46:31–41
32. Tezduyar TE, Takizawa K, Brummer T, Chen PR (2011) Space-time fluid-structure interaction modeling of patient-specific cerebral aneurysms. Int J Numer Methods Biomed Eng 27:665–1710

Chapter 3

CFD Modelling of Abdominal Aortic Aneurysm on Hemodynamic Loads using a Realistic Geometry with CT.

Title: CFD Modelling of Abdominal Aortic Aneurysm on Hemodynamic Loads using a Realistic Geometry with CT.
Authors: E.Soudah, E.Y.K. Ng, T.H Loong, M.Bordone, P. Uei and N.Sriram.
Journal: Computational and Mathematical Methods in Medicine. Volume 2013-472564, 01/06/2013. (OPEN ACCESS JOURNAL)
DOI: 10.1155/2013/472564

Scientific contribution: Computational fluid dynamics studies of abdominal aortic aneurysms (AAA) to find a correlation between the thermodynamics parameters and AAA geometrical factors.

Contribution to the paper: The principal author developed the segmentation and mesh procedures together with M.Bordone and T.H Loong. He also had a major active part in the interpretation of the results together with E.Y.K. Ng, P. Uei and N.Sriram. This overall work was carried out in collaboration with Tan Tock Seng Hospital and Nanyang Technological University of Singapore under the NTU-NHG Innovation Seed Grant Project no. ISG/11007.

Hindawi Publishing Corporation
Computational and Mathematical Methods in Medicine
Volume 2013, Article ID 472564, 9 pages
http://dx.doi.org/10.1155/2013/472564

Research Article

CFD Modelling of Abdominal Aortic Aneurysm on Hemodynamic Loads Using a Realistic Geometry with CT

Eduardo Soudah,[1] E. Y. K. Ng,[2] T. H. Loong,[3] Maurizio Bordone,[1] Uei Pua,[3] and Sriram Narayanan[3]

[1] *Centre Internacional de Mètodes Numèrics en Enginyeria, Biomedical Engineering Department, Technical University of Catalonia, C/Gran Capità, s/n, 08034 Barcelona, Spain*
[2] *School of Mechanical and Aerospace Engineering, Nanyang Technological University, 50 Nanyang Avenue, Singapore 639798*
[3] *Department of General Surgery, Tan Tock Seng Hospital, 11 Jalan Tan Tock Seng, Singapore 308433*

Correspondence should be addressed to E. Y. K. Ng; myknng@ntu.edu.sg

Received 2 November 2012; Revised 17 May 2013; Accepted 1 June 2013

Academic Editor: Eun Bo Shim

The objective of this study is to find a correlation between the abdominal aortic aneurysm (AAA) geometric parameters, wall stress shear (WSS), abdominal flow patterns, intraluminal thrombus (ILT), and AAA arterial wall rupture using computational fluid dynamics (CFD). Real AAA 3D models were created by three-dimensional (3D) reconstruction of in vivo acquired computed tomography (CT) images from 5 patients. Based on 3D AAA models, high quality volume meshes were created using an optimal tetrahedral aspect ratio for the whole domain. In order to quantify the WSS and the recirculation inside the AAA, a 3D CFD using finite elements analysis was used. The CFD computation was performed assuming that the arterial wall is rigid and the blood is considered a homogeneous Newtonian fluid with a density of 1050 kg/m^3 and a kinematic viscosity of 4×10^{-3} Pa·s. Parallelization procedures were used in order to increase the performance of the CFD calculations. A relation between AAA geometric parameters (asymmetry index (β), saccular index (γ), deformation diameter ratio (χ), and tortuosity index (ε)) and hemodynamic loads was observed, and it could be used as a potential predictor of AAA arterial wall rupture and potential ILT formation.

1. Introduction

Most of abdominal aortic aneurysms (AAA) (about 90%) are located below the level of the renal arteries and are known as infrarenal aortic aneurysms. Infrarenal aortic aneurysm is a pathological enlargement of the aorta in the inferior thoracic area taking a fusiform shape and may extend into the iliac arteries. The mortality of this pathology is high (15% for ruptured aneurysms), and the current standard of determining rupture risk is based on the anteroposterior diameter. It is known that smaller AAAs that fall below the threshold of 5.5 cm diameter may also rupture, and yet larger AAAs (diameter > 5.5 cm) may remain stable [1–3]. However, occasionally the AAA diameter is lower than 5 cm and an unexpected ruptured is produced [4], in these cases, other biomechanical factors [5–8], such as Wall Shear Stress (WSS), or geometrical factors [9–12] can play an important role in the rupture of the aneurysm.

To estimate the AAA rupture risk, from a biomechanical point of view (material failure), an aneurysm ruptures when the stresses acting on the arterial wall exceed its failure strength. According to Laplace's law, the wall stress on an ideal cylinder is directly proportional to its radius and intraluminal pressure. Even though an AAA is not an ideal cylinder, Laplace's law still applies and with an increasing aortic diameter, the internal pressure increases, and so does the risk of rupture. The increase in internal pressure against the aortic walls results in progressive growth of the AAA diameter, and, eventually, this pressure may overcome the resistance of the aortic wall resulting in rupture [1, 2]. On the other hand, abnormal flow patterns and recirculation develop in the AAA sac leading to the formation of the intraluminal

thrombus (ILT) [6, 13]. This phenomenon can provoke the AAA stabilization and start a vicious circle inside the AAA [14]. It is reflected by the interaction between the arterial wall structural remodeling and the forces generated by blood flow within the AAA [2, 13]. Therefore, it is apparent that Laplace's Law is insufficient when investigating AAA collapsibility. Rather, the aneurysm shape has a strong influence on flow patterns, ILT formation, wall stress distribution (peak values and locations), and consequently its potential rupture [1, 15].

The aim of this study is to analyze and to characterize the effect of wall shear stress and the internal pressure together with the main AAA geometric parameters (maximum diameter (D_{AMAX}), length (L_{AAA}), AAA proximal neck diameter ($d_{\mathrm{proximal\_neck}}$), tortuosity ($\varepsilon$), and asymmetry ($\beta$)) in order to assess its potential rupture. Five patient-specific AAA models were created from CT scans. A normal descending aorta was also simulated to provide a comparison.

2. Material and Methods

Five patients with infrarenal aneurysms on followup at Tan Tock Seng Hospital (Singapore) were included in this study. The patients chosen for this study were selected with different sized AAAs, in order to cover the different stages of this pathology. All the patients participated in this trial analysis volunteered and provided written informed consent of the study. This study was reviewed and approved by the Ethics Committee of the Tan Tock Seng Hospital, Singapore. For the medical image acquisition, a computed tomography (CT) Somatom Plus Scanner (*AS+*) (Siemens Medical Solutions) was used with the following parameters: $512 \times 512 \times 110$, pixel spacing: 0.785/0.785 with a resolution of 1.274 pixels per mm and 5 mm slice thickness. CT scanning was conducted while the volunteer was awake in the head first-supine position using an endoleak protocol. The CT covered the entire abdomen and pelvis and was performed after the administration of intravenous Omnipaque 350 as IV contrast medium.

To characterize the structure of the AAA, the main geometrical AAA parameters are measured: aneurysm length (L_{AAA}) and maximum diameter of the aneurysm (D_{AMAX}) (Figure 1(a)). The factor which assesses the length (L_{AAA}) and the diameter (D_{AMAX}) of the AAA sac is known as saccular index (γ) (1) [16]. If the saccular index is close to 1, the aneurysm is saccular (spherical), but if it is close to 0 the aneurysm is more fusiform. The deformation diameter rate (χ) (1) [17] characterizes the nondeformed abdominal aorta diameter ($d_{\mathrm{proximal\_neck}}$) with the maximum diameter of the aneurysm sac, D_{AMAX}. A nonaneurysmal aorta is defined as ($D_{\mathrm{AMAX}} = d_{\mathrm{neck}}$)

$$\begin{aligned} \beta &= \frac{r}{R}, \\ \gamma &= \frac{D_{\mathrm{AMAX}}}{L_{\mathrm{AAA}}}, \\ \chi &= \frac{D_{\mathrm{AMAX}}}{d_{\mathrm{proximal\_neck}}}, \\ \varepsilon &= \frac{L}{\tau} - 1. \end{aligned} \tag{1}$$

To evaluate the asymmetry (β) [18] of the aneurysm (1), r and R are defined as the radii measured at the midsection of the AAA sac from the longitudinal z-axis to the posterior and anterior walls, respectively, as shown in the inset of Figure 1(b). Thus, $\beta = 1.0$ yields an azimuthal symmetry and $\beta = 0.2$ is an AAA for which only the anterior wall is dilated while the posterior wall is nearly flat. The tortuosity index (ε) (1) [19] is the relation between the actual lengths of the centerline of the AAA with the length of a hypothetical healthy aorta (Figure 1, center).

Based on these indexes and the wide clinical empirical evidence, there are several criteria of the AAA grade. However, at present, there is no clinical consensus to use it. Table 1 shows the main AAA geometrical characteristics for each patient in our study.

To create the computational model, the medical data were sent directly to a personal computer and stored in Digital Imaging and COmmunications in Medicine format (DICOM format). Figure 2 shows the segmentation workflow. The region of interest (ROI) analyzed was segmented using the three-dimensional computer-aided design system DIPPO software [20]. The segmented area for each patient started at the abdominal aorta (approximately in the infra renal arteries) and extended down to the common iliac arteries (Figure 2). The abdominal images were segmented from CT DICOM images combining two different segmentation procedures, thresholding and level set method (based on snakes). Thresholding is a nonlinear operation that converts a gray-scale image into a binary image where the two levels are assigned to pixels that are below or above the specified threshold value. The image snake operation creates or modifies an active contour/snake in a greyscale image. The operation iterates to minimize the snake's energy which consists of multiple components including the length of the snake, its curvature, and image gradient [21].

After AAA segmentation, we get a 3D volume image useful to create a 3D computational model to analyze the blood flow behavior inside the AAA using computational fluid dynamics (CFD). A mesh sensitivity analysis was performed to ensure the accuracy of the simulations using steady test. Depending on the complexity of the AAA model, a 3D mesh consisted of 2.000.000–2.500.000 tetrahedral elements. Using the isosurface stuffing algorithm [22], we have obtained a smooth element and an aspect radio for the whole of the meshes higher than 0.9 (ideal ratio = 1 for an equilateral triangle). For the five acquisitions, the same medical image protocol, image processing, and volume mesh reconstruction were used.

3. Computational Fluid Mechanics Solver

CFD analysis was performed using BioDyn, a friendly user interface based on the commercial software Tdyn [23]. Tdyn is a fluid dynamics and multiphysics simulation environment based on the stabilized finite element method that solved the Navier-Stokes equations. To characterize accurately the blood flow in the AAA, a Reynolds number was calculated for whole cases. Reynolds number is a dimensionless number that determinates the dynamic of the fluid. Reynolds number

Table 1: Patient and AAA geometrical characteristics (L, τ, $d_{\text{proximal\_neck}}$, r, R, D_{AMAX}, and L_{AAA}), and all the measurements are expressed in centimeter. AAA geometrical indexes (β, γ, χ, and ε).

Case	Sex	Thoracic aorta length (L)	Hypothetic thoracic aorta length (τ)	AAA proximal neck ($d_{\text{proximal\_neck}}$)	r	R	AAA max diameter (D_{AMAX})	AAA length (L_{AAA})	χ	β	γ	ε
1	Male	359,94	320,44	2,8	1,49	2,45	3,945	6,7	1,408	0,608	0,588	0,123
2	Male	319,5	310,2	1,7	0,67	1,74	2,416	4,1	1,421	0,388	0,589	0,029
3	Male	216,28	176,8	2,6	1,02	2,03	3,056	8,98	1,176	0,508	0,340	0,223
4	Male	293,55	255,26	2,6	0,95	3,07	4,031	15,6	1,55	0,309	0,258	0,150
5	Male	310,34	296,24	2,5	1,25	1,25	2,5	—	1	1	—	0,047

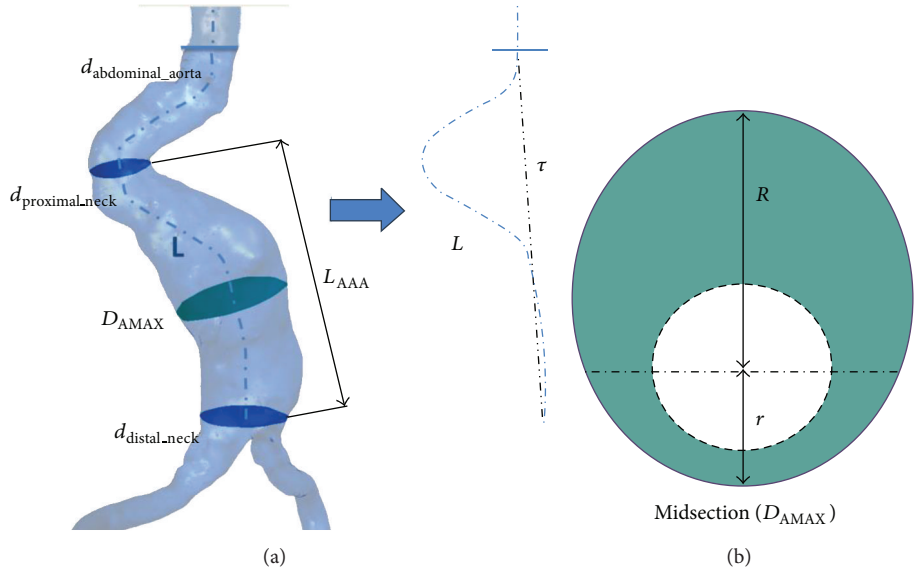

Figure 1: (a) Main geometrical parameters: L_{AAA} aneurysm length, D_{MAX} maximum diameter of the aneurysm $d_{\text{proximal\_neck}}$ beginning of the AAA sac, $d_{\text{distal\_neck}}$ ending of the AAA sac, $d_{\text{abdominal\_aorta}}$ nondeformed abdominal aorta diameter, L is the absolute length of the tortuous vessel, and τ is the imaginary straight line. (b) Schematic visualization of a cross-sectional AAA section, where r and R are defined as the radii measured at the midsection of the AAA sac from the longitudinal z-axis to the posterior and anterior walls.

is defined as $\text{Re} = UD/\nu$, where U is the mean velocity, ν is the kinematic viscosity of air, and D is the characteristic length given as the hydraulic diameter $D = 4A/P$ for the inlet velocity, and here A is the cross-sectional area and P is the perimeter of the aorta. Because the Reynolds number in inlet is low (<1000), we decided to use a CFD solver for laminar flow considering steady, homogeneous, incompressible, adiabatic, and Newtonian fluid. However, three-dimensional flow features such as flow separation and recirculation might trigger a transition to turbulence at lower Reynolds numbers [9]. Based on a preliminary study [6], the effect of the turbulence has been considered to be negligible. Following, we show the Navier-Stokes equations (2)

$$\begin{aligned} &\rho\left(\frac{\partial u}{\partial t} + (u\cdot\nabla)\,u\right) + \nabla p \\ &-\nabla\cdot(\mu\nabla u) = \rho f, \qquad \text{in } \Omega\times(0,t), \\ &\nabla\cdot u = 0, \qquad \text{in } \Omega\times(0,t), \end{aligned} \tag{2}$$

where $u = u(x,t)$ denotes the velocity vector, $p = p(x,t)$ the pressure field, and the density (ρ) is considered constant with a value of 1050 Kg·m^{-3} and dynamic viscosity (ν), fixed at 0.004 Pa·s and f the volumetric acceleration. The spatial discretization of the Navier-Stokes equations has been done by means of the finite element method (FEM), while for the time discretization an iterative algorithm that can be considered as an implicit two steps fractional step method has been used. A new stabilisation method, known as finite increment calculus, has recently been developed [24]. By considering the balance of flux over a finite sized domain, higher order terms naturally appear in the governing equations, which supply the necessary stability for a classical Galerkin finite element discretization to be used with equal order velocity and pressure interpolations. The inlet velocity waveform was taken from the literature [25], and Figure 3 shows the pulsatile waveforms used. For inlet condition, a transient blood flow was imposed in the descendent abdominal aorta. The velocity U was calculated for each patient in order to obtain a total fluid volumetric flow rate of 500 mL for an entire cardiac cycle. The outlet boundaries were located at the common iliac arteries where the pressure follows pulsatile waveforms as defined

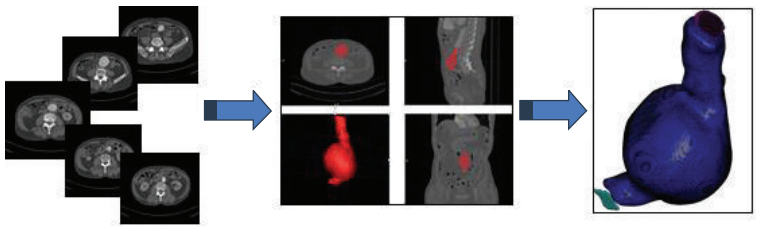

Figure 2: Workflow of the 3D AAA model. Obtaining the CT image of the abdominal aorta, segmentation of the vessel lumen using thresholding and level set method, and 3D model of the AAA.

in Figure 4(b). It is important to remark that these profiles are not patient-specific data (MR velocity mapping was not performed on these subjects), which can be a limitation of this study. In further studies, a patient-specific velocity and pressure profile will be used as boundary conditions.

Mathematically, the boundary conditions can be expressed as in (3a), (3b), and (3c). No-slip condition (vessel rigid wall) was imposed on the surface of the arteries, (3a). This choice is motivated by the fact that the physiological parameters characterizing the arterial mechanical behaviour of the AAA wall are not well determined. This approach, however, reduces the discretization effort considerably, in particular boundary layer gridding and the computational cost although other approaches consider fluid structure interaction (FSI) models [13, 25–28]. The inlet velocity is assumed to fully developed their parabolic profile at the inlet (3b), and time-dependent normal traction due to luminal pressure at the outlet (3c) as

$$V = 0\big|_{\text{wall}}, \tag{3a}$$

$$u_z = 2\,(u\,(t))\left(1 - \left(\frac{2r}{d_r}\right)^2\right); \qquad u_r = 0\big|_{z=0}, \tag{3b}$$

$$\tau_{nn} = \widehat{n} \cdot p\,(t)\, I \cdot \widehat{n}, \tag{3c}$$

where d_r is the inner radius of the abdominal aorta, u_r is the Cartesian component of the velocity vector in the "z" direction, and $u(t)$ and $p(t)$ are the time-dependent velocity and pressure waveforms designated in Figure 3. The pressure boundary conditions are given by (3c), where τ_{nn} is the normal traction designates at the outlet, I is the standard identity matrix, and $\widehat{n}$ designates the normal of the respective boundary. Figure 4 shows case 4 of the AAA reconstructed model and the layers in which our domain is divided in order to impose the boundary conditions.

4. Results

Five models of infrarenal aneurysm with patient-specific geometry were analyzed using computational fluid dynamics in order to evaluate the flow patterns, wall shear stress, and pressure over the aneurysm sac. Patients 1 to 4 had infrarenal aneurysms whilst patient 5 is the control case. ILT was not found in any case. The unsteady flow simulations were performed through two pulsatile cycles to eliminate the influence of initial transients. The results of pressure, stress, and flow patterns are shown for the peak systole (0.2 s) of the second cardiac cycle.

Figure 5 shows the flow patterns, velocity streamlines inside the infrarenal aneurysms sac, and three cross-sectional areas of the AAA (proximal, midsection, and distal neck) for the five patients studied. Note that forward flow points downwards and has a negative value in the adopted coordinate system. The direction of the flow is from top to bottom (direction Z negative). We notice that when the AAA has asymmetry, the velocity streamlines correspondingly show an asymmetric flow pattern inside the AAA sac. As shown in [6, 7, 26, 29], the asymmetric flow patterns can provide an insight into the mechanism that promotes the thrombus renewal and possibly enlargement inside the aneurysm. Rapid decrease in the velocity and regions of very high (or low) hemodynamic stresses gradients may all contribute in various ways to the vascular disease, primarily via their effects on the endothelium. For example, platelets trapped in recirculation zones tend to be deposited in areas of low shear stress (stenosis) [14], since this and the presence of vortices cause prolonged contact of the platelets with the surface in the layer of slow fluid motion [6, 19]. This effect can be observed for the pathological cases; however, in case 4 we observe a flow recirculation in the middle section and the asymmetry is low. Consequently, the flow patterns of the aneurysm not only depend of the asymmetry of the aneurysm but also depend of the AAA tortuosity. Details of the flow patterns for the AAAs is shown in Figure 5 (cross-sectional areas column). From the top to the bottom: neck section, midsection (maximum diameter in the aneurysm sac), and distal section. We notice that the tortuosity of the AAA provokes an asymmetric flow patterns in the AAA sac. When ε is high, we observe that in the AAA proximal neck section there is a strong irregular flow, causing also an irregular flow in the AAA sac meanwhile, when ε is low, this effect does not appear. From these findings, the greater the asymmetry and tortuosity of the AAA, the higher the possibility of blood recirculation, ILT formation, and a possible rupture. Thus, the importance of geometry in the hemodynamic behavior of AAAs is supported.

Anterior and posterior wall shear stress views are shown in Figure 6, as well as the pressure on the aneurysm sac at the peak systole. The mean WSS in the aneurysm sac of the 5 patients varied between 0.28 (case 5) and 12.72 Pa (case 4) with a median of 3.52 Pa and mean of 5.74 Pa. The areas with WSS values under the mean value have been classified as low

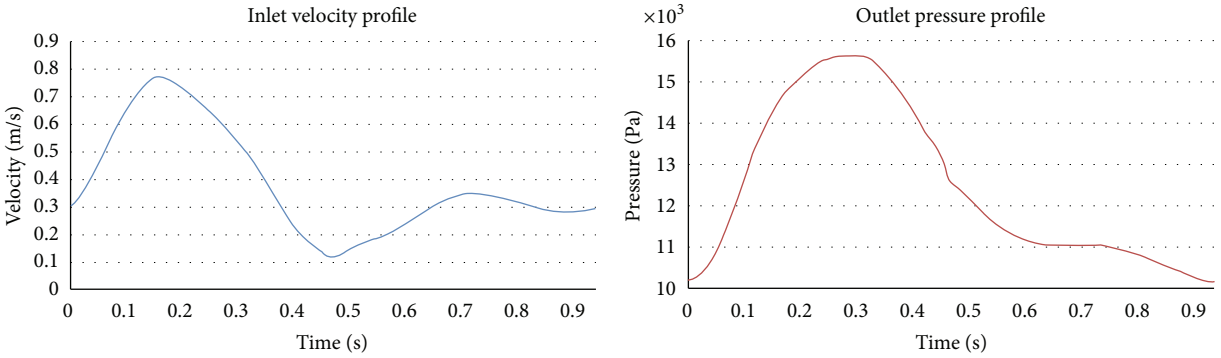

FIGURE 3: Boundary conditions for the hemodynamic simulations, adapted from [11].

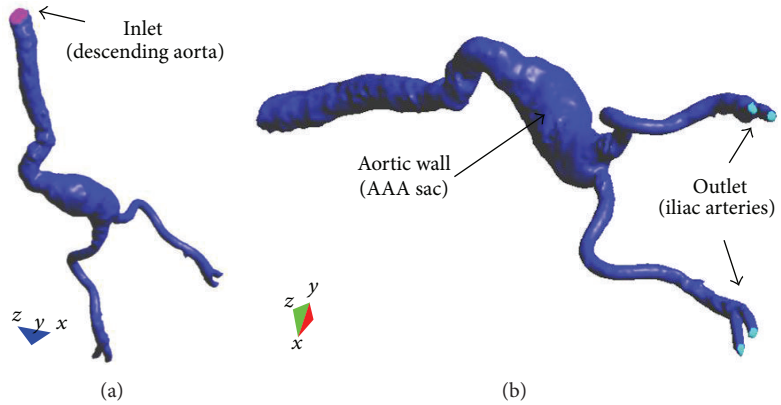

FIGURE 4: Mesh surface: different layers are shown: aortic wall (dark blue) and inlet (purple) and outlet sections (light blue).

WSS areas (blue) and areas with WSS values higher than the mean value as high WSS (red). Analysis of WSS maps for all cases shows that the area of low WSS coincides with the location of the recirculation areas (low velocities), and higher WSS values are found in two regions: in the neck area and in the corresponding area where the blood flow jet has an impact on the aneurismal sac. The blood flow jet has an impact directly on the arterial wall producing higher WSS values. The blood flow jet path is provoked by the proximal neck angle, consequently by the AAA tortuosity (see Figure 5). These WSS peak values do not influence too much in aneurysm growth; however, in these areas a material failure could be produced provoked by blood flow jet. It is interesting to note that shear stress levels in all infrarenal aneurysms models are higher than those in the normal aorta, where ε is low, which has a fairly uniform stress shear spatial distribution. Maximal values are found in the neck region, where ε is high.

Due to the increasing of the internal pressure, against the aortic walls, the AAA diameter grows progressively, and eventually it could be able to overcome the resistance of the aortic wall with its breakup. This internal pressure is directly proportional with the aneurysm diameter; thereby, when the diameter grows, the pressure increases. High deformation diameter rate (χ) index could indicate higher internal pressure however, it should be noticed that the pressure also depends on the tortuosity index (inversely proportional) and the flow characteristics (see Figure 5). For instance, in case 4 even when the section diameter is large, the internal pressure is lower than that in case 2. This is originated by a notably pressure drop as a result of the vorticity and flow recirculation (energy losses) in the cases with a high tortuosity index. This effect also provokes a pressures gradient between the anterior and posterior arterial wall in the interior of the AAA sac. These internal high pressure areas inside the sac may indicate the growth directions of AAA sac.

5. Discussions

The objective of this study is to use patient-specific AAA models for correlating the geometric indices of the aneurysm with the hemodynamic loads and, eventually, with the potential risk of AAA rupture. From a mechanical point of view, AAA ruptures when a maximum stress value over the wall is exceeded. The stress peak refers to the mechanical load sustained by the AAA wall, during maximal systolic pressurization. In addition, it is known that wall stress alone does not completely govern failure as an AAA will usually rupture when the wall stress exceeds the wall strength. Its value depends on arterial systolic pressure, the mechanical properties, and the geometric configuration of the material

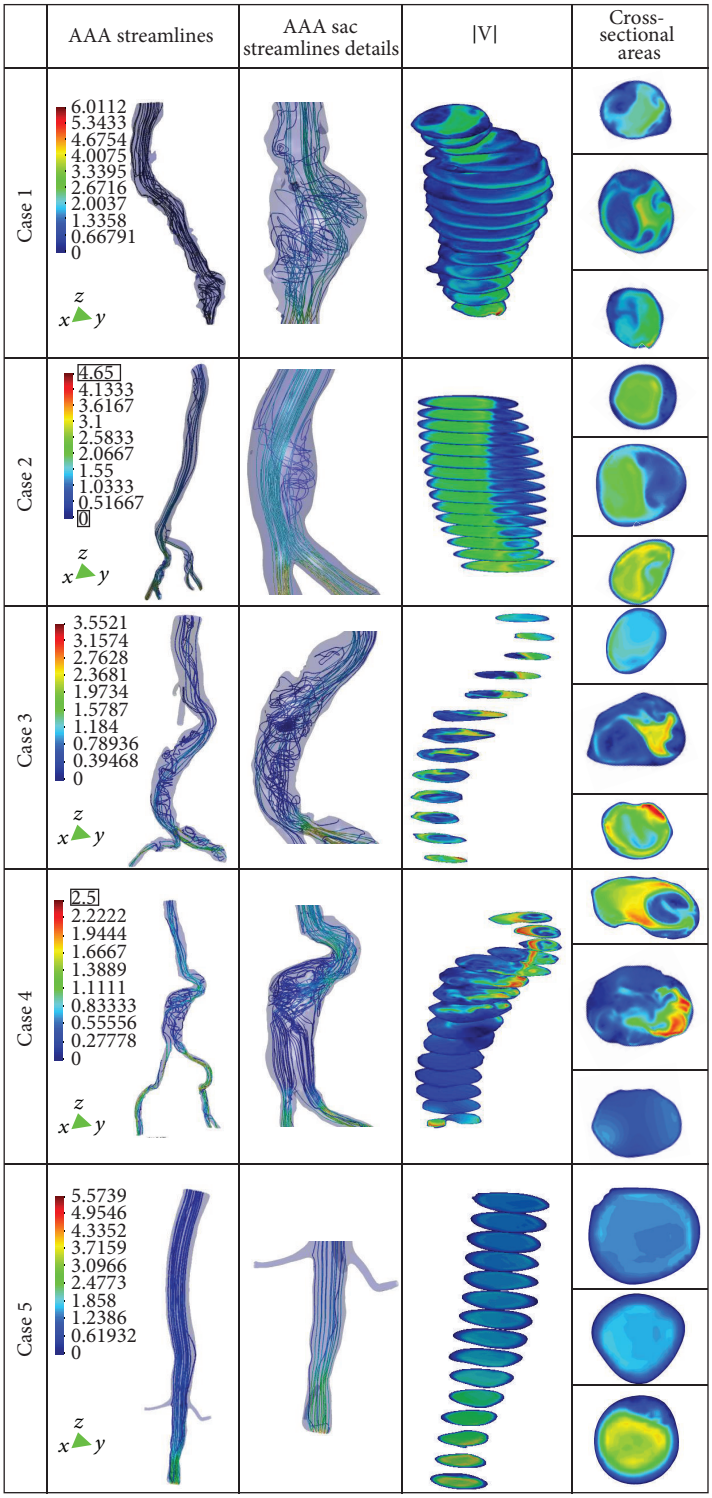

FIGURE 5: Streamlines, details of AAA sac streamline, blood flow velocity, and three cross-sectional areas (from the top to the bottom: proximal AAA neck and midsection and distal AAA neck) for the five patient studied.

under study. However, the mechanism of arterial wall failure due to (1) the AAA shape or (2) the pressure distribution is physically different. The first is because of a punctual force over a wall point, and the second is because a consequence of a pressure distribution over the AAA wall. Based on the AAA shape, several authors have proposed different criteria for the AAA collapsibility; if the AAA diameter is higher than 5.5 cm [4], the AAA may rupture or if the asymmetry index

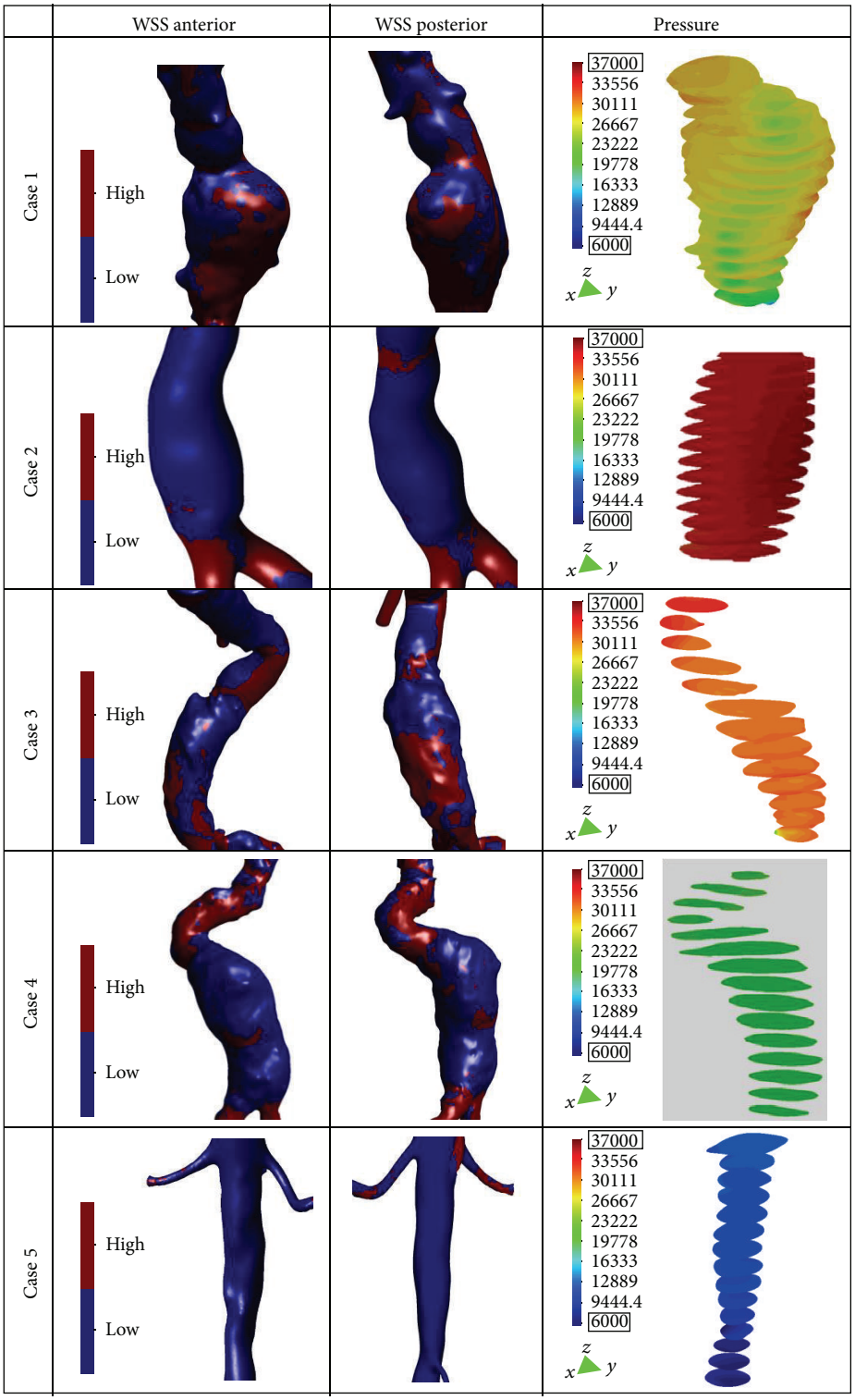

Figure 6: Anterior and posterior wall shear stress views (high WSS in red, and low WSS in blue) and normalized pressure on the aneurysm sac at the peak systole for the five patients.

factor (β) is $\beta < 0.4$, the AAA rupture is high [8]. In [10] the AAA collapses when the deformation diameter ratio is $\chi > 3.3$ or if the saccular index is <0.6 [11]. But depending on the index that is analysed, the surgical criteria are different. More recently, the proposed AAA rupture risk is related with the presence of intraluminal thrombus (ILT) [6, 26]. The intraluminal thrombus plays an important role in expansion and rupture of advanced aneurysms through direct mechanical as well as indirect chemomechanical effects [6]. Therefore, the AAA dilatation (and a potential rupture) is dependent on the correlation between the geometrical factor and the hemodynamic load. Consequently, alternative methods of AAA rupture assessment are needed.

The majority of these new approaches involve the numerical analysis of AAAs using computational fluid dynamics (CFD) to determine the wall shear stress (WSS) distributions and flow patterns in the aneurysm sac [5, 12, 13, 15, 16, 30]. In our study, we did not evaluate the patient-specific wall strength or the effect of intraluminal thrombus. Nevertheless, the AAA cases analyzed provide useful information to understanding how hemodynamic loads can affect aneurysm growth and possible rupture. The pathological cases (cases 1 to 4) always present irregular flow in the aneurysm sac, no uniform distribution of WSSs and great WSS values in the curvatures of the aortic vessel. These anomalies are proportional to the shape of the aneurysm and the angles of twist that the aorta has. Asymmetric flow is always correlated to the modified curvature of the vessel or when some enlargement in the aneurysm is present (high saccular index (γ) and tortuosity (ε) index). The AAA tortuosity could initiate ILT formation and at the same time could provoke arterial wall failure. In a situation where the tortuosity is high and the saccular index is low, the WSS has more effects than the pressure distribution in a possible AAA failure. However, where the AAA is not twisted and the saccular index is high, the pressure effect takes priority. In Figure 6, the highest shear stress values are dependent especially on the tortuosity of the AAA. The neck angle substantially impacts flow fields, causing strong irregular flow patterns in the AAA sac (Figure 5) significantly influencing wall stress distribution (Figure 6). The relationship between these indexes can provide an insight into the mechanism that promotes the thrombus renewal and possibly enlargement inside the aneurysm.

6. Conclusions

To conclude, in this work, the wall shear stress, internal pressure, and flow patterns of five patients-specific aortas have been analyzed using a finite element method, and the results have been correlated with the geometrical features. Results from the patient-specific infrarenal aneurysm models (cases 1–4) were compared with those of a normal aorta (case 5) and it has been found that the normal aorta has a uniform distribution of the velocity streamlines, wall shear stress, and pressure compared to that in the pathological cases. Maximum wall shear stresses in all infrarenal aneurysm models are higher than those in the normal aorta and these values are not directly related to the maximum aneurysm diameter, providing evidence that a patient-specific aorta shape analysis is necessary for a more reliable assessment of the rupture risk of aortic aneurysms. Therefore, based on one or two simple indexes alone, to determine the risk of rupture accurately is insufficient. AAA rupture is a complex situation, depending on the maximum diameter, internal pressure, wall stress, asymmetry, saccular index, intraluminal thrombus, and tortuosity, among others. Our results demonstrate how the hemodynamic loads as simulated by computational fluid dynamics (CFD) are influenced by the geometrical factors of the aneurysm.

Acknowledgment

This project was supported by the NTU-NHG Innovation Seed Grant Project no. ISG/11007.

References

[1] D. A. Vorp, "Biomechanics of abdominal aortic aneurysm," *Journal of Biomechanics*, vol. 40, no. 9, pp. 1887–1902, 2007.

[2] J. D. Humphrey, *Cardiovascular Solid Mechanics. Cells, Tissues, and Organs*, Springer, New York, NY, USA, 2002.

[3] J. T. Powell, L. C. Brown, J. F. Forbes et al., "Final 12-year follow-up of surgery versus surveillance in the UK Small Aneurysm Trial," *British Journal of Surgery*, vol. 94, no. 6, pp. 702–708, 2007.

[4] S. C. Nicholls, J. B. Gardner, M. H. Meissner, and K. H. Johansen, "Rupture in small abdominal aortic aneurysms," *Journal of Vascular Surgery*, vol. 28, no. 5, pp. 884–888, 1998.

[5] M. L. Raghavan and D. A. Vorp, "Toward a biomechanical tool to evaluate rupture potential of abdominal aortic aneurysm: identification of a finite strain constitutive model and evaluation of its applicability," *Journal of Biomechanics*, vol. 33, no. 4, pp. 475–482, 2000.

[6] J. Biasetti, F. Hussain, and T. Christian Gasser, "Blood flow and coherent vortices in the normal and aneurysmatic aortas: a fluid dynamical approach to intraluminal thrombus formation," *Journal of the Royal Society Interface*, vol. 8, no. 63, pp. 1449–1461, 2011.

[7] C. M. Scotti and E. A. Finol, "Compliant biomechanics of abdominal aortic aneurysms: a fluid-structure interaction study," *Computers and Structures*, vol. 85, no. 11–14, pp. 1097–1113, 2007.

[8] D. A. Vorp, M. L. Raghavan, and M. W. Webster, "Mechanical wall stress in abdominal aortic aneurysm: influence of diameter and asymmetry," *Journal of Vascular Surgery*, vol. 27, no. 4, pp. 632–639, 1998.

[9] E. A. Finol, K. Keyhani, and C. H. Amon, "The effect of asymmetry in abdominal aortic aneurysms under physiologically realistic pulsatile flow conditions," *Journal of Biomechanical Engineering*, vol. 125, no. 2, pp. 207–217, 2003.

[10] W. A. Cappeller, H. Engelmann, S. Blechschmidt, M. Wild, and L. Lauterjung, "Possible objectification of a critical maximum diameter for elective surgery in abdominal aortic aneurysms based on one- and three-dimensional ratios," *Journal of Cardiovascular Surgery*, vol. 38, no. 6, pp. 623–628, 1997.

[11] K. Ouriel, R. M. Green, C. Donayre, C. K. Shortell, J. Elliott, and J. A. DeWeese, "An evaluation of new methods of expressing aortic aneurysm size: relationship to rupture," *Journal of Vascular Surgery*, vol. 15, no. 1, pp. 12–20, 1992.

[12] T. C. Gasser, M. Auer, F. Labruto, J. Swedenborg, and J. Roy, "Biomechanical rupture risk assessment of abdominal aortic

aneurysms: model complexity versus predictability of finite element simulations," *European Journal of Vascular and Endovascular Surgery*, vol. 40, no. 2, pp. 176–185, 2010.

[13] M. Bonert, R. L. Leask, J. Butany et al., "The relationship between wall shear stress distributions and intimal thickening in the human abdominal aorta," *BioMedical Engineering Online*, vol. 2, article 18, 2003.

[14] D. Bluestein, L. Niu, R. T. Schoephoerster, and M. K. Dewanjee, "Steady flow in an aneurysm model: correlation between fluid dynamics and blood platelet deposition," *Journal of Biomechanical Engineering*, vol. 118, no. 3, pp. 280–286, 1996.

[15] M. L. Raghavan, D. A. Vorp, M. P. Federle, M. S. Makaroun, and M. W. Webster, "Wall stress distribution on three-dimensionally reconstructed models of human abdominal aortic aneurysm," *Journal of Vascular Surgery*, vol. 31, no. 4, pp. 760–769, 2000.

[16] C. Kleinstreuer and Z. Li, "Analysis and computer program for rupture-risk prediction of abdominal aortic aneurysms," *BioMedical Engineering Online*, vol. 5, article 19, 2006.

[17] J. Shum, G. Martufi, E. di Martino et al., "Quantitative assessment of abdominal aortic aneurysm geometry," *Annals of Biomedical Engineering*, vol. 39, no. 1, pp. 277–286, 2011.

[18] D. A. Vorp, P. C. Lee, D. H. J. Wang et al., "Association of intraluminal thrombus in abdominal aortic aneurysm with local hypoxia and wall weakening," *Journal of Vascular Surgery*, vol. 34, no. 2, pp. 291–299, 2001.

[19] D. Bluestein, K. Dumont, M. de Beule et al., "Intraluminal thrombus and risk of rupture in patient specific abdominal aortic aneurysm—FSI modelling," *Computer Methods in Biomechanics and Biomedical Engineering*, vol. 12, no. 1, pp. 73–81, 2009.

[20] E. Soudah, J. Pennecot, J. S. Perez, M. Bordone, and E. Oñate, "Medical-GiD: from medical images to simulations, 4D MRI flow analysis," in *Computational Vision and Medical Image Processing: Recent Trends*, chapter 10, Springer, New York, NY, USA, 1871.

[21] E. Soudah, M. Bordone, and J. S. Perez, "Gmed: a platform for images treatment inside GiD system," in *Proceedings of the 5th Conference On Advances And Applications Of GiD*, Barcelona, 2010, GiD—the personal pre and postprocessor, http://www.gidhome.com/.

[22] W. E. Lorensen and H. E. Cline, "Marching cubes: a high resolution 3d surface construction algorithm," in *Proceedings of the 14th Annual Conference on Computer Graphics and Interactive Techniques (SIGGRAPH '87)*, pp. 163–169, 1987.

[23] M. Bordone, C. García, J. García, and E. Soudah, "Biodyn User Manual. TDYN: theoretical Background," COMPASSIS, 2012, http://www.compassis.com/compass.

[24] E. Oñate, S. Idelsohn, O. C. Zienkiewicz, and R. L. Taylor, "A finite point method in computational mechanics. Applications to convective transport and fluid flow," *International Journal for Numerical Methods in Engineering*, vol. 39, no. 22, pp. 3839–3866, 1996.

[25] Y. Papaharilaou, J. A. Ekaterinaris, E. Manousaki, and A. N. Katsamouris, "A decoupled fluid structure approach for estimating wall stress in abdominal aortic aneurysms," *Journal of Biomechanics*, vol. 40, no. 2, pp. 367–377, 2007.

[26] A.-V. Salsac, S. R. Sparks, J.-M. Chomaz, and J. C. Lasheras, "Evolution of the wall shear stresses during the progressive enlargement of symmetric abdominal aortic aneurysms," *Journal of Fluid Mechanics*, vol. 560, pp. 19–51, 2006.

[27] C. M. Scotti, J. Jimenez, S. C. Muluk, and E. A. Finol, "Wall stress and flow dynamics in abdominal aortic aneurysms: finite element analysis vs. fluid-structure interaction," *Computer Methods in Biomechanics and Biomedical Engineering*, vol. 11, no. 3, pp. 301–322, 2008.

[28] A. Borghia, N. B. Wooda, R. H. Mohiaddinb, and X. Y. Xua, "Fluid-solid interaction simulationof flow and stress pattern in thoraco abdominal aneurysms: a patient-specific study," *Journal of Fluids and Structures*, vol. 24, pp. 270–280, 2008.

[29] A. Sheidaei, S. C. Hunley, S. Zeinali-Davarani, L. G. Raguin, and S. Baek, "Simulation of abdominal aortic aneurysm growth with updating hemodynamic loads using a realistic geometry," *Medical Engineering and Physics*, vol. 33, no. 1, pp. 80–88, 2011.

[30] T. Hatakeyama, H. Shigematsu, and T. Muto, "Risk factors for rupture of abdominal aortic aneurysm based on three-dimensional study," *Journal of Vascular Surgery*, vol. 33, no. 3, pp. 453–461, 2001.

Chapter 4

Modelling human tissues an efficient integrated methodology.

Title: Modelling human tissues an efficient integrated methodology.
Authors: M.Cerrolaza, G.Gavidia, E.Soudah, M. Martín-Landrove.
Journal: Biomedical Engineering: Applications, Basis and Communications. (2014) Vol. 26, No 1. 1450012 (21 pages)
DOI: 10.4015/S1016237214500124

Scientific contribution:Design of an efficient methodology for pre and post-processing of medical images to generate computational meshes for numerical simulations.

Contribution to the paper: Pre and Postprocessing tools for mesh generation for finite element analysis in cooperation with G.Gavidia.

Biomedical Engineering: Applications, Basis and Communications, Vol. 26, No. 1 (2014) 1450012 (21 pages)
DOI: 10.4015/S1016237214500124

MODELING HUMAN TISSUES: AN EFFICIENT INTEGRATED METHODOLOGY

M. Cerrolaza[*,§], G. Gavidia[†], E. Soudah[*] and M. Martín-Landrove[‡]
[*]*International Center for Numerical Methods in Engineering*
Polytechnic University of Catalonia, Barcelona, Spain
[†]*Biomedical Engineering Research Center*
Polytechnic University of Catalonia, Barcelona, Spain
[‡]*National Institute of Bioengineering*
Central University of Venezuela, Caracas, Venezuela
[§]*mcerrolaza@cimne.upc.edu*

Accepted 7 April 2013
Published 26 February 2014

ABSTRACT

Geometric models of human body organs are obtained from imaging techniques like computed tomography (CT) and magnetic resonance image (MRI) that oallow an accurate visualization of the inner body, thus providing relevant information about their its structure and pathologies. Next, these models are used to generate surface and volumetric meshes, which can be used further for visualization, measurement, biomechanical simulation, rapid prototyping and prosthesis design. However, going from geometric models to numerical models is not an easy task, being necessary to apply image-processing techniques to solve the complexity of human tissues and to get more simplified geometric models, thus reducing the complexity of the subsequent numerical analysis. In this work, an integrated and efficient methodology to obtain models of soft tissues like gray and white matter of brain and hard tissues like jaw and spine bones is proposed. The methodology is based on image-processing algorithms chosen according to some characteristics of the tissue: type, intensity profiles and boundaries quality. First, low-quality images are improved by using enhancement algorithms to reduce image noise and to increase structures contrast. Then, hybrid segmentation for tissue identification is applied through a multi-stage approach. Finally, the obtained models are resampled and exported in formats readable by computer aided design (CAD) tools. In CAD environments, this data is used to generate discrete models using finite element methed (FEM) or other numerical methods like the boundary element method (BEM). Results have shown that the proposed methodology is useful and versatile to obtain accurate geometric models that can be used in several clinical cases to obtain relevant quantitative and qualitative information.

Keywords: 3D modeling; Human tissues; Segmentation; Medical images; Finite element method.

INTRODUCTION

Geometric models of human body parts, such as organs and tissues, as well as their pathologies, planning and surgery are usually carried out by using numerical methods to get approximate models of such organs. To obtain a tissue model using numerical methods, such as the finite element method (FEM), the geometric model of the organ is divided into surface or volumetric elements, the properties of each element are formulated, and then the elements are combined to compute the organ's deformation states under the influence of external forces applied by surgical instruments.[1] However,

[§]Corresponding author: M. Cerrolaza, International Center for Numerical Methods in Engineering, Polytechnic University of Catalonia, Barcelona, Spain. Tel:+34 93 4134167, +34 660 702061; Fax: +34 93 4016035; E-mail:mcerrolaza@cimne.upc.edu

the generation of these models is not a trivial task, considering the complex shape of human anatomic parts, which are generally not symmetric. Likewise, the imposition of boundary conditions and biological loadings in the model are neither trivial nor simple tasks. Actually, soft tissues such as brain or heart and hard tissues such as bone have a diverse and complex morphology, usually overlapping. Current techniques such as magnetic resonance (MR), computed tomography (CT) and positrons emission tomography (PET) have been used, among others, based on radiations which produce images when interacting with human tissues. The reconstruction of human tissues is carried out with digital processing techniques. A gray-scale medical image is represented by a $m \times n \times z$ matrix, formed by several parallel slices of images in the z direction, having $m \times n$ pixels. Each matrix element has a gray-intensity value obtained by the interaction between radiation and human tissue. Processing and visualization techniques for medical images involve a set of mathematical algorithms, applied to the matrix representation described above in order to modify their elements values. There exist some previous works on this subject[2–4] that have studied the process to extract and to analyze human anatomic structures from these radiological techniques. The aforementioned authors agree to define three main steps, once the medical data have been digitalized: (a) images preprocessing to reduce noise and enhance contrast, (b) segmentation to extract regions of interest for further analysis and (c) visualization of segmented regions (volume, surfaces, discretized meshes) for further manipulation.

These studies, based on the manipulation and visualization of medical images, are a key aspect for medical diagnosis and diseases treatment. These techniques not only allow medical doctors and scientists to obtain vital information by using non-invasive techniques but also they are essential tools in getting more accurate geometric models of human body parts. Some works on this research line can be mentioned here. 3D models of highly heterogeneous bone from CT images have been obtained in Ref. 5. The authors then used the FEM for the mechanical analysis of bone. In Ref. 6, a new methodology to get titanium-prostheses designs from CT bone-structures has been proposed. These authors applied processing techniques for images and modeling using the FEM. Isaza *et al.*[7] reconstructed facial-skull structures from CT images by applying image processing techniques to get the segmentation of structures of interest. Then they applied the FEM to simulate a device used in orthodontics, both for the dental and skeletal use in cervical traction.

The main goal of this work is to propose an integrated methodology to obtain geometric models of human-body parts, which will help in medical visualization, measurement, biomechanical simulation, rapid prototyping and prosthesis design.

IMAGE PROCESSING AND VISUALIZATION

Medical imaging provides major aid in many branches of medicine: it enables and facilitates the capture, transmission and analysis of medical images as well as provides assistance for medical diagnoses. Medical imaging is still on the rise with new imaging modalities being added and continuous improvements of devices' capabilities. Preprocessing, segmentation and contour extraction are important steps in tissue models generation. Preprocessing is necessary because biomedical images are often corrupted by noise and sampling artifacts, which can cause considerable problems when applying rigid methods. Segmented images and contour extraction are used to obtain anatomical structures and they are commonly used in a wide variety of applications: diagnosis, preoperative planning, pathology localization and computer-integrated surgery. However, preprocessing and image segmentation remain a difficult task due to both the variability of object shapes and image quality. Medical images frequently display high-intensity variations throughout the regions that correspond to the same tissue type. Also, two different tissues can share very similar intensity profiles.

Preprocessing and segmentation using traditional low-level image processing techniques such as thresholding, histogram, convolution and other classical operations, require a considerable amount of interactive guidance in order to get satisfactory results. Automating these model-free approaches is diffcult because of shape complexity, shadows and variability within and across individual objects. Noise and other image artifacts can cause incorrect regions or boundary discontinuities in objects recovered from these methods. For these reasons, it is accepted that despite the more complex algorithms developed so far, the preprocessing and segmentation of medical images remain highly dependent on the image modality and the type of tissue under study.

In this work, the main methods commonly used in medical images are explored. Finally the proposed methodology is applied to several hard and soft tissues including jaw, spine, skull and brain.

Main Problems and Characteristics of Medical Images

Medical images are usually contaminated by noise generated by interference or other sources. Usually, noise is inherent to the medical images acquisition and to the performance of medical instruments as well.[4] Moreover, radiological procedures modify the image contrast and visualization details.[2] Thus, it is mandatory to modify the gray-intensity range of images in order to improve the visualization of more brilliant zones as compared to other not so brilliant ones. The success in getting reliable tissue geometric-models will depend on the techniques used in this first step.

Noise in image space

Image noise is usually characterized by the distribution and amplitude values and their levels vary according to the tissue and to the spatial resolution of each image. In medical images, the noise is due to stochastic processes in image acquisition or during their reconstruction. To address this problem, some reduction filters (to be used further as shown in Figs. 8, 12 and 14) have been developed using Gauss distribution. An image corrupted by noise can be described as follows:

$$v(x,y) = g[u(x,y)] + n(x,y), \tag{1}$$

$$g[u(x,y)] = \iint n(x,y,x',y')u(x',y')dx'dy', \tag{2}$$

where $u(x,y)$ is the original image and $v(x,y)$ is the observed image (corrupted by noise); $n(x,y)$ stands for the additive noise. The formation image process can be modeled by the linear system described in Eq. (1), where $n(x,y,x',y')$ is the response to the image acquisition.

The interpretation of noise in a medical image will depend on the image itself and on the visual perception. The estimation of the statistical characteristics of noise in an image is needed to separate the noise from the image. Four kinds of noise are usually reported (see Ref. 9): additive, multiplicative, impulsive and quantification noise. Since additive and multiplicative are the most commonly observed noises in medical images, we include a brief description below:

- *Additive noise.* This is generated by white Gaussian sensors, as defined in Eq. (3), where $g(x,y)$ is the observed image having noise resulting from the image $I(x,y)$ corrupted by additive noise $n(x,y)$

$$g(x,y) = I(x,y) + n(x,y). \tag{3}$$

Figure 1 shows an example of additive noise, resulting from adding Gaussian-type noise to a phantom image which simulates a MRI of brain. The behavior of added noise can be observed in the histogram shown in Fig. 1(D).

- *Multiplicative noise.* This is a kind of speckle noise, observed in medical images, particularly in ultrasound and MRI. This kind of noise is represented in Eq. (4), where $g(x,y)$ is the observed image having noise, $I(x,y)$ is the image in formation, $c(x,y)$ is the multiplicative noise component and $n(x,y)$ is the added noise.

$$g(x,y) = I(x,y)c(x,y) + n(x,y). \tag{4}$$

Figure 2 shows an example of multiplicative noise added to a phantom image that represents a MR brain

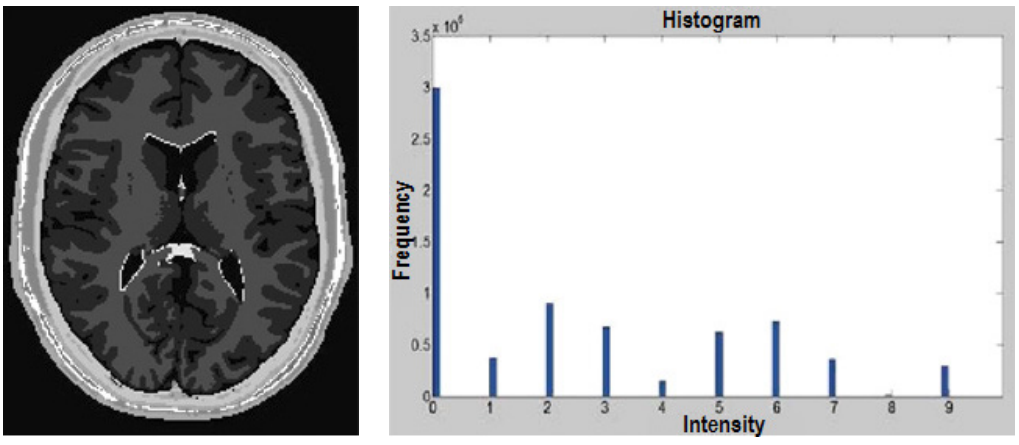

(A) **(B)**

Fig. 1 Brain phantom corrupted by additive noise. **(A)** Axial slice of original phantom. **(B)** Histogram of A. **(C)** Original image in A with Gaussian additive noise. **(D)** Histogram of C.

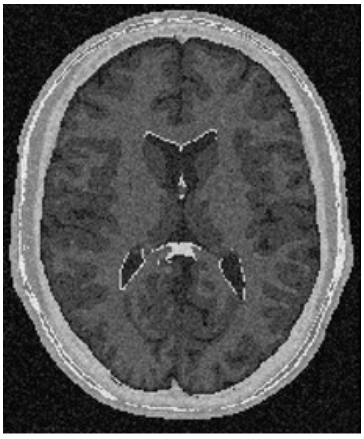

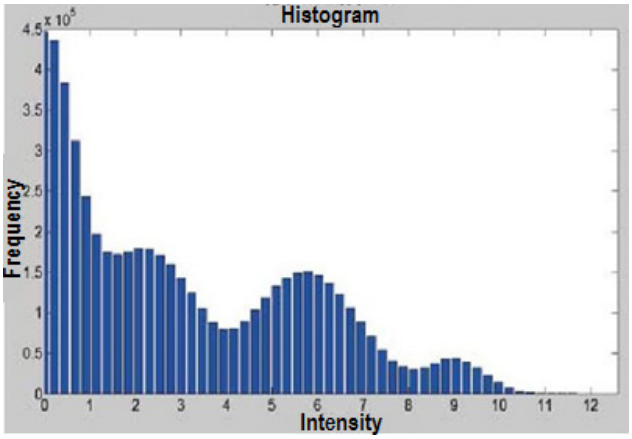

(C) **(D)**

Fig. 1 (*Continued*)

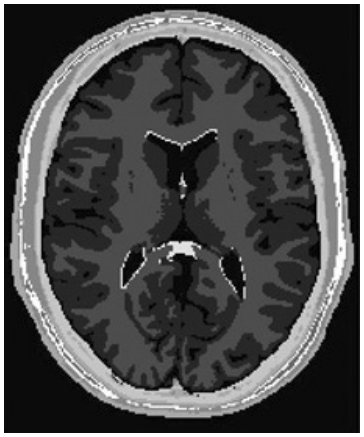

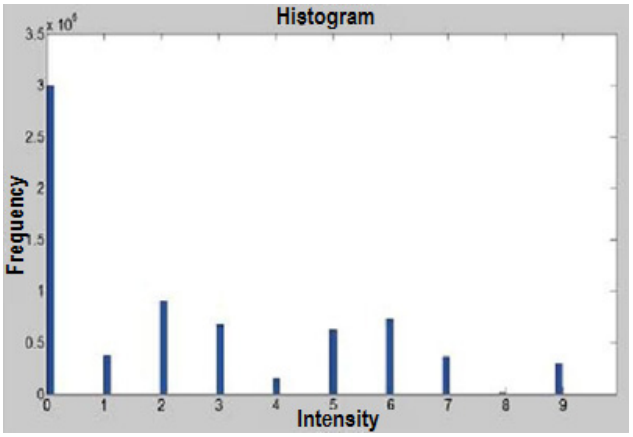

(A) **(B)**

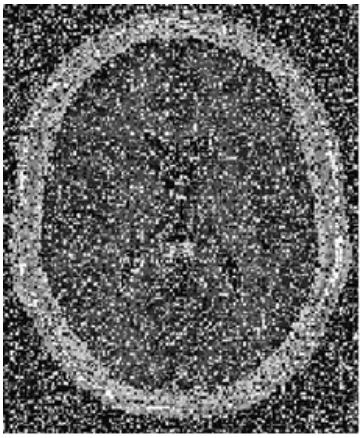

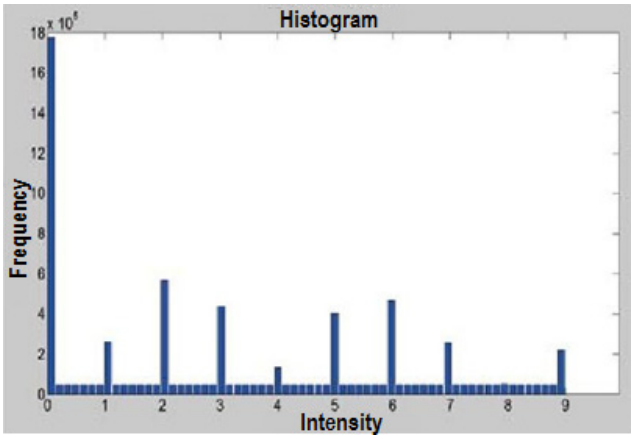

(C) **(D)**

Fig. 2 Brain phantom corrupted by multiplicative noise: **(A)** Axial slice of original phantom. **(B)** Histogram of A. **(C)** Original image corrupted by multiplicative noise. **(D)** Histogram of C.

image. For the sake of simplicity, $c(x, y)$ was assumed constant in Fig. 2. The noise behavior can be observed in Fig. 2(D).

Edge and discontinuous zones between tissues

The edge is defined as an abrupt increase in the intensity values which shows the boundaries, or separation lines, among the different objects in it. In the image the objects boundaries are seen as discontinuities of certain properties such as intensity, color and texture. In medical images, tissues are separated by edges and discontinuous zones that are detected through diverse techniques. However, a zone of interest may not be necessarily detected without further processing. In the present study, the image-gradient technique was used to enhance medical-image edges, previously smoothed using the anisotropic diffusion filter. When these filters are applied on a gray-scale image, they calculate the image gradient (∇I) at each point (pixel or voxel) providing the direction of the largest possible increase (black or white). The gradient of the image "I" at a point in the directions X, Y, Z is computed by Eq. (5).

$$\nabla I = \left[\frac{\partial I}{\partial x}, \frac{\partial I}{\partial y}, \frac{\partial I}{\partial z}\right]. \tag{5}$$

The final results show how abrupt or soft the image changes at each point are. It also shows how a specific point represents an image edge and its orientation. Figure 3 depicts a facial-skull CT image with the boundaries highlighted through the gradient calculation in directions X, Y, Z. Note that Eq. (5) can also be used in MRI.

Segmentation of Images into Contiguous Regions

Once the intensity levels are improved and medical images devices are corrected, the next stage is segmentation, which consists in dividing images into contiguous regions (sub-regions or sub-volumes) whose elements (pixels or voxels) have common cohesion properties. A previous step is to extract the quantitative and qualitative parameters and evaluate the morphology and functioning of the segmented object. Success depends on an optimal pre-processing.

The segmentation algorithms of medical images play an important role in medical diagnosis and treatment. These are used in anatomic structures analysis, type of tissue, spatial distribution function and organs activity and pathological regions. Its application includes brain tumor detection,[10] extraction of an area affected by extra-pulmonary tuberculosis,[11] heart pathologies visualization,[12] coronary borders in angiograms, multiple sclerosis damage quantification, surgery planning and simulation, tumor volume measuring and tumor response to therapies, blood cells automated classification, brain development study, micro calcifications in mammographies among other applications.

The methods used to carry out the segmentation process vary according to the specific need, image type, among other factors. For example, the brain tissue segmentation is different from the heart or bone segmentation, such as a jaw or femur. It has been found that specialized methods for specific applications can lead to better results when having a prior knowledge. However, the choice of the right method for segmentation problems, when dealing with all types of medical images, is sometimes diffcult due to the lack of robust methods. We

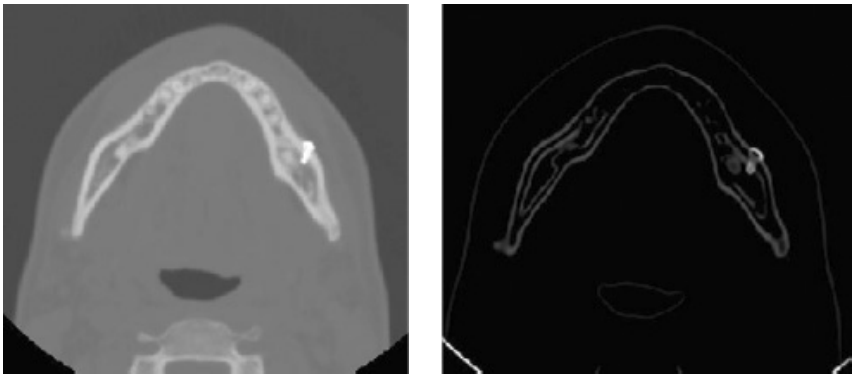

(A) **(B)**

Fig. 3 Craneofacial CT image with highlighted boundaries: **(A)** Original CT image. **(B)** Boundaries detection in A with the gradient size calculation in directions X, Y, Z.

have combined several segmentation methods which is known as the hybrid segmentation approach.

Manual segmentation vs. automated segmentation

The performance of image segmentation approaches is nowadays a persistent challenge. Manual segmentation based on interactive drawing of the desired segmentation by domain experts is often the only acceptable approach and yet suffers from intraexpert and interexpert variability. Automated image segmentation algorithms have been sought in order to remove the variability introduced by experts. The balance between manual interaction and performance is an important consideration in any segmentation application while manual interaction can improve accuracy by incorporating prior knowledge of an operator. Nevertheless, for large population studies, this can be laborious and time consuming. The type of interaction required by segmentation methods can range from completely manual delineation of an anatomical structure to the selection of a seed point for a region growing algorithm (see Sec. 3.3.1). The differences in these types of interactions are the amount of time and effort required, as well as the amount of training required by the operator. Methods that rely on manual interaction can also be vulnerable to reliability issues. However, even "automated" segmentation methods typically require some interaction for specifying initial parameters that can significantly affect performance.

Validation of segmented volumes

The accuracy of segmentation method of medical images has been difficult to quantify in the absence of a "ground truth" segmentation for clinical data. Validation is typically performed using one of two different types of truth models. The most straightforward approach to validation is by comparing the volumes obtained by automated segmentation with volumes obtained by manual segmentation. This approach, besides suffering from the drawbacks outlined in the previous section, does not guarantee a perfect truth model since an operator's performance can also be flawed. The other common approach for validating segmentation methods is the use of physical phantoms or computational phantoms. Physical phantoms provide an accurate depiction of the image acquisition process but typically do not present a realistic representation of anatomy. Computational phantoms can be more realistic in this latter regard, but simulate the image acquisition process using only simplified models. Although digital or computational phantoms can provide a level of known "ground truth", it has so far been unable to reproduce the full range of imaging characteristics (partial volume artifact, intensity inhomogeneity artifact, noise) and normal and abnormal anatomical variability observed in clinical data.[13] A common alternative to phantom studies has been a behavioral comparison of algorithms: an automated algorithm is compared to the segmentations generated by a group of experts and, if the algorithm generates segmentations suffciently similar to the experts, it is regarded as an acceptable substitute for the experts. Typically, good automated segmentation algorithms will also require less time to apply, having better reproducibility than interactive segmentation by an expert.

Tissue Visualization

3D visualization of tissues strongly depends on computational tools which make easier the human–machine interaction when dealing with hard and soft tissues exploration and analysis. From the engineering point of view, these aspects pose a challenge because functional characteristics must be displayed in different visual forms to help the interpretation of multi-dimensional information and the correlation of qualitative and quantitative information at the same time. Another critical issue is to guarantee the 3D perspective realism for the spatial representation of the data, temporal information representation and other visual signals such as textures and tones as well as solving the interaction model between users and the information through visualization systems. Modeling is a breakthrough in biomedical research by making analytical formulations to describe physiological functions. Nowadays, a new approach has been assumed by biomedical and mechanical engineers to tackle the modeling problems based on visualization because it allows the validation of the qualitative model. Likewise, the visualization techniques required now for modeling applications and biomedical simulation should cover multidisciplinary areas such as the finite element modeling and computational fluid dynamics among others. This should help in getting faster the prototypes and their parameters.

3D visualization refers to a visual representation obtained through a set of slices of the same resolution, aligned parallel with respect to an adjacent position (z-coordinate) obtaining a volume consisting of voxels.[14] The birth of medical images based on 3D information such as MR, CT, PET, among others, set the beginning of diverse research studies in 3D medical images reconstruction to obtain a volumetric view of soft tissues[15–18] and hard tissues.[5–7,19]

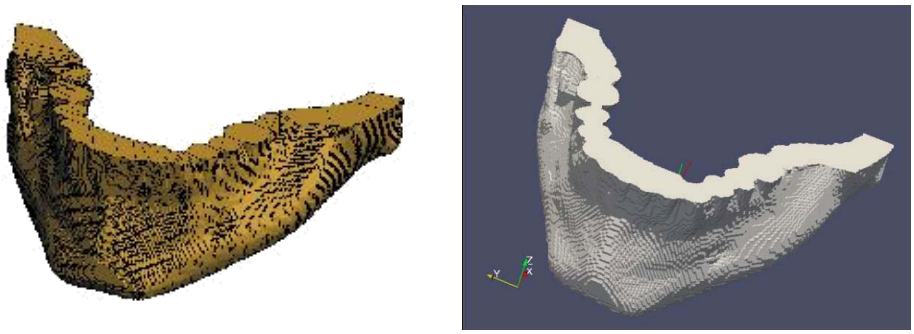

(A) **(B)**

Fig. 4 3D reconstruction of a jaw bone: **(A)** Volumetric view **(B)** isosurfaces view.

The 3D visualization of human-body parts from medical image reconstruction is an advantage for medical doctors as it adds a third dimension to the views displayed on the computer providing a more complete information. However, one of the main problems in 3D representation is how users can interpret and manipulate the information in a faster way. Thus, it is advisable to use specific visualization routines that focus on areas of interest and showing the results in a faster and more reliable way. Another aspect to take into consideration is the computational cost of 3D visualization systems, which tends to be high because of the amount of data.

One approach to reduce the high computational cost involved in 3D visualization of biological structures was presented in Ref. 20, in which isosurfaces were extracted from volumes obtained through CT. An isosurface is a visual representation of a structure obtained through a voxel, which has the same or similar intensity value. This technique is also known as 3D boundary extensions, 3D boundaries or sometimes boundary surfaces.[3] The main idea is to extract a surface from a volume of 3D data as a collection of adjacent polygons and visualizing the extracted surfaces with appropriate algorithms.[14] With this technique it is possible to display, manipulate and extract geometric information from structures in a faster way. One of the best known isosurfaces extracting algorithms from volumetric data is the Marching Cubes Algorithm proposed in Ref. 21. The authors examined each basic element (volume cell) and generated a triangulation over it. In Fig. 4(B) a jaw bone surface obtained from a 3D volume [Fig. 4(A)] is shown.

PROPOSED METHODOLOGY

To obtain useful geometric tissue models it is necessary to properly apply a set of image-processing techniques to deal with the complexity of human tissues and to get simplified models. These models will reduce the complexity of the subsequent numerical analysis. In this way, the geometric models obtained by this methodology will be used to generate surface and complex finite element meshes, which will help in visualization, measurement, biomechanical simulation, rapid prototyping and prosthesis design. Thus we propose an integrated methodology based in the observation of tissue type, its intensity profiles and its boundary quality, which consists of five main steps integrated into the computational tool biomedical view.[22,23] The algorithms were developed using MATLAB tool[8] and the Insight ToolKit (ITK) library code.[24] The flowchart of the proposed methodology is shown in Fig. 5.

The first step of the methodology, called 3D reconstruction, leads to an initial volume from 2D medical images. The second step consists in to apply preprocessing techniques to the original volumes in order to reduce noise and other artifacts. These techniques are chosen according to the image characteristics.

The third step is the segmentation of the initial volume considering regions-of-interest (ROI) such as soft and hard tissues. The fourth step refines the obtained models by applied morphological operators and gaussian filter. Finally, in the last step, the volumes are saved in standard output format readable by the most of CAD programs or the geometric model discretization through numerical methods. Each one of the steps of the methodology are explained in detail in the following sections.

Step 1: Reading Images and 3D Reconstruction

The initial 3D reconstruction of Digital Imaging and Communication in Medicine (DICOM) images was done by parallel stacking of each slice with respect to the Z axis. The next step was to select a ROI in the initial 3D image to obtain sub-volumes containing zones of

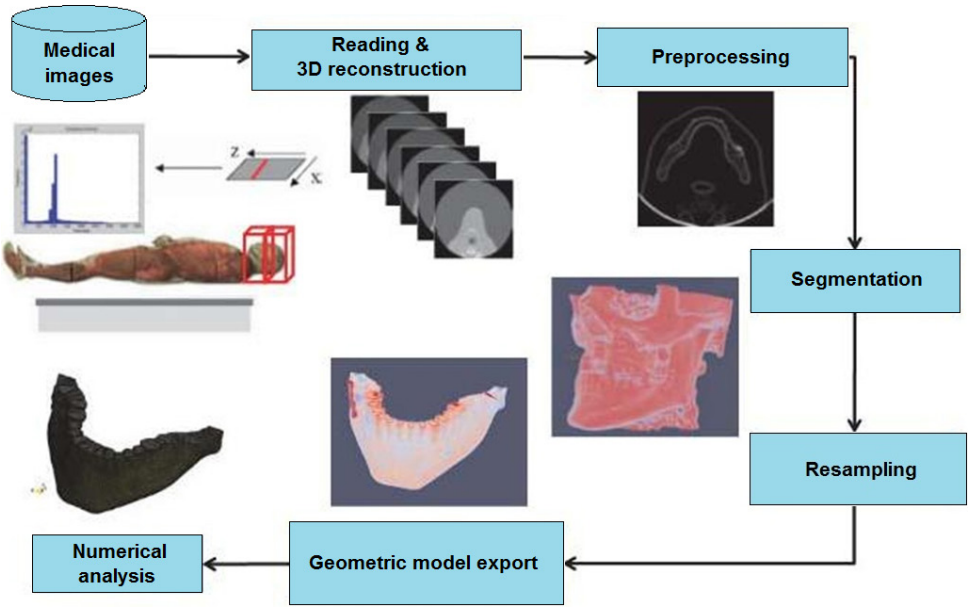

Fig. 5 Schematic flowchart of integrated methodology.

interest. In each one of the sub-volumes a flowchart consisting of algorithms was applied from the preprocessing step to obtain the relevant tissue-volume.

Step 2: Preprocessing

Noise and artifact reduction in image space

For image noise elimination, the gradient anisotropic diffusion filter of ITK was used to implement a N-dimensional version of the classic equation of anisotropic diffusion proposed by Preona and Malik.[25] (see Eq. (6)). In this equation, an edge detector $|\nabla I|$ is used, which is responsible for noise smoothing and whose value becomes infinite when approaching a perfect edge

$$I_t = \nabla \cdot (g(|\nabla I|)\nabla I). \tag{6}$$

The function $|\nabla I|$ is used to reduce conductance in high value areas. $|\nabla I| = 0$ where the gradient is high and decreases completely in low gradients. It means $g(x) \to 0$, if $x \to \infty$ (reached value in one edge) and $g(x) \to 1$, if $x \to 0$ (reached value within a region).

Edge enhacement in regions of interest

Different tissues or ROI can be visualized in the images and it may be hard to separate from each other. The solution is to calculate the gradient image and its module, which is useful to determine the boundaries and the separation of the left ventricle from the right ventricle and the descending aorta. The gradient shows how abrupt or smooth an image changes in each analyzed voxel, and a specific point represents an edge in the image as well as the orientation of that edge, i.e. the vector obtained gives us the direction of the largest possible increase (black or white) and the value of that change in direction for each voxel. In fact, it is easier to calculate the module of the gradient (see Eq. (7)) than to interprete its direction. The reason is that using the gradient size, a gray-scale image is generated with the defined boundaries, which helps in separating homogenous regions

$$|\nabla I| = \sqrt{\left(\frac{\partial I}{\partial x}\right)^2 + \left(\frac{\partial I}{\partial y}\right)^2 + \left(\frac{\partial I}{\partial z}\right)^2}. \tag{7}$$

The gradient can be highly sensitive to noise if a smoothing technique is not applied before, so the input images passing through this filter were the images previously smoothed by the anisotropic diffusion filter. In some cases, after improving the boundaries with the gradient calculation, an additional filter was applied to strengthen the boundaries and to ensure a suitable segmentation. The library of sigmoid filter provided by ITK[24] was integrated. It transforms the gray-scale intensity values of the image generating an image I_{sigmoind} with the voxels of the strengthen boundaries and the other voxels of the regions progressively smoothed. This filter is configurated using four parameters as follows:

$$I_{\text{sigmoid}} = (\text{Max} - \text{Min})\frac{1}{\left(1 + e^{-\left(\frac{I-\beta}{\alpha}\right)}\right)} + \text{Min}, \tag{8}$$

where I contains the input voxels intensity. The image I_{sigmoid} contains the output voxels intensities, Min and Max are the minimum and maximum values of the output image, α is the width of the input intensity range while β defines the intensity over which the range is centered.

Step 3: Image Segmentation

For the segmentation of structures of interest, hybrid algorithms were applied in a sequential manner, and the technique used depended on the type of tissue. Regardless of the segmentation technique chosen, the results would be affected by the image noise causing holes in the extracted regions and even disconnection. To address this problem, the segmentation was carried out after the image preprocessing step through noise reduction and boundaries enhancement techniques.

Region growing

Region growing is widely used in medical applications to extract body structures and its pathologies. In some studies (see for instance Ref. 26) this algorithm was used in brain ventricle segmentation. In Ref. 6 an extra pulmonary tuberculosis infection was segmented by modifying the region growing algorithm while in Ref. 27 the authors extracted the left ventricle in a CT for further numerical analysis.

This technique was used to extract texture connected regions with similar characteristics. The first step of the algorithm establishes manually one or more seeds (spherical volume) within the region of interest. The next step analyzes the neighbor voxels to the region, calculating the average and the standard deviation σ, adding the pixels of position X whose gray-scale intensity values meets the required condition in Eq. (9):

$$I(X) \in [m - f\sigma, m + f\sigma], \tag{9}$$

where I: image, X: neighbor voxel position analyzed, m: mean, σ: standard deviation, f: multiplying factor. The second step was implemented until no more voxels can be added. Finally, the segmented object was represented by all the elements being accepted during the searching process.

Watershed algorithm

The Watershed algorithm is another approach widely used in image segmentation.[28] Its general concept was introduced in Ref. 29 and it is based on mathematical morphology. In this algorithm the image is seen as a topographic surface with rivers and valleys, where the landscape elevation values are defined by the gray-scale value of each pixel or its gradient size. Based on a 3D reconstruction, the image is divided in regions called catchment basins. For each local minimum, a catch basin comprises all the points whose steepest way ends down to its minimum. Finally, watershed is defined by the border lines that separate one basin from the other. The catch basins are labeled by different gray-scale intensity. For each local minimum, a catchment basin comprises all points whose path of steepest descent terminates at this minimum. In this work, watershed was used for big structures segmentations such as the left ventricle and with a continuous texture as with bone structures. In our algorithm, the input image was the gradient magnitude image *Img* obtained during the preprocessing stage (see Eq. (7)), which is considered as a height function where high values represent the borders presence. The first step eliminates the shallow regions below the threshold minimum value which helped to control the over segmentation. From this point, the algorithm created an initial segmentation allowing to track the fastest decrease of each pixel up to its local minimums. The initial result was passed through a second filter which only considered regions with depths lower than the established maximum depth level. In this way the segmentation was controlled up to the segmentation decrease level (catch basins). The parameters threshold and depth were established within the range $[0, 0, -1.0]$ and arbitrarily chosen. As a result of this function, a first image segmentation (I_w) was obtained comprising various segments connected in a non-related way and labeled with a different gray-scale level as described below:

$$I_w = \bigcup_{i=1}^{n} I_i, I_i \cap I_j = \varphi \quad \forall\, i \neq j. \tag{10}$$

One of the main problems of this technique is the over segmentation of regions caused by the images noise, hence the importance of the preprocessing stage to reduce noise and to enhance the edges. It was necessary to group some of the adjacent segments as per their gray-scale levels of the labeled regions in order to obtain the entire volume. Thus, in some cases the final volumes were obtained through the thresholding process, setting the lower threshold in t_0 and the highest threshold to t_f , where $t_0 \leq I_f \leq t_f$.

Step 4: Resampling

Once the segmentation techniques are applied, the volumes are subjected to a resampling process to correct

possible holes in the regions and to smooth surface overlapping. Morphological dilatation techniques and Gauss filters are used for this task.

Step 5: Exporting Geometric Models Using Computer-Aided-Design (CAD) Formats

Volumes were saved in Visualization Toolkit format (*.vtk)[a] to keep the voxels coordinates and their sizes in directions x, y, z and in the Stereolithography format (*.stl)[b] which stores a triangle mesh over the surfaces to define the object shape. We used GiD[30] and ParaView[c] to visualize surface models and mesh generation. Inventor Autodesk[d] was used to transform solid models and finally, Abaqus[e] was used for model discretization and finite-element analysis (FEA). Test boundary conditions were assigned to different regions of the solid volume of the models.

HARD AND SOFT TISSUE MODELS

The algorithms based on image processing techniques described in Sec. 3 were implemented by following the general flowchart shown in Fig. (5). Both algorithms and the results obtained with the proposed methodology applied to DICOM images[f] to obtain the different soft and hard tissue models (the same that were exported to CAD tools) are presented below.

Flowcharts for Hard Tissue Models

In CT images, bone structures are represented with gray levels higher in contrast than other types of tissues present in these images. For this reason, it is useful to apply thresholding techniques to separate the bone tissue from others. Nevertheless, the use of thresholding may have the disadvantage of generate small disconnected areas into the same structure or outside it, then creating overlapped areas on the bone zones. These characteristics make it necessary to use noise filters before the segmentation and resampling the segmented models using morphological dilation techniques to fill the holes and to smooth the outer layer of bone models.

To apply the methodology with hard tissue models, jaw and spine CT images were used combining watershed and threshold algorithms with other preprocessing and resampling filters.

Jaw and spine modeling

The flowchart displayed in Fig. 6 was used to obtain the jaw and spine models. Each process is described below:

- *Preprocessing*: the images noise was reduced using the filtered noise algorithm of anisotropic diffusion and the borders were detected by calculating the gradient module of the filtered image.
- *Segmentation*: for the segmentation stage, a watershed algorithm was applied in the gradient image obtaining a gray-scale image with uniform regions labeled by a gray-scale intensity, see Sec. 3.3.2. Among the obtained set of regions, a zone of interest was chosen with the threshold technique.
- *Resampling and CAD exportation*: a resampling of this initial geometric model was carried out by using a morphological dilatation with one spherical structural element of radio $3 \times 3 \times 3$ to smooth the overlapping surfaces and fill the possible holes that may arise from the segmentation. This model was saved in readable formats by visualization software.
- *Discretization*: finally, using these tools, test boundary conditions were applied to random zones of the model. The geometric model utility was verified for its discretization with the FEM.

Figure 7 shows the results obtained in jaw CT images in DICOM format, size 192×192 pixeles, voxel spacing $1.5625 \times 1.5625 \times 2.5$ mm. Also, Fig. 8 shows the results obtained for each step using spine CT images in format DICOM, 513 slices, size 512×512 pixels, voxel spacing: $0.782 \times 0.782 \times 1.0$ mm.

The geometric model of a jaw is displayed in Fig. 9. Different types of tissues of the jaw bone are discriminated [Fig. 9(A)]: cortical bone, medullary bone, alveoli

[a] *VTK User's Guide*, 5th edn., Kitware, Inc. 2006.
[b] *Stereolithography Interface Specification*, 3D Systems, Inc. 2010.
[c] *ParaView: Parallel Visualization Application. User's Guide, Version 1.6.*, Kitware, Inc. 2009.
[d] Autodesk Inventor Professional. User's Manual and Guide, 2009.
[e] Abaqus 6.9. ABAQUS/CAE User's Manual, 2009.
[f] National Electrical Manufacturers Association. *DICOM: Digital Imaging and Communications in Medicine*, 2008.

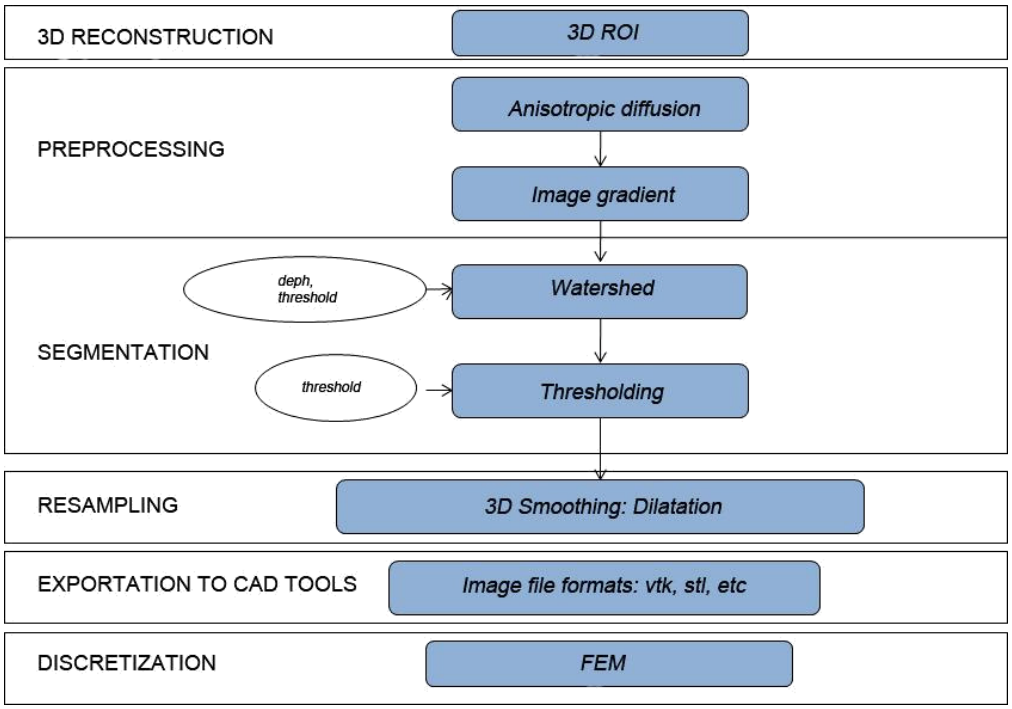

Fig. 6 Flowchart for jaw and spine models.

and even the prosthetic screw implanted to the patient. The surface and mesh views of the volume obtained are presented in Figs. 9(B) and 9(C).

A spine geometric model obtained by the proposed method is presented in Fig. 10. The views presented in this figure have been obtained using the Paraview and GiD softwares.

Flowcharts for Soft Tissue Models

In contrast to the hard tissues, visualization of soft tissue is affected by factors related to its gray values. Intensity variations between different images of soft tissues occur due to the use of different scanners as well as the time of data acquisition. Various contrast enhancements, used to make certain features more prominent, are yet another contribution to the intensity variations across images. Also, some images are affected by the presence of different tissues with similar gray levels and the absence of constant gray levels over the same tissue. On the other hand, soft tissues are characterized by different shape and size, the presence of other body tissue within the target regions or overlaps in medical image, which adds to the complexity of the problem.

The methodology was applied to brain images. To solve the difficulties mentioned above, the task of segmentation was performed using the region growing algorithm, due to its performance when dealing with the intensity and shape variations.

Gray matter modeling

In brain MRI, the brain tissue like other parts of the central nervous system contains white and gray matter, the last the least amount. The segmentation of these structures makes necessary the quantitative morphometric analysis for the diagnosis of various diseases and evaluation of the response to a given treatment. However, the segmentation of brain MRI is affected by the presence of different tissues with similar gray levels and the absence of constant gray levels. Also, medical images of the brain based on MRI and PET, among others, are characterized by noise associated with each type of imaging. The region growing technique can be useful to extract this type of brain tissues due to the flexibility of the method to indicate initial small zones into the desired target tissues through the selection of seeds. Also, it is possible to control and restrict areas that are added in each interaction of the algorithm by defining more sophisticated features as the combination of the mean, standard deviation, entropy, correlation, and other statistical classifiers [see Eq. (9)].

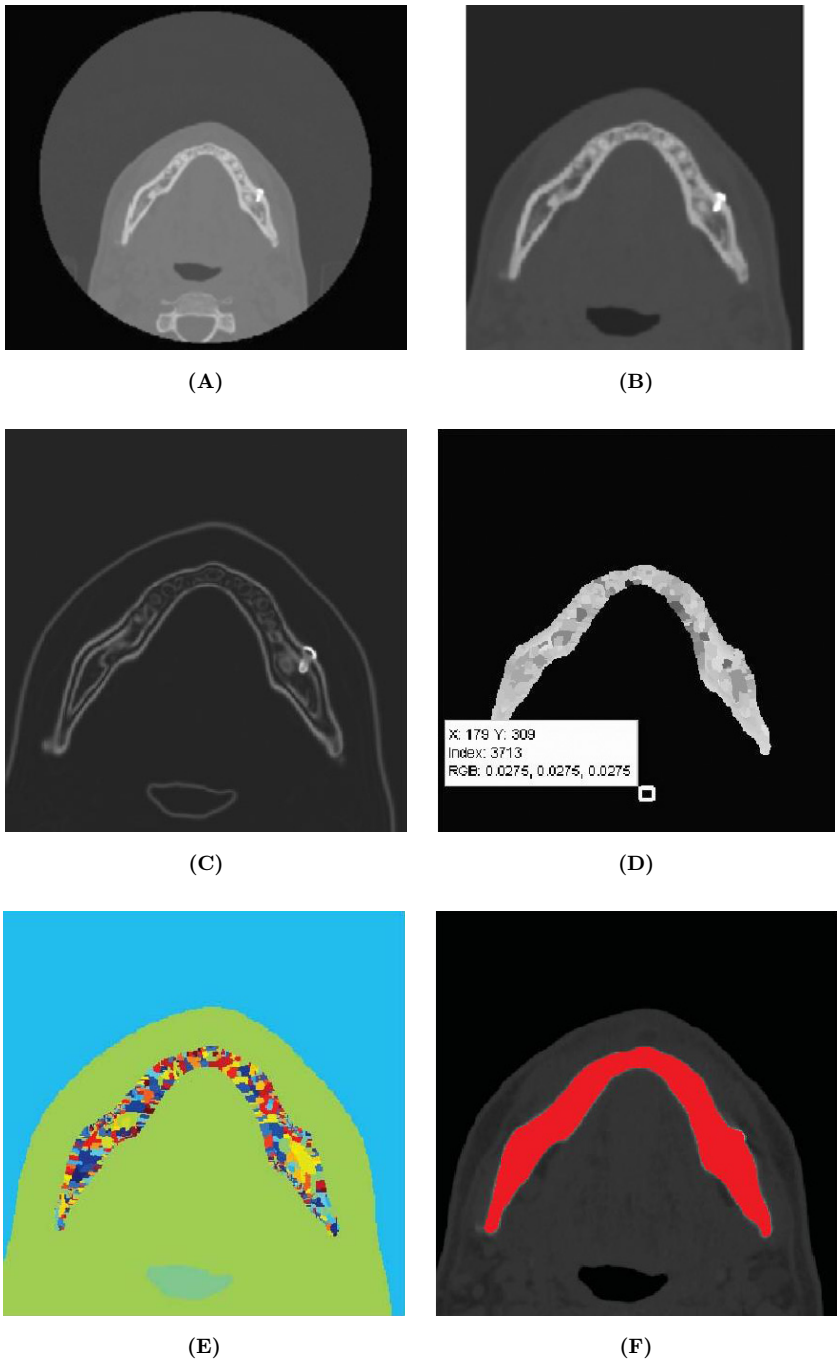

Fig. 7 Jaw bone preproccessing and segmentation. **(A)** CT skull axial slice view. **(B)** ROI with noise reduction through the anisotropic diffusion filter. **(C)** Image Gradient module of B. **(D)** Watershed segmentation applied to border image C. **(E)** Watershed image view on color map. **(F)** Jaw zone selection through threshold technique.

The techniques shown in the flowchart of Fig. 11 were applied to obtain the zone volume of the gray matter geometric model.

- *Preprocessing*: the images noise was filtered using the anisotropic diffusion algorithm smoothing the noise and preserving the images boundaries.
- *Segmentation*: the region growing algorithm was applied over the filtered image, placing spheres (seeds) in the zone of interest. The condition for inclusion is described in Eq. (9) based on the average and the standard deviation of the neighbor voxels (see Sec. 3.3.1). The resulting volume was a binary image with the white material zone colored white (value 255).

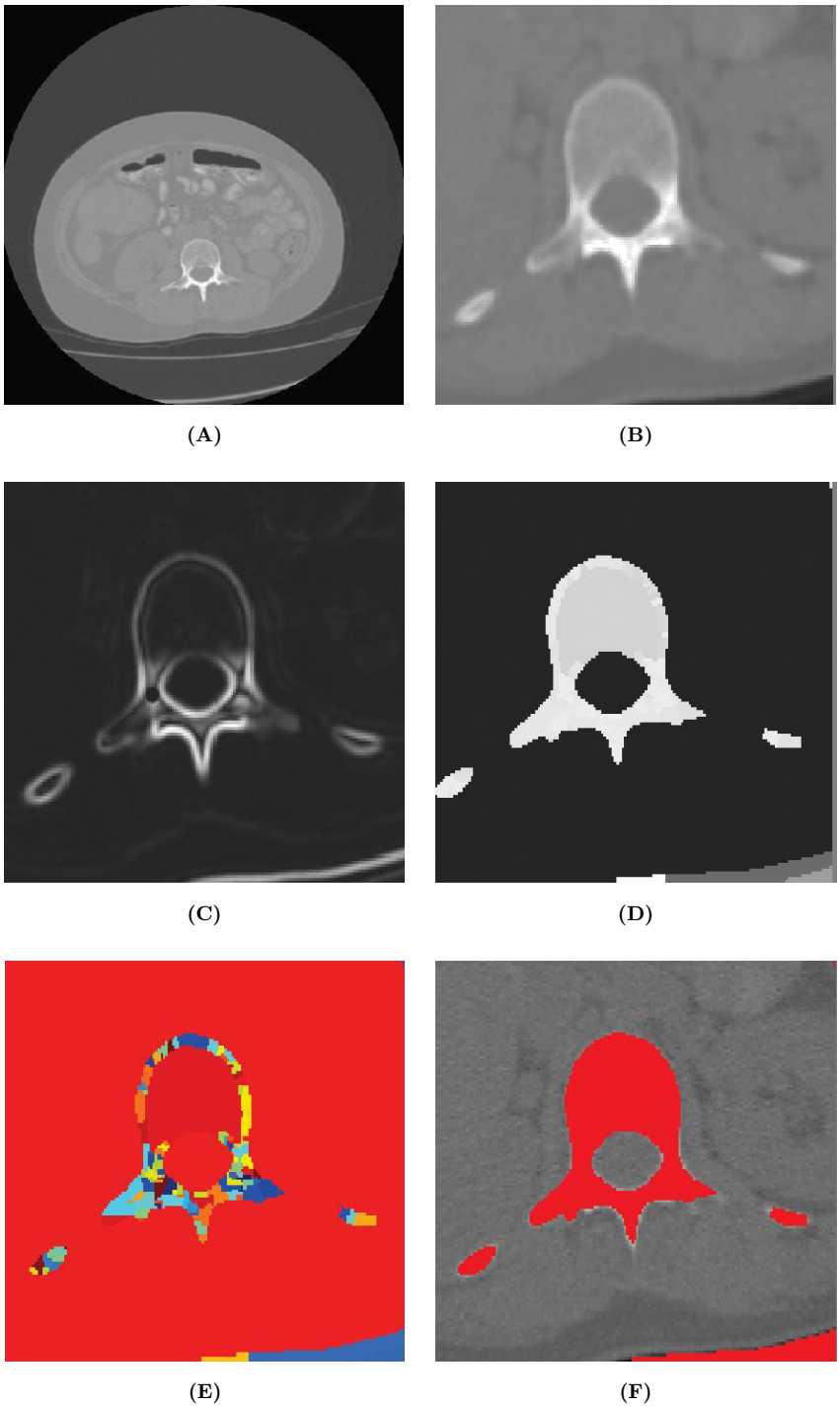

Fig. 8 Preproccessing and segmentation of CT images. **(A)** CT Axial slice view. **(B)** ROI with noise reduction through the anisotropic diffusion filter. **(C)** Image gradient module of B. **(D)** Watershed segmentation applied to border image C. **(E)** Watershed image view on color map. **(F)** Spine zone selection through threshold technique.

- *Resampling and CAD exportation*: in order to improve the initial geometric model, a resampling of the volume was carried out through the morphological dilatation technique with a structural round shaped element of radio $3 \times 3 \times 3$ to smooth the overlapping surfaces and fill the holes generated during the segmentation due to the sensitivity of the segmentation condition. The final geometric model was saved in a

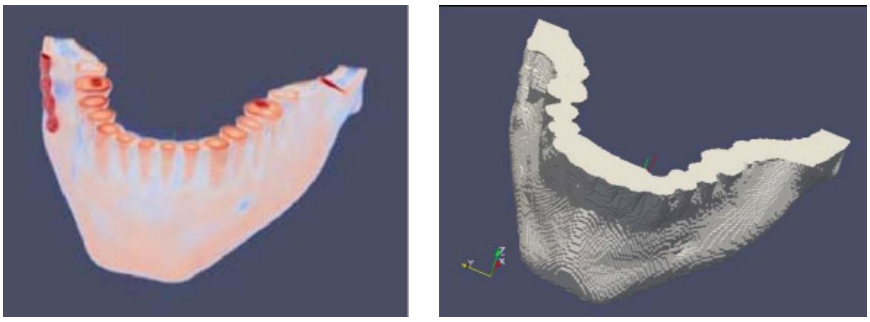

(A) (B)

(C)

Fig. 9 Jaw volumetric view. **(A)** Jaw bone 3D visualization. **(B)** Surface volume. **(C)** Mesh volume.

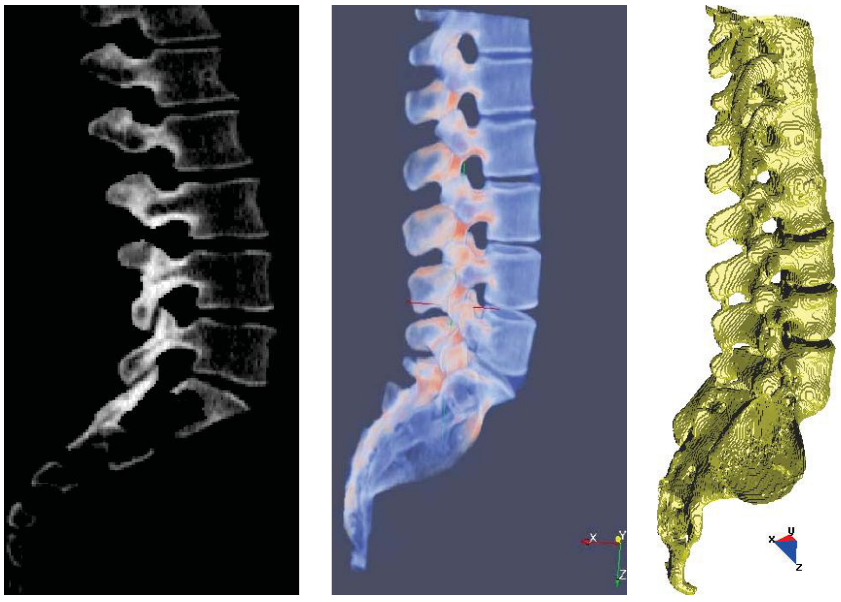

(A) (B) (C)

Fig. 10 Views of the spine model. **(A)** Sagittal slice view. **(B)** 3D view using paraview. **(C)** 3D view using GiD.

legible format by a visualization software and CAD tools.

- *Discretization*: finally, using these tools, test boundary conditions were applied over random zones of the model.

Figure 12 displays the results obtained in each stage in brain MRI of DICOM format, 60 slices of sizes 256×256 pixels, voxel spacing: $0.86 \times 0.86\,\text{mm} \times 3.0\,\text{mm}$. For visualization purposes, only one of the axial slices is presented. It can be observed in Fig. 12(B) the selection of

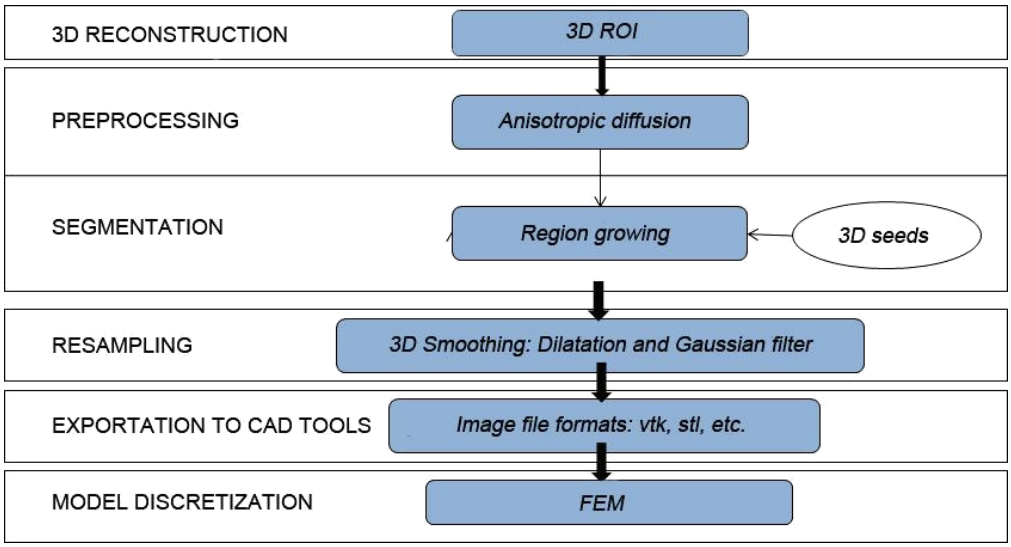

Fig. 11 Flowchart for gray matter model.

five seeds in the zone of interest. The success of the segmentation will depend on where the seeds are placed.

CPU Processing Time

Through the sequential execution of the proposed preprocessing, segmentation and resampling techniques and following the aforementioned flowcharts, soft and hard tissues geometric models were obtained at very attractive CPU times. The algorithms and libraries used for each study case were developed and integrated into a MATLAB script. In order to perform processing tasks interactively through control buttons and sliders, a graphical user interface (GUI) was developed under the GUI development environment (GUIDE) of MATLAB.

The CPU time required for the five compilations to obtain the three geometric models is presented in Table 1. The computer used was a 64-bits desktop with two processors (Core 2 Quad), 2.66 GHZ speed each one and 8 GB RAM memory.

Validation

Validation experiments are needed to assess the performance of any methodology based on preprocessing and segmentation of medical images. A common approach to validate segmentation methods is through the use of computational phantoms. They simulate the image acquisition process using only simplified models.

The proposed methodology was validated using a computational phantom obtained from brain MRI available in the web site BrainWeb.[13] The flowcharts used were the same applied to obtain de jaw and gray matter models (see Sec. 4.1 and 4.2.1), both based in the region growing and watershed algorithms, respectively. The results were compared to the volumes obtained from web site using statistical texture analysis to quantify the performance of the proposed methodology.

The texture analysis applied to images is related to the spatial distribution of digital levels of the image. For the validation, the texture analysis was applied using statistical descriptors that study the value of the pixel and describe its smoothness, rugosity, etc. Finally, the absolute error percentage of voxels was calculated between both segmented models (segmented and truth models). For consistency purposes only, the statistical descriptors are briefly discussed below:

- *Standard deviation.* It measures the dispersion or contrast among digital levels, being related to the homogeneity observed in the image. In dark images, the standard deviation σ is high if there are high intensity gray level pixels with low gray level background. If $\sigma = 0$, then the image intensity level is constant, if $\sigma = 1$, the image intensity level has high changing values.
- *Skewness.* It measures the histogram's asymmetry. A symmetric histogram will have a third-order moment value close to zero. In mathematical terms, skewness is the asymmetry value of the data with respect to the average. If it is negative, the data is distributed more to the left of the average than to the right. If it is positive, the data is distributed more to the right (or any perfectly symmetric distribution). The μ_3 of a normal distribution is zero. This descriptor is

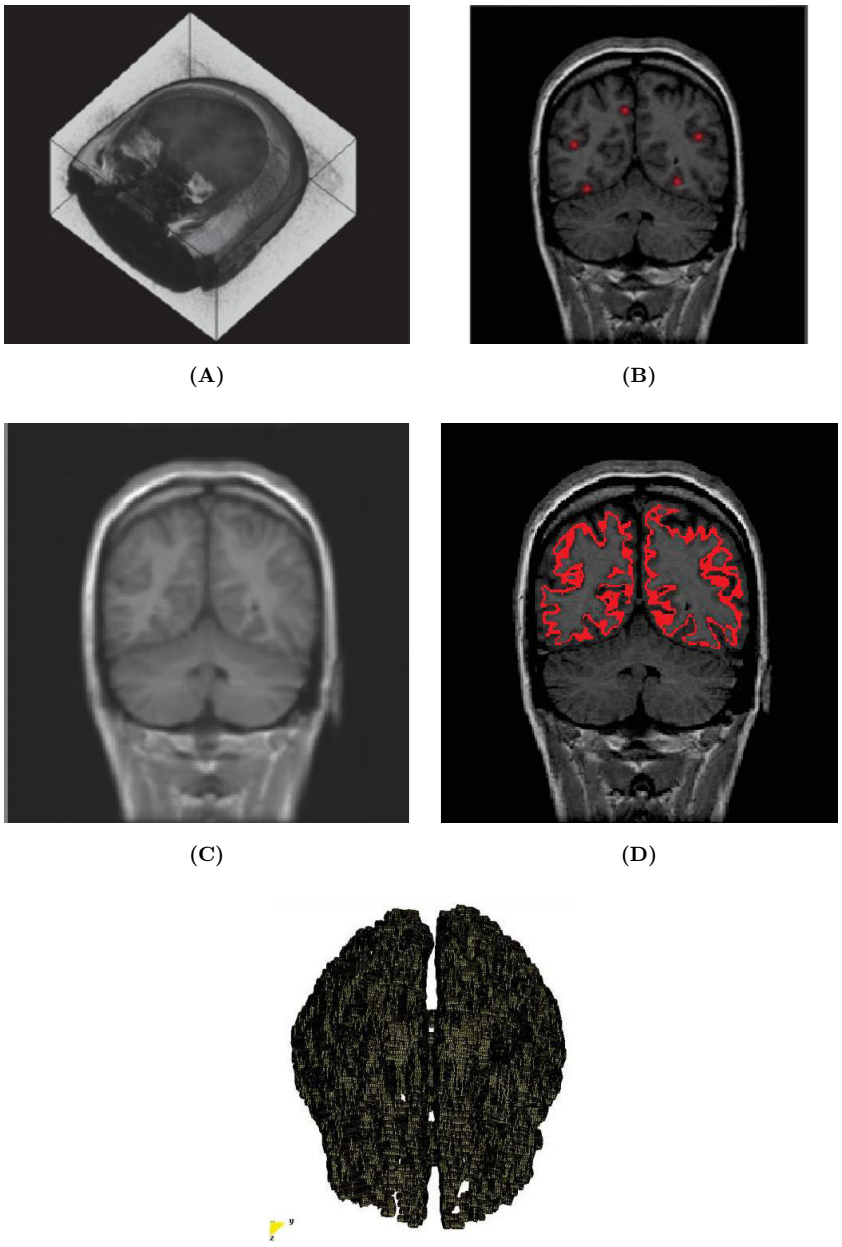

Fig. 12 Segmentation of gray matter using region growing algorithm. **(A)** Original volume from brain MR images. **(B)** Coronal slice view with selection of five initial seeds. **(C)** Denoising of image using anisotropic filter. **(D)** Coronal slice view B with segmented gray material through growing region. **(E)** Volumetric view of the segmented white material in D.

defined as:

$$\mu_3 = \frac{1}{\sigma^3} \sum (i - \mu)^3 h(i), \tag{11}$$

where μ is the mean of gray levels of image, σ is the standard deviation of image, $h(i)$ is the probability histogram for the gray levels.

- *Fourth-order moment (kurtosis).* Kurtosis (μ_4) measures the flattening of the histogram's upper peak. The smaller the value the smoother the peak. The value of a normal distribution is 3. Distributions likely to have more atypical values than the normal distribution have a value greater than 3. Distributions less likely to have atypical values have a value less than 3. Homogeneity of an image is defined as:

$$\mu_4 = \frac{1}{\sigma^4} \sum (i - \mu)^4 h(i), \tag{12}$$

Table 1. Preprocessing and Segmentation CPU Time (s).

Compilation ID	Flowchart Based on Watershed Algorithm		Flowchart Based on Region Growing Algorithm
	Jaw Bone	Spine Bone	Gray Matter
C_1	40.42	0.052	2.68
C_2	39.35	0.058	2.66
C_3	40.65	0.058	2.65
C_4	40.92	0.055	2.69
C_5	40.98	0.056	2.66

where μ is the mean of gray levels of image, σ is the standard deviation of image, $h(i)$ is the probability histogram for the gray levels.

- *Average entropy.* It measures the image granularity. It is a random statistical data used to charaterize the image texture. A high value indicates a thick texture and its value is zero if it is constant. The entropy is then defined as:

$$\text{Ent} = -\sum h(i), \tag{13}$$

where $h(i)$ is a probability histogram for the gray levels.

The phantom of Brainweb was used as "ground truth" with known substance classes which simulates brain MRI through "fuzzy" volumes where each type of tissue is represented. Global discrete anatomic volumes for each type of voxels were labeled with numerical values as follows:

- 0 = background (BG)
- 1 = cephalicmedulla liquid (CL)
- 2 = gray matter (GM)
- 3 = white matter (WM)
- 4 = fat (FA)
- 5 = muscle/skin (MS)
- 6 = skin (SK)
- 7 = skull (SU)
- 8 = glial matter (GL)
- 9 = connective tissue (CT)

Validation of soft tissue models

First, a region growing algorithm was used to segment a gray matter zone of interest. This segmentation algorithm was applied in three ways: (i) to the original complete discreet phantom, (ii) to the discrete phantom with Gaussian additive noise and a subsequent filtering using the average filtering and (iii) to the discrete phantom with Gaussian additive noise and a subsequent filtering with an anisotropic diffusion filter. These segmentation zones were compared to the gray matter zone provided by the Brainweb. For this purpose, the texture analysis was used by calculating the statistical descriptors in both volumes and the respective percentages of error (%) between the two volumes obtained.

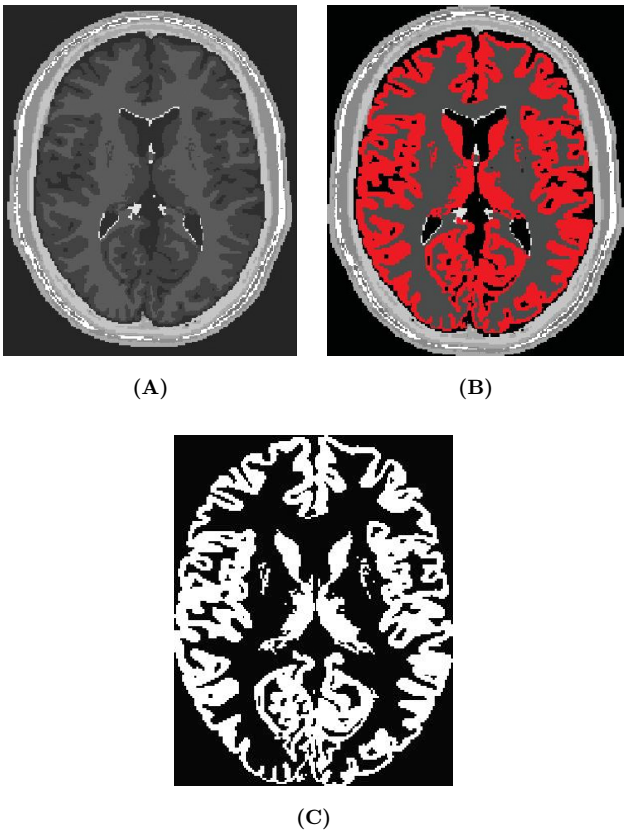

(A) **(B)** **(C)**

Fig. 13 Gray matter segmentation in phantom volume. **(A)** Axial slice number 98 of the original phantom image. **(B)** Gray matter segmentation by the proposed methodology using the region growing algorithm. **(C)** Gray matter zone segmentation by Brainweb.

Figure 13 shows the results obtained during the gray matter zone segmentation in the phantom volume with dimensions $181 \times 217 \times 181$ in directions x, y, z with isotropic voxels of $1.0\,\text{mm}^3$. For visualization purposes, the figure shows only the results corresponding to phantom's 98th slice. Figure 13(B) shows the segmentation zone using the region growing algorithm from four seed points. These points were chosen by the user according to the zone of interest. Spheres of 2-mm radius were used. The coordinates (X, Y, Z) of their centers are: Seed1 = (116, 100, 99), Seed2 = (113, 82, 99), Seed3 = (91, 64, 60), Seed4 = (83, 111, 60). Figure 13(C) shows the gray matter zone provided by the Brainweb.

The texture analysis was carried out to validate the segmentation results by calculating statistical descriptors in the volumes obtained in the gray matter zone. Table 2 collects the statistical values and their

Table 2. Validation of the Volume of the Gray Matter Zone Using the Region-Growing Algorithm and the Statistical Texture Analysis.

	# Pixels	Mean	Stand. Dev.	Asymmetry	Kurtosis	Entropy
Region growing	901195	0.1268	0.3327	2.2436	6.0337	0.5485
Phantom Brainweb	902912	0.1270	0.3330	2.2403	6.0191	0.5492
Error (%)	0.1902	0.1902	0.0813	0.1462	0.2440	0.1224

respective percentage of error, showing that the error in the statistical calculation in segmentation zones is less than 0.3%.

Figure 14 shows the results obtained by segmenting the gray matter in the phantom volumen with additive Gaussian noise and its filtering using the anisotropic diffusion filter following the flowchart of Fig. 11. In Fig. 14(A), the original phantom image is presented showing the axial slice number 98 of the phantom. Figure 14(B) shows the phantom image with Gaussian additive noise. Figure 14(C) shows the resulting image after filtering (B) with the anisotropic diffusion filter-parameters: interacting number = 7, time step = 0.0625 and conductance = 5.0. Also two seeds are observed (seed points) chosen to start the region growing segmentation. The seeds used were spherical with two pixels of radio 2 mm, with the center coordinates X, Y, Z, the seeds coordinates are: Seed1 = (99, 50, 99), Seed2 = (74, 124, 99). Figure 14(D) contains the segmenting results. In Fig. 14(E) the gray matter zone provided by the Brainweb is displayed.

Statistical values were calculated. Their respective percentages of error between the segmented volume and the volume provided by the Brainweb are presented in Table 3. Note that the percentage of error of the statistical calculation in both volumes is less than 7%.

Validation of hard tissue models

Segmenting with the proposed watershed algorithms was also validated using a brain phantom mapped from MRI. Figure 15 displays the results obtained after the graymatter zone segmentation in the phantom volume with dimensions $181 \times 217 \times 181$ (X, Y, Z), with isotropic voxels of 1.0 mm^3. Axial slice number 98 of the original image is presented for visualization purposes in Fig. 15(A). Figure 15(B) shows the segmentation obtained through the watershed algorithm, following the set of preprocessing and segmentation techniques mentioned in flowchart of Fig. 6. The gray matter zone provided by the BrainWeb is presented in Fig. 15(C).

The texture analysis was used to validate the results by calculating statistical descriptors in the obtained

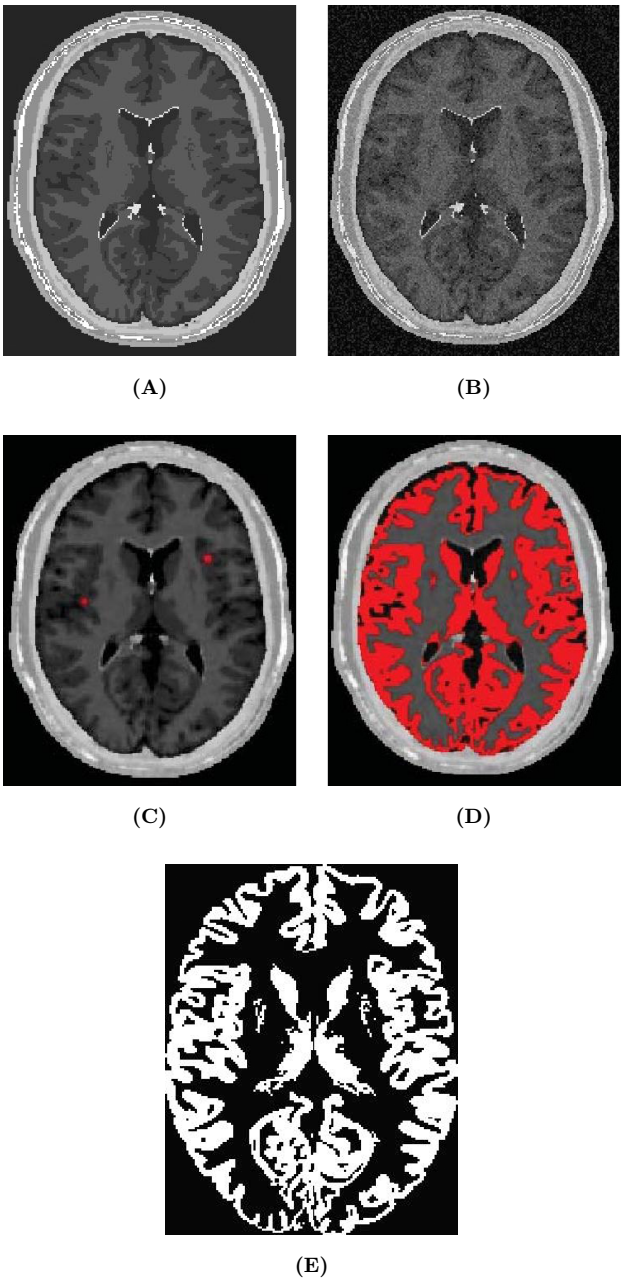

Fig. 14 The segmented gray matter in phantom volume. **(A)** Axial slice number 98 of the original phantom image. **(B)** Original image of the added Gaussian noise. **(C)** Image with noise filtered with an anisotropic diffusion filter and two seeds points. **(D)** Gray matter segmented by the region growing algorithm with five spherical seeds. **(E)** Gray matter zone segmented by Brainweb.

Table 3. Validation of Gray Matter Volume Obtained with Region Growing Algorithm After Adding Gaussian-Noise in a Brain Phantom and Applying the Anisotropic Diffusion-Filter.

	#Pixels	Mean	Stand.Dev.	Asymmetry	Kurtosis	Entropy
Diffusion filter and region growing	955876	0.1345	0.3411	2.1430	5.5926	0.5695
Phantom Brainweb	902912	0.1270	0.3330	2.2403	6.0191	0.5492
Error (%)	5.8659	5.8659	2.4512	4.3421	7.0843	3.7081

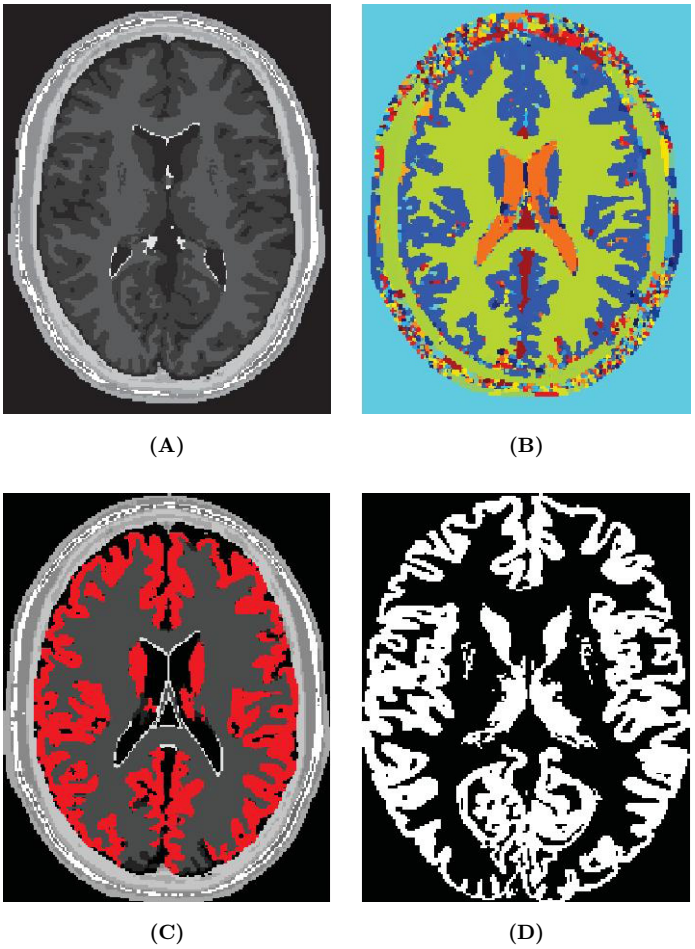

Fig. 15 Gray matter segmentation in brain phantom. **(A)** Axial slice number 98 of an original phantom image. **(B)** and **(C)** Gray matter segmentation through the proposed methodology using the watershed algorithm. **(D)** Gray matter zone segmentated by the BrainWeb.

Table 4. Gray Matter Volumen Validation through Watershed Algorithm.

	# Pixels	Mean	Stand. Dev.	Asymmetry	Kurtosis	Entropy
Diffusion filter and watershed	857718	0.1207	0.3257	2.3293	6.4256	0.5312
Phantom Brainweb	902912	0.1270	0.3330	2.2403	6.0191	0.5492
Error (%)	5.0054	5.0054	2.1806	3.9715	6.7550	3.2679

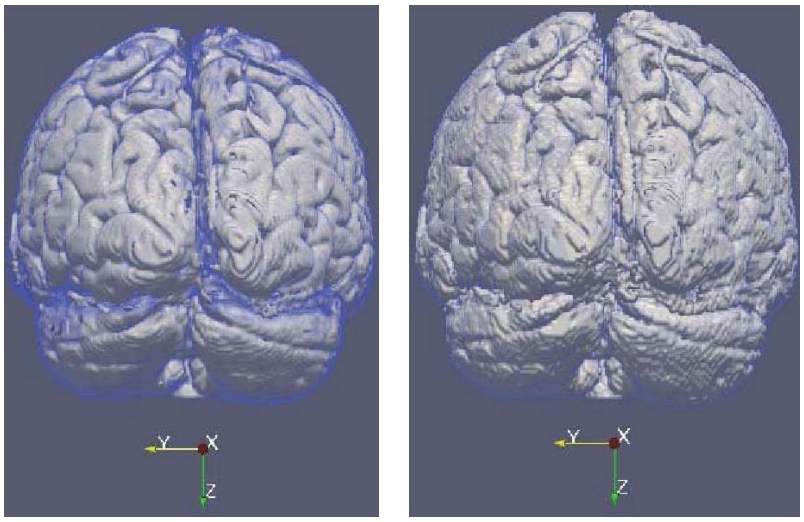

(A) **(B)**

Fig. 16 Volumetric view of the gray matter zone. **(A)** Original volumen of the gray matter provided by the Brainweb. **(B)** Volume obtained by region growing.

volumes. In Table 4 the statistical values and their respective percentage of error are presented. Note that the percentage of error of the statistical calculations in both volumes is less than 2%.

The 3D views of the gray matter zone volume provided by the Brainweb and our methodology are displayed in Fig. 16.

CONCLUDING REMARKS AND FUTURE WORK

One of the main advantages of the proposed approach is that it includes a set of preprocessing and segmentation algorithms that can be combined to create hybrids techniques, which can also adapt themselves to the anatomic structures under study and formulate new flowcharts. The input parameters of the implemented algorithms can be easily calibrated, according to the expert opinions, the observation of tissue type, its intensity profiles and its boundary quality. The computational cost to obtain the tissue models was also attractive and competitive (see Table 1). Also, the results obtained using the proposed methodology are in good agreement when comparing the obtained models against the validated models provided by the Brainweb. The statistical values difference of both volumes was very small. In critical conditions, when corrupting the images with Gaussian-noise (see Table 3), low percentages of error were obtained: number of pixels error = 5.9, average error = 5.9, standard deviation error = 2.5, asymmetry error = 4.3, homogeneity error = 7.1 and entropy error = 3.7. Likewise, it was verified that the implemented techniques are suitable to generate and export volumes in formats *.vtk y *.stl, easy to read from other programs and CAD tools. Their usefulness to generate different meshes, solids and surfaces views was also demonstrated. As for CAD tools, test values were applied in boundary conditions and models were discretized using the FEM, showing the usefulness of the generated volumes for their further numerical analysis.

It should be remarked herein that the current implementation of the proposed approach has some limitations. First, the methodology is demonstrated using only MRI and CT images, other medical images modalities such as PET, 4D MRI could be used. Also, there exist other more sophisticated image-processing algorithms which could be integrated into the methodology.

Finally, the methodology is independent of the underlying properties of the FEM. We only use the morphological operators and Gaussian-filters to smooth the surfaces of tissue models, but other techniques could be applied in order to reduce the mathematical complexity of the soft and hard tissue models and the size and irregularity of the FE mesh as well.

REFERENCES

1. Peterlik I, Sedef M, Basdogan C, Matyska L, Medical imaging analysis of the three dimensional (3D) architecture of trabecular bone: Techniques and their applications, *Comput Graphics* **34**(1):43–54, 2010.

2. Bankman I, *Handbook of Medical Imaging, Processing and Analysis*, Academic Press, UK, 2000.
3. Preim B, Bartz D, *Visualization in Medicine. Theory, Algorithms, and Applications*, Morgan Kaufmann Publishers, Elsevier, NY, 2007.
4. Semmlow J, *Biosignal and Biomedical Image Processing, MATLAB Based Applications*, CRC Press, Boca Raton, 2004.
5. Müller-Karger CM, Rank E, Cerrolaza M, P-version of the finite element method for highly heterogeneous simulation of human bone, *Finite Elem Anal Design* **40**(7):757–770, 2004.
6. Pattijn V, Gelaude F, Vander J, Van R, Medical image-based preformed titanium membranes for bone reconstruction, in Leondes CT, (ed.), *Medical Imaging Systems Technology, Methods in General Anatomy*, Vol. 5, World Scientific Publishing Co. Pte. Ltd., Singapore, 2005.
7. Isaza J, Correa S, Congote J, Methodology for 3D reconstruction of craniofacial structures and their use in the finite element method (in spanish), in *IV Latin American Congress on Biomedical Engineering 2007, Bioengineering Solutions for Latin America Health*, Vol. 18, Springer Berlin, pp. 766–769, 2007.
8. MathWorks, *Image Processing Toolbox TM 6 User's Guide. Release 2009a.* MAT-LAB: Matrix Laboratory, 2009.
9. Acharya T, Ray AK, *Image Processing. Principles and Applications*, John Wiley, NY, 2005.
10. Chuang C-L, Chen C-M, A novel region-based approach for extracting brain tumor in CT images with precision, in Magjarevic R, Nagel JH, Magjarevic R, (eds.), *World Congress on Medical Physics and Biomedical Engineering 2006, IFMBE Proceedings*, Vol. 14, Springer Berlin Heidelberg, pp. 2488–2492, 2007.
11. Avazpour I, Saripan MI, Nordin AJ, Abdullah RSAR, Segmentation of extrapulmonary tuberculosis infection using modified automatic seeded region growing, *Biol Procedures Online* **11**(1):241–252, 2009.
12. Ciofolo C, Fradkin M, Segmentation of pathologic hearts in long-axis late-enhancement MRI, *Med Image Comput Comput Assist Interv* **11**:186–193, 2008.
13. Cocosco C, Kollokian V, Kwan R-S, Evans A, Brainweb: online interface to a 3D MRI simulated brain database, *NeuroImage* **5**(4):S425, 1997.
14. Landini L, Positano V, Santarelli M, 3D medical image processing, in E. Neri, D. Caramella, C. Bartolozzi, (eds.), *Image Processing in Radiology*, Springer, pp. 67–85, 2008.
15. Park H, Kwon M, Han Y, Techniques in image segmentation and 3D visualization in brain MRI and their applications, in Leondes CT, (ed.), *Medical Imaging Systems Technology — Methods in Cardiovascular and Brain Systems*, Vol. 5, World Scientific Publishing Co. Pte. Ltd., Singapore, pp. 207–253, 2005.
16. Goldenberg R, Kimmel R, Rivlin E, Rudzsky M, Techniques in automatic cortical gray matter segmentation of three-dimensional (3D) brain images, in Leondes CT, (ed.), *Medical Imaging Systems Technology — Methods in Cardiovascular and Brain Systems*, Vol. 5, World Scientific Publishing Co. Pte. Ltd., Singapore, 2005.
17. Liew AW-CA, Yan H, Computer techniques for the automatic segmentation of 3D MR brain images, In Leondes CT, (ed.), *Medical Imaging Systems Technology — Methods in Cardiovascular and Brain Systems*, Vol. 5. World Scientific Publishing Co. Pte. Ltd., Singapore, 2005.
18. Peitgen H-O, Oeltze S, Preim B, Geometrical and structural analysis of vessel systems in 3D medical image datasets, in Leondes CT, (ed.), *Medical Imaging Systems Technology — Methods in Cardiovascular and Brain systems*, Vol. 5, World Scientific Publishing Co. Pte. Ltd., Singapore, pp. 1–60, 2005.
19. Accardo AP, Strolka I, Toffanin R, Vittur F, Medical imaging analysis of the three dimensional (3D) architecture of trabecular bone: Techniques and their applications, *Med Imaging Syst Technol, Meth Diagnosis Optimiz* **5**:1–41, 2005.
20. Levoy M, Volume rendering: Display of surfaces from volume data, *IEEE Comput Graphics Appl* **8**(3):29–37, 1988.
21. Lorensen WE, Cline HE, Marching cubes: A high resolution 3D surface construction algorithm, *Comput Graphics* **21**(4):163–169, 1987.
22. Gavidia G, Soudah E, Suit J, Cerrolaza M, Onate E, Development of a Matlab tool to medical image processing and its integration into medical GID software, Technical Report IT-595, CIMNE, International Center of Numerical Methods in Engineering, Barcelona, Spain, 2009.
23. Gavidia G, Soudah E, Martin-Landrove M, Cerrolaza M, Discrete modeling of human body using preprocessing and segmentation techniques of medical images, *Rev. Int'l Met Num Analy Des Eng (in Spanish)* **27**(3):220–226, 2011.
24. Ibáñez L, Schroeder W, Ng L, Cates J, *The ITK Software Guide*, 2nd edn., Kitware Inc, NY, 2005.
25. Perona P, Malik J, Scale-space and edge detection using anisotropic diffusion, *IEEE Trans. Pattern Anal Mach Intell* **12**:629–639, 1990.
26. Liu J, Huang S, Nowinski W, Automatic segmentation of the human brain ventricles from MR images by knowledge-based region growing and trimming, *Neuroinformatics* **7**(2):131–146, 2009.
27. Mühlenbruch G, Das M, Hohl C, Wildberger JE, Rinck D, Flohr T, Koos R, Knackstedt C, Gunther RW, Mahnken AH, Global left ventricular function in cardiac CT evaluation of an automated 3D region-growing segmentation algorithm, *Eur Radiol* **16**(5):1117–1123, 2005.
28. Hahn HK, Peitgen H-O, IWT —interactive watershed transform: A hierarchical method for efficient interactive and automated segmentation of multidimensional gray-scale images, *SPIE Med Imaging* **5032**:643–653, 2003.
29. Digabel H, Lantuejoul C, Iterative algorithms, *Proc 2nd European Symp Quantitative analysis of microstructures*, Vol. 1, Riederer Verlag, pp. 85–99, 1978.
30. Ribó R, Pasenau M, Escolano E, Pérez J, Coll A, Melendo A, *GiD The Personal Pre and Postprocessor. Reference Manual, Version 9*, Internal report, CIMNE, International Center for Numerical Methods in Engineering, Barcelona, 2009.

Chapter 5

Mechanical Stress in Abdominal Aneuryms using Artificial Neural networks.

Title: Mechanical stress in abdominal aortic aneurysms using artificial neural networks.
Authors: Eduardo Soudah, José F. Rodríguez, Roberto López
Journal of Mechanics in Medicine and Biology. Vol. 15, No. 3 (2015) 1550029
DOI: 10.1142/S0219519415500293

Scientific contribution:Combination of artificial neural networks with computational mechanics procedures to estimate the principal stresses in the Aneurismatical sac in idealized AAA geometries.

Contribution to the paper: Pres and Post-processing tools for mesh generation for numerical simulations. Development, implementation and application of the artificial neural model together with José F. Rodríguez and Roberto López. This overall work was carried out in collaboration with Group of Applied Mechanics and Bioengineering from University of Zaragoza.

Journal of Mechanics in Medicine and Biology
Vol. 15, No. 3 (2015) 1550029 (13 pages)

DOI: 10.1142/S0219519415500293

World Scientific
www.worldscientific.com

MECHANICAL STRESS IN ABDOMINAL AORTIC ANEURYSMS USING ARTIFICIAL NEURAL NETWORKS

EDUARDO SOUDAH*,§, JOSÉ F. RODRÍGUEZ† and ROBERTO LÓPEZ‡

*International Center for Numerical Methods in Engineering (CIMNE)
Biomedical Engineering Depart., Technical University of Catalonia (UPC)
08034 Barcelona, Spain

†Aragón Institute of Engineering Research
Group of Applied Mechanics and Bioengineering
(I3A), University of Zaragoza, 50018 Zaragoza, Spain

‡Research and Development Department, Intelnics.
Carretera de Madrid 13, 37900 Santa Marta de Tormes,
Salamanca, Spain
§esoudah@cimne.upc.edu

Received 2 August 2014
Revised 27 August 2014
Accepted 28 August 2014
Published 14 October 2014

Combination of numerical modeling and artificial intelligence (AI) in bioengineering processes are a promising pathway for the further development of bioengineering sciences. The objective of this work is to use Artificial Neural Networks (ANN) to reduce the long computational times needed in the analysis of shear stress in the Abdominal Aortic Aneurysm (AAA) by finite element methods (FEM). For that purpose two different neural networks are created. The first neural network (Mesh Neural Network, MNN) creates the aneurysm geometry in terms of four geometrical factors (asymmetry factor, aneurism diameter, aneurism thickness, aneurism length). The second neural network (Tension Neural Network, TNN) combines the results of the first neural network with the arterial pressure (new factor) to obtain the maximum stress distribution (output variable) in the aneurysm wall. The use of FEM for the analysis and design of bioengineering processes often requires high computational costs, but if this technique is combined with artificial intelligence, such as neural networks, the simulation time is significantly reduced. The shear stress obtained by the artificial neural models developed in this work achieved 95% of accuracy respect to the wall stress obtained by the FEM. On the other hand, the computational time is significantly reduced compared to the FEM.

Keywords: Artificial neural network; AAA; real time.

1. Introduction

About 90% of Abdominal Aorta Aneurysms (AAA) are located below the level of the renal arteries. This pathology is known as infrarenal aneurysm, and involves the

§Corresponding author.

enlargement of the aorta in the inferior thoracic area. It takes a fusiform shape and might extend into the iliac arteries. The mortality by infrarenal aneurysms is high (15% for ruptured aneurysms), and the current standard of determining rupture risk is based on the maximum diameter. One of these AAA rupture criteria are based on the aortic size (diameter) and the rate of growth.[1] This criterion is based on Laplace law for hollow cylinders, which establishes that maximum stress in the artery increases with the radius. Other authors[2–5] based on the AAA shape as its asymmetry or tortuosity have proposed different criteria for the AAA collapsibility, if the AAA diameter is higher than 5.5 cm the AAA may rupture[2]; if the asymmetry index factor, $\beta < 0.4$ the AAA rupture risk is high[3]; if the deformation diameter ratio is $\chi > 3.3$ the AAA might collapse[4]; if the saccular index is < 0.6 the rupture risk is high.[5] But depending on the index that is analyzed the surgical criteria is different. All above studies suggest that not only size but also the shape of the aneurysm appears to be important factors in determining the risk of rupture of a given aneurysm. Therefore, alternative approach of AAA rupture assessment and other biomechanical variables are needed. The majority of these new approaches involve the numerical analysis using finite element methods (FEM) to determine new biomechanical variables inside the AAA.[6–9]

In this line, during the last period, some authors suggest that peak wall stress correlated with the AAA geometrical factors is the more reliable parameter for the assessment of the rupture risk of aortic aneurysms.[10–14] Filinger *et al.*[14] found that peak wall stress in aneurysms has a higher sensitivity (patients that went under rupture) and specificity (patients which did not undergo rupture) than maximum diameter. These findings appear to be supported by the results obtained by Ref. 8, who analyzed 27 aneurysms (15 nonruptured and 12 ruptured) using the finite element method. In their study, the peak wall stress in the ruptured aneurysms was found to be about 60% higher than for the nonruptured aneurysms. Also, the rupture location matched the area of maximum stress.[15,16] However, the use of finite element methods for the analysis of AAA often requires long computational times. For that reason, the purpose of this work is to develop an artificial neural network to compute the peak stress in real time over the aneurysm wall. To achieve our goal we combine, in a multidisciplinary framework, numerical analysis (finite element) and artificial neural networks (ANN) for the simulation of an aneurysms rupture. To study the peak stress over the AAA wall, a hyperplastic isotropic model without considering the fiber orientation has been implemented using FEM. Based on this arterial model, 243 idealized AAA were generated and simulated. Using the results obtained using the finite element technique, two different neural networks were developed and trained, a Mesh Neural Network (MNN) and a Tension Neural Network (TNN). The first one (MNN) creates an aneurysm mesh in terms of four geometrical factors (asymmetry factor, aneurysm diameter, aneurysm thickness, aneurysm length). And the second neural network (TNN) is coupled with the MNN to calculate the peak wall shear stress on every node of that mesh for a given arterial pressure.

2. Geometrical and Material Model

The shape of an aneurysm can be defined by a "parabolic-exponential shape" function proposed by Elger *et al.*,[4] see Fig. 1.

The mathematical function of this geometry is given by:

$$R(z) = R_a + \left(R_{\text{an}} - R_a - c_3 \frac{Z^2}{R_a^2}\right) \cdot e^{-(c_1 \cdot |\frac{Z}{R_a}|^{c2})}, \tag{1}$$

where R_a is the radius of the un-diseased artery, R_{an} is the maximum radius of the aneurysm. On the other hand, c_1 is a constant to be taken as 5.0, c_2 and c_3 are dimensionless geometrical parameters depending on the geometry of the aneurysm according to:

$$c_2 = \frac{4.605}{(0.5 L_{\text{an}} R_a)^{c_1}}, \tag{2}$$

$$c_3 = \frac{R_{\text{an}} - R_a}{R_a \cdot (\frac{0.8 L_{\text{an}}}{R_a})^2}, \tag{3}$$

where L_{an} defines the length of the aneurysm and e is the eccentricity between the aneurysm and the nonpathological arterial vessel.

In order to study the effect of the AAA geometry on the distribution of the wall stresses we introduce three (dimensionless) geometrical parameters:

$$F_R = \frac{R_{\text{an}}}{R_a}, \tag{4a}$$

$$F_L = \frac{L_{\text{an}}}{R_{\text{an}}}, \tag{4b}$$

$$F_E = \frac{e}{R_a \cdot (F_R - 1)}, \tag{4c}$$

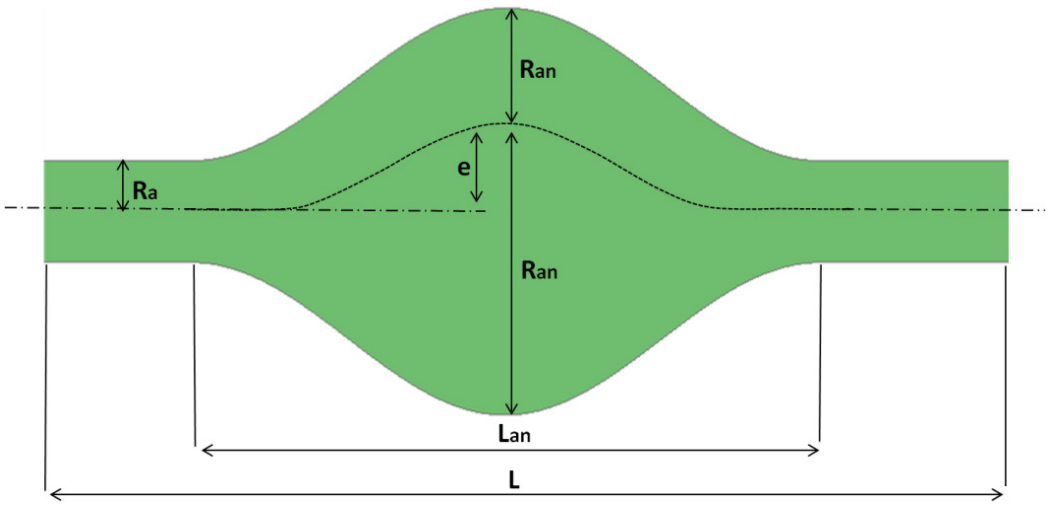

Fig. 1. Idealized geometric model of an AAA with "parabolic-exponential shape".

Table 1. Range of the values F_R, F_L, F_T and β.

Parameter	Description	Range
B	Asymmetry factor	0–1
F_R	Radius factor	2–2.75
F_L	Length factor	1.5–3
F_T	Thickness factor	0.6–1

where $F_R \geq 1$ defines the ratio between the maximum AAA radius and the undiseased arterial radius, F_L defines the ratio between the length of the aneurysm and the maximum AAA radius, and $F_E \in [0, 1]$ is a measure of the aneurismal eccentricity, with e as indicated in Fig. 1 (e is the actual eccentricity between the center of the nonpathological arterial vessel and the center of the section where the maximum aneurismal diameter is located).

The extreme cases are symmetric $F_E = 0$ (with $e = 0$), intermediate eccentric $F_E = 0.5$ and extreme eccentric $F_E = 1$ (with $e = R_{\text{an}} - R_a$). The range of the values F_R and F_L given in Table 1 is in good agreement with values used in previous parametric studies[2] as well as with clinical investigations [4, 10, 11, 19], where F_R ranges from 2.0 to 2.75 and F_L from 1.5 to 3.0. The wall thickness is assumed to be uniform, with 1.5 mm,[7] and the arterial radius is considered to be $R_a = 10.1$ mm. The constant wall thickness assumption has been used in a number of previous studies.[2,6,7,15] In this work random combinations of these parameters were used to create different AAA geometries using GiD.[17] All parametric solid models were meshed with 16896 hexahedral incompressible elements and 25536 nodes using GiD.[17] Figure 2 illustrates six different AAA configurations for different parameters.

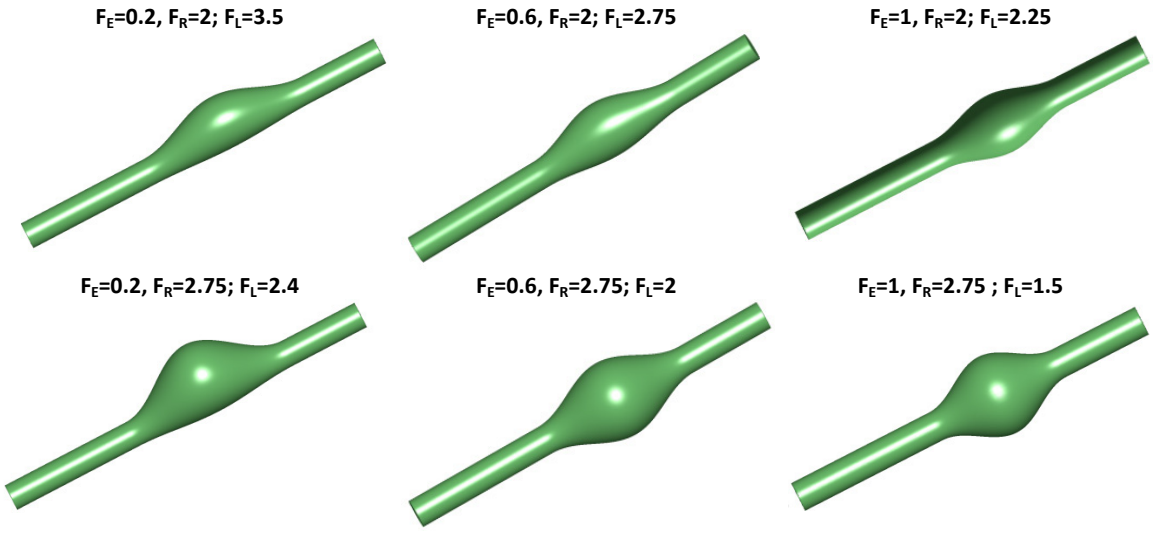

Fig. 2. Geometric models of AAA for three values of aneurismal eccentricity (0.2, 0.6, 1) and for the extreme values for F_R (2–2.75) and F_L (1.5–3).

On the other hand, experimental studies of mechanical properties of the AAA show that high peak wall stress can provoke damage over the arterial wall, and its value can be used as predictor of arterial failure.[18] Therefore, the material model should be able to accurately draw a relation between geometric factors and peak wall shear stress.[19] Based on the knowledge that the AAA wall is incompressible and most likely undergoes large deformations,[18] we can employ the multiplicative decomposition of the deformation gradient F into a volumetric part $J^{-1/3}I$, and an isochoric part $\bar{F}$, with the volume ratio $J = \det F > 0$ and $\det \bar{F} = 1$. By using an additive decomposition of W, we can write[20]:

$$\Psi(C) = U(J) + \bar{\Psi}(\bar{I}_1 \bar{I}_2 \bar{I}_4, \ldots, \bar{I}_8), \tag{5}$$

where $\bar{C} = \overline{F^T} \cdot \bar{F}$ is the right Cauchy Green tensor, and the volumetric elastic response U and the isochoric elastic response Ψ of the material are given scalar-valued objective functions of J and the invariants $\bar{I}_1, \bar{I}_2, \bar{I}_4, \ldots, \bar{I}_8$, respectively.

On assumption that the behavior of the AAA wall is hyperplastic isotropic, and without considering the fiber orientation, the strain energy density W for this material can be written as:

$$W = U(J) + c_{10}(\bar{I}_1 - 3) + c_{20}(\bar{I}_1 - 3)^2, \tag{6}$$

where I_1 is the first invariant, $\bar{I}_1 = \mathrm{tr}(\bar{C})$, of the deviatoric right Cauchy Green tensor $\bar{C}$ is the deviatoric deformation gradient tensor and C_{10} and C_{20} are the model parameters indicative of the mechanical properties of the AAA wall ($C_{10} = 174\,\mathrm{kPa}$, $C_{20} = 1880\,\mathrm{kPa}$).[7]

A range of pressure between 12.3–15.7 kPa was applied to simulate the end systolic conditions, since this pressure represents the stage of the cardiac cycle in which the AAA experiences the largest wall stress. The longitudinal constraining at the proximal and distal parts of the aneurysm due to the renal and iliac arteries was simulated by constraining the displacements to be zero at both ends.[7,15]

After developing the geometrical and computational model, 243 AAA were simulated as a random combination of the geometrical factor (see Table 1) and the internal pressure (12.3–15.7 kPa).

3. Artificial Neural Networks

During the last few years, ANN have found a wide range of applications. One of the most popular learning tasks here is function regression, also called data modeling. The function regression problem can be regarded as the problem of approximating a function from data. These applications always involve a data set, a neural network, a performance functional and a training strategy. The learning problem is then formulated as to find a neural network which optimizes a performance functional by means of a training strategy.[21]

The data set contains the information for creating the model. It comprises a matrix in which columns represent variables and rows instances. Variables in a data set can be of two types: The inputs will be the independent variables, and the targets will be the dependent variables. On the other hand, instances can be: Training instances, which are used to construct the model; generalization instances, which are used for selecting the complexity and testing instances, which are used to validate the functioning of the model.

The neural network defines a function which represents the model. The neural network used here is based on a multilayer perceptron (MLP) with a sigmoid hidden layer and a linear output layer, which is a class of universal approximator.[21] That neural network is also extended with scaling and unscaling layers.

The performance functional plays an important role in the use of neural networks, since it defines the task that the neural network is required to accomplish. The mean squared error is the performance functional used in this work. It measures the difference between the outputs from the neural network and the targets in the data set.[23] The procedure used to carry out the learning process is called training strategy. The training strategy is applied to the neural network in order to obtain the best possible performance. The type of training is determined by the way in which the adjustment of the parameters in the neural network takes place. The quasi-Newton method is the training strategy used here.[23]

In this work, we have designed, trained and validated two artificial neural networks: a MNN to create the computational mesh of the AAA based on the geometrical factors, and a TNN to compute the peak wall shear stress over the AAA wall. The open neural networks library OpenNN[24] has been used for that purpose.

3.1. *Mesh neural networks*

The aim of the MNNs is to create the computational mesh of the AAA in a precise and fast mode. Here, a vector of neural networks with size the number of nodes in the mesh will be created. The number of nodes for all the computational mesh is the same, 25,536 nodes. The inputs to the MNN are the aneurism geometry factors (F_L, F_R, F_T) and the asymmetric factor (β) defined previously. The outputs from the MNN are the corresponding node coordinates (X, Y and Z). While the numbers of inputs and outputs are constrained by the problem, the complexity of the model, defined by the number of hidden neurons in the network, is a design variable. A model order selection analysis showed that 12 neurons in the hidden layer is the optimal architecture for this problem. Figure 3 is a graphical representation of this network architecture.

Defined the input–output variables of the MNN, a data set must be generated for training. In this work an iso-topological hexahedral mesh is considered (Fig. 4). That means that the number and arrangement of nodes and elements is always the same, only the node coordinates can change. All parametric solid models were meshed using the commercial software GiD with 16,896 hexahedral incompressible

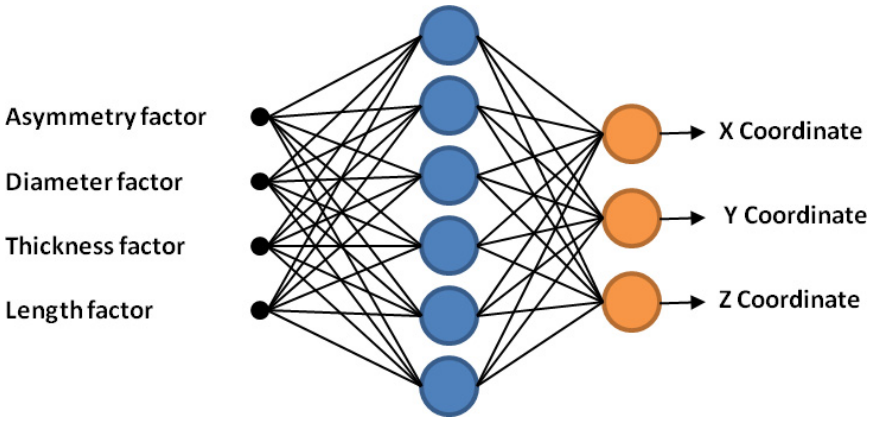

Fig. 3. Neural network architecture for the mesh multilayer perceptron, with 4 inputs, 12 neurons in the hidden layer and 3 output neurons.

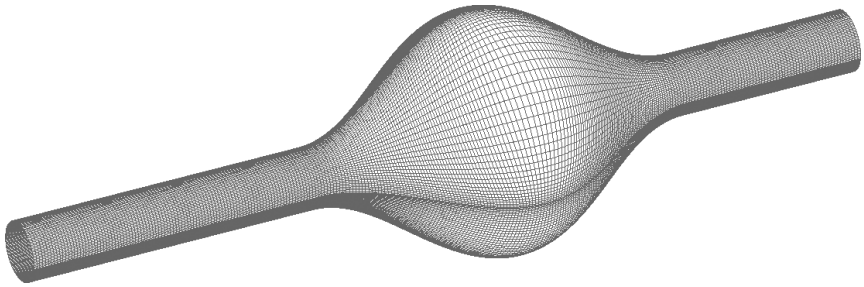

Fig. 4. Hexahedral finite element mesh used for the analysis.

elements and 25,536 nodes. In this way, a vector of data sets has been created, where the number of elements in the vector is equal to the number of nodes, that is, 25,536. Therefore, each element of the MNN will predict the coordinates of the corresponding node.

The number of samples in the data set is a design variable in the problem. In this work, we have used an input target data set with 243 samples for training. The ranges of the input variables are shown Table 1.

Figure 5 shows two examples of the MNN. Table 2 illustrates the data set for a given node.

As nodes positions are not smoothly distributed, the mesh obtained by the MNN gives us noisy results. However, results for meshes already seen by the neural network are not that noisy, and therefore we can use a nearest neighbor approach to solve this problem.

3.2. *Tension neural network*

The aim of the TNN is to calculate the peak wall shear stress over each node of the computational mesh generated by the MNN in a precise and fast mode. The first step for creating the TNN was to choose the network architecture to represent the main shear stress components T_x, T_y, T_z on the mesh generated previously by the

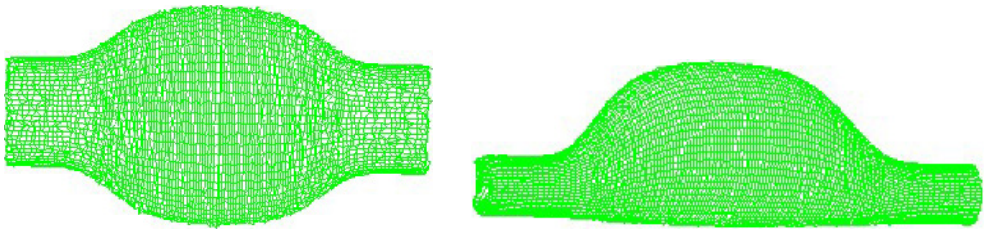

(a) (b)

Fig. 5. MNN for $\beta = 0$, $F_R = 2$, $F_T = 0.6$ and $F_L = 1.5$ (a), neural network mesh for $\beta = 1$, $F_R = 2.75$, $F_T = 1$ and $F_L = 2.5$ (b).

MNN. In this way, a vector of neural networks has been created, where the number of elements in the vector is equal to the number of nodes (25,536 in this case).

As before, a MLP with a sigmoid hidden layer and a linear output layer was used. The number of hidden neurons used in the TNN was 10, as it proved good generalization capabilities in this problem. The inputs to the neural network must characterize the X, Y, Z coordinate obtained in the MNN plus the pressure on that artery (P). We include the arterial pressure as an input variable to the neural network (range of pressure between 12.3–15.7 kPa) as inlet conditions for the numerical simulations. The outputs from each neural network are the main shear stress components on the artery, main shear stress x (T_x), main shear stress y (T_y) and main shear stress z (T_z). Figure 6 is a graphical representation of that network architecture.

Defined the input–output variables of the TNN, the second step was to generate the input-target data set. As previously, we have used an input target data set with 243 samples for training. For each sample a numerical simulation was done in a dual-core 2.83 GHz CP, Microsoft Windows XP 32-bit PC with 4 GB-RAM, with a total computation time of approximately five hours. Each simulation provides the shear stress state for each node (T_x, T_y and T_z), and the number of elements in the vector is equal to the number of nodes, that is, 25,536. Each input-target data set will be used for training the TNN.

The number of input variables in the data set must be equal to the number of input variables in the neural network, that is, 4. Similarly, the number of target variables in the data set must be equal to the number of output variables in the

Table 2. Data set for the MNN, with 243 samples, 4 input variables and 3 target variables.

Input variables				Output variables		
β	F_R	F_T	F_L	X coordinate	Y coordinate	Z coordinate
0.0	2.0	0.6	1.5	10.198	0.000	−39.395
0.5	2.75	0.6	1.5	15.154	10.541	−54.169
...	...	...	...	...	...	...
1.0	2.75	1.0	2.5	26.687	25.142	1.255

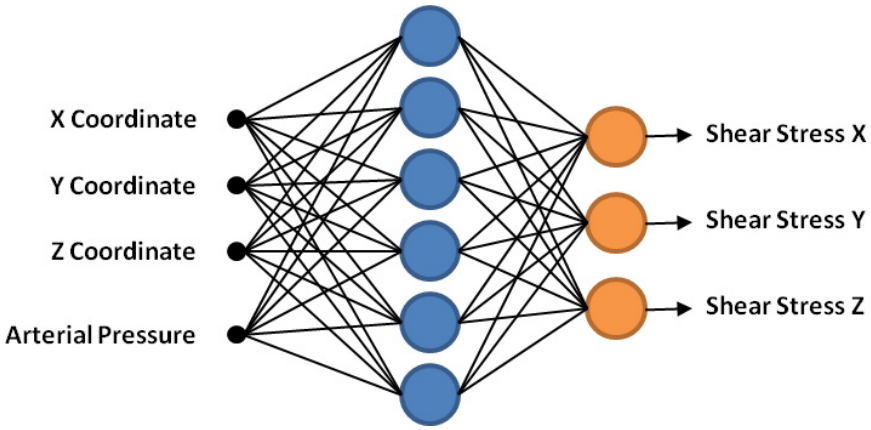

Fig. 6. Network architecture for the TNN.

neural network, that is, 3. Table 3 is a graphical representation of that input target data set.

The third step was to choose a suitable objective functional in order to formulate the function regression problem. Here we use the mean squared error between the outputs from the network and the targets in the data set. And the last step was to choose a training algorithm for solving the reduced function optimization problem. As before a quasi-Newton method with BGFS train direction and Brent optimal train rate is used.[23] The training algorithm is set to stop after 250 iterations. Once the TNN has been created it is ready for use. Figure 7 shows the results, main stresses, for three different cases based on aneurism geometry factors defined previously F_L, F_R, F_T, asymmetric factor (β) and an internal pressure (P).

4. Final ANN and Validation

Figure 8 shows the final neural network developed, where four dimensionless parametric factors: (1) AAA asymmetric factor, (2) AAA diameter factor, (3) AAA thickness factor and (4) AAA length factor are used together with hemodynamic arterial pressure factor to obtain the maximum peak stress over each node of the computational mesh.

Table 3. Data set for the MNN, with 243 samples, 4 input variables and 3 target variables.

Input variables				Output variables		
X coordinate	Y coordinate	Z coordinate	P	T_X	T_Y	T_Z
10.198	0.000	−39.395	12.3	10.198	0.000	−39.395
15.154	10.541	−54.169	12.3	15.154	10.541	−54.169
...	...	...		...	...	...
26.687	25.142	1.255	15.7	26.687	25.142	1.255

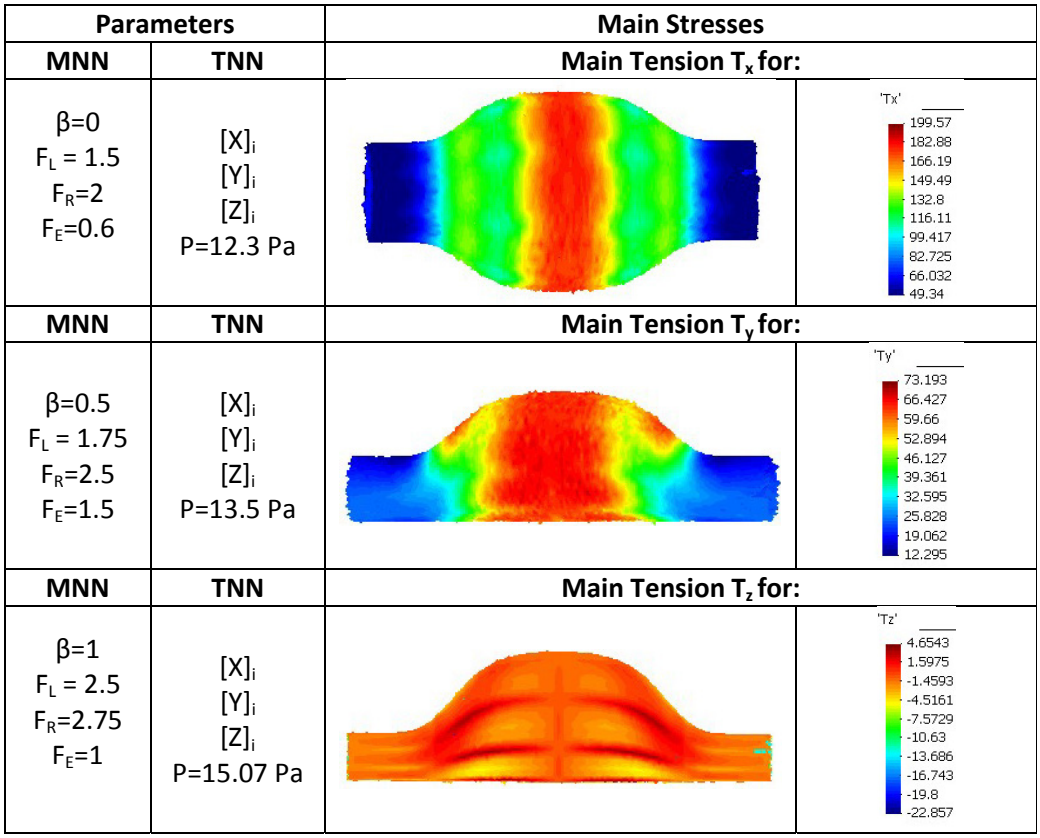

Fig. 7. Main shear stress components T_x, T_y and T_z calculations using the TNN for 3 different cases. $[X]$, $[Y]$, $[Z]$ represent the i-node coordiantes created using the aneurism factor (F_L, F_R, and F_T and the asymmetric factor (β)).

To validate the final network developed, the aneurismal principal stresses predicted by the AAA were compared with results obtained from finite element calculations for an aneurismal internal pressure for 27 random cases. The prediction of the error for each principal stress has been quantified according to:

$$\mathbf{error} = \frac{|\mathbf{S} - \mathbf{S}^{\mathbf{TNN}}|_\infty}{|\mathbf{S}|_\infty},$$

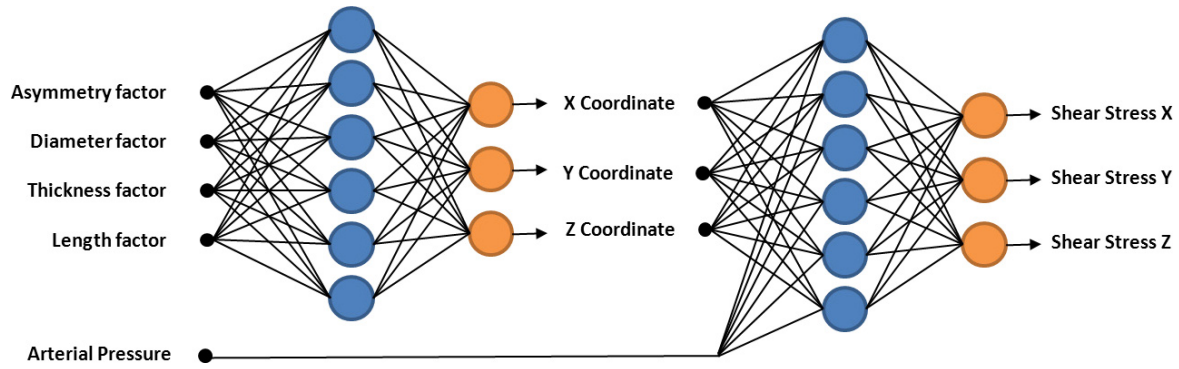

Fig. 8. Final artificial neural network developed. Input variables (F_R, F_L, F_T, β, pressure) and output variables (shear stress X, shear stress Y, shear stress Z).

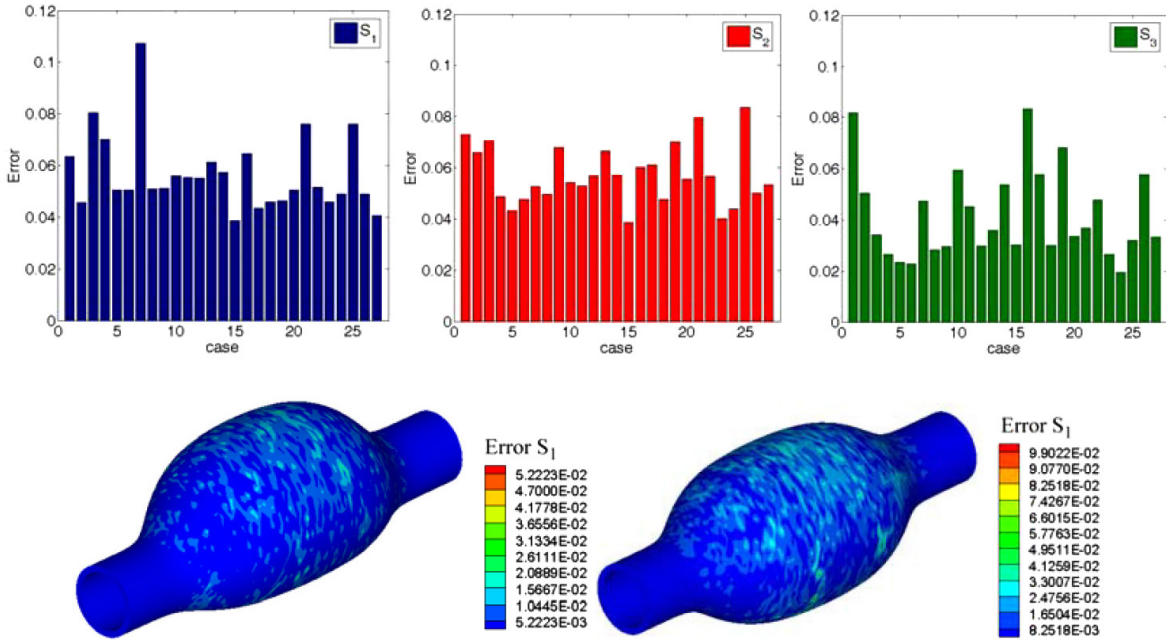

Fig. 9. Shown the error in the maximum principal stress for 27 cases analyzed (top). Shown the error S between the ANN against FEM for two different geometries (bottom).

where S is the vector of the principal stress at each node obtained using FE and S^{TNN} is the vector of principal stress at each node obtained by the TNN. According to Fig. 9, the results obtained in these 27 cases analyzed, the error for the principal stresses between the final network and the FE is negligible, less than 10%, and moreover the time is reduced in more than 95%.

5. Conclusions

The overall goal of this paper is to propose a comprehensive computational methodology based on structural analysis and ANN to predict the main stresses in the aneurysm wall in real time. A key feature of the proposed methodology is that the ANN are capable to reproduce the abdominal geometry and approximate the results of the FEM analysis up to a high degree of accuracy. In order to achieve the objective of this work, two different neural networks were created, a MNN to approximate the computational mesh and a TNN to approximate the shear stress components in the AAA. The main stresses obtained by the TNN compared with the FE are negligible as we have shown in Fig. 9. We recognize that the computational model used to simulate the AAA (hyperplastic isotropic and without considering the fiber orientation) is not the most accurate to reproduce the mechanical behavior of the wall. However the methodology suggested in this work could be used to predict the evolution or rupture of the AAA based only on geometrical factors and internal pressure in a real time. A full AAA structural analysis to obtain the main stresses over the wall requires 5 h in a desktop computer (aneurism model CAD, volume mesh generation and a structural analysis), whereas the framework proposed in this

work requires less than 2 min. The only parameters needed are the F_L, F_R, F_T, β and an internal pressure (P). Since this work was not based on patient-specific geometry, the geometrical parameters can be easily obtained using image processing techniques and pressure can be measured using a pressure cuff. Note that we have used a constant wall thickness, which is an assumption, the thickness distribution along the AAA changes.

To conclude, it is important to emphasize that computational modeling techniques combined with artificial intelligence procedures can provide an insight into the patient-specific conditions for AAA evolution or rupture in real time. Also, the methodology proposed allows to understanding the geometrical factors governing the maximum stresses in the aneurysm wall. Future studies, an improved material model (anisotropic model) will be developed, as well as, other geometrical factors as the tortuosity of the AAA. In addition, further studies are required to include the effect of the intraluminal thrombus.

References

1. Vorp DA, Biomechanics of abdominal aortic aneurysm, *J Biomech* **40**:1887–1902, 2007.
2. Vorp DA, Raghavan ML, Webster M, Mechanical wall stress in abdominal aortic aneurysm: Influence of diameter and asymmetry, *Eur J Vasc Surg* **27**(4):632–639, 1998.
3. Cappeller WA, Engelmann H, Blechschmidt S, Wild M, Lauterjung L, Possible objectification of a critical maximum diameter for elective surgery in abdominal aortic aneurysms based on one-and three-dimensional ratios, *J Cardiovasc Surg* **38**:623–628, 1997.
4. Elger DF, Blackketter RS, Budwig RS, Johansen KH, The influence of shape on the stresses in model abdominal aortic aneurysms, *J Biomech Eng* **118**:326–332, 1996.
5. Ouriel K, Green RM, Donayre C, Shortell CK, Elliott J, Deweese JA, An evaluation of new methods of expressing aortic aneurysm size: Relationship to rupture, *J Vasc Surg* **15**:12–20, 1992.
6. Venkatasubramaniam AK, Fagan MJ, Mehta T, Mylankal KJ, Ray B, Kuhan G, Chetter IC, McCollum PT, A comparative study of aortic wall stress using finite element analysis for ruptured and non-ruptured abdominal aortic aneurysms, *Eur J Vasc Surg* **28**(2):168–176, 2004.
7. Raghavan ML, Vorp DA, Toward a biomechanical tool to evaluate rupture potential of abdominal aortic aneurysm: Identification of a finite strain constitutive model and evaluation of its applicability, *J Biomech* **33**:475–482, 2000.
8. Gasser TC, Auer M, Labruto F, Swedenborg J, Roy J, Biomechanical rupture risk assessment of abdominal aortic aneurysms: Model complexity versus predictability of finite element simulations, *Eur J Vasc Endovasc* **40**:176–185, 2010.
9. Kleinstreuer C, Li Z, Analysis and computer program for rupture-risk prediction of abdominal aortic aneurysms, *Biomed. Eng. OnLine* **5**:19, 2006.
10. Soudah E, Ng EYK, Loong TH, Bordone M, Pua U, Narayanan S, CFD modelling of abdominal aortic aneurysm on hemodynamic loads using a realistic geometry with CT, *Comput Math Methods Med* **2013**, 2013, doi:10.1155/2013/472564.
11. Soudah E, Villalta G, Bordone M, Nieto F, Vilalta JA, Vaquero C, Hemodynamic on abdominal aortic aneurysm: Parametric study, Revista Int de Métodos Numéricos para Cálculo y Diseño en Ingeniería, Available at: http://dx.doi.org/10.1016/j.rimni.2014.02.003

12. Ouriel K, Green RM, Donayre C, Shortell CK, Elliott J, Deweese JA, An evaluation of new methods of expressing aortic aneurysm size: Relationship to rupture, *J Vasc Surg* **15**:12–20, 1992.
13. Georgakarakos E, Ioannou CV, Kamarianakis Y *et al.*, The role of geometric parameters in the prediction of abdominal aortic aneurysm wall stress, *Eur J Vasc Endovasc Surg* **39**:42:48, 2010.
14. Fillinger MF, Marra SP, Raghavan ML, Kennedy FE, Prediction of rupture risk in abdominal aortic aneurysm during observation: Wall stress versus diameter, *J Vasc Surg* **37**(4):724–732, 2003.
15. Inzoli F, Boschetti F, Zappa M, Longo T, Fumero R, Biomechanical factors in abdominal aortic aneurysm rupture, *Eur J Vasc Surg* **7**:667–674, 1993.
16. Vorp DA, Lee PC, Wang DHJ, Makaroun MS, Nemoto EM, Ogawa S *et al.* Association of intraluminal thrombus in abdominal aortic aneurysm with local hypoxia and wall weakening, *J Vasc Surg* **34**:291–299, 2001.
17. GiD — The personal pre and postprocessor, http://www.gidhome.com/ CIMNE.
18. Drangova M, Holdsworth D, Boyd CJ, Dunmore PJ, Roach MR, Fenster A, Elasticity and geometry measurements of vascular specimens using a high-resolution laboratory CT scanner, *Physiol Meas* **14**:277–290, 1993.
19. Rodríguez JF, Ruíz C, Doblaré M, Holzapfel GA, Mechanical stresses in abdominal aortic aneurysm: Influence of diameter, asymmetry and material anisotropy, *J Biomech Eng* **130**(2):021023, 2008.
20. Holzapfel GA, Gasser TC, Ogden RW, A new constitutive framework for arterial wall mechanics and a comparative study of material models, *J Elast* **61**:1–48, 2000.
21. Hornik K *et al.*, Multilayer feed forward networks are universal approximators, *Neural Netw* **2**(5):359–366, 1989.
22. Press WH *et al.*, *Numerical Recipes in C++: The Art of Scientific Computing* Cambridge University Press, 2002.
23. Bishop C, *Neural Networks for Pattern Recognition*, Oxford University Press, 1995.
24. López R, An open source neural networks C++ library. OpenNN, Intelnics (2013), Available at (www.intelnics.com/opennn).

Chapter 6

Estimation of Wall Shear Stress using 4D flow Cardiovascular MRI and Computational Fluid Dynamics.

Title: Estimation of Wall Shear Stress using 4D flow Cardiovascular MRI and Computational Fluid Dynamics (article in preparation)

Scientific contribution: Designed new methodology to estimate the Wall Shear Stress(WSS) using 4D flow cardiovascular MR data and computational fluid dynamics. The methodology proposed is based on interpolate the data acquired from the 4D flow CMR sequence into a patient-specific refined-mesh computational mesh. This paper is a proof-of-concept to validate WSS using CFD data.

Contribution to the paper: This work is being carried out in collaboration with the E.T.S. d'Enginyeries Industrial i Aeronáutica de Terrassa (ETSEIAT), UPC and the Unidad de Imagen Cardiaca, Servicio de Cardiología, Hospital de la Santa Creu i Sant Pau. The simulation in the OPENFOAM software([80]) was performed during the final career project of Jordi Casacuberta in the ETSEIAT. The author of this thesis has developed the algorithm and the methodology for the calculation of the WSS using 4D flow CMR data in collaboration with Jorge S.Pérez (CIMNE). The author of this thesis has also contributed in the segmentation and the analysis of results.

Estimation of Wall Shear Stress using 4D flow Cardiovascular MRI and Computational Fluid Dynamics

(In preparation)

November 14, 2015

Abstract

In the last years, wall shear stress has arisen as a new diagnostic indicator in patients with arterial disease. There is substantial evidence that the wall shear stress plays a significant role, together with hemodynamic indicators, in initiation and progression of the vascular diseases. Estimation of wall shear stress values, therefore, may be of clinical significance and the methods employed for its measurement are crucial for clinical community. Recently, four-dimensional flow cardiovascular magnetic resonance has been widely used in a number of applications for visualization and quantification of blood flow, and although the sensitivity to blood flow measurement has increased, it is not yet able to provide an accurate three-dimensional wall shear stress distribution. The aim of this work is to evaluate the aortic blood flow features and the associated wall shear stress by the combination of 4D flow cardiovascular magnetic resonance and computational fluid dynamics technique. In particular in this work, we used the 4D flow cardiovascular magnetic resonance to obtain the spatial domain and the boundary conditions needed to estimate the wall shear stress within the entire thoracic aorta using computational fluid dynamics. Similar wall shear stress distributions were found for cases simulated. A sensitivity analysis was done to check the accuracy of the method. 4D flow cardiovascular magnetic resonance begins to be a reliable tool to estimate the wall shear stress within the entire thoracic aorta using computational fluid dynamics. The combination of both techniques may provide the ideal tool to help tackle these and other problems related to wall shear estimation.
Keywords: Phase-contrast MRI, velocity mapping, blood flow patterns, wall shear stress, computational fluid dynamics

1 Introduction

The endothelium is the first-line defense against atherogenesis. A key stimulus to maintain the protective status of the endothelial lining at the inner vessel wall is the wall shear stress (WSS). WSS is the tangential force that blood flow exerts on the endothelium. To quantify WSS, three dimensional blood flow patterns need to be measured in vivo, which has been a challenge in medical imaging for many years(17)(22)(13)(24)(12). Although recent preclinical data of 3D ultrasound studies for general flow visualizations in the left ventricle are promising, at present Magnetic Resonance Imaging (MRI) is the only non-invasive imaging modality that can measure 3D blood velocity in 3D in a standardized fashion. Although MR imaging resolution and acquisition speed has increased over the past decades, assessment of WSS is still challenging in complex flow geometries. The cardiac magnetic resonance imaging allows visualization of spatial distribution of velocity in a two-dimensional plane (2D). This technique is valuable non-invasively tool for evaluation of the cardiovascular flow patterns owing to its unique possibility to simultaneously acquire sectional imaging without restriction, anatomy and blood flow velocities with a single scan.

The majority of the commercial systems offer the bi-dimensional phase-contrast sequence to quantify blood velocity and derivative cardiac flow. These sequences are reliable and precise methods to calculate stroke volume for pulmonary/systemic flow ratios estimation (Qp:Qs) and to calculate volume regurgitation in valvular insufficiencies (6)(27). At present, 4D flow cardiovascular magnetic resonance imaging (4D CMRI) sequences are being processed to allow obtaining information of the 4D flow as well as the software to visualize and quantify 4D images. There are several research groups working on these techniques, allowing visualization of the blood flow patterns in any segment of the cardiovascular system (9)(10)(11)(23). Nevertheless, the visualization of these images entails an important manual work, becoming a very time-consuming task and then turning out to be not useful in the current clinical practice. Therefore, it is important to improve the methods of automatic representation of the 4D flows, and to do so it is crucial to have a powerful visualization tool able to analyze the DICOM information from the medical image. In that sense, the International Centre for Numerical Methods in Engineering (CIMNE) has developed a home-made ad-hoc software (Aorta4D) oriented to make progress in this field of work (3)(1)(5)(27)(20). Aorta4D will afford analysis and spatially visualization of the registered 3-directional blood flow velocities, and perform a 3D semi-automatic segmentation based on the 4D flow CMRI data. The purpose of this study is to demonstrate that 4D flow CMRI technique is a reliable tool to provide the boundary conditions for the Computational Fluid Dynamics(CFD) in order to estimate the WSS within the entire thoracic aorta in a short computation time. Our image-based CFD methodology exploits the morphological MRI for geometry modelling and 4D flow CMRI for setting the boundary conditions for the fluid dynamics modelling. The aim is to evaluate visualization of well-defined aortic blood flow features and the associated wall shear stress by the combination of both techniques.

2 Material and Methods

2.1 Medical Image processing

Measurements were carried out using a 3 T MR system (Magnetom TRIO; Siemens, Erlangen, Germany) time-resolved, 3-dimensional MR velocity mapping based on an RF-spoiled, gradient-echo sequence with interleaved 3-directional velocity encoding (predefined fixed velocity sensitivity = 150 cm/s for all measurements). Data were acquired in a sagittal-oblique, 3-dimensional volume that included the entire thoracic aorta and the proximal parts of the supra aortic branches. Each 3-dimensional volume was carefully planned and adapted to the individual anatomy (spatial resolution, 1.78 $\times$ 1.78 $\times$ 2 mm). In the in vivo situation, measurements may be compromised by the active cyclic motion of the heart (cardiac contraction and dilation) and the passive motion of the heart due to respiration. These motion components may lead to image artifacts and uncertainties about the exact measurement site in the aorta. Only if the breathing state was within a predefined window data was accepted for the geometrical reconstruction. To resolve the temporal evolution of vascular geometry and blood flow, measurements were synchronized with the cardiac cycle. The velocity data was recorder in intervals of Temporal Resolution (TeR) throughout the cardiac starting after the R-wave of the ECG. The initial delay after R-wave detection was required for execution of the navigator pulse and processing of the navigator signal. Two-fold acquisition (k-space segmentation factor = 2) of reference and 3-directional velocity sensitive scans for each cine time frame resulted in a temporal resolution of 8 repetition time = 45 to 49 milliseconds. To minimize breathing artifacts and image blurring, respiration control was performed based on combined adaptive k-space reordering and navigator gating. Further imaging parameters were as follows: rectangular field of view = 400x(267-300) mm2, flip angle = 15 degrees, time to echo = 3.5 to 3.7 milliseconds, repetition time = 5.6 to 6.1 milliseconds, and bandwidth = 480 to 650 Hz per pixel. Velocity measurements a voluntary healthy, male subject underwent MR examinations; written informed consent was obtained from the subject.

2.1.1 Segmentation based on 4D CMRI data

In order to explain how the computational domain was obtained a brief description of the segmentation process is explained. Firstly, we select the time step where velocities are higher (t=0.27 s). For that time step, we have four different set of images (Vx, Vy, Vz and Magnitude), and for each pixel of those images the following equations are evaluated:

$$A(v_{x,y,z}) = X_{max} - \sigma(M_x) \tag{1}$$

$$B(v_{x,y,z}) = \sigma(v_x, v_x, v_x) \tag{2}$$

$$C(v_{x,y,z}) = max(\sigma(T_{vx}), \sigma(T_{vy}), \sigma(T_{vz})) \tag{3}$$

$$D(v_{x,y,z}) = 1/S(v_{x,y,z}) \tag{4}$$

Equation 1 is used to remove air from the images. X_{max} is the maximum value of the v_x component in all the vector pixels in the image. M_x is the collection containing all the v_x components of radius 1 voxel neighborhood of $v_{x,y,z}$. Basically, Ec.1 tries to give higher values to points where the signal-to-noise ratio is higher, i.e., non air pixels. Equation 2 tries to gives higher values to pixels in which the vector direction is stronger in one horizontal or vertical direction, since blood in aorta travels vertically (ascending an descending aorta) or horizontally (aortic arch). In Ec.2, v_x, v_y, v_z are the velocity component values for each pixel$v_{x,y,z}$. Equation 3 makes uses of the fact that blood pumped out from the heart has strong changes of velocity at the highest and lowest peak over time. Ec.3 gives the higher pixel values to pixels where that change occurs. T_{mag} is the collection of magnitude values of a voxel $v_{x,y,z}$ over time. T_{vx}, T_{vz} and T_{vy} means the velocity vector components over time. Equation 4 tries to penalize voxels where the behavior of velocity is irregular. Blood in the aorta has smooth behavior of gaining and loosing speed from diastole to systole and then back. $S(v_{x,y,z})$is a measure of the smoothness of the value changes of a given pixel over time. Each function is encapsulated as ITK filter(30). Therefore, the segmentation pipeline process is:

- Eliminate air class using a mask obtained from the Ec.1. Another practical solution may be using an associated magnitude image and apply a threshold to eliminate lower intensities values.
- Apply Ec2, Ec3, Ec4 (a scalar value is assigned to each pixel).
- Define a threshold in which most aorta pixels lies.
- Binarize the image where (p=1 $\rightarrow if \in aorta$, p=0 $\rightarrow otherwise$)
- Apply morphological filters binary erosion and dilation. This will remove small voxels that can be separated from the aorta.
- The aorta remains as the largest connected component. Select the largest connected component.
- Smooth the resulting image from step 6 and binarize again to achieve a binary mask.

The only requirement is to set interactively the threshold parameters of the aorta. Once the aorta is segmented, a center line must be defined for visualization and quantification purposes. The skeletonizing process is described in (15). The centerline will allow identifying the inlet and outlet surface to define the boundary conditions needed for the CFD. The segmentation is then used as a mask for the velocity image and is superimposed on a slice of the scalar data. Figure 2 shows respectively the longitudinal cross section of the Aorta, a surface mesh obtained and streamlines inside the aorta. Once we have finished, we use this mask as initial conditions for the other time steps. For an expert user, total time for the segmentation process is less than 5 minutes.

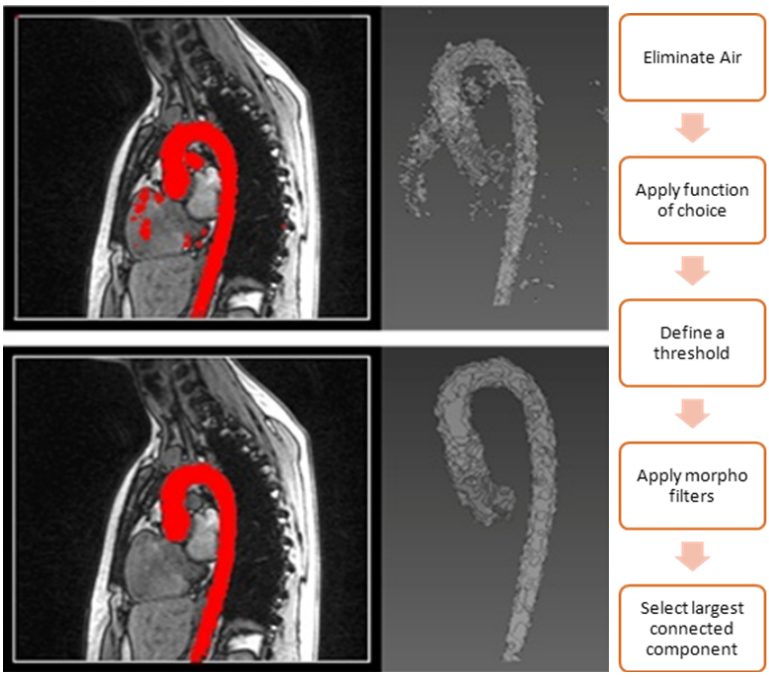

Figure 1: Segmentation workflow

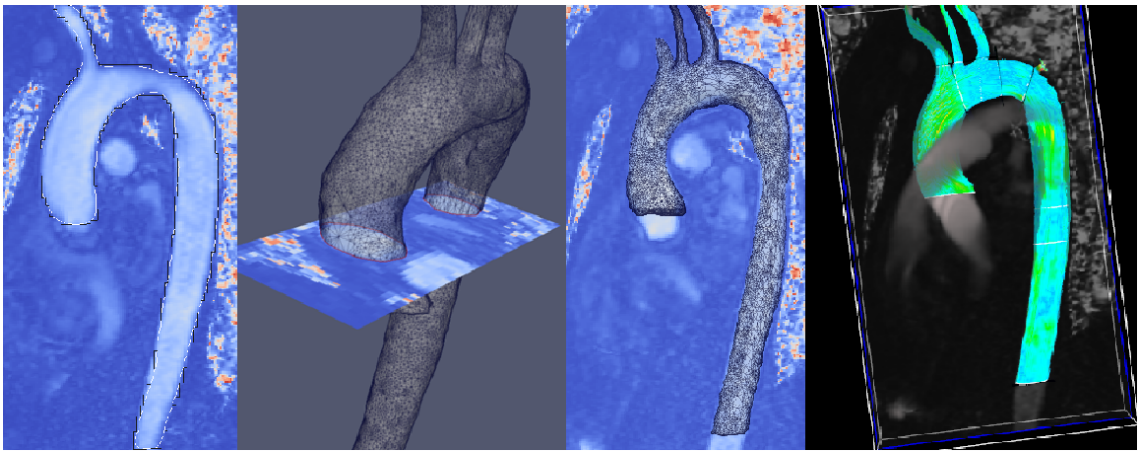

Figure 2: Aorta longitudinal cross section (left), black line in the Aorta longitudinal cross section (left) shows the voxels chosen during the segmentation process, while the white line shows the smoothing approach based on the voxelization process. The two images on the center of the figure show the 3D surface mesh obtained during the smoothing process. A Velocity streamlines(right) obtained using directly the volume mesh at the peak systole.

2.1.2 Aorta Meshing

The surface of the aorta segmented is irregular and rough as a consequence of the complexity of the segmentation process. If it were directly meshed, these flaws might lead to misleading conclusions regarding the wall shear stress. Therefore, a Laplacian smoother was applied to the initial aorta segmented, with the aim of smoothing the main irregularities (see figure 2 (center)). The mesh used for the simulations was based on hexahedral cells and was divided into three main parts: an internal uniform core with cells whose size were 0.938 mm x 0.938 mm x 0.969 mm, layers of cells at the aorta wall whose volumes were eight times lower than the central core, and an intermediate region of cells separating the previous regions (see figure 3). In particular, two layers of cells have been added (first layer, 40% thicker than the 6-level cells and second layer 50% thicker than the first layer). The distance between the wall and the first node is of the order of micrometers (10^{-6} m).

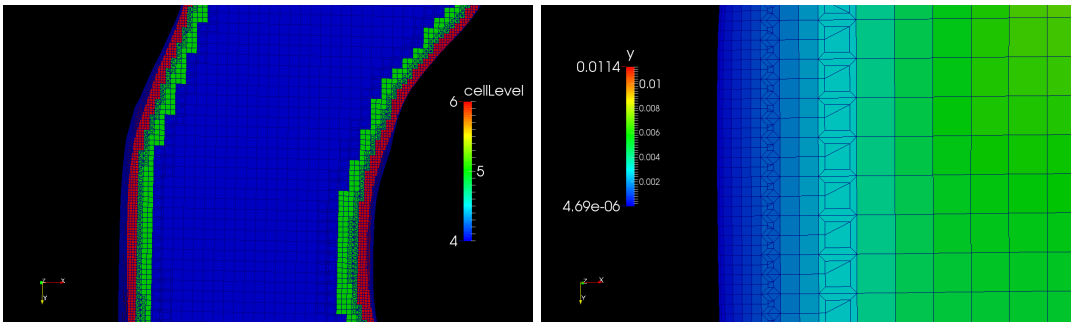

Figure 3: Detail of the cell refinement at the walls of the aorta with the magnitude of the distance between the wall and the nodes. Cellevel represents the number of the cell generated close to the wall. y^+ is the wall coordinate (distance y to the wall).

A very accurate discretization of the arterial wall is needed because one of the objectives of the work is to compute WSS by combining CFD and 4D CMRI data. To achieve this purpose, three computational mesh were created (see figure 5) with different wall refinement. The mesh was highly refined at the walls of the aorta in order to be able to solve the boundary layer correctly (the distances for the first nodes of the original mesh were the order of millimeters, and for the last mesh was the order of micrometers)(2). All the pre-processing was performed using OpenFOAM software package(18).

2.1.3 Computational Fluid Dynamics

The use of CFD techniques in simulating blood patterns and modelling cardiovascular systems has become widespread within bioengineering and medical research in the past few decades. However, the increasing reliance on CFD for hemodynamic simulations requires a close look at the various assumptions required by the modelling activity, and in particular, to assess the sensitivity to assumptions regarding boundary conditions (25)(29). Nowadays, thanks the new advances in 4D flow CMR imaging, we can obtain highly resolved blood flow patterns in anatomically realistic models. Consequently, these realistic blood flow patterns can be used as boundary conditions of the CFD models. Therefore, coupling medical imaging and CFD allows to calculate new hemodynamics indicators, as WSS. An important aspect to compute the distribution of the WSS is the anatomical domain. Local arterial geometry components as curvature and smoothness will highly influence the WSS results(24). Computationally, WSS can be defined in terms of the surface traction vector t whose components are given as:

$$t_i = (-p * \delta_{ij} + \tau_{ij}) * n_j \tag{5}$$

p denoting the pressure, τ_{ij} are the components of the viscous stress tensor and n_j are the components of the normal n to the surface. The WSS is then defined, on each point on the surface, as

$$t_w = |t_w| = |t - (t * n) * n| \tag{6}$$

that is, the magnitude of the traction vectors component in a plane tangential to the surface.

In order to perform a realistic simulation, it is recommended to prescribe outflow boundary conditions based on in vivo accurate measurements. Depending on its location and type, the inlet velocity profile seems to influence both bulk flow and wall shear stress distribution(24). For all case studied in this work, instead of using standard boundary conditions based on lumped models (25)(29), we have fixed the flow rate waveform at the supra-aortic vessels based on the 4D flow CMRI data. The inlet flow profile was measured with 4D CMRI and prescribed in the ascending aorta. The velocity profile at the outlet, simulations were performed without direct constraints on the shape of the outlet velocity profiles, but prescribing zero normal gradient for all flow variables with the exception of pressure. Velocity contours in the descending aorta were found to be in very good agreement with 4D CMRI measurements, with prediction of flow reversal on the inner side in the descending aorta (5). The average peak Reynolds number was higher in the ascending (≈4500) and descending aorta (≈4200) than in the aortic arch (≈3400). The supercritical Reynolds number, indicating flow instabilities, is significantly correlated with body weight, aortic diameter and cardiac output. While the findings might suggest the presence of flow instabilities in the healthy aorta at rest, this does not involve fully turbulent flow(28). In this study, we focus on the WSS distribution at the systolic peak, therefore it is not necessary consider elastic wall. Arterial walls were assumed to rigid, and no-slip condition was imposed. The CFD code used to solve the WSS was the open source code OpenFoam(18). The OpenFoam library solves differential partial equations with the Finite Volume Method. The solver used in the present work is for steady-state flow with the SIMPLE (Semi-Implicit Method for Pressure Linked Equations) algorithm for solving the velocity-pressure coupling(19).

2.1.4 Hypotheses and boundary conditions

The main hypotheses assumed for the aorta simulation are incompressible and laminar flow, Newtonian fluid, rigid wall and uniform inlet velocity profile. Right and left coronaries and intercostal arteries are not included in this study. As one of the main goals of the study was to determine wall shear stress that blood causes in order to prevent medical diseases, the most critical conditions were simulated for the thoracic aorta. As a consequence, the simulations were carried out at the peak systolic time (t=0.27 s). At this time step, blood velocities pulsing through the aorta are high and subsequently the wall shear will be higher. Realistic boundary conditions were applied to the computational model, thanks to the information provided by the 4D flow CMR images. Since the pressure in each outlet is different and difficult to obtain from the 4D CMRI data, we use the velocities and flow rates at each boundary conditions. The uniform inlet velocity profile was applied parallel to the inlet faces normal vector, and its module was computed considering the flow rate and the surface of the inlet face. On the other hand, at the supra-aortic vessels, outlet flow rates were imposed, since the direction of the outlet velocities are not relevant. At the outlet of the descending aorta, null pressure was applied and taken as the reference value. The outlet flow rates used at the supra-aortic branches were the following:

- Brachiocephalic artery: 27.13 ml/s
- Left common carotid artery: 10.15 ml/s

- Left subclavian artery: 18.00 ml/s

For the computation of the inlet velocity vector, the following steps were followed. By considering the real measures obtained from the 4D CMRI, the inlet volumetric flow rate for that aorta was 259.14 ml/s. As the velocity boundary condition needs to be a vector and a standard model was considered, its direction was set parallel to the normal vector of the inlet patch.The area vector of patch inlet was computed $\left|\overline{A}\right| = 4.31163 \times 10^{-4} m^2$. The module of the main inlet velocity was computed considering the inlet area and the volumetric flow rate is: $U_{mean} = k_c \Delta Q_{inlet} / \left|\overline{A}\right|$. Where k_c is a constant that needs to be included because the inlet patch is not completely bidimensional: k_c=flux required/flux of a 3D inlet. This constant was necessary because when the simulation was carried out with an inlet velocity according to U_{mean} without k_c, the inlet flow rate computed after the simulation was higher than expected. It was concluded that this was because of the fact that the inlet patch was not completely two-dimensional. Constant k_c then expresses the relation between the flow rate that was erroneously obtained and the required volumetric flow rate (259.14 ml/s). The area vector of patch inlet was normalized. A comparison between the outlet flow rates at the outlets can be observed in Table 1.

Artery	4D CMRI data	Estimated
Brachiocephalic	10.47 %	13.73 %
Left common carotid	3.92 %	4.20 %
Left subclavian	6.85 %	6.56 %
Descending Aorta	72.86 %	75.51 %

In order to limit the study, the intercostal arteries and left and right coronaries arteries are left out (aprox. 6% of the total flow (16)). It can provide and approximate idea of the error committed.

3 Results

Based on WSS indicators, it has been demonstrated that WSS play an important role in the development and progression of vessel wall pathologies (4). As it is explained in section 3, wall shear computation is based on the velocity gradient close to the wall. For that reason, firstly we have compared the 4D flow CMRI velocities against the CFD velocities obtained. The assumptions taken during the CFD simulation were: flat inlet velocity profile, outlet velocity profiles as boundary conditions and laminar Newtonian flow; and WSS computation will be perform only for the peak systolic instant time, therefore we assume rigid and static aorta walls. Next figure 4 shows the velocity profile obtained using the OpenFOAM software against the 4D flow CMRI velocity distribution at different sections along the entire aorta. Evaluating quantitatively the results, we can observe that the CFD results are capable to capture the vorticity and the flow distribution along of the aorta. However, we can also notice some differences in the ascending aorta due to the assumption of flat inlet velocity profile, as also is reported on (14). For this analysis we do not consider the eccentricity of the aortic valve(7).

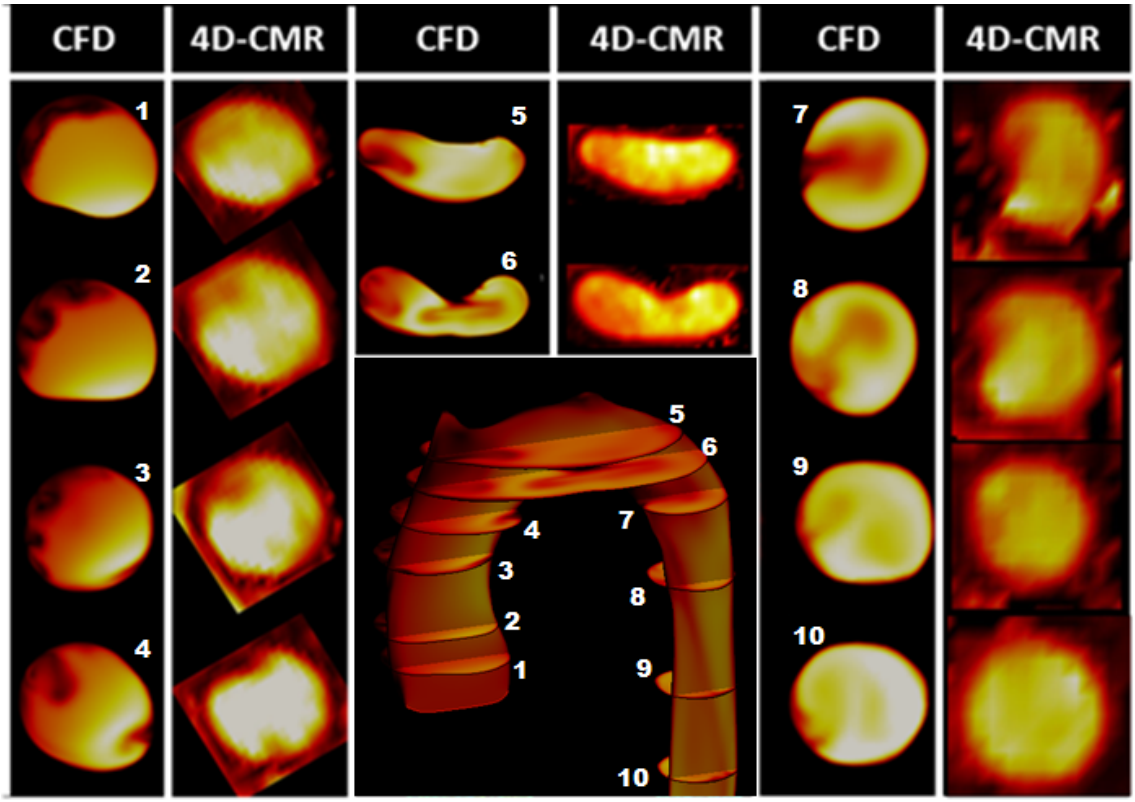

Figure 4: Velocity distribution (CFD versus 4D flow CMRI) through different cross-sectional planes along the aorta (ascending aorta (planes 1-4), aortic arch (planes(5-6), descending aorta(planes 7-10)).

Following table shows the differences between the flow$_{4DCMR}$ and flow$_{CFD}$ for the different cross-sectional planes at the ascending and descending aorta. We observe the flow differences provoked by coronaries arteries in the ascending aorta and by the intercostal arteries in the descending aorta. Another source of error could be the segmentation process.

Cross-sectional Plane	flow$_{4DCMR}$	flow$_{CFD}$	Error
Ascending Aorta Plane 1	259.14 ml/s	259.14 ml/s	0%
Ascending Aorta Plane 2	248.7 ml/s	259.14 ml/s	4.1%
Ascending Aorta Plane 3	248.5 ml/s	259.14 ml/s	4.1%
Ascending Aorta Plane 4	248.2 ml/s	259.14 ml/s	4.2%
Descending Aorta Plane 7	196 ml/s	195.67 ml/s	0.16%
Descending Aorta Plane 8	193.30 ml/s	195.67 ml/s	1.21%
Descending Aorta Plane 9	191.47 ml/s	195.67 ml/s	2.14%
Descending Aorta Plane 10	190.95 ml/s	195.67 ml/s	2.41%

Once mass conservation is satisfied, we obtain the WSS *(WSS_{CFD})*. To check the accuracy of the WSS_{CFD}, a sensitivity analysis was carried out to assure grid independence: three meshes were created, with a number of cells ranging from 10^4 to 1.5 X10^6 (figure 5).

- 4D CMR Model: 4D flow CMR data. Original 4D flow CMRI data. Voxels size: 1.78 $\times$ 1.78 $\times$ 2 mm.

- Mesh Model 1: computational mesh using same spatial discretization as 4D CMR Model.
- Mesh Model 2: Refined of Mesh Model 1 (2.1.2).
- Mesh Model 3: Refined of Mesh Model 2 (see figure 3)(2.1.2).

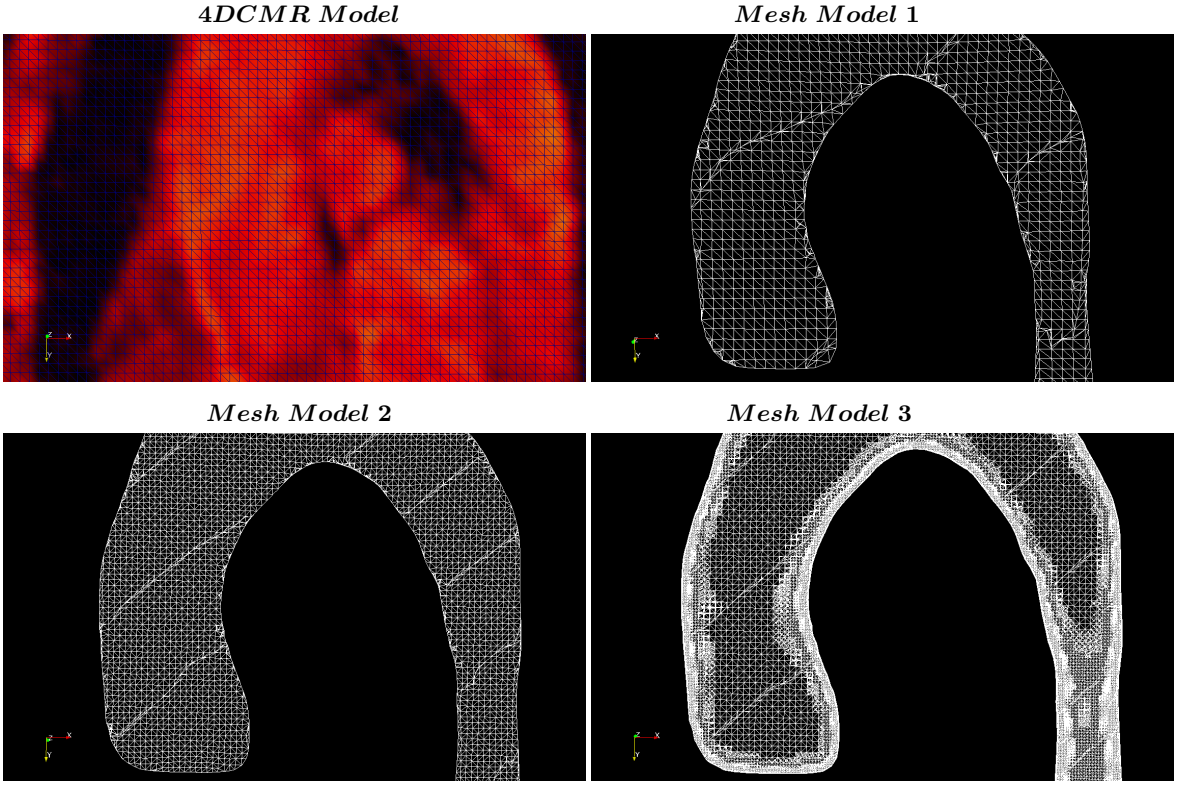

Figure 5: Different computational meshes used to compute the wall shear stress

Next, we have computed the WSS (WSS_{4DCMR}) based on the 4D flow CMR data. To compute the WSS_{4DCMR}, firstly we have calculate the Δvelocity and the Δdistance map function for the aorta binary mask image as a convolution with the derivative of gaussian kernel, after that, the WSS_{4DCMR} is calculated as the directional derivative of the velocity in the direction of the normal to the vessel wall $\mu\Delta\delta\text{V}/\delta\mathbf{n}$. Where μ is the viscosity of the blood.

Figure 6 shows wall shear stress distribution for each case (4D CMR Model, Mesh Model 1, Mesh Model 2 and Mesh Model 3). In order to compare the results, WSS_{4DCMR} and WSS_{CFD} are normalising with their corresponding peak value. The main reason to normalize the WSS_{CFD} is due to artificially high WSS at the vessel boundaries, furthermore in the MRI velocity data (due to image resolution) this end effects are not present. The grid sensitivity study on the aorta model under steady flow conditions (peak systole), demonstrated that there are differences in the maximum WSS scalars. Therefore, it must be noted in this context that the boundary layer plays an important role in the WSS values. Computational time was (Model 1: 64 *sec*, Model 2: 101 *sec* and Model 3: 3534 *sec*). artificially high WSS at then vessel boundaries

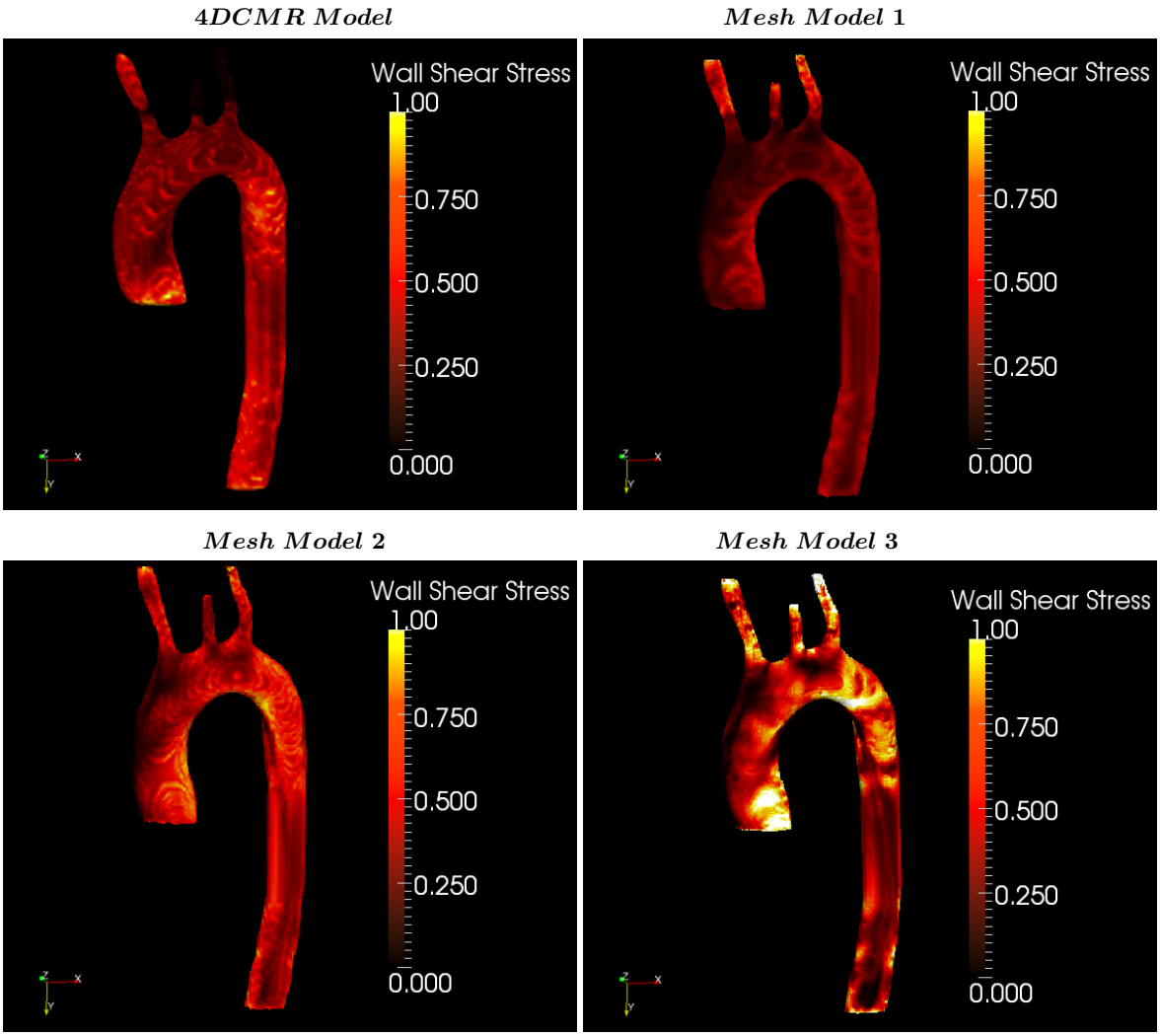

Figure 6: Wall shear stress for the different computational meshes

Due to the lack of 4D flow CMR resolution, for the 4D CMR model, WSS_{4DCMR} at the supra-aortic arteries cannot be estimated. To compute the WSS_{4DCMR}, we based on the directional derivative of the velocity in the direction of the normal to the vessel wall, at least a minimum number of voxels are needed. If we need to estimate WSS_{4DCMR} in small arteries, 4D flow CMR resolution should be increased. For the CFD computation, maximum velocities are reached at the supra-aortic arteries provoking WSS_{CFD} peak values. We have not removed those peak WSS_{CFD} in the outlet arteries because of we are interested to WSS patterns in the ascending and descending aorta. For the cases analysis, we observe that WSS follows the same pattern, and there are two aortic areas when the WSS values are higher, one in the ascending aorta (close to the aortic valve) and other in the internal part of the descending aorta just behind the aortic arch. We can see these aortic areas in other works as (5). When we increase the computational mesh resolution, we notice that the WSS areas and the peak values begin to improve. After that, we have interpolated the 4D velocity CMR data into the Mesh Model 3 (high resolution) with the objective to compare the $\text{WSS}_{4DCMR->MeshModel3}$ against $\text{WSS}_{CFD->MeshModel3}$ and the WSS_{4DCMR}.

In order to do this, we use a B-Spline approximation in order to evaluate at any point the 4D velocity CMR over the Mesh Model 3 taking into account null velocity over the wall. Afterward, we compute the WSS based on the directional derivative of the velocity ($WSS_{4DCMR->MeshModel3}$), figure 7. We notice that the WSS areas for the three cases are similar but the peak values are different for each model. The main differences between WSS_{4DCMR} and $WSS_{4DCMR->MeshModel3}$ are related with the mesh or spatial resolution. The fact that use a velocity B-Spline approximation over Mesh Model 3 makes a more realistic velocities close to the wall and subsequently the WSS. The differences between the $WSS_{4DCMR->MeshModel3}$ and $WSS_{CFD->MeshModel3}$ are related with the flow distribution inside the aorta, as we have explained previously, in Mesh Model 3 we are not taking into account the coronary arteries and the intercostal arteries, and the effects provoked by these arteries. Due to the fact we are using a cubic B-Spline interpolation function to interpolate the velocity, the $WSS_{4DCMR->MeshModel3}$ obtained are smoother. In view of the foregoing that results, the interpolation of 4D flow CMR data over a high resolution mesh can be another option to estimate properly the wall shear stress values.

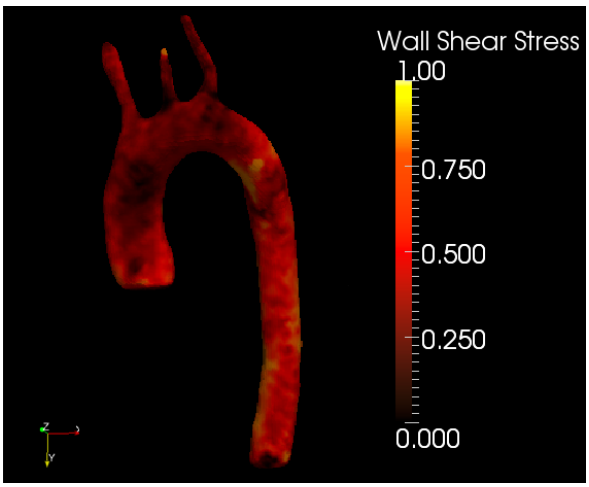

Figure 7: $WSS_{4DCMR->MeshModel3}$ estimated using 4D velocity CMR data into the Mesh Model 3.

4 Discussion

This study has investigated the WSS in a 4D CMRI based subject specific human aorta, using both CFD and 4D flow CMRI models. The methodology proposed can be considered a starting point to compute physiological WSS starting from blood flow measures acquired by 4DMRI in an effective and efficient manner. In fact, 4D flow CMR technique is able to provide us a 3D domain and velocity distribution for any cross-sectional plane of the domain through non-invasive measurements. With the aim to demonstrate that the methodology proposed is possible, wall shear stress distribution was computed for different computational meshes from a healthy patient-specific human aorta. The different computational meshes resolution show differences between the numerical results. However, wall shear distribution along the aorta follows same pattern for the different computational meshes and the areas with low and high WSS may be differentiated. To correctly evaluate the WSS values, a high resolution mesh is in fact necessary with a reasonable computational time. We notice that for the 4D flow CMRI model the image resolution is not enough compared to the CFD analysis. The CFD analysis show similar results compared to the literature (5)(21). Also it is important to remark that, as we are able to compute the flow profile at the outlets of

our domain, we do not need to use a multiscale modelling to estimate the boundary conditions of the CFD problem. In (5) the authors notice that there were large differences for the instantaneous WSS between the elastic and rigid wall models. This methodology also avoids to perform CFD Fluid Structure Interaction(FSI) analysis, eluding the difficulties related to setting the patient-specific mechanical properties of the arterial wall. In order to avoid a CFD-FSI problems, the computational mesh and flow measures at the inlet and outlets can be obtained using the 4D flow CMR data for each time step, and for each one we perform a steady-state CFD analysis. Thanks to that, other hemodynamic parameters as the time-averaged WSS (TAWSS), the oscillating shear index (OSI) and the relative residence time (RRT) can be estimated taking the displacement of the aorta into consideration. Where OSI describes the cyclic departure of the WSS vector from its predominant the axial alignment (8), the TAWSS is used to evaluate the total WSS on the wall throughout a cardiac cycle, and it is calculated by integrating each nodal WSS vector magnitude at the wall over the cardiac cycle (14), and the RRT is inversely proportional to the magnitude of the time-averaged WSS vector and it indicates the average amount of time that a particle (molecule) spends at the endothelium. These hemodynamic parameters are emerging as new diagnostic indicators for cardiovascular diseases, such as, atherosclerosis localization (20) or abdominal aortic aneurysm rupture risk prediction (26). In a future study, based on these preliminary results, these hemodynamic parameters will be explored. In this work, we only focus on the computation of the WSS at peak systole.

The main limitation of this study might be represented by the fact that it was carried out considering only one image-based healthy aorta and at the peak systole, but the strategy used to compute the WSS using the 4D flow CMRI data shows promising results. There might be small errors in the segmentation process compared to the real geometry because of the limited 4D flow CMRI resolution during the diastolic phase due to the low velocities at the aorta during this period. This aspect could affect the WSS, but, as the simulations are based on at peak velocity time, and as the main goal is to investigate the differences between the resolution of the models (computational mesh) taking into account the same geometry, a good estimate of WSS can be obtained. It is worth also to take into account that in this study the outflow conditions were all exposed to the same waveform shape at the inlet section of the ascending aorta, and modelling blood as a Newtonian fluid. In our opinion, this does not entail a loss of generality in our study, which aims at investigating a single aspect, i.e., the methodology used to compute faster the WSS distributions combining 4D flow CMRI data and CFD. Due to the lack of 4D flow CMRI resolution, the induced effects of the intercostal arteries and coronaries arteries cannot be captured in our study.

Bibliography

[1] Blum R.D. Numerical simulations of aortic blood flow with a bicuspid aortic valve. Technical report, Emory University, 2010.

[2] Casacuberta J, OpenFOAM Guide for Beginners. www.http://the-foam-house5.webnode.es/

[3] Cootes T.F. and Taylor C.J. Statistical models of appearance for medical image analysis and computer vision, Proc. SPIE Medical Imaging, p236-248, Vol. 4322, 2001.

[4] Hiratzka LF, Bakris GL, Beckman JA, et al. 2010 ACCF/AHA/AATS/ACR/ASA/SCA/SCAI/SIR/STS/SVM guidelines for the diagnosis and management of patients with thoracic aortic disease. Catheter Cardiovasc Interv. 1;76(2):E43-86, 2010.

[5] Lantz J., Renner J. and Karlsson M. Wall shear stress in a subject specific human aorta. influence of fluid-structure interaction. Internal Journal of Applied Mechanics, (3), 4, 759-778, 2011.

[6] Lotz J. Flow measurements in cardiac MRI. Radiologe. Apr;47(4):333-41, 2007.

[7] Kari FA, Kocher N, Beyersdorf F, Tscheuschler A, Meffert P, Rylski B, Siepe M, Russe MF, Hope MD.Four-dimensional magnetic resonance imaging-derived ascending aortic flow eccentricity and flow compression are linked to aneurysm morphology. Interact Cardiovasc Thorac Surg. 20(5):582-8. 2015.

[8] Ku DN, Giddens DP, Zarins CK and Glagov S, Pulsatile flow and atherosclerosis in the human carotid bifurcation. Positive correlation between plaque location and low oscillating shear stress, Arteriosclerosis. 5:293-302, 1985.

[9] Markl M, Harloff A, Bley T.A et al. Time-Resolved 3D MR Velocity Mapping at 3T: Improved Navigator-Gated Assessment of Vascular Anatomy and Blood Flow. Journal of Magnetic Resonance Imaging Art: 06-0195. 25:000000, 2007.

[10] Markl M, Draney MT, Hope MD, et al. Time-resolved 3-dimensional velocity mapping in the thoracic aorta: visualization of 3-directional blood flow patterns in healthy volunteers and patients. J Comput Assist Tomogr 28:459468, 2004.

[11] Markl M, Kilner PJ, Ebbers T. Comprehensive 4D velocity mapping of the heart and great vessels by cardiovascular magnetic resonance. J Cardiovasc Magn Reson. 14;13:7, 2011.

[12] Markl M, Frydrychowicz A, Kozerke S, Hope M, Wieben O. 4D flow MRI. J Magn Reson Imaging 36: pp. 1015-36, 2012.

[13] Markl M, Wallis W, Harloff A. Reproducibility of flow and wall shear stress analysis using flow-sensitive four-dimensional MRI. J Magn Reson Imaging 33: pp. 988-94, 2011.

[14] Morbiducci U, Ponzini R, Rizzo G, Cadioli M et al. In Vivo Quantification of Helical Blood Flow in Human Aorta Flow in Human Aorta by Time-Resolved Three-Dimensional Cine Phase Contrast Magnetic Resonance Imaging. Annals of Biomedical Engineering March 2009, Volume 37, Issue 3, pp 516-531

[15] Tran S. and Shih L.Efficient 3D binary image skeletonization. Computer Engineering, University of Houston. Clear Lake (UHCL). IEEE Computational Systems Bioinformatics ConferenceIEEE Computer Society. p-364-372, 2005.

[16] Olufsen MS, Peskin CS, Won Yong Kim, Pedersen EM, Nadim A, Larsen J. Numerical Simulation and Experimental Validation of Blood Flow in Arteries with Structured-Tree Outflow Conditions. Annals of Biomedical Engineering. Volume 28, Issue 11, pp 1281-1299, 2000.

[17] Ooij P van, Potters WV, Guedon A, Schneiders JJ, et al. Wall shear stress estimated with phase contrast MRI in an in vitro and in vivo intracranial aneurysm. Journal of Magnetic Resonance imaging pp. 876-884, 2013.

[18] OpenCFD Ltd., OpenFoam. The open source CFD toolbox (2012).

[19] Patankar, S.V. and Spalding, D.B., Numerical Prediction of Three-dimensional Flows (Imperial College of Science and technology Mechanical Engineering Department, 1972).

[20] Petersson S. Fast and Accurate 4D Flow MRI for Cardiovascular Blood Flow Assessment. Thesis Dissertations No. 1380. Linköping University Medical. ISBN 978-91-7519-506-3, 2103.

[21] Petersson S, Dyverfeldt P and Ebbers T. Assessment of the Accuracy of MRI Wall Shear Stress Estimation Using Numerical Simulations. Journal of Magnetic Resonance Imaging 36:128138. 2012.

[22] Potters WV,Marquering A, VanBavel E., Nederveen AJ. Measuring Wall Shear Stress Using Velocity-Encoded MRI. Current Cardiovascular Imaging Reports. 7:9257, 2014.

[23] den Reijer PM, Sallee D 3rd, van der Velden P, et al. Hemodynamic predictors of aortic dilatation in bicuspid aortic valve by velocity-encoded cardiovascular magnetic resonance. J Cardiovasc Magn Reson. 13;12:4, 2014

[24] Renner J. Towards subject specific aortic wall shear stress. Technical report, Linköping University 2011.

[25] Soudah E, Rossi E, Idelsohn E, Oñate E. A Reduced Order Model based on Coupled 1D/3D Finite Element Simulations for an Efficient Analysis of Hemodynamics Problems. Journal of Computational Mechanics. 54:10131022. 2014.

[26] Soudah E, EYK Ng, Loong TH., Bordone M., et al. CFD Modelling of Abdominal Aortic Aneurysm on Hemodynamic Loads using a Realistic Geometry with CT. Computational and Mathematical Methods in Medicine, Volume 13, Article ID 472564, 9 p, 2013.

[27] Srichai MB, Lim RP, Wong S, Lee VS. Cardiovascular applications of phase-contrast MRI. AJR Am J Roentgenol. 192(3):662-75, 2009.

[28] Stalder A.F., Frydrychowicz A., Russe M.F, Korvink, J.G., Hennig J., Li K. and Markl M. Assessment of flow instabilities in the healthy aorta using flow-sensitive MRI. Journal of Magnetic Resonance Imaging, 2011.

[29] Vignon-Clementel IE, Figueroa AC, Jansen KE, Taylor CA. Outflow boundary conditions for three-dimensional finite element modelling of blood flow and pressure in arteries. Comput Methods Appl Mech Eng 195(2932):37763796, 2006.

[30] Yoo T.S. , Ackerman M. J. ,Lorensen W. E. , Schroeder W., et al. Engineering and Algorithm Design for an Image Processing API: A Technical Report on ITK - The Insight Toolkit. In Proc. of Medicine Meets Virtual Reality, J. Westwood, ed., IOS Press Amsterdam pp 586-592, 2002.

Chapter 7

Related Work

Thanks to the scientific contributions of paper 1, paper 2, paper 3 and paper 4, in this chapter the following applications have been studied:

- Qualitative evaluation of flow patterns in the Ascending aorta with 4D phase contrast sequences.
- Study new mechanical factor related to the Abdominal Aortic Aneurysm.
- Computational fluid dynamics in coronaries.

7.1 Qualitative evaluation of flow patterns in the Ascending aorta with 4D phase contrast sequences

Phase-contrast (PC) 4D MRI sequences allows to obtain three-dimensional flow images (see section 1.4.1.1) and to analyze of the patient-specific characteristics of intravascular flows under normal and pathological conditions. In clinical practice, this sequence allows to advance the understanding of the pathophysiology of vascular diseases through the interaction between flow and anatomy. Besides of this, it also help to understand the origin of diagnostic errors of 2D flow PC sequences. The aim of this study is to describe and characterize qualitatively different patterns of systolic flow in the Ascending Aorta(AoAsc) against to its aortic diameter with different degrees of root dilatation and against the different aortic valve pathologies using 4D-PC CardioRM sequences. All the patients (31 patients) who participated in this trial were volunteered and provided written consent to be part of this study. This study was reviewed and approved by the Ethics Committee of the Hospital Sant Pau i Creu Blanca, Barcelona, Spain. The 31 patients have different aortic problems, 12 patients suffer cardiomyopathy, 6 patients have a dilated aorta, 4 patients have aortic valve disease, 1 patient has a mitral valve disease, 1 patient has an atrial fibrillation and another suffers syncope, as well as 5 were healthy volunteers. For each patient an anatomy/flow cross-sectional of AoAsc was done. The flow pattern studied was: (i) at the Valsalva sinus (SV), where the flow adopts a uniformity velocity with a peak in the middle of the aorta (see figure 7.1.A and 7.1.B) or an eccetric flow jet with a maximun speed located at the periphery (see figure

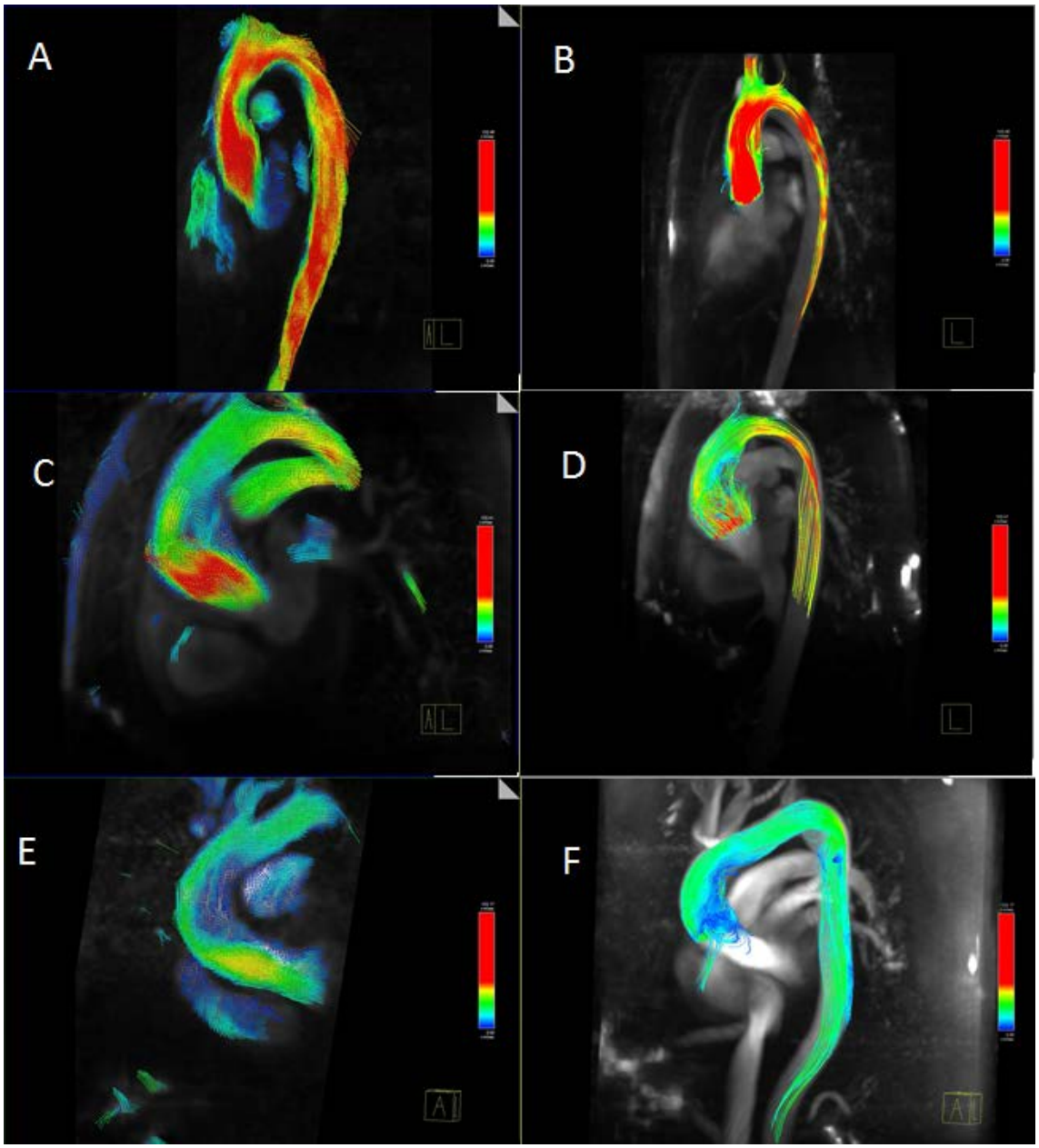

Figure 7.1: Blood flow patterns in ascending aorta, left (velocity vector), right (streamlines). A and B show a laminar flow with maximum speed in the center of the aortic flow. C and D show a turbulent flow into the dilation of the aorta with an eccentric jet. D and E show a turbulent flow into the elongation of the aorta with an eccentric jet.

7.1.C and 7.1.D), and (ii) at the AoAsc level, where the flow keep constast along the systole phase (see figure 7.1.A and 7.1.B) or the Systolic Turbulent Flow (FTS) can be defined as vortices or circular paths in opposite direction to the normal aortic systolic flow (see figure 7.1.D and 7.1.E).

The AoAsc diameter was measured to the level of the bifurcation of the pulmonary artery, and the elongation of the aorta was defined as the maximum distance from the front wall of the AoAsc to the rear wall of the descending aorta at the level also to the bifurcation of the pulmonary artery. Jet's direction is defined as maximum velocity in the streamline related to the perpendicular plane at the aortic root.

In 29 patients (93.5%) the left ventricular ejection fraction was normal. The aortic valve was bicuspid in 4 patients and 3 of them show a dilated AoAsc.The average diameter of the AoAsc was 16.80±4.41mm. The mean aortic elongation diameter was 5.15±0.99cm. From the 4D sequences, 15 patients have a central jet at the Valsalva sinus (48.4%) and 16 patients have an eccentric jet (51.6%). 10 patients have laminar flow at the AoAsc level (32%), 13 patients show a vortex during the systolic phase(42%) and 8 patient during the protosystolic phase(26%) (see figure 7.1). Statistical correlation between FTS against the AoAsc diameter and elongation of the aorta was done 7.2. The analysis shows that the diameter of the AoAsc has a significant linear relationship with the flow pattern in aortic systolic, which indicates higher prevalence of turbulence flow (proto-systolic vs systolic) for a higher aortic diameter (figure 7.2). The flow characteristics in the AoAsc were analyzed by two independent clinicians getting a good concordance. The jet eccentricity in the SV indicates a trend (p = 0.06) for the FTS origin in AoAsc. The presence of a bicuspid valve is also associated with the formation of vortices (p = 0.047), although when it is adjusted by the AoAsc's diameter, statistical significance (P = 0.48) decreases.

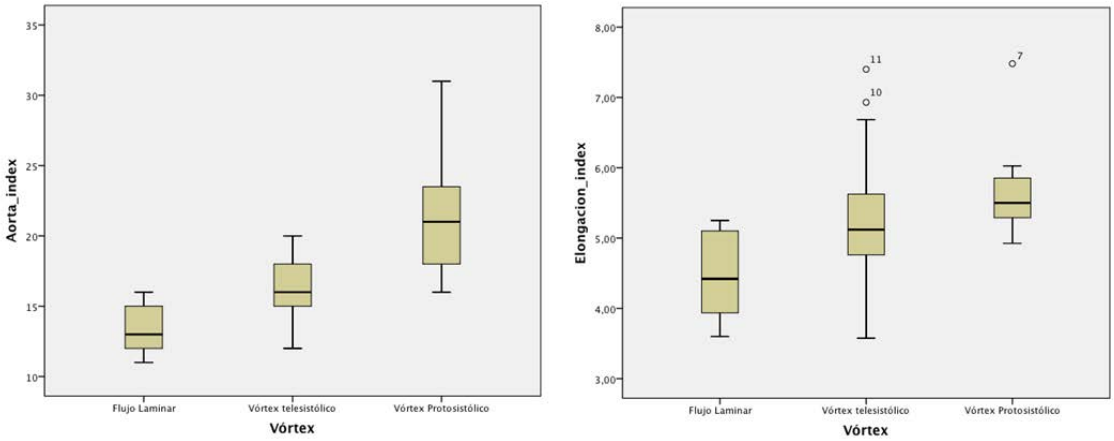

Figure 7.2: Left, Aortic index versus flow characteristics. Right, Aortic elongation versus flow characteristics.

7.1.1 Conclusions

The flow pattern during systolic phase in the ascending aorta changes progressively from laminar flow with directional jet in not-dilated aortas to turbulent flow with eccentricity jet in dilated aortas. Other factors, such as bicuspid aortic valve can increase the turbulence effect but there are not essential to provoke it. This study was done in collaboration with Dr.Francecs Carreras, Dr.Chi-

Hion Pedro Li and Dr.Xavier Alomar from Hospital Sant Pau i Creu Blanca and Clinica Creu Blanca, Barcelona, Spain, respectivily. The equipment used was a Magnetom Verio 3T Siemens, Erlangen, Germany.

7.2 Study new mechanical factor related to the Abdominal Aortic Aneurysm

The primary goal of this further work was to motivate a new phenomenological approach for identifying regions of possible formation of Intra Luminal Thrombus (ILT) on an intact but susceptible endothelium within AAAs. Following the idea of paper 2, *"CFD Modelling of Abdominal Aortic Aneurysm on Hemodynamic Loads using a Realistic Geometry with CT"*, thirteen new patients with infrarenal aneurysms on follow up from Clinical Hospital of Valladolid (Spain) have been studied. The patients chosen for this study were selected during the first phase of the AAA development. All the patients who participated in this trial analysis volunteered and provided written consent to be part of the study. This study was reviewed and approved by the Ethics Committee of the Clinical Hospital of Valladolid (Spain). To characterize the AAA shape and size, the main geometrical AAA parameters were determined using the lumen center line [109][4] of the segmented images. Twelve indices were defined and computed for the thirteen AAA patient-specific models. Figure 7.3 shows the seven geometrical parameters defined (AAA morphometry).

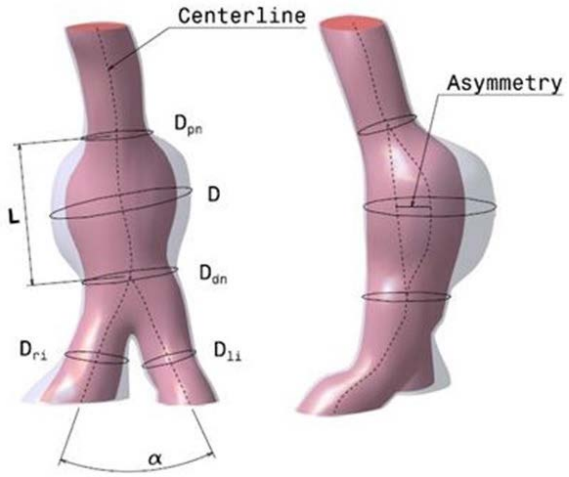

Figure 7.3: Abdominal Aneuryms 1D geometrical parameters. D: maximum transverse diameter, D_{pn}: neck proximal diameter(smallest diameter of the infrarenal artery, just before the AAA), D_{dn}: neck distal diameter (smallest diameter of the aorta, just after the AAA), L: aneurismal length (length between proximal and distal necks), D_{li}: left iliac diameter (left iliac diameter), D_{ri}: right iliac diameter (right iliac diameter) and α is the angle between the right and left iliac arteries.

Another four geometrical indices[87] were defined: γ(saccular index) assesses the length of the AAA region, this region will be affected by the formation and further development of the ILT, χ (deformation rate) characterizes the deformation of the aorta, relation between D_{pn} and D, ϵ (tortuosity index) is the ratio of the length of the curve to the distance between the proximal and distal neck and β (symmetry index) is the result of the non-symmetry expansion of the aneurysm sac. Next table 7.1 shows the parameters for the 13 new cases analyzed.

n	V_{AAA} (mm^3)	D (mm)	D_{pn} (mm)	D_{dn} (mm)	L (mm)	D_{li} (mm)	D_{ri} (mm)	γ	χ	ϵ	β	α
1	49223,2	30,34	19,77	23,36	80,42	14,74	12,50	0,377	1,533	0,0389	0,460	56,70
2	43623,0	33,07	26,91	29,70	82,71	15,73	17,62	0,399	1,22	0,022	0,60	57,20
3	51862,0	42,96	20,90	17,82	102,19	12,22	11,85	0,420	2,056	0,140	0,769	50,62
4	55935,0	41,39	24,53	33,56	94,23	18,27	12,32	0,439	1,687	0,0308	0,529	66,27
5	44386,1	34,80	20,88	30,35	109,71	20,23	15,16	0,317	1,667	0,0660	0,490	61,87
6	32740,0	33,51	20,53	23,92	114,88	15,50	13,01	0,29	1,632	0,0147	0,380	64,33
7	40608,0	40,05	32,18	34,86	104,16	23,43	15,67	0,384	1,245	0,0383	0,430	54,67
8	83186,0	50,99	24,23	39,33	105,47	14,81	21,45	0,483	2,104	0,0445	0,748	43,01
9	46676,0	37,28	23,45	24,28	89,19	11,44	11,45	0,417	1,590	0,0645	0,573	38,67
10	45780,0	40,88	25,60	25,90	80,38	9,90	11,18	0,508	1,597	0,0817	0,642	25,56
11	43130,0	42,23	22,02	30,15	85,50	21,63	19,94	0,493	1,918	0,0409	0,709	48,96
12	30538,0	29,81	20,71	19,00	92,39	15,70	11,88	0,322	1,439	0,0655	0,505	43,77
13	51388,0	37,52	33,39	21,66	99,12	12,20	14,80	0,378	1,124	0,0343	0,755	40,58

Table 7.1: Geometrical parameters of the 13 AAA cases analyzed

ECAP(eq.1.6) index was studied in an attempt to localize regions of the aneurismatic sac prone to

develop a ILT. Higher values of the ECAP index correspond to the development of intraluminal thrombus(ILT). The AAA simulations were performed for three cardiac cycles, and the simulations results from the last cardiac cycle were used to compute WSS(eq.1.2), OSI(eq.1.4), ECAP(eq.1.6) and RRT(eq.1.5). The WSS-based diagnostic indicators were computed in the aneurismatic sac. Next image shows the WSS, OSI, ECAP and RRT values for three different AAAs. Furthermore, an statistical analysis was carried out in order to establish the potential correlations between geometrical indices and hemodynamic stresses.

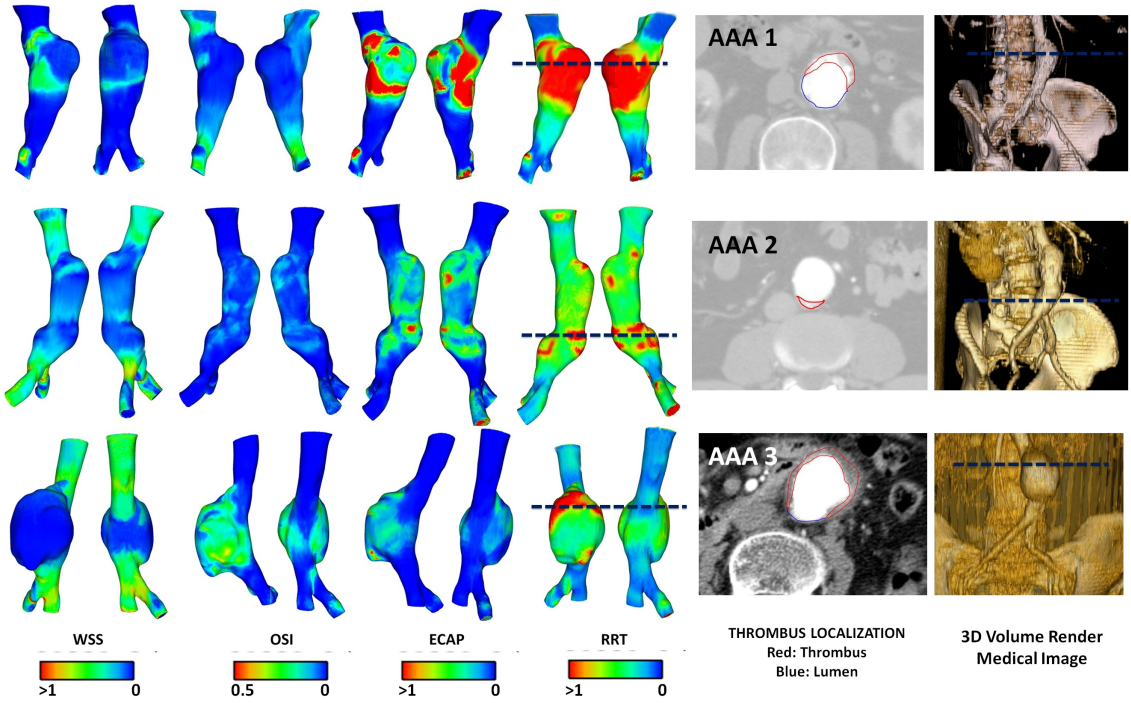

Figure 7.4: Spatial distribution of WSS, OSI, ECAP and RRT in three abdominal aortic aneurysm. For each AAA, anterior and posterior views of the lesions. On the right, 3D volume render and a CT slice showing the localization of the incipient thrombus (red line: thrombus, blue line: lumen). Dark Blue line represents the localization of the CT slice.

7.2.1 Conclusions

The computed ECAP combined with the geometrical factors may provide more information about ILT development for a complex AAA geometries. The present findings motivate consideration of the ECAP as diagnostic indicator. The results show that aneurysmal wall regions with increased flow ECAC and high tortuosity index may be prone to thrombus deposition, and consequently, ILT formation. The study shows that hemodynamic stresses can provide important additional information on aneurysm progression on a patient-specific basis. Statistical analysis confirmed that the length, asymmetry and saccular index significantly influence in the WSS distribution and

intraluminal pressure peak, which highlight the weight of these variables on the rupture risk predictions. No correlations between maximum diameter and hemodynamics stresses were obtained as expected. This finding is in agreement with the strategy adopted in the research, all AAAs are considered small with diameter less than 40 mm, and therefore the rupture risk is not significant. AAA rupture is a complex phenomenon involving a lot of factors. By the results it is possible to hypothesize that the correct and accurate characterization of AAA morphometry and its influence on the regional and temporal distribution of the hemodynamic stresses would be necessary for patient-specific assessment of rupture risk. Statistical techniques have significant potential to be an efficient tool for improving the AAA rupture risk. The methodology here developed can correctly predict the hemodynamic stresses from size and shape indices. To improve the reliability of the results, now expands the number of cases in the study and is studying the possibility of applying other statistical tools that better respond to situations where the data number is small. Changing the clinical management of this pathology is a very complex task. The use of the maximum diameter criterion is very easy to implement for the surgeon, in that the physician should simply measure the maximum diameter from CT scans. The results here obtained could be an indicative that other indices like, asymmetry, deformation rate, AAA length, saccular index, are important and could also be readily incorporated into surgeon's decision making.

7.3 Computational fluid dynamics in coronaries

Coronary artery disease (CAD) is the leading cause of death and serious illness in the western world. Approximately 35 million people are affected by CAD in Europe and around 25000 FFR measurements are annually performed. In the United States greater than one million diagnostic and 500 thousand interventional cases are performed each year, representing a $15 billion industry and causing about 25% of total deaths in the U.S [5], [67]. The significance of the coronary disease has motivated the development and application of state of the art clinical imaging and measurement techniques to aid diagnosis, perform patient stratification and guide interventions to restore coronary flow. However, greater than 95% of patients receive only a visual assessment of this data, that is subjective and unreliable. For this reason, many patients receive unnecessary interventions for non-significant lesions with others are denied intervention for lesions that are significant, an outcome that places patients at increased risk.

To address this issue a number of flow related measures have been proposed to provide an improved functional, rather than an anatomical, predictor of the severity of a given coronary stenosis. Of these diagnostic indicator, the fractional flow reserve (FFR) index (derived from measuring the ratio of aortic pressure and pressure beyond a stenosis) has demonstrated superior sensitivity and specificity for identifying coronary lesions that cause ischemia when compared with angiography alone and indeed with any other non-invasive imaging technique. In fact the results of patient stratification using invasive FFR were so good that these clinical trials had to be terminated early because it was considered unethical to keep patients on the control arm to emphasise the clinical usefulness. The accurate computation of FFR requires the measurement of the aortic pressure and pressure distal to the lesion. These pressures are determined by the overall dynamics of the cardiac and cardiovascular systems. Currently the pressures are measured invasively in specialised interventional cardiology departments using pressure wires that are passed across the lesion, under a pharmacologically-induced condition of hyperaemia. Furthermore, there are several limitations and pitfalls related to invasive FFR measurement. Recent years several computational methods have been proposed to compute FFR [45][94], but the computational times are high (from clinical point of view).

The methodology proposed in paper 1 ("A Reduced Order Model based on Coupled 1D/3D Finite Element Simulations for an Efficient Analysis of Hemodynamics Problems") can be used to estimate the pressure drop in non-healthy coronaries under different situations (rest and hyperaemia states). Next image (figure 7.5) shows the 3D-1D coupled approach schematics for the left coronary. Based on multiple angiographic X-ray projections the coronary tree is obtained. These projections are used to calculate the true geometric shape in 3D space and create an interactive rendered view of the coronary artery of interest using PMI's software (Maastricht, Netherlands). The coronary area of interest is segmented and reconstructed into a 3-D anatomical computer model. Coronary flow and pressure can be estimated by solving the governing equations of computational fluid dynamics(CFD), which relate to conservation of mass and balance of momentum, and which have been known in their current forms as the Navier-Stokes equations (section 1.4.2). These equations are solved for the unknown blood pressure and blood velocity, which are functions of

position and time. The physical properties of blood, the fluid density and the fluid viscosity, are known when solving these equations. Although blood exhibits complex rheological properties, it can be approximated as a Newtonian fluid with a constant viscosity in large/medium arteries (see appendix A).

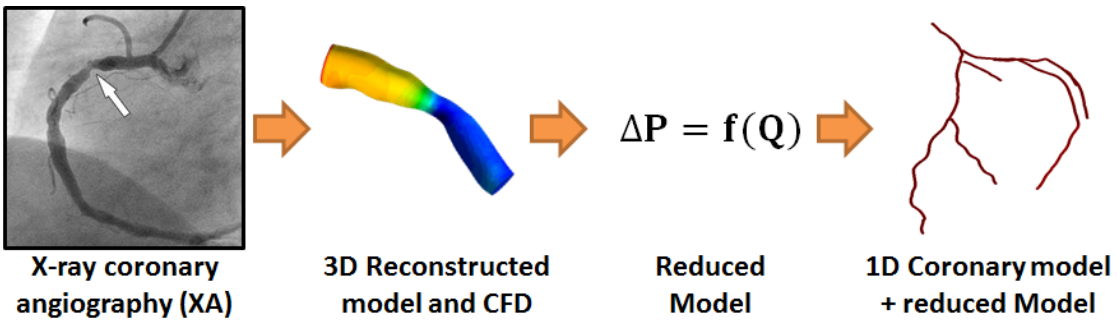

Figure 7.5: Methodology proposed to compute pressure drop in the coronaries

Solving these equations using a transient blood flow as inlet in the 3D domain allow to estimate the temporal pressure drop generated in the estonosis. Based on the transient flow and pressure drop a reduced order model can be defined (see equation 4 in paper 2). The reduced order model is expressed as a sum of two terms (viscous term and turbulent or Bernoulli term). After fitting the reduced order model, the resulting equation can be added into the 1D model (see apendix B). The reduced order model takes into account all the energy loss due to the estenosis. The reduced order model takes into account all the energy loss due to the estenosis. The full coronary tree (right and left branches) is represented by a one-dimensional network coupled with the fitted reduced model. Furthermore, thanks to this approach, 3D reconstructed model can be used to obtain diagnostic indicators as WSS or OSI. These diagnostic indicators allows identifying low and oscillating wall shear stress (likely) athero-prone sites (low mean WSS regions with non-zero OSI regions) [3]. Next figure (figure 7.6) shows the local effects in the estenosis.

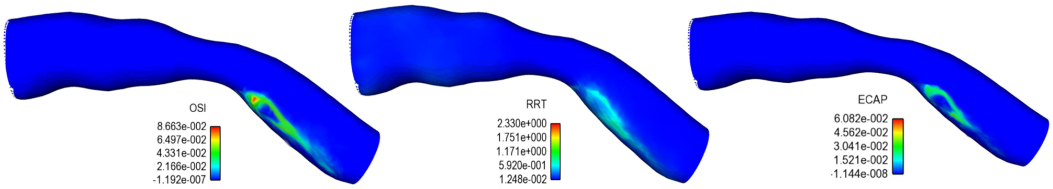

Figure 7.6: Spatial distribution of OSI, RRT and ECAP in an right coronary artery.

7.3.1 Conclusions

Coronary physiopathology is a complex process in which a lot of factors are involved. The methodology proposed is able to capture the local effects in the stenosis area and at the same

time it allows to estimate the pressure drop under different situation. As it is explained in paper 1, the most important numerical approximation introduced is that the training of the reduced-order model is performed using the 3D patient-specific anatomical data. The 1D coronary model and the trained reduced model is correctly capable to capture the pressure gradient and the energy losses in coronaries diseases. The advantage of the 1D coronary model and the reduced model is to reduce the computational time when different patient's situations are required, for example at hyperaemia. Using this approach the index FFR can be also calculated in a non-invasive way.

Chapter 8

Conclusions and Future work

8.1 Conclusions

The increasing availability and efficiency of computational tools for patient-specific simulations provides useful data to understand the psychopathology of cardiovascular diseases. The rationale for this thesis is to reinforce the clinical utility of computational hemodynamics, contributing to its translation into clinical practice through the diagnostic indicators. The results of this thesis will provide useful quantitative data for proof-of-concept studies. Hopefully, this will enable clinicians to gain insights, develop intuitions, and provide constructive feedback and guidance for the development of more representative models. Moreover, the increasing sophistication of therapeutic solutions for cardiovascular pathologies require the development of tools for quantitative patient-specific simulations to aid therapeutic planning through the assessment of pre-operative scenarios and the prediction of therapeutic intervention outcomes. The integration of technical developments into prototypes will allow the clinicians to become acquainted with the newly developed technology underpinning exploitation in new products. It should be noted that part of the development performed during this thesis is being integrated into clinical prototypes. Another general objective of this thesis is to generate and share a common technology infrastructure, resources and knowledge across/between clinical practice, physics and bio-engineering. The key findings of the four papers and related work are summarized below.

In this thesis we have developed a geometrical multiscale framework for simulation cardiovascular diseases under different physiological and pathological conditions. The cardiovascular diseases studied under this multiscale framework were the Aorta Coartaction and Coronary Disease, but, the technology underlying is applicable to other common cardiovascular conditions, including peripheral, cerebrovascular, and reno-vascular disease, and may be used to determine whether vascular stenosis are hemodynamically significant as well as the relative benefit of therapeutic interventions. In this line, we have also proposed a new coronary indicator to evaluate the stenosis without hyperemia condition (under evaluation). At the same time, we have developed and validated a 1D numerical model coupled with the reduced order model. A 1D-reduced order model validation for other groups of people or patients could also be useful for research and clinical outcome analysis. The 1D model is able to describe the pulse wave dynamics and the interaction

between the heart and the circulatory system. We have also studied the hemodynamics factors that may be important in triggering the onset of aneurysms correlated with the patient-specific anatomy. The hemodynamics factor and the geometry are directly related with the ILT formation. More AAA cases are needed to define a direct correlation between the hemodynamics factors and AAA development. Quantification of WSS, as well as other informative hemodynamic parameters, was central, due to the importance of comparable measures for the predictive use. In this way, the feasibility of CFD as a predictive tool to use for treatment planning of cardiovascular diseases has been demonstrated. A methodology to obtain computational meshes from medical image has been defined. A new procedure to segment the aorta using 4D flow CMR data has also been proposed. Beyond this, 4D flow CMR visualization offers a more qualitative and comprehensive description of the flow fields than any other in-vivo imaging technique. The velocity data provided by 4D flow CMR has been complementary to the higher resolution velocity fields computed by the CFD in order to estimate the WSS. We have also developed an algorithm to compute WSS based on the 4D flow CMR data. Based on that approach other diagnostic indicators could be estimated, as pulse wave velocity(PWV)[60], turbulent kinetic energy[71], relative pressure fields[23] or volume and kinetic energy of ventricular flow compartments[26]. For full details refer to the *"Results"* sections of papers.

8.2 Limitations and Future work

The diagnostic indicators obtained in this thesis need to be validated and reproducible if they are to be useful for clinical workflows. Multicenter studies are necessary to establish the repeatability of various aspects of the technique used in the papers across centers. Widespread clinical usage would be facilitated by further integration into the standard clinical environment. The methodology developed in this thesis makes the process more robust and transparent, in the way that the models can be incorporated into clinical workflows. This means to develop interfaces and put them in a clinical context (in connection with imaging and clinical data accessed directly from the hospital's computer system) where physicians can use it. Several improvements and further possibilities are offered on the basis on the present papers.

The presented techniques are currently employed for patient-specific modeling of aorta and coronary arteries acquired from different modalities, both from geometric and fluid-dynamics points of view. A study (still to be published) on 20 coronary models reconstructed at Pie Medical Imaging (PMI), Maastricht, Netherlands has further demonstrated the validity of the computation method proposed. The coronary index for all 20 models will be computed in 1 hour with full automation and acceptable results. Further work will consist on reduce the computational time to be useful in a clinical routine and setting properly the hyperemia conditions of the patients. Another study (still to be published) on 23 Abdominal aneurysm model reconstructed at the International Center of numerical Methods in Engineering (CIMNE), Barcelona, Spain and Mechanical Engineering Division, CARTIF Technological, Valladolid, Spain has the objective to correlate the Intra Luminal Thrombus (ILT) with the hemodynamics parameters and the geometrical factor, in the sense of predicting the ILT evolution based only on the geometrical factor. Another indices can

be estimated, for example, the flow-induced platelet activation (TFP) proposed by [22]. The main purpose of this index is to identify local regions of the wall that at the same time were exposed to prothrombotic WSS stimuli and a flow rich in activated platelets. TFP is defined as:

$$\mathbf{TFP} = \mathbf{ECAP} \cdot \mathbf{PLAP} = \frac{\mathbf{OSI} \cdot \mathbf{PLAP}}{\mathbf{TAWSS}} \tag{8.1}$$

where PLAP is the PLatelet Activation Potential recently proposed [84]. TFP index combines the ECAP-based on WSS and the fluid shear history-based PLAP obtained by particle tracking. Briefly, the PLAP is a non-dimensional scalar index that represents the magnitude of shear rates that a fluid particle accumulates while travelling throughout the fluid domain.

$$\mathbf{PLAP(x,t)} = \int_{t-2T}^{t} |D(x(\tau), \tau)| d\tau \tag{8.2}$$

where |D(x(τ),τ)| is the Frobenius norm of the symmetric part of the spatial gradient of velocity tensor, t is the time of injection of the particle and 2T indicates how long the particle has been tracked. Collecting particle information for multiple cardiac cycles allows one to capture flow stagnation events that might be of importance in thrombogenesis [84].

Two new collaborations with the Hospital Sant Pau i Creu Blanca, Barcelona, Spain are now beginning. Both are related with the 4D flow CMR acquisition, Aortic Dissection and Portal pressure. Related to the Aortic Dissection, the objective is to improve the clinical intervention procedure, we are going to combine 4D flow CMR sequences with CFD to estimate the relative pressure in the true and false lumen. And related to the Portal pressure, the goal is to use 4D flow CMR sequence to estimate the flow and pressure in the Portal system with the objective of check the liver function. Besides of the clinical applications, a prototype of the software (AORTA4D) to visualize and quantify 4D flow CMR data is currently being developed in collaboration with GiD Department of CIMNE.

Several improvements and further technological possibilities are offered on the basis on the present papers. In the current papers there are a number of limitations to obtain the hemodynamics parameters that can be gradually removed. For instance, the autoregulation phenomenon, in response to hemodynamic stimuli, which is an important issue in coronary blood flow mechanisms, was not considered in the related work and it could be included in the future. For the 1D model used in the Paper 1, small distal vessels such as arterioles, capillaries, venules and veins were not modeled directly and may need to be investigated in detail. In that line, a more robust methodology to estimate the lumped parameters in patient-specific models would be needed. Addition of the pulmonary circulation could also close the circulation loop and make an even more useful model. For paper 2, the interaction between arterial blood flow and intraluminal thrombus was not taken into account, and it could play an important role in the development of some abdominal aneurysms, as well as, it would be needed to increase the number of the cases to get more evidences with the hemodynamics parameters obtained. For paper 4, the constitutive arterial model used for the AAA did not take into account the fiber distributions and the model used were geometrical model.

About 4D flow CMR technologies there are still some uncertainties related to the clinical use, chapter 6 and chapter 7. Derived flow parameters, need further development or validation for clinical use, to include measurements of WSS, pressure difference, TKE or intracardiac flow components. The accuracy on the acquisition parameters measured is quite dependent of the clinical sequence (image-protocol) used. In our particular case, the WSS is quite dependent of the spatial resolution, therefore an accurate segmentation is needed. We are working on new segmentation algorithm (see figure 8.1). Additionally, a validation protocol using a phantom model would be needed.

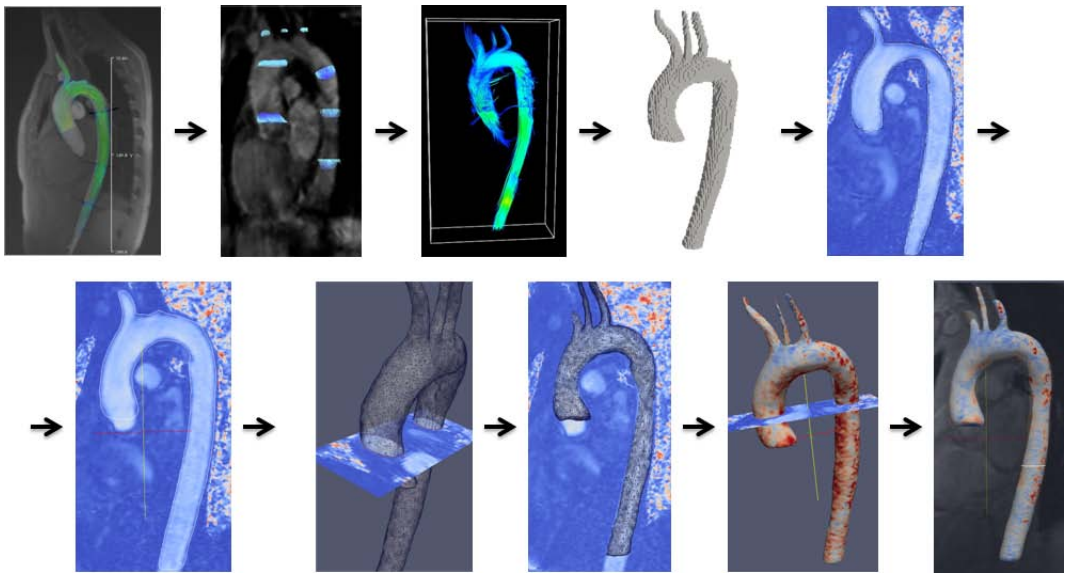

Figure 8.1: Preliminary concept of automatic segmentation of the Aorta based on 4D MRI data

Appendix A

Cardiovascular physiology

The purpose of this Appendix is to introduce which are the basics of the cardiovascular physiology. This brief overview of the cardiovascular physiology is only included for the purpose of providing essential information to scientists without a background in medicine. In this appendix the macroscopic and microscopic structure of arterial walls, blood modeling and cardiovascular system is briefly explained. For a more detailed exposition of the different mechanical/rheological characteristics of cardiovascular system and the overall functioning of the blood vessel see [97].

A Cardiovascular physiology

Cardiovascular physiology is the study of the cardiovascular system, specifically addressing the physiology of the heart (cardiac physiology) and blood vessels (circulatory physiologic). The cardiovascular system is a pressurized closed system responsible for transporting nutrients, hormones, and cellular waste throughout the body. From a physical point of view, there are three independent circuits:

- Systemic Circulation: The former brings oxygenated blood from the heart, thought arteries and capillaries, to the various organs (systemic arterial system) and then brings it back to heart (systemic venous system). The systemic arterial system is an extensive high-pressure system; hence the structure of its blood vessels reflects the high pressures to which they are subjected. The systemic venous system acts as a collecting system, returning blood from the capillary networks to the heart passively down a pressure gradient.

- Pulmonary circulation: The latter pumps the venous blood into the pulmonary artery where it enters the pulmonary system, through the pulmonary veins, get oxygenated and is finally received by the heart, ready to be sent to the systemic circulation (where the blood is pumped through the aortic valve into the aorta).

- The coronary circulation arises from the aorta and provides a blood supply to the myocardium, the heart muscle

This thesis will focus on systemic arterial system and coronary circulation.

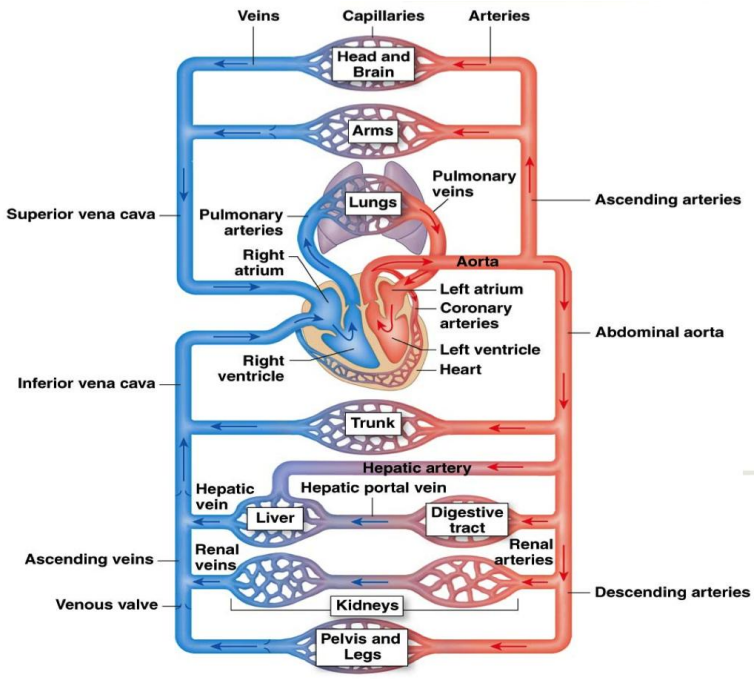

Figure A1: The cardiovascular system is a close loop. The heart is a pump that circulates blood through the system. Arteries take blood away from the heart (systemic circulation) and veins (pulmonary circulation) carry blood back to the heart[39].

A.1 Blood Vessels

The blood vessels are the part of the circulatory system that transport blood throughout the body. The vascular system is composed of arteries, arterioles, capillaries, venules and veins. The three main types of blood vessels are:

1. Arteries, which carry blood away from the heart at relatively high pressure,
2. Veins, which carry blood back to the heart at relatively low pressure and
3. Capillaries, which provide the link between the arterial and venous blood vessels.

Regarding the small vessels mention that arterioles are the smallest branches of the arterial network. Arterioles vary in diameter ranging from 0.3 mm to 0.4 mm. Any artery with a diameter smaller than 0.5 mm is considered to be an arteriole. Capillaries are specialized for diffusion of substances across their wall. Capillaries are the smallest vessels of the blood circulatory system and form a complex inter linking network. Pressure is essentially lost in the capillaries. As the capillaries begin to thicken and merge, they become venules. Venules eventually become veins and head back to the heart.

In general, arteries are roughly subdivided into two types: elastic (or large arteries) and muscular (or small arteries). Elastic arteries have relatively large diameters and are located close to

the heart (for example, the aorta, the carotid and iliac arteries), while muscular arteries are located at the periphery (for example, femoral, celiac, cerebral arteries). The walls of all the blood vessels, except the capillaries which are only one cell thick, have the same basic components but the proportion of the components varies with function. Therefore, the structure of the vessels in the different parts of the circulatory or vascular system varies and the differences relate directly to the function of each type of vessel (Table A1). Arteries are not just tubes through which the blood flows.

Table A1: Vessel Type

Vessels	Diameter of lumen (mm)	Wall thickness (mm)	Mean pressure (kPa)
Aorta	25	2	12.5
Large arteries	1-10	1	12
Small arteries	0.5-1	1	12
Arteriole	0.01-0.5	0.03	7
Capillary	0.006-0.01	0.001	3
Venule	0.01-0.5	0.003	1.5
Vein	0.5-15	0.5	1
Vein cava	30	1.5	0.5

All blood vessels, except capillaries, are composed of three distinct layers (tunica intima, tunica media and tunica externa or adventicia) surrounding a central blood carrying canal (known as the lumen). The constituents of arterial walls from the mechanical perspective are important to researchers interested in constitutive issues.

- Tunica intima. The tunica intima is the innermost layer of the artery. It composed of a lining layer of highly specialized multi-functional flattened epithelial cells termed endothelium. This sits on a basal lamina; beneath this is a very thin layer of fibro-collagenous support tissue.

- Tunica media. The tunica media is the middle layer in a blood vessel wall and is a complex three-dimensional network of smooth muscle cells reinforced by organized layers of elastic tissue which form elastic laminae. The tunica media is particularly prominent in arteries, being relatively indistinct in veins and virtually non-existent in very small vessels. From the mechanical perspective, the media is the most significant layer in a healthy artery.

- Tunica Adventicia. The tunica adventitia or externa is the outermost layer of blood vessels. It is composed largely of collagen, but smooth muscle cells may be present, particularly in veins. The tunica adventitia is often the most prominent layer in the walls of veins. Within the tunica adventitia of vessels with thick walls (such as large arteries and veins) are small blood vessels which send penetrating branches into the media to supply it with blood.

Veins do not have as many elastic fibers as arteries. Veins do have valves, which keep the blood from pooling and flowing back to the legs under the influence of gravity. When these valves

break down, as often happens in older or inactive people, the blood does flow back and pool in the legs. The result is varicose veins, which often appear as large purplish tubes in the lower legs.

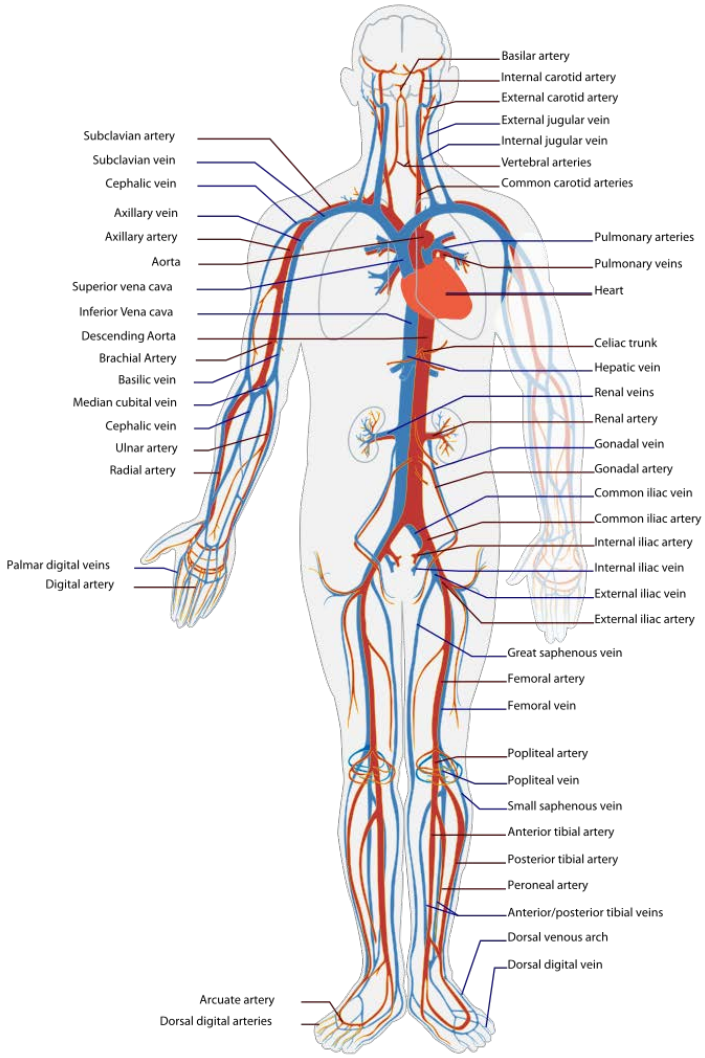

Figure A2: The human circulatory system (simplified). Red indicates oxygenated blood (arterial system), blue indicates deoxygenated (venous system)[106].

A.2 Blood Modelling

Blood is a suspension of cells into a fluid called plasma. It delivers oxygen and nutrients to the cells and remove CO_2 and waste products. Blood also enables hormones and other substances

to be transported between tissues and organs. The blood makes up about 7% of the weight of a human body, with a volume of about 5 litters in an average adult. Understanding blood physiology depends on understanding the components of blood. Blood is made up of plasma (about 55%) and cellular elements (about 45%). These cellular elements include red blood cells (also called RBCs or erythrocytes), white blood cells (also called leukocytes) and platelets (also called thrombocyte) suspended in a plasma. Plasma is essentially a blood aqueous solution containing 92% water, 8% blood plasma proteins, and trace amounts of other materials (i.e albumin or globulin). Plasma has many functions as involving colloid, osmotic effects, transport, signaling, immunity and clotting.

- $5*10^{12}$ erythrocytes or red cells (45.0% of blood volume)in a woman 4.800.000 and in a men 5.400.400 erythrocytes per mm^3 (or microliter) Size: disc biconcave 7 or 7.5 μm of diameter. Erythrocytes are responsible for the exchange of oxygen and CO_2 with the cells.
- $9*10^9$ leukocytes or white cells(1.0% of blood volume) 4.500 y 11.500 per mm^3 (or microliter) in the blood. Size: between 8 and 20 μm. Leukocytes play a major role in the human immune system.
- $3*10^{11}$ thrombocytes ($>$1.0% of blood volume): Platelets are responsible for blood clotting (coagulation).

Blood viscosity is a measure of the resistance of blood to flow. The blood viscosity increases as the percentage of cells in the blood increases: more cells mean more friction, which means a greater viscosity. The percentage of the blood volume occupied by red blood cells is called the haematocrit. With a normal haematocrit of about 40 (that is, approximately 40% of the blood volume is red blood cells and the remainder plasma), the viscosity of whole blood (cells plus plasma) is about 3 times that the viscosity of the water. Other factors influencing blood viscosity include temperature, where an increase in temperature results in a decrease in viscosity. This is particularly important in hypothermia, where an increase in blood viscosity will provoke problems with blood circulation.

Blood compressibility is the relation between all of its components and their volume fraction or a measure of the relative volume change of a fluid as a response to a pressure change. The 92% of the blood is water, and how the water has a high relation of compressibility, blood can be consider an incompressible fluid. Mathematically, it is mean that the mass is conserved within the domain.

Usually, for small arteries (less than 1mm in diameter) blood is consider as Non-Newtonian fluid, however in medium/large arteries blood may be considered as Newtonian fluid. To explain this behaviour it is necessary to explain which the Fahraeus-Lindqvist effect is. Fahraeus-Lindqvist effect is characterized by a decrease in the apparent blood viscosity as the arteries diameter decreases below 500 mm. The minimum apparent viscosity is reached when the tube diameter is higher than 8 mm, upon further decreases in tube diameter, the apparent viscosity increases very rapidly. The physical reason behind the Fahraeus-Lindqvist effect is the formation of a cells-free layer near the wall of the tube [4]. The layer is devoid of RBCs and has a reduced local viscosity.

The extent of the cell-free layer, which depends on the vessel size and haematocrit, is a major factor that determinate the apparent viscosity of the blood. The core of the tube, on the contrary, is rich with RBCs and has a higher local viscosity. However, in large arteries with internal diameter > 500 mm, although the blood density depends on the red cells concentration, the blood may be considered a homogeneous fluid with standard behaviour(Newtonian fluid)[70]. The viscosity μ of the fluid is proportional to τ_{ij}. Therefore, the rheological properties of blood depends on the vessels size, for instance, when the vessel diameter reduces to size comparable with the one of the red cells (below 12μm), blood cannot be considered as continuum any longer, therefore, blood is a complex fluid whose flow properties are significantly affected by the arrangement, orientation and deformability of red blood cells.

Appendix B

Numerical Model

One-Dimensional (1D) models of blood flow have been extensively used to study wave propagation phenomena in arteries. These models allow us to investigate physical mechanisms underlying changes in pressure and flow pulse waveforms that are produced by cardiovascular disease, however these models do not taken into account the effects provoked by the 3D geometry. In this appendix, the 1D mathematical formulation and the reduced model used in paper 1 (*"A Reduced Order Model based on Coupled 1D/3D Finite Element Simulations for an Efficient Analysis of Hemodynamics Problems."*) are briefly explained.

B 1D Mathematical Model

A preliminary basic knowledge about the cardiovascular system was given in appendix A. We introduce an one-dimensional mathematical model to describe the flow motion in arteries and its interaction with the wall displacement in order to provide a better understanding of the hemodynamics in large vessels. In absence of branching, a short of an artery may be considered as a cylindrical compliant tube, and it can be described by using a curvilinear cylindrical coordinate system $(\mathrm{r}, \Theta, \mathrm{z})$ with the corresponding base unit vector $(\mathrm{e_r}, \mathrm{e_\Theta}, \mathrm{e_z})$ radial, circumferential and axil unit vector, respectively, as show in figure B1. The vessel extends from $\mathrm{z} = 0$ to $\mathrm{z} = \mathrm{L}$ and this length L is constant with time, therefore, the spatial domain Ω_c in cylindrical coordinate is defined as follows:

$$\Omega_c = \{(\mathrm{r}, \Theta, \mathrm{z}) : 0 \leqslant \mathrm{r} \leqslant \mathrm{R}(\mathrm{z}, \mathrm{t}); \Theta\epsilon[0, 2\Pi); \mathrm{z}\epsilon(0, L); \Delta t > 0\} \tag{B.1}$$

Defined our domain, the following assumptions must be taken into account in order to deduce the one-dimensional mathematical model:

- Radial displacements. The wall displaces along the radial direction solely, thus at each point on the tube surface we may write $\eta = \eta \mathrm{e_r}$, where $\eta = \mathrm{R_z} - \mathrm{R_0}$ is the displacement with respect to a reference radius $\mathrm{R_0}$.

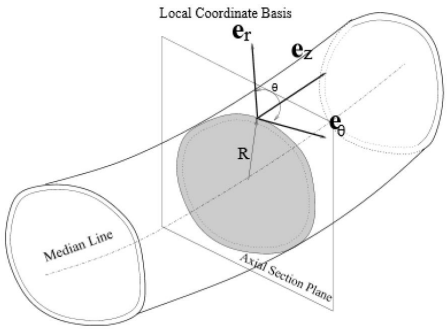

Figure B1: Section of an artery with the principal geometrical parameters

- Axial symmetry. All quantities are independent from the angular coordinate Θ. As a consequence, every axial section, $\mathrm{z} = \mathrm{constant}$, remains circular during the wall motion. The arteries radius R is a function of z and t. A generic axial section will be indicated by $\mathrm{S} = \mathrm{S}(\mathrm{z}, \mathrm{t})$ where,

$$S(z,t) = \{(r, \Theta, z) : 0 \leqslant r \leqslant R(z,t); \Theta\epsilon[0, 2\Pi); \Delta t > 0\} \tag{B.2}$$

  and, its measure A is given by

$$A(z,t) = \int_S d\sigma = \pi R^2(z,t) = \pi \left[R_0(z) + \eta(z,t)\right]^2 \tag{B.3}$$

- Dominance axial velocity, the velocity components orthogonal to the z axis are negligible compared to the component along z. The latter is indicated by $\mathrm{u_z}$ and its expression in cylindrical coordinates reads:

$$u_z(r,z,t) = \overline{u}(z,t)s\left[\frac{r}{R(z,t)}\right] \tag{B.4}$$

  where $\overline{\mathrm{u}}$ is the mean velocity in each axial section and s is a velocity profile.

$$\overline{u}(z,t) = \frac{1}{A}\int_S u_z \, d\sigma \tag{B.5}$$

- Constant pressure, we assume that the pressure P is constant on each axial section S, so that it depends only on z and t.

$$\overline{p}(z,t) = \int_S p_z \, d\sigma \tag{B.6}$$

- No body forces. We neglect body forces.

The resulting state variables are

$$\begin{aligned} \overline{Q}(z,t) &= \int_S (z,t) u_z \, d\sigma = A(z,t)\overline{u} \\ A(z,t) &= \int_{\mathcal{S}(z,t)} d\sigma = \pi R^2(z,t) \end{aligned} \tag{B.7}$$

where A is the cross-sectional area and Q is the volumetric flow rate.

Therefore, we have three independent variables $(\mathrm{A}, \mathrm{u}, \mathrm{p})$, or equivalently $(\mathrm{A}, \mathrm{Q}, \mathrm{p})$. Thus, we require three independent equations to get a solution. These three equations will be provided by equations of conservations of mass and momentum and an algebraic law that link the pressure and area of the artery.

B.1 Conservation equations

The conservation equations reflect a certain physical amount of a continuous medium that must always be satisfied and which are not limited in their application to the material. By applying the conservation equations in the domain Ω the body β leads to an integral relationship. Since the integral relationship must hold for any sub-domain of the body, then the conservation equations can be expressed as partial differential equations. Before continuing with the conservation equations, the material time derivative of an integral relationship to any property space is defined by

$$\frac{d}{dt}\int_\Omega (\bullet) = \int_\Omega (\frac{d(\bullet)}{dt} + \nabla(\bullet)\cdot \mathbf{v}) d\Omega \tag{B.8}$$

which is the Reynold's transport theorem.

B.2 Conservation of the mass

A fundamental law of Newtonian mechanics is the conservation of the mass, also called continuity equation, contained in a material volume. Considering the vessel shown in Figure B1 as our control volume, the principle of mass conservation requires that the rate of change of mass within the domain Ω_t plus the net mass flux out of the control volume is zero.

Denoting the vessel volume as

$$V(t) = \int_0^L A dz, \tag{B.9}$$

where L is the length of the vessel and assuming there are no infiltration through the side walls, the mass conservation can be written as

$$\rho \frac{dV(t)}{dt} + \rho Q(L,t) - \rho Q(0,t) = 0 \tag{B.10}$$

where ρ is the blood density. If infiltration does occur we must add a source term to this equation [101]. To determine the one-dimensional equation of mass conservation, we insert the volume into equation B.10 and, note that

$$Q(L,t) - Q(0,t) = \int_0^L \frac{\partial Q}{\partial z} dz,$$

we obtain

$$\rho \frac{d}{dt} \int_0^L A(z,t) dz + \rho \int_0^L \frac{\partial Q}{\partial z} dz = 0.$$

If we assume L is independent of time we can take the time derivative inside the integral to arrive at

$$\rho \int_0^L \left\{ \frac{\partial A}{\partial t} + \frac{\partial Q}{\partial z} \right\} dz = 0$$

Since we have not specified the length L, the control volume is arbitrary and so the above equation must be true for any value of L and so in general we require that the integrand is zero. We therefore obtain the differential one-dimensional mass conservation equation:

$$\frac{\partial A}{\partial t} + \frac{\partial Q}{\partial z} = \frac{\partial A}{\partial t} + \frac{\partial (uA)}{\partial z} = 0 \tag{B.11}$$

B.3 Conservation of the momentum

The momentum equation, also called the equation of motion, is a relation equating the rate of change of momentum of a selected portion of the body and the some of all forces acting on that portion. Again we consider the vessel as our control volume and assume that there is no flux through the side walls in the z-direction. In this case, it states that the rate of change of momentum within the integration domain Ω_t plus the net flux of the momentum out of the domain itself is equal to the applied forces on the domain and can be expressed over an arbitrary length L as

$$\frac{\partial}{\partial t} \int_0^L \rho Q dz + (\alpha \rho Q u)_L - (\alpha \rho Q u)_0 = F \tag{B.12}$$

where F is defined as the applied forces in the z-direction acting on the domain. The equation B.12 includes the *momentum-flux correction coefficient* α, also called *Coriolis coefficient*, which accounts for the fact that the momentum flux calculated with averaged quantities ($\bar{u}$) does not consider non-linearity of sectional integration of flux momentum. So we may assume

$$\frac{\partial}{\partial t} \int_S \rho \tilde{u}^2 A \equiv \alpha \rho \tilde{u}^2 A = \alpha \rho Q \tilde{u} \quad \Rightarrow \quad \alpha(z,t) = \frac{\int_S \tilde{u}^2 d\sigma}{A \tilde{u}^2} = \frac{\int_S \tilde{s}^2 d\sigma}{A} \tag{B.13}$$

In general, the coefficient α vary in time and space, yet in our model it is taken constant as a consequence of B.5 It is immediate to verify that $\alpha \geq 1$.

The axial velocity profile *s(y)* is chosen a priori through the power-law relation

$$s(y) = \gamma^{-1}(\gamma + 2)(1 - y^{\gamma}) \tag{B.14}$$

where y is the radial coordinate and γ is a proper coefficient. Commonly accepted approximation are $\gamma = 2$ ($\alpha = 4/3$), which corresponds to the Poiseuille solution (parabolic velocity profile), while $\gamma = 9$ ($\alpha = 1.1$) leads to a more physiological flat profile, following the Womersley theory. The blood profile trend with these values are shown in Figure B2.

We will see that the choice of $\alpha = 1$, which indicates a completely flat velocity profile, would lead to certain simplification in our analysis.

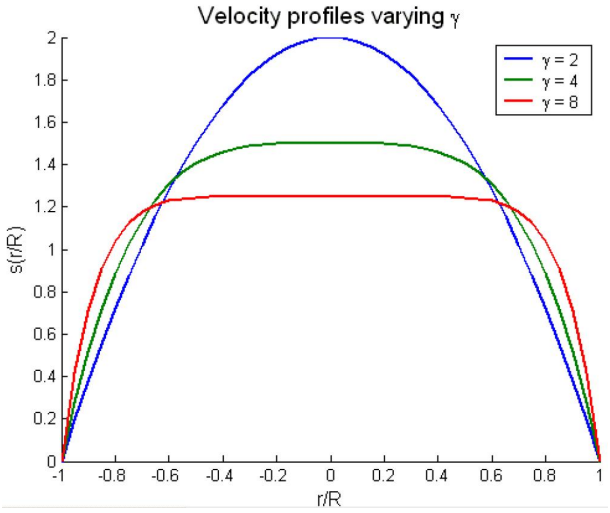

Figure B2: Blood flow profile adopting different values of γ.

To complete the equation B.12 we need to define the applied forces $\mathbf{F}$ which typically involve a pressure and a viscous force contribution,

$$F = (PA)_0 - (PA)_L + \int_0^L \int_{\partial S} \hat{P} n_z ds dz + \int_0^L f dz \tag{B.15}$$

where ∂S represents the boundary of the section S, n_z is the z-component of the surface normal and f stands for the friction force per unit of length. The pressure force acting on the side walls, given by the double integral, can be simplified since we assumed both constant sectional pressure and axial symmetry of the vessel; so we have

$$\int_0^L \int_{\partial S} \hat{P} n_z ds dz = \int_0^L P \frac{\partial A}{\partial z} dz \tag{B.16}$$

If we finally combine equations B.12,B.15 and B.16 we obtain the momentum conservation for the computation domain expressed as

$$\frac{d}{dt} \int_0^L PQ dz + (\alpha \rho Q u)_L - (\alpha \rho Q u)_0 = (PA)_0 - (PA)_L + \int_0^L P \frac{\partial A}{\partial z} dz + \int_0^L f dz \tag{B.17}$$

To obtain the one-dimensional differential equation for the momentum we note that

$$(\alpha\rho Qu)_L - (\alpha\rho Qu)_0 = \int_0^L \frac{\partial(\alpha\rho Qu)}{\partial z} dz$$
$$(PA)_0 - (PA)_L = -\int_0^L \frac{\partial(PA)}{\partial z} dz$$

which inserted into B.17, taking L independent of time and ρ constant, gives

$$\rho \int_0^L \left\{ \frac{\partial Q}{\partial t} + \frac{\partial(\alpha Qu)}{\partial z} \right\} dz = \int_0^L \left\{ -\frac{\partial(PA)}{\partial z} + P\frac{\partial A}{\partial z} + f \right\} dz$$

Once again this relationship is satisfied for an arbitrary length L and therefore can only be true when the integrands are equal. So the one-dimensional equation for the momentum conservation becomes

$$\frac{\partial Q}{\partial t} + \alpha \frac{\partial}{\partial z}\left(\frac{Q^2}{A}\right) = -\frac{A}{\rho}\frac{\partial P}{\partial z} + \frac{f}{\rho} \tag{B.18}$$

The viscous term in the equation B.15 can be taken proportional to the averaged velocity $\bar{u}$, thus we write

$$\frac{f}{\rho} = K_R \frac{Q}{A}$$

Therefore we finally obtain the equation of the momentum continuity

$$\frac{\partial Q}{\partial t} + \alpha \frac{\partial}{\partial z}\left(\frac{Q^2}{A}\right) = -\frac{A}{\rho}\frac{\partial P}{\partial z} + K_r \bar{u} \tag{B.19}$$

where K_R is a strictly positive quantity that represents the viscous resistance of the flow per unit length of tube. It depends on the kinematic viscosity $\nu = \frac{\mu}{\rho}$ of the fluid and the velocity profile s chosen. For a power law profile $s(y)$, we have $K_R = 2\pi\nu(\gamma + 2)$. In particular, for a parabolic profile $K_R = 8\pi\nu$, while for a flat profile we obtain $K_R = 22\pi\nu$.

B.4 Vessel wall constitutive model

Once we obtained the two governing equations B.11 and B.19, it is possible to write the one-dimensional system as

$$\begin{cases} \dfrac{\partial A}{\partial t} + \dfrac{\partial Q}{\partial z} = 0 \\ \dfrac{\partial Q}{\partial t} + \dfrac{\partial}{\partial z}(\alpha\dfrac{Q^2}{A}) + \dfrac{A}{\rho}\dfrac{\partial P}{\partial z} + K_R\dfrac{Q}{A} = 0 \end{cases} \tag{B.20}$$

for all $z \in (0, L)$ and $t > 0$, where the unknown variables are A, Q and P. The system of equations B.20 may be also expressed alternatively in terms of the variables $(A, \bar{u})$ instead (A, Q).

$$\begin{cases} \dfrac{\partial A}{\partial t} + \dfrac{\partial A\bar{u}}{\partial z} = 0 \\ \dfrac{\partial \bar{u}}{\partial t} + \bar{u}\dfrac{\partial \bar{u}}{\partial z} + \dfrac{1}{\rho}\dfrac{\partial P}{\partial z} + K_R\bar{u} = 0 \end{cases} \tag{B.21}$$

As we can notice the number of unknown variables is greater than the number of equations (three against two); therefore we must provide another equation in order to close the system. A possibility is to introduce an algebraic relation linking the area of the vessel and pressure to the wall deformation. For the FFR-Project we have considered the *Generalised string model* [77], which is written in the following form

$$\rho_w h_0 \frac{\partial^2 \eta}{\partial t^2} - \tilde{\gamma}\frac{\partial \eta}{\partial t} - \tilde{a}\frac{\partial^2 \eta}{\partial z^2} - \tilde{c}\frac{\partial^3 \eta}{\partial t \partial z^2} + \tilde{b}\eta = (P - P_{ext}), \qquad z \in (0, L), t > 0 \tag{B.22}$$

We may identify the physical significance of the various terms:

- *Inertia term:* $\rho_w h_0 \dfrac{\partial^2 \eta}{\partial t^2}$, proportional to the wall acceleration
- *Voigt viscoelastic term:* $\tilde{\gamma}\dfrac{\partial \eta}{\partial t}$, viscoelastic term, proportional to the radial displacement velocity
- *Longitudinal pre-stress state of the vessel:* $\tilde{a}\dfrac{\partial^2 \eta}{\partial z^2}$,
- *Viscoelastic term:* $\tilde{c}\dfrac{\partial^3 \eta}{\partial t \partial z^2}$,
- *Elastic term:* $\tilde{b}\eta$.

Besides ρ_w is the vessel density, h_0 is the wall thickness, $\tilde{a}$, $\tilde{b}$ and $\tilde{c}$ are three positive coefficients. We can develop the last term of B.22 being

$$\eta = R - R_0 \qquad \Rightarrow \qquad \eta = \frac{\sqrt{A} - \sqrt{A_0}}{\sqrt{\pi}}, \qquad A_0 = \pi R_0^2$$

Elastic model

The elastic response is the dominating effect, while the other terms are less important. Consequently, a first model is obtained by neglecting all derivatives in B.22. Pressure and area will then be related by the following algebraic law

$$\tilde{b} = \frac{E h_0}{k R_0^2} = \frac{\pi E h_0}{k A_0}, \qquad k = 1 - \nu^2$$

where E is the Young modulus of elasticity and ν represents the Poisson ratio, typically taken to be $\nu = 0.5$ (then $k = 0.75$) since biological tissue is practically incompressible. We have taken $k = 1$.

$$P - P_{ext} = \tilde{b}\eta = \beta \frac{\sqrt{A} - \sqrt{A_0}}{A_0} \tag{B.23}$$

where

$$\beta = E h_0 \sqrt{\pi}$$

is in general a function of z trough the Young modulus E. In a more general setting, the algebraic relationship may be expressed as

$$P = P_{ext} + \psi(A; A_0, \beta) \tag{B.24}$$

where we outlined that the pressure will depend not only on A, but also on A_0 and on a set of coefficients $\beta = \beta_1, \beta_2, \ldots, \beta_n$ which accounts for the physical and mechanical characteristics of the arterial vessel. Both A_0 and β are given functions of z, but they do not vary in time. It is required that ψ be at least a C^1 function of its arguments and be defined for each positive value of A and A_0. In addition we must have, for all the allowable values of A, A_0 and β that

$$\frac{\partial \psi}{\partial A} > 0, \qquad \psi(A_0; A_0, \beta) = 0$$

There are several examples of algebraic pressure-area relationship for one-dimensional models of arterial flow Langewouters$_1$984, $Smith_2$003; $hereweassumedtherelationship B.23, where \beta = \beta_1$ and, for the sake of simplicity, $P_{ext} = 0$. The function ψ can be written as

$$\psi(A; A_0, \beta_1) = \beta_1 \frac{\sqrt{A} - \sqrt{A_0}}{A_0} \tag{B.25}$$

It is useful introduce the Moens-Korteweg velocity

$$c_1(A; A_0, \beta) = \sqrt{\frac{A}{\rho} \frac{\partial \psi}{\partial A}}$$

which represents the propagation speed of waves along the cylindrical vessels. In our case may be readily computes as

$$c_1 = \sqrt{\frac{\beta}{2\rho A_0}} A^{\frac{1}{4}} \tag{B.26}$$

Taking into account B.23 the system B.20 can be written in the conservation form

$$\frac{\partial \mathbf{U}}{\partial t} + \frac{\partial \mathbf{F}(\mathbf{U})}{\partial z} = \mathbf{S}(\mathbf{U}), \quad z \in (0, L), \quad t > 0 \tag{B.27}$$

where

$$\mathbf{U} = \begin{bmatrix} A \\ Q \end{bmatrix} \tag{B.28}$$

are the conservative variables,

$$\mathbf{F}(\mathbf{U}) = \begin{bmatrix} Q \\ \alpha \dfrac{Q^2}{A} + C_1 \end{bmatrix}$$

the corresponding fluxes, and

$$\mathbf{S}(\mathbf{U}) = \begin{bmatrix} 0 \\ -K_R \dfrac{Q}{A} + \dfrac{\partial C_1}{\partial A_0} \dfrac{dA_0}{dz} + \dfrac{\partial C_1}{\partial \beta} \dfrac{d\beta}{dz} \end{bmatrix}$$

a source term of the system. In our modelling, A_0 and β_1 are taken constant along the axial direction z because we assume that both the initial area A_0 and the Young modulus E do not vary in space; so the expression of $\mathbf{S}$ accounts only for the friction term depending on K_R.

C_1 is a primitive of the wave speed c_1, given by

$$C_1(A; A_0, \beta) = \int_{A_0}^{A} c_1^2(\tau; A_0, \beta) d\tau$$

Applying the relationship B.26 and B.4, we obtain

$$c_1 = \sqrt{\frac{\beta_1}{2\rho A_0}} A^{\frac{1}{4}} \quad \Rightarrow \quad C_1 = \frac{\beta_1}{3\rho A_0} A^{\frac{3}{2}} \tag{B.29}$$

B.5 Characteristic analysis

One of the methods for solving non-linear hyperbolic system of partial differential equations, like the one-dimensional elastic model B.27 , is the *characteristic analysis* [76]. After some simple manipulations the system B.27 may be written in the *quasi-linear* form:

$$\frac{\partial \mathbf{U}}{\partial t} + \mathbf{H}(\mathbf{U}) \frac{\partial \mathbf{U}}{\partial z} = \mathbf{B}(\mathbf{U}), \qquad z \in (0, L), t > 0 \tag{B.30}$$

where

$$\mathbf{H}(\mathbf{U}) = \begin{bmatrix} 0 & 1 \\ \frac{A}{\rho}\frac{\partial \psi}{\partial A} - \alpha \bar{u}^2 & 2\alpha \bar{u} \end{bmatrix} = \begin{bmatrix} 0 & 1 \\ c_1^2 - \alpha \left(\frac{Q}{A}\right)^2 & 2\alpha \frac{Q}{A} \end{bmatrix}$$

is the Jacobian matrix. If A_0 and β are constant $\mathbf{B} = -\mathbf{S}$. Considering B.30, we can calculate the eigenvalues for the matrix $\mathbf{H}(\mathbf{U})$

$$\lambda_{1,2} = \alpha \frac{Q}{A} \pm c_\alpha \tag{B.31}$$

where

$$c_\alpha = \sqrt{c_1^2 + \alpha(\alpha - 1)\frac{Q^2}{A^2}}$$

Since the Coriolis coefficient $\alpha \geq 1$ (we considered, for simplicity, $\alpha = 1$), c_α is a real number; besides, under the assumption that $A > 0$, indeed a necessary condition to have physical relevant solution, $c_1 > 0$; therefore we have $c_\alpha > 0$ which means $\mathbf{H}$ has two real distinct eigenvalues and so, by definition, the system B.30 is *strictly hyperbolic*. For typical values of velocity, vessel section and mechanical parameter β_1 encountered in main arteries under physiologically conditions, we find that $\lambda_1 > 0$ and $\lambda_2 < 0$, i.e., the flow is *sub-critical* everywhere. Furthermore, it may be shown [8] that the flow is smooth. Discontinuities, which would normally appear when treating a non -linear hyperbolic system, do not have the time to form on out context because of the pulsatility of the boundary conditions. Afterwards this considerations, from now on we will assume sub-critical regime and smooth solutions.

Let $(\mathbf{l}_1, \mathbf{l}_2)$ and $(\mathbf{r_1}, \mathbf{r_2})$ be two couples of left and right eigenvectors of $\mathbf{H}$. The matrices $\mathbf{R}$, $\mathbf{L}$ and $\mathbf{\Lambda}$ are defined as

$$\mathbf{L} = \begin{bmatrix} \mathbf{l}_1^T \\ \mathbf{l}_2^T \end{bmatrix}, \quad \mathbf{R} = \begin{bmatrix} \mathbf{r}_1 & \mathbf{r}_2 \end{bmatrix}, \quad \mathbf{\Lambda} = \begin{bmatrix} \lambda_1 & 0 \\ 0 & \lambda_2 \end{bmatrix} \tag{B.32}$$

Since left and right eigenvalues are mutually orthogonal, we choose them so that $\mathbf{LR} = \mathbf{I}$, being $\mathbf{I}$ the identity matrix. Matrix $\mathbf{H}$ may then be decomposed as

$$\mathbf{H} = \mathbf{R\Lambda L}$$

and the system B.30 takes the equivalent form

$$\mathbf{L}\frac{\partial \mathbf{U}}{\partial t} + \mathbf{\Lambda L}\frac{\partial \mathbf{U}}{\partial z} + \mathbf{LB}(\mathbf{U}) = 0 \tag{B.33}$$

If there exist two quantities W_1 and W_2 which satisfy

$$\frac{\partial W_1}{\partial \mathbf{U}} = \mathbf{l_1}, \quad \frac{\partial W_2}{\partial \mathbf{U}} = \mathbf{l_2} \tag{B.34}$$

we will call them *characteristic variables* of the hyperbolic system. By setting $\mathbf{W} = [W_1, W_2]^T$ the system B.33 may be elaborated into

$$\frac{\partial \mathbf{W}}{\partial t} + \mathbf{\Lambda}\frac{\partial \mathbf{W}}{\partial z} + \mathbf{G} = 0 \tag{B.35}$$

where

$$\mathbf{G} = \mathbf{LB} - \frac{\partial \mathbf{W}}{\partial A_0}\frac{dA_0}{dz} - \frac{\partial \mathbf{W}}{\partial \beta}\frac{d\beta}{dz}$$

Under the assumption that A_0 and β_1 are constant in space and taking $\mathbf{B}$ negligible, the equation B.35 becomes

$$\frac{\partial \mathbf{W}}{\partial t} + \mathbf{\Lambda}\frac{\partial \mathbf{W}}{\partial z} = 0$$

which is a system of decoupled scalar equation written as

$$\frac{\partial W_i}{\partial t} + \lambda_\mathbf{i}\frac{\partial W_i}{\partial z} = 0 \tag{B.36}$$

From B.36 we have W_1 and W_2 are constant along two *characteristics curves* in the (z,t) plane B3 described by the differential equations

$$\frac{dz}{dt} = \lambda_1 \quad , \quad \frac{dz}{dt} = \lambda_2$$

The expression for the left eigenvectors $\mathbf{l}_1$ and $\mathbf{l}_2$ is given by

$$\mathbf{l}_1 = \xi \begin{bmatrix} c_\alpha - \alpha\bar{u} \\ 1 \end{bmatrix}, \quad \mathbf{l}_2 = \xi \begin{bmatrix} -c_\alpha - \alpha\bar{u} \\ 1 \end{bmatrix}, \tag{B.37}$$

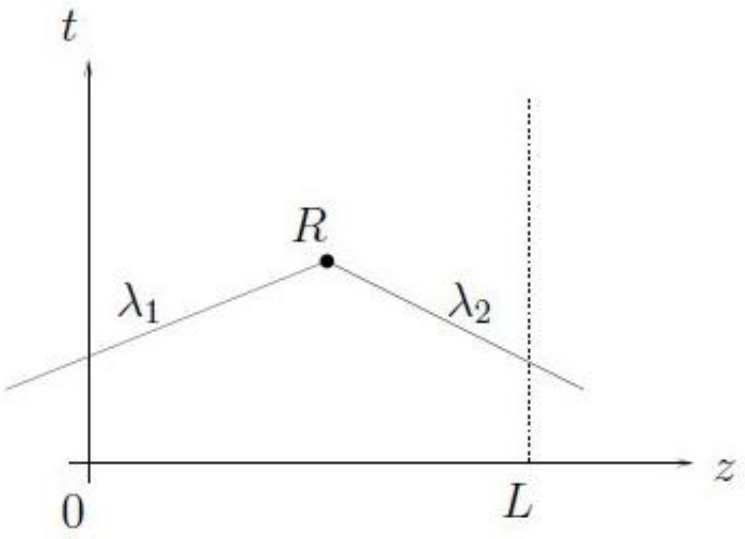

Figure B3: Diagram of characteristics in the (z,t) plane. The solution on the point R is obtained by the superimposition of the two characteristics W_1 and W_2.

where $\xi = \xi(A, \bar{u})$ is any arbitrary smooth function of its arguments with $\xi > 0$. Here we have expressed $\mathbf{l}_1$ and $\mathbf{l}_2$ as functions of $(A, \bar{u})$ instead of (A, Q) in order to simplify the next developments.

For an hyperbolic system of two equations is always possible to find the characteristic variables (or, equivalently, the Riemann invariants) locally, that is in a small neighbourhood of any point **U** [33], yet the existence of global characteristic is not in general guaranteed. However, assuming $\alpha = 1$ the relationship B.37 take the much simpler form

$$\frac{\partial W_1}{\partial A} = \xi c_1, \qquad \frac{\partial W_1}{\partial \bar{u}} = \xi A \tag{B.38}$$

$$\frac{\partial W_2}{\partial A} = -\xi c_1, \qquad \frac{\partial W_2}{\partial \bar{u}} = \xi A \tag{B.39}$$

We now show that a set of global characteristic variables do exist for the problem at hand. Since we note, from B.38, that $W_{1,2}$ are exact differentials being

$$\frac{\partial^2 W_i}{\partial A \partial \bar{u}} = \frac{\partial^2 W_i}{\partial \bar{u} \partial A}$$

for any values of A and $\bar{u}$, we also have that c_1 does not depend on $\bar{u}$ and then, from above relationship we obtain

$$c_1 \frac{\partial \xi}{\partial \bar{u}} = \xi + A \frac{\partial \xi}{\partial A}$$

In order to satisfy this relation we have to choose $g = g(A)$ such that $g = -A \dfrac{\partial g}{\partial A}$. To do this we can take $g = A^{-1}$. As a consequence we can write

$$\partial W_1 = \frac{c_1}{A} \partial A + \partial \bar{u}, \quad \partial W_2 = -\frac{c_1}{A} \partial A + \partial \bar{u} \tag{B.40}$$

Taking $(A_0, 0)$ as a reference state for our variables $(A_0, \bar{u})$ we can integrate the above relationships obtaining

$$W_1 = \bar{u} + \int_{A_0}^{A} \frac{c_1(\epsilon)}{\epsilon} d\epsilon, \qquad W_2 = \bar{u} - \int_{A_0}^{A} \frac{c_1(\epsilon)}{\epsilon} d\epsilon \tag{B.41}$$

Introducing the expression B.4 for c_1 we have

$$W_{1,2} = \frac{Q}{A} \pm 4\left(\sqrt{\frac{\beta_1}{2\rho A_0}} A^{\frac{1}{4}} - c_0\right) \tag{B.42}$$

with c_0 is the wave speed related to the reference state. We finally can write the variables (A, Q) in terms of the characteristic ones,

$$A = \left(\frac{2\rho A_0}{\beta_1}\right)^2 \left(\frac{W_1 - W_2}{8}\right)^4, \qquad Q = A\frac{W_1 + W_2}{2} \tag{B.43}$$

allowing in particular, the implementation of boundary and compatibility conditions, that we will discuss in the next section.

B.6 Boundary conditions

By the characteristic analysis of the one-dimensional model we pointed out the hyperbolic nature of the one-dimensional system of blood flow in arteries; consequently the solution is given by the superimposition of two waves whose eigenvalues $\lambda_{1,2}$ represent the propagation speeds of such waves. As we have seen previously, they always have opposite sign and so blood flow is *subcritical*; under this condition, we need an initial condition along all the spatial domain and two boundary conditions to close the governing system: one at the inlet section $z = 0$ and the other at the outlet $z = L$ (see Figure B4).

Figure B4: Boundary and initial conditions of the hyperbolic system.

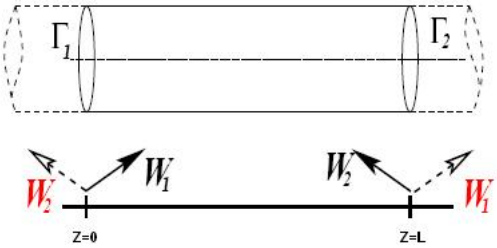

Figure B5: One-dimensional model with absorbing conditions.

Different type of boundary conditions can be imposed. An important class of boundary conditions is represented by the so-called *non-reflecting* or *absorbing* boundary conditions [96], which

allows the simple wave associated with the characteristics to enter or leave the domain without spurious reflections (see Figure B5). Absorbing boundary conditions can be imposed by defining values for the wave entering the domain; in our case we have $\lambda_1 > 0$ and $\lambda_2 < 0$ so W_1 is the entering characteristic in $z = 0$ and W_2 the inlet characteristic in $Z = L$. In Hedstrom [36], non-reflecting boundary conditions for an hyperbolic problem are written as

$$\mathbf{l}_1 \cdot \left[\frac{\partial \mathbf{U}}{\partial t} - \mathbf{B}(\mathbf{U})\right]_{x=0} = 0, \quad \mathbf{l}_2 \cdot \left[\frac{\partial \mathbf{U}}{\partial t} - \mathbf{B}(\mathbf{U})\right]_{x=L} = 0$$

When there is an explicit formulation of the characteristic variables, it is possible impose the boundary conditions directly in terms of incoming characteristics, for example

$$W_1(t) = g_1(t), \qquad \text{in} \quad z = 0, t > 0$$

being $g_1(t)$ a given function. However, the problem rarely have boundary data in terms of variable characteristics, they are normally expressed in terms of physical variables.

In addition to absorbing boundary conditions based on characteristic variables, it may impose a function that describes the temporal trend on the edge of one of the unknown functions of the problem, then the flux flow Q (or the speed u) or the area A. Conditions of this type are typically used on the proximal node $z = 0$ and can be expressed as follows:

$$Q(0,t) = g_q(t), \quad t > 0$$
$$A(0,t) = g_a(t), \quad t > 0$$

The boundary conditions imposed by the knowledge of the physical variables are *reflective*. Therefore, if we impose such a condition in the proximal node, the incoming characteristic variable, that we denoted by W_2, will be partially reflected in the computational domain. This is a real physical phenomenon.

The *initial conditions* are the conditions to be imposed by defining the value of $A(z,t)$ and $Q(z,t)$ along the spatial domain $z \in (0, L)$ at the initial time $t = 0$. For instance if we require the area at the initial time, the initial condition is expressed as

$$A(z,t) = A_0(z), \quad z \in (0, L)$$

B.6.1 Terminals lumped parameter

The assumptions made for the 1-D model become less appropriate with decreasing the size of the arteries; for example, the blood flow in the larger arteries is pulsatile and is dominated by inertia while in the capillaries is almost stable and dominant by the viscosity. Consequently, the 1-D model should be limited until at the distal section of the domain ($z = L$). We have seen a first approach which imposes not reflective boundary conditions in the vessels terminals B.6, but this solution is not adherent to reality. We then introduce the lumped parameter models (0-D) who consider the fact that the pressure waves are physically in part reflected and partly absorbed. These models coupled with the one-dimensional constitutive equation B.27 leads to a

multiscale framework 1-D/0-D. Therefore, the hemodynamic effects of the blood vessels after the distal section limit are generally simulated using a lumped parameter model governed by ordinary differential equations that relate the pressure with the flow at the outlet of the 1-D model [61].

Expressing the system B.30 in terms of (A, P, Q) with $Q = A\bar{u}$ and linearising around the state of reference $(A_0, 0, 0)$, with β an A_0 be constant along z, is obtained.

$$\begin{cases} C_{1D}\dfrac{\partial p}{\partial t} + \dfrac{\partial q}{\partial z} = 0 \\ L_{1D}\dfrac{\partial q}{\partial t_a} + \dfrac{\partial p}{\partial z} = -R_{1D}q \\ p = \dfrac{a}{C_{1D}} \end{cases} \tag{B.44}$$

where a,p and q are the perturbation variables for area, pressure and volume flux, respectively $(A_0 + a, p, q)$ and

$$R_{1D} = \frac{\rho c_0}{A_0}, \qquad C_{1D} = \frac{A_0}{\rho c_0^2}, \qquad L_{1D} = \frac{\rho}{A_0} \tag{B.45}$$

are the viscous resistance to flow, wall compliance and blood inertia, respectively, per unit of length of vessel l. Integrating system B.44 over the length l yields the lumped parameter model, where the variables are $R_{0D} = R_{1D}l$, $C_{0D} = C_{1D}l$, $L_{0D} = L_{1D}l$ and $\hat{p} = \frac{1}{l}\int_0^l p dz$, $\hat{q} = \frac{1}{l}\int_0^l q dz$ are the mean pressure and flow over the whole domain. In physiological conditions pulsatile waves travel at a speed greater compared to that of the blood, then $\hat{p} = p_{in}$ and $\hat{q} = q_{out}$. Therefore, the final 0-D model is the following:

$$\begin{cases} C_{0D}\dfrac{\partial p_{in}}{\partial t} + q_{out} - q_{in} = 0 \\ L_{0D}\dfrac{\partial q_{out}}{\partial t} + R_{0D}q_{out} + p_{out} - p_{in} = 0 \end{cases} \tag{B.46}$$

where $q_{in} = q(0, t)$, $q_{out} = q(L, t)$, $p_{in} = p(0, t)$ and $p_{out} = p(L, t)$ are the flows and pressures at the inlet and outlet of the 0-D domain. As it is represented in Figure B6 ,the system B.46 is analogous to an electric circuit, in which the role of the flow and pressure are played by the current and potential, R_{0D} corresponds to an electric resistance, C_{0D} to a capacitance and L_{0D} to an inductance.

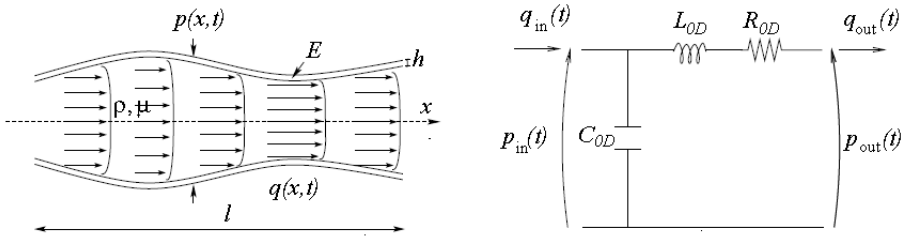

Figure B6: 1-D arterial vessel domain (left) and the equivalent 0-D system discretises at first order in space (right).

Hydraulic	Physiological variables	Electric
Pressure $P[Pa]$	Blood pressure $[mmHg]$	Voltage V
Flow rate $Q[m^3/s]$	Blood flow rate $[L/s]$	Current I
Volume $V[m^3]$	Blood volume $[L]$	Charge $q[C]$
Viscosity η	Blood viscosity $\mu[Pa \cdot s]$	Electrical resistance R
Elastic coefficient	Vessel's wall compliance	Capacitance C
Inertance	Blood inertia	Inductance L

Table B1: Analogy between hydraulic and electrical network [46].

B.7 Implementation

The nonlinear hyperbolic system B.27 has been discretized using a Taylor-Galerkin scheme [24], which is the finite element equivalent of Lax-Wendroff (based on the expansion in Taylor series) stabilisation for the finite difference method. This method may result in short computational times, and is second order accurate in both time and space.

Considering the equation B.27 and having $\mathbf{H} = \dfrac{\partial \mathbf{F}}{\partial \mathbf{U}}$ we may write

$$\begin{aligned} \frac{\partial \mathbf{U}}{\partial t} &= \mathbf{S} - \frac{\partial \mathbf{F}}{\partial z} \\ \frac{\partial^2 \mathbf{U}}{\partial t^2} &= \frac{\partial \mathbf{S}}{\partial \mathbf{U}} \frac{\partial \mathbf{U}}{\partial t} - \frac{\partial}{\partial z}\left(\mathbf{H}\frac{\partial \mathbf{U}}{\partial t}\right) \\ &= \frac{\partial \mathbf{S}}{\partial \mathbf{U}}\left(\mathbf{S} - \frac{\partial \mathbf{F}}{\partial z}\right) - \frac{\partial \mathbf{H}\mathbf{B}}{\partial z} + \frac{\partial}{\partial z}\left(\mathbf{H}\frac{\partial \mathbf{F}}{\partial z}\right) \end{aligned} \tag{B.47}$$

For simplicity the dependence of $\mathbf{S}$ and $\mathbf{F}$ from $\mathbf{U}$ is dropped. Starting from the above equations, we now consider the time intervals (t^n, t^{n+1}), for $n = 0, 1, \ldots, T$; then we discretize the equation in time using a Taylor series which includes first and second order derivatives if $\mathbf{U}$. Therefore we obtain the following *semi-discrete* schemes for the approximation $\mathbf{U}^{n+1}$ of $\mathbf{U}(t^{n+1})$:

- **Taylor-Galerkin scheme:**

$$\mathbf{u}^{n+1} = \mathbf{u}^n + \Delta t \mathbf{u}_t^n + \frac{\Delta t^2}{2}\mathbf{u}_{tt}^n \tag{B.48}$$

$$\begin{aligned} \mathbf{U}^{n+1} =& \mathbf{U}^n - \Delta t \frac{\partial}{\partial z}\left(\mathbf{F}^n + \frac{\Delta t}{2}\mathbf{H}^n\mathbf{S}^n\right) + \frac{\Delta t^2}{2}\left[\mathbf{S}_{\mathbf{U}}^n \frac{\partial \mathbf{F}^n}{\partial z} - \frac{\partial}{\partial z}\left(\mathbf{H}^n \frac{\partial \mathbf{F}^n}{\partial z}\right)\right] \\ &+ \Delta t\left(\mathbf{S}^n + \frac{\Delta t}{2}\mathbf{S}_{\mathbf{U}}^n\mathbf{S}^n\right), \qquad n = 0, 1, \ldots \end{aligned} \tag{B.49}$$

where $\mathbf{S}^n_{\mathbf{U}} = \dfrac{\partial \mathbf{S}^n}{\partial \mathbf{U}}$ and $\mathbf{F}^n$, stands for $\mathbf{F}(\mathbf{U^n})$, just as $\mathbf{H}^n$, $\mathbf{S}^n$ and $\mathbf{S}^n_{\mathbf{U}}$; the value $\mathbf{U}^0$ is given by the initial conditions.

For each time interval (t^n, t^{n+1}) we apply a spatial discretization carried out using the Galerkin finite element method. To this purpose we subdivide the domain $\Omega = \{z : z \in (0, L)\}$, which is the 1-D counterpart of the 3-D domain Ω_t, into a finite number N_{el} of linear elements length l (Figure B7).

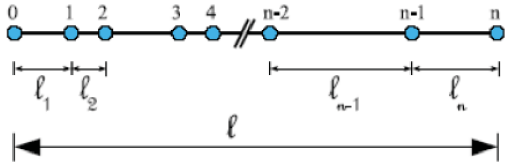

Figure B7: One-dimensional mesh representing a vessel.

Moreover we introduce a trial function space, $\mathcal{T}$, and a weighting function space, $\mathcal{W}$. These spaces are both defined to consist of all suitably smooth functions and to be such that

$$\mathcal{T} = \Big\{\mathbf{U}(z,t) | \mathbf{U}(z,0) = \mathbf{U}^0(z) \text{ on } \Omega_t \quad \text{at} \quad t = t^0\Big\}, \qquad \mathcal{W} = \Big\{\mathcal{W}(\mathbf{z})\Big\}$$

Considering the scheme, we multiply the equation B.49 for the weight function $\mathbf{W}$ and we integrate it over the domain Ω_t obtaining, for $\forall t > 0 t^0$

$$\begin{aligned}\int_\Omega \Big(\mathbf{U}^{n+1} - \mathbf{U}^n\Big) d\Omega = &- \Delta t \left[\int_\Omega \frac{\partial \mathbf{W}}{\partial z} \mathbf{F}^n_{LW} d\Omega - \int_\Omega \mathbf{S}^n_{LW} \mathbf{W} d\Omega\right] - \\ &- \frac{\Delta t^2}{2}\left[\int_\Omega \frac{\partial \mathbf{W}}{\partial z} {\mathbf{S}_{\mathbf{U}}}^n \mathbf{F}^n - \int_\Omega \frac{\partial \mathbf{W}}{\partial z}\frac{\partial \mathbf{F}^n}{\partial z}\mathbf{H}^n\right] - \\ &- \Delta t \left[N_i \bar{\mathbf{F}}^n_r|_{z=L} - N_i \bar{\mathbf{F}}^n_l|_{z=0}\right]\end{aligned} \tag{B.50}$$

where we have assumed

$$\mathbf{F}^n_{LW}(\mathbf{U}_j) = \mathbf{F}^n + \frac{\Delta t}{2}\mathbf{H}^n \mathbf{S}^n$$

and

$$\mathbf{S}^n_{LW}(\mathbf{U}_j) = \mathbf{S}^n + \frac{\Delta t}{2}{\mathbf{S}_{\mathbf{U}}}^n \mathbf{S}^n$$

Starting from the weak form of the problem B.50 we build the subspaces $\mathcal{T}^h$ and $\mathcal{W}^h$ for the

trial and weighting function spaces $\mathcal{T}$ and $\mathcal{W}$ defining them as

$$\begin{aligned}\mathcal{T}^h &= \left\{ \hat{\mathbf{U}}(z,t) | \hat{\mathbf{U}}(z,t) = \sum_{j=1}^{N} \mathbf{U}_j(t) N_j(z); \quad \mathbf{U}(t^0) = \bar{\mathbf{U}}(z_j) = \mathbf{U}_j^0 \right\} \\ \mathcal{W}^h &= \left\{ \mathcal{W}(z,t) | \mathcal{W}(z) = \sum_{j=1}^{N} W_j(t) N_j(z) \right\}\end{aligned} \tag{B.51}$$

where N_j is the standard linear finite element shape function (Figure B8) associated to the $j-th$ node, located at $z = z_j$, and $\mathbf{U}_j$ and $\hat{\mathbf{U}}$ at the node j. Since we are using the Galerkin method, the base shape functions defined above are used as weighting. Adopting the following notation

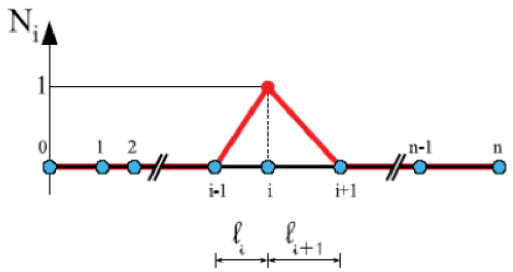

Figure B8: Sketch of a 1D linear shape function.

$$(W,U)_{\Omega_e} = \int_{\Omega_e} W \cdot U d\Omega,$$

and considering the sum of each element contribution

$$\int_{\Omega} \cdots = \sum_{el} \int_{\Omega_e} \cdots,$$

the equation B.50 becomes

$$\begin{aligned}\sum_{el} (N_i, N_j)_{\Omega_e} (\mathbf{U}_j^{n+1} - \mathbf{U}_j^n) = \Delta t \sum_{el} [(N_{i,z}, N_j)_{\Omega_e} \mathbf{F}_{LW}^n(\mathbf{U}_j) + N_i, N_j)_{\Omega_e} \mathbf{S}_{LW}^n(\mathbf{U}_j)] - \\ - \frac{\Delta t^2}{2} \sum_{el} \left((N_i, N_j)_{\Omega_e} \mathbf{S_U}^n(\mathbf{U}_j) \frac{\partial \mathbf{F}_j^n}{\partial z} \right) - \\ - \frac{\Delta t^2}{2} \sum_{el} \left((N_{i,z}, N_j)_{\Omega_e} \mathbf{H}_j^n(\mathbf{U}_j) \frac{\partial \mathbf{F}_j^n}{\partial z} \right) - \\ - \Delta t \left[N_i \bar{\mathbf{F}}_r^n|_{z=L} - N_i \bar{\mathbf{F}}_l^n|_{z=0} \right]\end{aligned} \tag{B.52}$$

For what concerns the border nodes, we have to consider the boundaries condition. Starting from the equation B.52, we have the term of boundary conditions represented by

$$\Delta t \left[N_i \bar{\mathbf{F}}_r^n|_{z=L} - N_i \bar{\mathbf{F}}_l^n|_{z=0} \right], \qquad i = 1, 2$$

which implies the knowledge of the flux terms depending from the values of A and Q at inlet and outlet sections of the domain. To extract them from the characteristic information $W_1(0,t)$ and $W_2(L,t)$ we need an additional expression for the other characteristic variables $W_2(0,t)$ and $W_1(L,t)$ to recover $\mathbf{U}(A,Q)$ using the equation B.43. To this purpose we adopted a technique based on the extrapolation of the outgoing characteristics. Having the friction parameter K_r small with respect to the other equation terms in B.27, we assume that at the boundary points $z = 0$ and $z = L$ the flow is generated by the characteristic system B.36. At a generic time step n we have $\mathbf{U}^n$ known and we linearise the eigenvalues $\lambda_{1,2}$ of B.27 by taking their values at respective boundary for $t = t^n$. The solution corresponding to this linearised problem at time t^{n+1} gives

$$W_2^{n+1}(0) = W_2^n(-\lambda_2^n(0)\Delta t)$$
$$W_1^{n+1}(L) = W_1^n(-\lambda_1^n(L)\Delta t)$$

which is a first-order approximation of the outgoing characteristic variables from the previous step. By using these information together with the values of $W_1^{n+1}(0)$ and $W_2^{n+1}(L)$, we are able to compute, through B.43, the required boundary data.

We choose to use, for time integration, both a second and fourth order explicit Runge-Kutta scheme; such methods are diffused in computational fluid dynamics, and show good properties, e.g ease of programming, simple treatment of boundary conditions and good stability. Regarding the stability, the second order Taylor-Galerkin scheme entails a time step limitations. A linear stability analysis [75] indicates that the following Courant-Friedrichs-Lewy condition should be satisfied

$$\Delta t \leq \frac{\sqrt{3}}{3} \min_{0 \leq i \leq N} \left[\frac{h_i}{\max(\lambda_{1,i}, \lambda_{1,i+1})} \right] \tag{B.53}$$

where $\lambda_{1,i}$ here indicates the value of λ_1 at mesh node z_i. This condition, which is necessary to obtain the stability of a method explicitly imposes a constraint on the choice of the discretization time and space of the method used; it corresponds to a CFL number of $\frac{\sqrt{3}}{3}$.

B.7.1 Branching

The vascular system is characterized by the presence of branching. The flow in a bifurcation is intrinsically 3-D, however may be still described by means of a 1-D model. In order to manage a branching zone, when using a 1-D formulation, we follow a technique called *domain decomposition* [78]. The numerical solver accounts for the treatment of two types of bifurcation: the bifurcation 2-1 typical of the arterial system and the bifurcation 1-1 which represents two vessel linked together with different mechanical properties.

Bifurcation 1-2 The bifurcation 1-2 represents the typical branching of the arterial system. As we have introduced we have used the domain decomposition method to solve this problem. We divide the domain Ω into three partitions Ω_1,Ω_2 and Ω_3 as is showed at Figure B9; doing this we have 3 sub-problems which must be coupled imposing adequate boundary conditions. Then we have to evaluate 6 variables, (A_i, Q_i) with $i = 1, 2, 3$, corresponding to the problem unknowns, area and flow rate for each one of the vessels composing the branching. From the decomposition

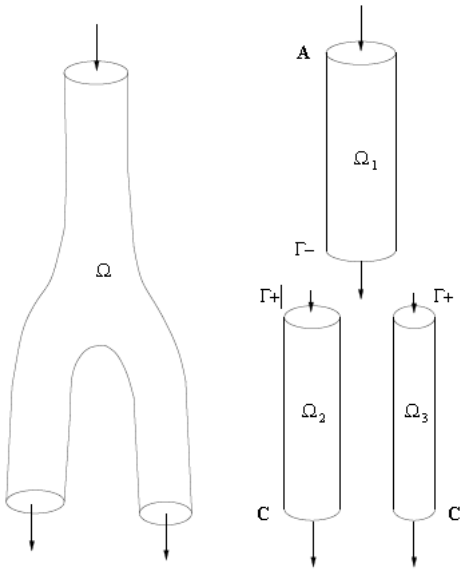

Figure B9: Domain decomposition of a bifurcation 1-2.

of the governing system into characteristic variables we know that the system can be interpreted in terms of a forward and backward travelling waves. Considering the model of a splitting bifurcation shown in Figure B9, we denote the parent vessel by an index 1 and its two daughter vessels by the indices 2 and 3, respectively.

The simplest condition we can impose to require the mass conservation through the bifurcation and therefore the flow rate balance can be written

$$Q_1 = Q_2 + Q_3$$

remembering that the flow moves from the sub-domain Ω_1 to the sub-domain Ω_2 and Ω_3. Other two assumptions can be obtained from the requirement of continuity of the momentum flux at the bifurcation. This lead to consider the *total pressure* term continuous at the boundary. So we may write

$$P_1 + \frac{1}{2}\rho\left(\frac{Q_1}{A_1}\right)^2 = P_2 + \frac{1}{2}\rho\left(\frac{Q_2}{A_2}\right)^2$$

$$P_1 + \frac{1}{2}\rho\left(\frac{Q_1}{A_1}\right)^2 = P_3 + \frac{1}{2}\rho\left(\frac{Q_3}{A_3}\right)^2$$

The remaining three relationship can be derived using the characteristic variables. The parent vessel can only reach the junction by a forward travelling wave. This wave is denoted as W_1^1, where the superscript is the vessel number while the subscript stands for the forward direction. Similarly, the characteristics variables of daughter vessels, which can reach the bifurcation only by backwards travelling wave, are represent by W_2^2 and W_2^3.

$$W_1^1 = \frac{Q_1}{A_1} + 4\sqrt{\frac{\beta_1}{2\rho A_{01}}}A_1^{1/4} = u_1 + 4(c_1 - c_0^1)$$
$$W_2^1 = \frac{Q_2}{A_2} - 4\sqrt{\frac{\beta_2}{2\rho A_{02}}}A_2^{1/4} = u_2 + 4(c_2 - c_0^2)$$
$$W_2^2 = \frac{Q_3}{A_3} - 4\sqrt{\frac{\beta_3}{2\rho A_{03}}}A_3^{1/4} = u_3 + 4(c_3 - c_0^3)$$

where c_0^1,$c_0^2$and c_0^3 are the values of the wave speed evaluated using the area A_0 in the vessels 1,2 and 3. In summary, the resulting system which determines the values (A_1, Q_1),(A_2, Q_2) and (A_3, Q_3) at the bifurcation is the following

$$\begin{cases} W_1^1 = \dfrac{Q_1}{A_1} + 4\sqrt{\dfrac{\beta_1}{2\rho A_{01}}}A_1^{1/4} \\ W_2^1 = \dfrac{Q_2}{A_2} - 4\sqrt{\dfrac{\beta_2}{2\rho A_{02}}}A_2^{1/4} \\ W_2^2 = \dfrac{Q_3}{A_3} - 4\sqrt{\dfrac{\beta_3}{2\rho A_{03}}}A_3^{1/4} \\ Q_1 = Q_2 + Q_3 \\ P_1 + \dfrac{1}{2}\rho\left(\dfrac{Q_1}{A_1}\right)^2 = P_2 + \dfrac{1}{2}\rho\left(\dfrac{Q_2}{A_2}\right)^2 \\ P_1 + \dfrac{1}{2}\rho\left(\dfrac{Q_1}{A_1}\right)^2 = P_3 + \dfrac{1}{2}\rho\left(\dfrac{Q_3}{A_3}\right)^2 \end{cases} \tag{B.54}$$

We can solve it through the Newton-Raphson technique for differential systems of non-linear equations.This type of modelling does not consider the geometry of the junctions. For instance, the angle between the various vessels are not take into account.

Bifurcation 1-1 The discontinuity at the interface between arteries with different materials(mechanical behaviour) or geometrical properties is solved with a similar process used in the treatment of the bifurcations 2-1. Following the domain decomposition method adopted before, we proceed by splitting the problem in two sub-domains Ω_1 and Ω_2, and solving the following non-linear system

for the interface variables, namely

$$\begin{cases} W_1 = \dfrac{Q_1}{A_1} + 4\sqrt{\dfrac{\beta_1}{2\rho A_{01}}} A_1^{1/4} \\ W_2 = \dfrac{Q_2}{A_2} - 4\sqrt{\dfrac{\beta_2}{2\rho A_{02}}} A_2^{1/4} \\ Q_1 = Q_2 \\ P_1 + \dfrac{1}{2}\rho\left(\dfrac{Q_1}{A_1}\right)^2 = P_2 + \dfrac{1}{2}\rho\left(\dfrac{Q_2}{A_2}\right)^2 \end{cases} \tag{B.55}$$

Again, We solve the non-linear system obtained through the Newton-Raphson method. In both systems B.54 and B.55, it has been verified that the determinant of the Jacobian is different from zero for all allowable values of the parameters, thus guaranteeing that the Newton iteration is well-posed [28].

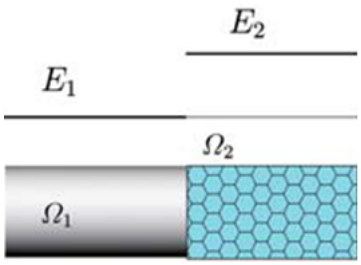

Figure B10: Domain decomposition of a bifurcation 1-1.

B.7.2 Coupling 1-D and 3D-reduced model

In order to consider into the 1D model an external pressure drop, we need to modify the total pressure term (B.55) adding the function $f^{3D}(k_1,k_2)$:

$$P_i + \frac{1}{2}\rho\frac{{Q_i}^2}{{A_i}^2} = P_j + \frac{1}{2}\rho\frac{{Q_j}^2}{{A_j}^2} + {f^{3D}}_j(k_1, k_2) \tag{B.56}$$

where indexes *i* and *j* denote the parent and the daughter vessels respectively and the function $f^{3D}(k_1,k_2)$ denotes the external pressure drop (or energy losses). In our case f^{3D} is the pressure drop of the 3D model.

$${f^{3D}}_j(k_1, k_2) = k_1 Q_j + k_2 \mid Q_j \mid Q_j \tag{B.57}$$

k_1 and k_2 are the viscous and turbulent coefficients that should be adjusted according to the pressure drop between the inlet/outlet planes defined in the 3D model.

B.7.2.1 Personalized 3D reduced order model In our particular case, firstly we need to solve the 3D problem (real case). To estimate the coefficients k1 and k2 of the equation (B.57), at each time step t_n, we calculate and store the mean values of the flow and the pressure at the inlet and the outlet of our 3D domain. Using these values we choose k_1 and k_2 that minimizes the sum of squared pressure drop by least squares method. In this way we are able to capture the energy losses provoked by the geometry of our 3D model, and take into account in the 1D model.

B.8 Coupling 1-D and 0-D models

The existence and uniqueness of the solution of a coupled problem between the 0-D model system B.46 and the hyperbolic 1-D system B.35, has been proven by Formaggia [27] for a sufficiently small time so that the characteristic curve leaving the 1-D/0-D interface does not intersect with incoming characteristic curves. Numerically, the coupling problem between a 1-D domain and a 0-D model is established through the solution of a Riemann problem at the interface (Figure B11). An intermediate state (A^*, U^*) originates at time $t + \Delta t$ from the states (A_L, U_L) and (A_R, U_R) at time t. The state (A_L, U_L) corresponds to the end point of the 1-D domain, and (A_R, U_R) is a virtual state selected so that (A^*, U^*) satisfies the relation between A^* and U^* dictated by system B.46. The 1-D and 0-D variables at the interface are related through $q_{in} = A^*U^*$ and $p_{in} = \frac{\beta}{A_0}(\sqrt{A^*} - \sqrt{A_0})$, and p_{out} is prescribed as a constant parameter that represents the pressure at which flow to the venous system ceases.

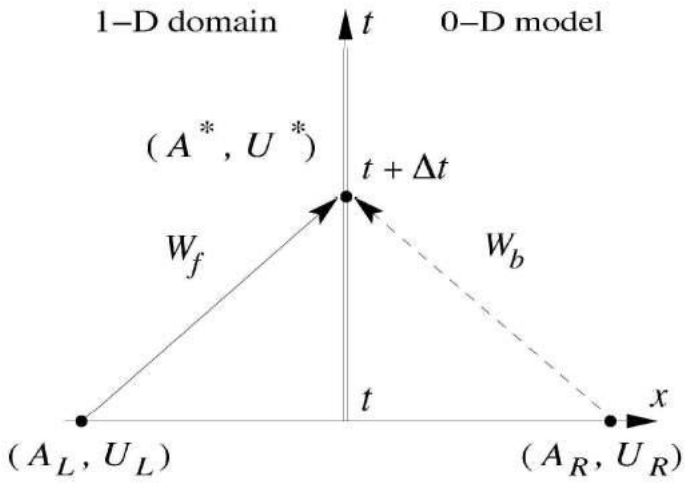

Figure B11: Coupling 1-D/0-D model.

According to the method of characteristics, if $G = 0$ equation B.35 leads to

$$W_1(A^*, U^*) = W_1(A_L, U_L) \tag{B.58}$$

$$W_2(A^*, U^*) = W_2(A_R, U_R) \tag{B.59}$$

Solving B.58 for A^* and U^* yields

$$A^* = \left[\sqrt{\frac{2\rho A_0}{\beta}}\frac{W_1(A_L,U_L) - W_2(A_R,U_R)}{8} + A_0^{\frac{1}{4}}\right]^4 \tag{B.60}$$

$$U^* = \frac{W_1(A_L,U_L) + W_2(A_R,U_R)}{2} \tag{B.61}$$

The 1-D outflow boundary condition is imposed by enforcing that either $U_R = U_L$, which reduces Eq. B.60 to

$$A_R = \left[2(A^*)^{\frac{1}{4}} - (A_L)^{\frac{1}{4}}\right]^4 \tag{B.62}$$

or $A_R = A_L$, which reduces Eq. B.61 to

$$U_R = 2U^* - U_L \tag{B.63}$$

B.8.1 Terminal resistance (R) model

This model simulates the peripheral circulation as a purely resistive load Rp, (R_{0D}=Rp, L_{0D}=0, C_{0D}= 0) (Figure B6) and in which the state (A^*, U^*) satisfies

$$A^*U^* = \frac{P(A^*) - p_{out}}{R_p} \tag{B.64}$$

Combining with B.46 we leads to a non-linear equation

$$\mathcal{F}(A^*) = R_p\left[\left[U_L + 4c(A_L)\right]A^* - 4c(A^*)A^*\right] - \frac{\beta}{A_0}\left(\sqrt{A^*} - \sqrt{A_0}\right) + p_{out} = 0 \tag{B.65}$$

which is solved using Newton-Raphson method, with the initial value of $A^* = A_L$. Once A^* has been obtained, U^* is calculated from Eq. B.61. If we consider both C and L equal to zero, we lead to the single terminal resistance model.

B.9 Validation

A validation against in-vivo data is very difficult because some of the geometrical and elastic properties of the biological system are very complicated to measure. This is the reason because experimental replicas of the cardiovascular system to assess numerical tool are commonly used. To validate the 1D formulation implemented, the experimental model developed by Matthys et al. has been used [61] (1:1 silicone human arterial network). The silicone network is connected proximal to a pulsatile pump providing for a periodic input flow with the following settings: 70 bpm and a stroke volume of 70 ml, creating a mean pressure of approximately 100 $mmHg$ at the aortic root, these are typical values of a normal healthy person. Outflow boundary conditions were set of terminal resistance tubes connected to overflow reservoirs, creating a closed loop hydraulic system

which induces a back pressure of 3.2 $mmHg$. A $65-35\%$ water$-$glycerol mixture, with density ρ = 1050 $kg \cdot m^3$ and viscosity μ =5 $mPa \cdot s$, was used to simulate the blood. The elastic wall properties of the silicone sample have a constant Young's modulus of 1.2 MPa. The properties of the silicone network are summarize in table B2, as we can see the measurement report an interval of confidence, which unfortunately will affect the comparison between the experimental data and our results. For the simulations we have used the mean values show in the table[61].

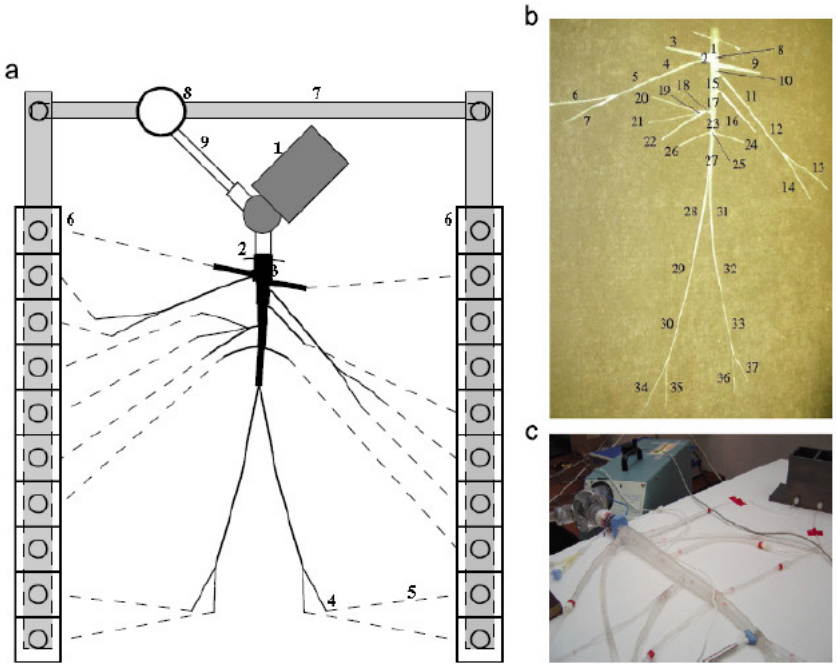

Figure B12: a) Plan view schematic of the hydraulic model. 1: Pump (left heart); 2: catheter access; 3: aortic valve; 4: peripheral resistance tube; 5: stiff plastic tubing (veins); 6: venous overflow; 7: venous return conduit; 8: buffering reservoir; 9: pulmonary veins. (b) Topology and references labels of the arteries simulated, whose properties are given in table B2. (c) Detail of the pump and the aorta [61].

Although the experimental set-up is only an approximation to the human systemic circulation, it is able to reproduce pulse waveforms with significant physiological features in the aortic vessels. Figure B13 shows some of the main physiological features of pulse pressure, velocity and flow rate described previously. We observe that the numerical solver is able to describe the peaking and steepening pulse pressure as we move away from the heart, and a reduction in amplitude of the flow with the distance from the heart.

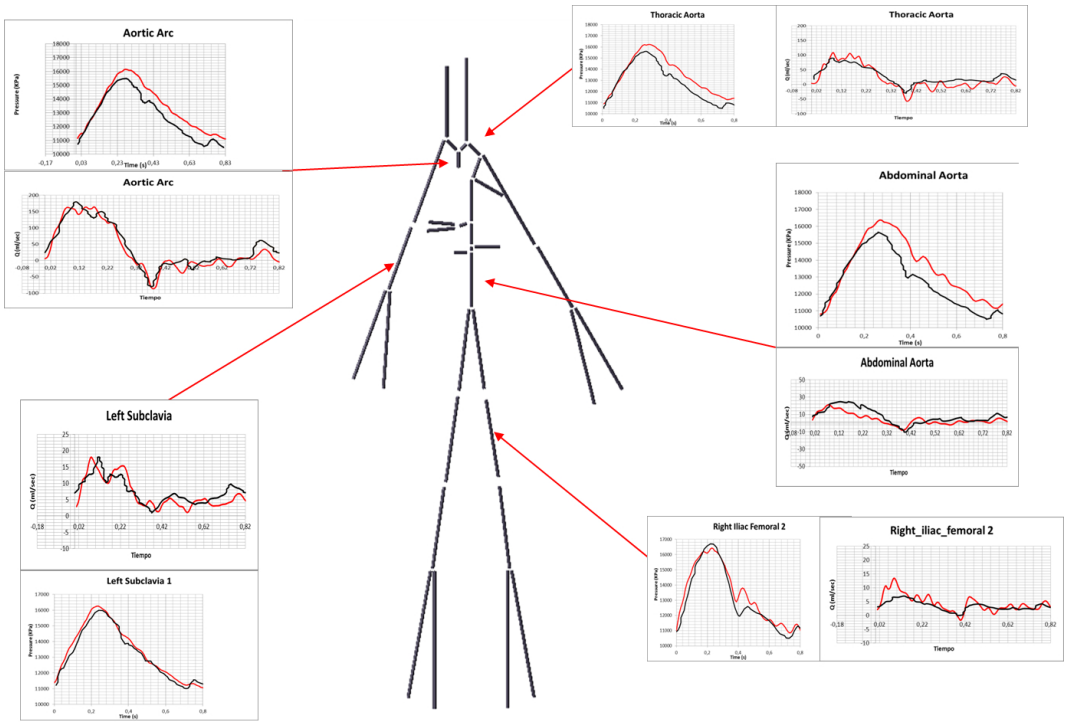

Figure B13: Simulated physiological(blank line) versus numerical results(red line) features of pressure and flow rate in difference section of the cardiovascular system.

n	Arterial segment	l [cm] $\pm$ 2.0%	r [cm] $\pm$ 3.5%	h [mm] $\pm$ 2.5%	c[ms^{-1}]	$R_p[GPa \cdot s \cdot m^{-3}]$
1.	Ascending Aorta	3.6	1.440	0.51	5.21	-
2.	Innonimate	2.8	1.100	0.35	4.89	-
3.	R. Carotid	14.5	0.537	0.28	6.35	2.67
4.	R. Subclavian I	21.8	0.436	0.27	6.87	-
5.	R. Subclavian II	16.5	0.334	0.16	6.00	-
6.	R. radial	23.5	0.207	0.15	6.78	3.92
7.	R. ulnar	17.7	0.210	0.21	8.81	3.24
8.	Aortic arch I	2.1	1.300	0.50	5.41	-
9.	L. Carotid	17.8	0.558	0.31	6.55	3.11
10.	Aortic arch II	2.9	1.250	0.41	4.98	-
11.	L. Subclavian I	22.7	0.442	0.22	6.21	-
12.	L. Subclavian II	17.5	0.339	0.17	6.26	-
13.	L. radial	24.5	0.207	0.21	8.84	3.74
14.	L. ulnar	1.91	0.207	0.16	7.77	3.77
15.	Thoracic Aorta I	5.6	1.180	0.43	5.29	-
16.	Intercostals	19.5	0.412	0.27	7.07	2.59
17.	Thoracic Aorta II	7.2	1.100	0.34	4.84	-
18.	Celiac I	3.8	0.397	0.20	6.20	-
19.	Celiac II	1.3	0.431	1.25	14.9	-
20.	Splenic	19.1	0.183	0.13	7.24	3.54
21.	Gastric	19.8	0.192	0.11	6.73	4.24
22.	Hepatic	18.6	0.331	0.21	6.95	3.75
23.	Abdominal Aorta I	6.2	0.926	0.33	5.19	-
24.	L. renal	12.0	0.259	0.19	7.39	3.46
25.	Abdominal Aorta II	7.0	0.790	0.35	5.83	-
26.	R. renal	11.8	0.255	0.16	6.95	3.45
27.	Abdominal Aorta III	10.4	0.780	0.30	5.41	-
28.	R. iliac-femoral I	20.5	0.390	0.21	6.47	-
29.	R. iliac-femoral II	21.6	0.338	0.15	5.89	-
30.	R. iliac-femoral III	20.6	0.231	0.20	8.04	-
31.	L. iliac-femoral I	20.1	0.402	0.20	6.19	-
32.	L. iliac-femoral II	19.5	0.334	0.16	6.11	-
33.	L. iliac-femoral III	20.7	0.226	0.13	6.67	-
34.	R. anterior tibial	16.3	0.155	0.15	8.47	5.16
35.	R. posterior tibial	15.1	0.153	0.12	7.73	5.65
36.	L. posterior tibial	14.9	0.158	0.11	7.23	4.59
37.	L. anterior tibial	12.6	0.156	0.10	7.01	3.16

Table B2: Properties of the 37 silicon vessels used in the in-vitro model [61]. The interval of confidence of the geometrical measurements is indicated in the heading.

Appendix C

Python Script

C1 Phyton Script

```
# ------------------------------------------------------------------------------
# SHEAR FORCE SECTION
# ------------------------------------------------------------------------------
# Ok. For this routine, Shear Stress components is NOT GIVEN, and therefore
# calculated with the velocity gradient, fluid dynamic viscosity, and fluid
# shear routine therefore, we will have to do some pre-operations.
#
# version 2 calculated an intermediate variable from velocity components to pass
#           into Grad calc function
# version 3 includes variables for viscosity, part nums, and velocity
# ------------------------------------------------------------------------------
# NOTE:
#   Using Solution (FAQ) "Fluid Forces, Drag Calculations in EnSight" (#3),
#   under "II. Shear Forces" steps a-i we have:
#
################################################
#Procedure:
# a. in  the fluid  domain surrounding  the surface, define vx,  vy, vx, the
#  velocity components, as three new scalars
# b. using the Grad operator in the variable calculator, compute the gradient of
#  each of  these components  in the  fluid, resulting  in new  gradient vectors
#  of these components, i.e. grad_vx, grad_vy, grad_vz
# c. these gradients must be mapped from the fluid onto the surface. This is
#  done either by using the Case Map feature in EnSight, or creating an
#  isosurface (velocity = 0.) or a clip plane that corresponds to the surface
#  of interest.
# d. Compute the fluid shear stress components using the FluidShear function
#  in the variable calculator and the mapped velocity gradients.
#  A value  for the fluid's  dynamic viscosity must  be provided. This may
#  also be a scalar variable.
# e. Create a fluid shear stress vector from these components using the MakeVect
```

```
#  function in the variable calculator.
# f. We need the tangential component of the fluid shear stress vector in
#  order to integrate the shear stress forces and moments.
#  The tangential  component may be  displayed by projecting  this from the
#  Feature Detail Editor (Vector Arrows)
# g. Compute the  tangential component of the shear stress. This is done
#  using vector algebra.
#  First, create a surface normal vector variable using the Normal function
#  in the variable calculator.
#  Next, dot this with the shear stress vector, and multiply this product
#  by the surface normal vector.
#  This produces the normal component of the shear stress vector.
#     The tangential component is now computed by subtracting this normal
#     component from the shear stress vector, or Vt = V - Vn, where V
#     represents the shear stress vector.
# h. We now use the tangential component of the surface shear stress, itself
#     a vector, to compute a shear stress force vector,
#     simple by multiplying the  x/y/z components of the tangential component
#     of the shear stress by the incremental surface area.

# Part #1 is Fluid Domain
# Part #2 is the Wall of interest.
# vel_name is velocity vector
#
#  Begin
vel_name = "_VelocityVEC"
fluid_part_num = 2
surface_part_num = 1
viscosity = 3.5
tbegin=0
tend=4
#unit=1000
num_steps = tend-tbegin+1 #added 1 for total num timesteps if start from 0
#
ensight.part.select_begin(fluid_part_num)
ensight.variables.activate(vel_name)
#
# b. With ONLY fluid part(s) selected...
# Calculate a gradient vector from each component these velocity components
ensight.part.select_begin(fluid_part_num)
#  Note gradient function requires additional step of extracting
#    vector components of velocity prior to calling it. You cannot,
#    for example, directly reference Velocity[X], and etc.
ensight.variables.evaluate("VelX = "+vel_name+"[X]")
ensight.variables.evaluate("VelY = "+vel_name+"[Y]")
ensight.variables.evaluate("VelZ = "+vel_name+"[Z]")
ensight.variables.evaluate("GradU = Grad(plist,VelX)")
ensight.variables.evaluate("GradV = Grad(plist,VelY)")
```

```
ensight.variables.evaluate("GradW = Grad(plist,VelZ)")
# c. Now select boundary part(s).
#    Map the 3 component gradient vectors from the fluid part(s)
#    to the surface part(s) via CaseMap using 1 case on itself.
#    Case  Map  CaseMap  (2D  or  3D  part(s),  case  to  map  from,
#    scalar/vector/tensor). Finds the  specified scalar, vector,  or tensor
#    variable  values for the specified part(s) from the indicated case.
ensight.part.select_begin(surface_part_num)
ensight.variables.evaluate("CaseMap_GradU = CaseMap(plist,1,GradU,1)")
ensight.variables.evaluate("CaseMap_GradV = CaseMap(plist,1,GradV,1)")
ensight.variables.evaluate("CaseMap_GradW = CaseMap(plist,1,GradW,1)")
#
# d. With boundary part(s) selected...
#    Compute the Fluid Shear stress (Tau) components
#    Compute the fluid shear stress components using the FluidShear function in
#    the variable calculator and the mapped velocity gradients.
#    A value for the fluid's  dynamic viscosity must be provided. This may also
#    be a scalar variable.
ensight.variables.evaluate("TauU = FluidShear(plist,CaseMap_GradU,"    +
str(viscosity) + ")")
ensight.variables.evaluate("TauV = FluidShear(plist,CaseMap_GradV,"    +
str(viscosity) + ")")
ensight.variables.evaluate("TauW = FluidShear(plist,CaseMap_GradW,"    +
str(viscosity) + ")")
#
# e. With boundary part(s) selected...
#    Create the fluid shear stress vector
#    Create a fluid shear stress vector from these components using the MakeVect
#    function in the variable calculator.
ensight.variables.evaluate("Tau = MakeVect(plist,TauU,TauV,TauW)")
#
# f. With boundary part(s) selected...
#    You can visually inspect the vector arrows of Tau on the boundary part
#    by creating these vector arrows and displaying the tangential component
#
# g. With boundary part(s) selected...
#    Compute the decomposed tangential vector component of the Tau vector by
#    1. Computing the surface Normal vector on the boundary part(s)
ensight.variables.evaluate("Normal = Normal(plist)")
#    2. Creating the decomposed normal vector component of the Tau vector
#       by dotting Tau with the surface Normal and multiplying this scalar
#       by the surface Normal again.
ensight.variables.evaluate("TauN = DOT(Tau,Normal)*Normal")
#    3. Creating the decomponed tangential vector component of the Tau vector
#       by subtracting, i.e. TauT = Tau - TauN
ensight.variables.evaluate("TauT = Tau-TauN")
#
# h. With boundary part(s) selected...
```

```
#    Compute the element shear-stress force
#    1. Extract the 3 component scalars from TauT
ensight.variables.evaluate("TauTx = TauT[X]")
ensight.variables.evaluate("TauTy = TauT[Y]")
ensight.variables.evaluate("TauTz = TauT[Z]")
#    2. Compute the element area scalar
ensight.variables.evaluate("EleSize = EleSize(plist)")
#    3. Compute the tangential shear-stress component forces
ensight.variables.evaluate("FtauTx = TauTx*EleSize")
ensight.variables.evaluate("FtauTy = TauTy*EleSize")
ensight.variables.evaluate("FtauTz = TauTz*EleSize")
#
# i. With boundary part(s) selected...
#  Now, sum up each shear-stress force component into constant values
ensight.variables.evaluate("sumFSX = StatMoment(plist,FtauTx,0)")
ensight.variables.evaluate("sumFSY = StatMoment(plist,FtauTy,0)")
ensight.variables.evaluate("sumFSZ = StatMoment(plist,FtauTz,0)")
# These three constant variables should contain the components of the shear
# stress.  Grab the variables from EnSight to be able to store in a python
# register or print
sumFX=ensight.ensvariable("sumFX")
sumFY=ensight.ensvariable("sumFY")
sumFZ=ensight.ensvariable("sumFZ")
sumFSX=ensight.ensvariable("sumFSX")
sumFSY=ensight.ensvariable("sumFSY")
sumFSZ=ensight.ensvariable("sumFSZ")
# place these variables into storage array for printing
print "---------------- Force Summary --------------------"
print "                        Fx             Fy        Fz"
print "Shear Force    : ",sumFSX[0], sumFSY[0], sumFSZ[0]
ensight.part.select_begin(surface_part_num)
# WSS = TauU,TauV,TauW
#|WSS| =Mod_Tau
ensight.variables.evaluate("Mod_Tau=SQRT(TauU^2+TauV^2+TauW^2)")
ensight.variables.evaluate("I_Mod_WSS = TempMean(plist,Mod_Tau, "
+  str(tbegin) + " , " + str(tend) + ")")
ensight.variables.evaluate("I_WSS = TempMean(plist,Tau, "
+ str(tbegin) + " ,  " + str(tend) + ")")
ensight.variables.evaluate("Mod_I_WSS=SQRT(I_WSS[X]^2+I_WSS[Y]^2+
I_WSS[Z]^2)")
ensight.variables.evaluate("OSI=0.5*(1-(Mod_I_WSS/I_Mod_WSS))")
ensight.variables.evaluate("RRT = 1/((1-2*OSI)*Mod_I_WSS)")
ensight.variables.evaluate("ECAP = OSI/Mod_I_WSS")
```

Appendix D

Projects

D1 Projects

This thesis was partially supported by:

- 6th Framework Programme Horizontal Research Activities Involving SME's Co-operative Research (European Commission) through the project **'Grid based Decision Support System (DISHEART)'** No. FP6-2002-SME-1

- Comisión Interministerial de Ciencia y Tecnología (CICYT-Spain) through the project **'Simulación del comportamiento del corazón y periferia vascular en condiciones sanas y patológicas. Aplicación al diseÃśo y evaluación de dispositivos intravasculares y válvulas cardiacas (SIMCV)'** No. DPI2005-C03-01

- ITEA programme (Application Domains: Cyber Enterprise and Intermediation Services and Infrastructures and in Technology Categories: Content Acquisition and Processing and Content Representation. ITEA is a strategic pan-European programme for advanced pre-competitive RD in software for Software-intensive Systems and Services (SiS) through the project **' Cooperative Advanced REsearch for Medical Efficiency (Care4Me)'** No.08004

- FP7-JTI-ARTEMIS ARTEMIS-ASP2 Person-centric health management Call 2009 through the project **'Integrated healthcare approach for home, mobile and clinical environments (CHIRON)'** No. 100228

- FP7-JTI-ARTEMIS ARTEMIS-ASP2 Person-centric health management Call 2012 through the project **'European Platform to Promote Healthy Lifestyle and improve care through a Personal Persuasive Assistant (WITH-ME)'** No. 332885

- NTU-NHG Innovation Seed Grant Project. no. ISG/11007. 'Mechanistic and pathological study of the genesis, growth, and rupture of abdominal aortic aneurysms'

- Proyecto de Investigación Fundamental no orientada. Ministerio de economia y competitividad. e-Scaffold: Simulator for the design and development of tissue engineering scaffolds. DPI2011-29216-C02-02

- Instituto de Salud Carlos III, Acción Estratégica en Salud, PI14/01356. Desarrollo de un Sistema de Apoyo a las Decisiones basado en Técnicas de Inteligencia Artificial para el manejo rutinario de la Artritis Reumatoide

I would like also to express my sincere gratitude to the following companies for their private funding during my thesis: Iberhospitex, Anaconda, NITTO-Denko, Piemedical Imaging and ADITAS.

And, furthermore during these years I have funded by Ministerio de Ciencia e Innovación (Spain) through grant No.AP2003-3813 of FPU program.

Appendix E

Publications

E1 Publications

Following the list of **journal articles**, **conferences**, **book chapter** and **technical reports** written throughout the thesis period:

1. **JOURNAL ARTICLES**

   - E.Soudah, J.F. Rodriguez, R.López 'Mechanical stress in aortic abdominal aneurysm using artificial neural network'. Journal of Mechanics in Medicine and Biology 2014. DOI: 10.1142/ S02195-194-1550-0293.
   - E.Soudah, R.Rossi, S.Idelsohn, E.Oñate. 'A Reduced Order Model based on Coupled 1D/3D Finite Element Simulations for an Efficient Analysis of Hemodynamics Problems.' Journal of Computational Mechanics. (2014) 54:1013-1022. DOI 10.1007/s00466-014-1040-2
   - E. Soudah; G. Villalta; J. Vilalta Alonso; M. Bordone; F. Nieto; M.A. Pérez; C. Vaquero. Abdominal aortic aneurysm shear stress study based on the geometrical parameterization. Revista Internacional de Métodos Numéricos para Cálculo y Diseño en Ingeniería 2014 -13-00052-R2
   - E. Soudah, P. Rudenick, M.Bordone, B.H. Bijnens, D.Garcia-Dorado., A. Evangelista and E. Oñate. 'Finite elements methods prediction validation in different Aortic dissection scenarios: a comparison with in-vitro phantoms models.' Computer Methods in Biomechanics and Biomedical Engineering. Published online: 25 Oct 2013 DOI: 10.1080/10255842.2013.847095
   - E.Soudah, E.Y.K. Ng, T.H Loong, M.Bordone, P. Uei and N.Sriram.'CFD Modelling of Abdominal Aortic Aneurysm on Hemodynamic Loads using a Realistic Geometry with CT' Computational and Mathematical Methods in Medicine. Volume 2013 - 472564, 01/06/2013.

- Miguel Cerrolaza; Miguel Landrove; Eduardo Soudah; Giovana Gavidia. 'Modeling human tissues: an efficient integrated methodology' Biomedical Engineering: Applications, Basis and Communications, Vol. 26, No. 1 (2014) 1450012 (21 pages) DOI: 10.4015/S1016237214500124
- Guillermo Vilalta, Eduardo Soudah, José A. Vilalta, Félix Nieto, Maurizio Bordone, María á. Pérez, Carlos Vaquero. 'Hemodynamic features associated with abdominal aortic aneurysm (AAA) geometry'. Journal of Biomechanics. Special Supplement ESB2012 - 18th Congress of the European Society of Biomechanics.Vol.45, pagS1-677.July 2012.
- P.A.Rudenick, Bordone M.Bijnens B. Soudah E.Oñate E. Rudenick. 'Understanding different haemodynamic patterns in chronic aortic dissections and the relation to tear position and size a modelling study' European Journal of Echocardiography. 11 - suppl 2, pp. ii42 - ii44. 2010.
- Paula A Rudenick; Maurizio Bordone; Bart H Bijnens; Eduardo Soudah; Eugenio Oñate; David Garcia-Dorado; Arturo Evangelista. 'Influence of tear configuration on false and true lumen haemodynamics in type B aortic dissection' Conf Proc IEEE Eng Med Biol Soc. 1, pp. 2509 - 12. 2010. ISSN 1557-170X.
- E. Soudah, M.Bordone, A.Alvarez, J.Cobo, F.A. De Carlos and B.Suarez. Comportamiento de los dispositivos mandibulares en el tratamiento de la apnea del sueño. Rev. Int.Métodos Numér.Cálc.Diseño Ingeniería. 2012. (10.1016/j.rimni.2012.07.002).
- G.Gavidia, E.Soudah, Miguel Martín-Landrove and M. Cerrolaza. 'Generación de modelos discretos de tejidos del ser humano a través del pre procesamiento y segmentación de imágenes médicas' Rev. Int.métodos numér.cálc.diseño e ing. 2011;27(3):200-226.

2. CONFERENCES

- 'Study of the Abdominal Aortic Aneurysms morphology influences on hemodynamics stresses. Some possible rupture risk prediction based on statistical correlations' 63 International congress of European Society for Cardiovascular and EndoVascular Surgery, 2014.
- 'Predicción de las tensiones hemodinámicas de Aneurisma de Aorta Abdominal en función de su morfología', XI Congreso Iberoamericano de Ingeniería Mecánica, 2013
- 'To the Phase-Contrast image to the Wall Stress'. 8th Symposium of cardiovascular Diseases, Rotterdam, 4/2013
- 'Supporting Clinical Professionals in the Decision-making for Patients with Chronic Diseases'. ICOST 2012
- 'Advanced Medical Expert Support Tool (A-MEST): EHR-based Integration of Multiple Risk Assessment Solutions for Congestive Heart Failure Patients' MEDICON 10/2013

- 'A 1D lumped-parameter/3D CFD approach for pressure drop in the Aortic Coarctation' MICCAI 2012, Niza,10/2012
- 'Supervised learning modelling and segmentation of cardiac scar in delayed enhanced MRI' MICCAI 2012, Niza,10/2012
- 'Using idealized Abdominal Aortic Aneurysm Geometry Parameters as Predictor of Hemodynamics Stresses. (AAA Statistical Study)' 6th European congress on computational methods in applied ciences and engineering (ECCOMAS 2012) , Viena, 09/2012
- 'Hemodynamic features associated with abdominal aortic aneurysm (AAA) geometry' 18th Congress of the European Society of Biomechanics (ESB2012). Lisboa, Portugal : 07/2012
- 'Biodyn: Multiphysic Analysis in Bio-Engineering Applications.' 6th Convention on Advances and Applications of GiD, Barcelona, 05/2012
- 'From Arterial Skeletal Structures to 3D Volume Reconstruction and Simulation: Willis' Circle.' 6th Convention on Advances and Applications of GiD, Barcelona, 05/2012.
- 'Effectiveness of the Mandibular Advancement Device for treating sleep Apnea and Snoring' Southerm Biomedical Engineering Conference: Texas, USA 2011.
- 'Computer-aided diagnosis of dementia using medical imaging processing and artificial neural networks.' Computational Vision and Medical Image Processing: VipIMAGE 2011
- '4D MRI phase-contrast image to determinate blood flow patterns in aorta.' Computational Mathematical Biomedical Engineering 2011. Washigton, Estados USA. 2011.
- 'Influence of tear configuration on false and true lumen haemodynamics in type B aortic dissection' IEEE Engineering in Medicine and Biology Society. September Argentina 2010
- 'Different haemodynamic patterns related to tear position and size in chronic aortic dissections - a modelling study' ESC 2010 - European Society of Cardiology Congress 2010. Septiembre-Stockholm.
- 'GMED: a platform for medical images treatment inside GiD system' 5th Conference On Advances And Applications Of GiD. Barcelona 2010. 'Study flow phenomena in aortic dissection' 5th Conference On Advances And Applications Of GiD. Barcelona 2010.
- 'A technique of 3D reconstruction of myocardial tissue damage after ischemic heart disease' X CIMENICS. Marzo 2010.Mérida-Venezuela.
- 'I Jornadas de Innovación en Biomedicina' 3 Noviembre 2009 Madrid Hospital Clinico San Carlos de Madrid.
- 'From medical images to simulations: 4d MRI flow analysis' Vision and Medical Image Processing (VIPIMAGE2009)

- 'Validation of the one-Dimensional Numerical Model In The Ascending-Descending Aorta with real flow profile' 8th World Congress on Computational Mechanics (WCCM8). 5th European Congress con Computational Methods in Applied Sciences and Engineering (ECCOMAS 2008). Venecia-July 2008.
- 'Fluid-Structure interaction in the femoral bifuractions' 'VIPIMAGE 2007-Thematic conference on computational vision and medical image processing' PORTO-PORTUGAL-17-19 OCTOBER 2007.
- 'Neural Networks for Simulation processes in Bioengineering' World Congress on Biomedical Engineering WACBE. Bangkok Thailand 2006.

3. **BOOK CHAPTERS and TECHNICAL REPORTS**

- Carlos Cavero Barca, Juan Mario Rodríguez, Paolo Emilio Puddu, Mitja Lutrek, Boidara Cvetkovi, Maurizio Bordone, Eduardo Soudah, Aitor Moreno, Pedro de la Peña, Alberto Rugnone, Francesco Foresti, Elena Tamburini. 'Advanced Medical Expert Support Tool (A-MEST): EHR-Based Integration of Multiple Risk Assessment Solutions for Congestive Heart Failure Patients', XIII Mediterranean Conference on Medical and Biological Engineering and Computing 2013. 1334-1337, Springer International Publishing. 2014/1/1
- E. Soudah, M.Bordone, P.Dadvand, R.Rossi 'A 1D lumped-Parameter/3D CFD Approach for Pressure Drop in the Aortic Coarctation', Lecture Notes in Computer Science series. STACOM 2012, LNCS 7746, pp. 26–33. Springer, Heidelberg (2013)
- Laura Lara, Sergio Vera, Frederic Perez, Nico Lanconelli, Rita Morisi, Bruno Donini, Dario Turco, Cristiana Corsi, Claudio Lamberti, Giovana Gavidia, Maurizio Bordone, Eduardo Soudah, Nick Curzen, James Rosengarten, John Morgan, Javier Herrero, and Miguel A. González Ballester. Supervised Learning Modelization and Segmentation of Cardiac Scar in Delayed Enhanced MR. ILecture Notes in Computer Science series. STACOM 2012, LNCS 7746, pp. 53–62. Springer.2013
- M..Bordone, J.Perez, E.Y.K. Ng, T.H Loong, E. Oñate, E.Soudah. Mechanistic and pathological study of the genesis, growth, and rupture of abdominal aortic aneurysms. CIMNE-IT. CIMNE, 2012.
- Giovana Gavidia, Eugenio Oñate, Eduardo Soudah. Clasificadores Basados en Máquinas de Soporte Vectorial para el Diagnóstico y Predicción de la Enfermedad de Alzheimer. Monograph-135. CIMNE,2012
- B. Suarez; E.Soudah; M.Bordone; J.I.Gonzalez; A.á.Suárez; J.Cobo; F.A.De Carlos Villafranca. Non-invasive upper airway study using computational fluid dynamics and ct-scan to improve the treatment of obstructive sleep apnea syndrome. CIMNE-Monograph .1,pp. 1 -68.CIMNE,2012.
- Jorge Pérez, Eduardo Soudah, Eugenio Oñate. 'Wall Shear Stress and vorticity estimation using Phase-contrast magnetic resonance imaging'. CIMNE-IT-631. CIMNE, 2012.

- E.Soudah, J.Pennecot, J, Pérez, Bordone M., E.Oñate. Chapter 10: 'Medical-GiD: From medical images to simulations, MRI Flow Analysis'. Book: Computational Vision and Medical Image Processing: Recent Trends. Ed.Springer. 2011.
- G.Gavidia, E.Soudah, J.S.Ronda, Cerrolaza M. and E.Oñate. 'Desarrollo de una Herramienta de Procesamiento de Imágenes Médicas en MATLAB y su Integración en GiD Medical'. Monograph CIMNE. Octubre 2009. Barcelona.
- Bordone M., E.Oñate, E.Soudah. 'One Dimensional F.E.M. Model for a Biological Neuron Network'. Cimne-Monograph 2009.Pennecot J, Oñate E, J.S.Pérez, Soudah E. 'Medical-GiD: From Medical Images to Simulations' Monograph CIMNE.October 2008.Barcelona
- E.Soudah, Oñate E, J. García, J. S. Pérez, A. Mena, E. Heidenreich,J.F. Rodríguez, and M.Doblaré. 'Chapter 15: Fluid-Structure Interaction Applied to Blood Flow Simulations' in Book:: 'Advances in Computational Vision and Medical Image Processing. Methods and Applications'. November 2008.M. Bordone, E. Soudah, M. Chiumenti, E. Oñate 'Desarrollo de un software metálico intravascular' Informe Técnico CINME-2008.
- E.Soudah, J.F Rodriguez, M. Bordone, E.Heidenreich, M.Doblaré, E.Oñate "Grid based decision support system for assisting clinical diagnosis and interventions in cardiovascular problems." M-IS88, ISBN: 88-95999-87-1, Vol 1-2.CIMNE, 2007.DISHEART. E.Soudah, J.F.Rodríguez, M.Bordone, E.Heidenreich, M.Doblaré, E.Oñate. 'Grid based decision support system for assisting clinical diagnosis and interventions in cardiovascular problems." M-IS88,ISBN:88-95999-87-1, Vol 1-Vol2. CIMNE, 2007.

References

[1] *Dcmtk - dicom toolkit*.

[2] EnSight. All Rights Reserved. 2014 CEI Inc., *Ceo ensight*.

[3] S. Alper A. Malek and S. Izumo., *Hemodynamic shear stress and its role in atherosclerosis.*, The Journal of the American Medical Association **282** (1999), no. 21, 2035–2042.

[4] Botti L Ene-Iordache B Remuzzi A Steinman DA. Antiga L, Piccinelli M, *An image-based modeling framework for patient-specific computational hemodynamics.*, Med. Biol. Eng. Comput. **46** (2008), 1097Ű1112.

[5] American Heart Association, *Coronary artery disease-the abcs of cad.*, April 2012.

[6] The National Electrical Manufacturers Association, *Digital imaging and communications in medicine (dicom).*, PS 3.1-PS 3.12, NEMA Publications, 1992, 1993, 1994, 1995.

[7] Bürk J Lorenz R Bock J Bauer S et al. Barker AJ, Markl M, *Bicuspid aortic valve is associated with altered wall shear stress in the ascending aorta.*, Circulation: Cardiovascular Imaging **5** (2012), 457Ű66.

[8] Canic.S and Kim.H, *Mathematical analysis of the quasilinear effects in a hyperbolic model of blood flow through compliant axisymmetric vessels*, Mathematical Methods in Applied Sciences, 2003.

[9] Marcelo A. Castro, *Understanding the role of hemodynamics in the initiation, progression, rupture, and treatment outcome of cerebral aneurysm from medical image-based computational studies*, ISRN Radiology **2013** (2013), 17.

[10] Jonas M Edelman ER Feldman CL Stone PH. Chatzizisis YS, Coskun AU, *Role of endothelial shear stress in the natural history of coronary atherosclerosis and vascular remodeling: molecular, cellular, and vascular behavior.*, Journal of the American College of Cardiology **49** (2007), no. 25, 2379–93.

[11] Gilwoo Choi, Joo Myung Lee, Hyun-Jin Kim, Jun-Bean Park, Sethuraman Sankaran, Hiromasa Otake, Joon-Hyung Doh, Chang-Wook Nam, Eun-Seok Shin, Charles A. Taylor, and Bon-Kwon Koo, *Coronary artery axial plaque stress and its relationship with lesion*

geometryapplication of computational fluid dynamics to coronary ct angiography, JACC: Cardiovascular Imaging **8** (2015), no. 10, 1156–1166.

[12] E. Choke, G. Cockerill, W.R.W. Wilson, S. Sayed, J. Dawson, I. Loftus, and M.M. Thompson, *A review of biological factors implicated in abdominal aortic aneurysm rupture*, European Journal of Vascular and Endovascular Surgery **30** (2005), no. 3, 227–244.

[13] CIMNE, *Gid. the personal pre and postprocessor.*, 2010.

[14] COMPASSIS, *Tdyn: Theoretical background.*, 2012.

[15] K. S. Cunningham and A. I. Gotlieb., *The role of shear stress in the pathogenesis of atherosclerosis*, Laboratory investigation, **85** (2005), no. 1, 9–23.

[16] C. K. Zarins D. N. Ku, D. P. Giddens and S. Glagov., *Pulsatile flow and atherosclerosis in the human carotid bifurcation. positive correlation between plaque location and low oscillating shear stress.*, Arteriosclerosis, Thrombosis, and Vascular Biology, **5** (1985), no. 3, 293–302.

[17] Oñate E Dadvand P, Rossi R, *An object-oriented environment for developing finite element codes for multi-disciplinary applications.*, Arch Comput Methods Eng **17** (2010), 253Ű297.

[18] Bernard De Bruyne, Nico HJ Pijls, Guy R Heyndrickx, Dominique Hodeige, Richard Kirkeeide, and K Lance Gould, *Pressure-derived fractional flow reserve to assess serial epicardial stenoses theoretical basis and animal validation*, Circulation **101** (2000), no. 15, 1840–1847.

[19] Groen HC et al de Weert TT, Cretier S, *Atherosclerotic plaque surface morphology in the carotid bifurcation assessed with multidetector computed tomography angiography*, Stroke **40** (2009), no. 4, 1334ï£¡1340.

[20] van der Velden P Zaaijer ER Parks WJ Ramamurthy S Robbie TQ Donati G Lamphier C Beekman RP Brummer ME. den Reijer PM, Sallee D, *Hemodynamic predictors of aortic dilatation in bicuspid aortic valve by velocity-encoded cardiovascular magnetic resonance.*, J Cardiovasc Magn Reson **12** (2010), 4.

[21] M. A. Gimbrone Jr. et al. DePaola, N., *Vascular endothelium responds to fluid shear stress gradients*, Arterioscler Thromb **12** (1992), no. 11, 1254–1257.

[22] P. Di Achille, G. Tellides, C. A. Figueroa, and J. D. Humphrey, *A haemodynamic predictor of intraluminal thrombus formation in abdominal aortic aneurysms*, Proceedings of the Royal Society of London A: Mathematical, Physical and Engineering Sciences **470** (2014), no. 2172.

[23] Smith NP Lamata P Nordsletten DA. Donati F, Figueroa CA, *Non-invasive pressure difference estimation from pc-mri using the work-energy equation.*, Med Image Anal. **26** (2015), no. 1, 159–172.

[24] J. Donea, S. Giuliani, and L. Quartapelle, *Time-accurate solutions of advenction-diffusion problems by finite elements*, Comp. Meth. Appl. Mech. Eng (**71** (1984), 93–122.

[25] Andinet Enquobahrie, Patrick Cheng, Kevin Gary, Luis Ibanez, David Gobbi, Frank Lindseth, Ziv Yaniv, Stephen Aylward, Julien Jomier, and Kevin Cleary, *The image-guided surgery toolkit igstk: An open source c++ software toolkit*, Journal of Digital Imaging **20** (2007), no. Suppl 1, 21–33.

[26] Ebbers T Carlhäll CJ. Eriksson J, Bolger AF, *Four-dimensional blood flow-specific markers of lv dysfunction in dilated cardiomyopathy.*, Eur Heart J Cardiovasc Imaging **15** (2013), no. 5, 417–24.

[27] M. A. Fernàndez, V. Mìlìsic, and A. Quarteroni, *Analysis of a geometrical multiscale blood flow model based on the coupling of ode's and hyperbolic pde's*, SIAM Journal Multiscale Mod.Sim **4** (2005), 215–236.

[28] D. Formaggia, D. Lamponi, and A. Quarteroni, *One-dimensional model for blood flow in arteries*, J.Eng. Math, 1992.

[29] L. Formaggia, F. Nobile, A. Quarteroni, and A. Veneziani, *Multiscale modelling of the circulatory system: a preliminary analysis.*, Computing and Visualization in Science. **2** (1999), 75–83.

[30] Yusaku Fukumoto, Takafumi Hiro, Takashi Fujii, Genta Hashimoto, Tatsuhiro Fujimura, Jutaro Yamada, Takayuki Okamura, and Masunori Matsuzaki, *Localized elevation of shear stress is related to coronary plaque rupture: a 3-dimensional intravascular ultrasound study with in-vivo color mapping of shear stress distribution*, Journal of the American College of Cardiology **51** (2008), no. 6, 645–650.

[31] Frank Gijsen, Alina van der Giessen, Anton van der Steen, and Jolanda Wentzel, *Shear stress and advanced atherosclerosis in human coronary arteries*, Journal of biomechanics **46** (2013), no. 2, 240–247.

[32] Frank JH Gijsen, Jolanda J Wentzel, Attila Thury, Frits Mastik, Johannes A Schaar, Johan CH Schuurbiers, Cornelis J Slager, Wim J van der Giessen, Pim J de Feyter, Anton FW van der Steen, et al., *Strain distribution over plaques in human coronary arteries relates to shear stress*, American Journal of Physiology-Heart and Circulatory Physiology **295** (2008), no. 4, H1608–H1614.

[33] E. Godlewski and P. A. Raviart, *Numerical approximation of hyperbolic systems of conservation laws*, 1996.

[34] Harald C Groen, Frank JH Gijsen, Aad van der Lugt, Marina S Ferguson, Thomas S Hatsukami, Anton FW van der Steen, Chun Yuan, and Jolanda J Wentzel, *Plaque rupture in the carotid artery is localized at the high shear stress region a case report*, Stroke **38** (2007), no. 8, 2379–2381.

[35] M. C. McDaniel J. Suo S. S. Dhawan C. Maynard L. H.Timmins A.A. Quyyumi H. Samady, P. Eshtehardi and D. P. Giddens, *Coronary artery wall shear stress is associated with progression and transformation of atherosclerotic plaque and arterial remodeling in patients with coronary artery disease.*, Circulation **124** (2011), no. 7, 779–788.

[36] G. W. Hedstrom, *Non-reflecting boundary conditions for nonlinear hyperbolic systems*, Journal of Computational Physics, 1979.

[37] Heather A. Himburg, Deborah M. Grzybowski, Andrew L. Hazel, Jeffrey A. LaMack, Xue-Mei Li, and Morton H. Friedman, *Spatial comparison between wall shear stress measures and porcine arterial endothelial permeability*, American Journal of Physiology - Heart and Circulatory Physiology **286** (2004), no. 5, H1916–H1922.

[38] L. Ibáñez, W. Schroeder, L. Ng, and J. Cates, *The ITK Software Guide*, Kitware, 2003.

[39] Pearson Education Inc, *Hypertension and physiology of the heart, pearson education inc*, 2013, [Online; accessed 15-July-2015].

[40] F. Hussain J. Biasetti and T. C. Gasser, *Blood flow and coherent vortices in the normal and aneurysmatic aortas: a fluid dynamical approach to intra-luminal thrombus formation*, J. R. Soc. Interface **8** (2011), 1449–1461.

[41] J. Swedenborg J. Biasetti, P. G. Spazzini and T. C. Gasser, *An integrated fluid-chemical model toward modeling the formation of intra-luminal thrombus in abdominal aortic aneurysms*, Front Physiol **3** (2012), no. 266.

[42] B. K. Rutt J. S. Milner, J. A. Moore and D. A. Steinman., *Hemodynamics of human carotid artery bifurcations: computational studies with models reconstructed from magnetic resonance imaging of normal subjects.*, Journal of Vascular Surgery, **28** (1998), 143Ű156.

[43] Allen Jeremias, Steven D Filardo, Robert J Whitbourn, Robert S Kernoff, Alan C Yeung, Peter J Fitzgerald, and Paul G Yock, *Effects of intravenous and intracoronary adenosine 5?-triphosphate as compared with adenosine on coronary flow and pressure dynamics*, Circulation **101** (2000), no. 3, 318–323.

[44] John F. Jr. LaDisa, Ronak J. Dholakia, C. Alberto Figueroa, Irene E. Vignon-Clementel, Frandics P. Chan, Margaret M. Samyn, Joseph R. Cava, Charles A. Taylor, and Jeffrey A. Feinstein, *Computational simulations demonstrate altered wall shear stress in aortic coarctation patients treated by resection with end-to-end anastomosis*, Congenital Heart Disease **6** (2011), no. 5, 432–443.

[45] HJ Kim, IE Vignon-Clementel, JS Coogan, CA Figueroa, KE Jansen, and CA Taylor, *Patient-specific modeling of blood flow and pressure in human coronary arteries*, Annals of biomedical engineering **38** (2010), no. 10, 3195–3209.

[46] I. Kokalari, T. Karaja, and M. Guerrisi, *Review on lumped parameter method for modeling the blood flow in systemic arteries*, Journal Biomedical Science and Engineering, 2013.

[47] Bon-Kwon Koo, Andrejs Erglis, Joon-Hyung Doh, David V Daniels, Sanda Jegere, Hyo-Soo Kim, Allison Dunning, Tony DeFrance, Alexandra Lansky, Jonathan Leipsic, et al., *Diagnosis of ischemia-causing coronary stenoses by noninvasive fractional flow reserve computed from coronary computed tomographic angiograms: results from the prospective multicenter discover-flow (diagnosis of ischemia-causing stenoses obtained via noninvasive fractional flow reserve) study*, Journal of the American College of Cardiology **58** (2011), no. 19, 1989–1997.

[48] Bon-Kwon Koo, Hyun-Jai Kang, Tae-Jin Youn, In-Ho Chae, Dong-Joo Choi, Hyo-Soo Kim, Dae-Won Sohn, Byung-Hee Oh, Myoung-Mook Lee, Young-Bae Park, et al., *Physiologic assessment of jailed side branch lesions using fractional flow reserve*, Journal of the American College of Cardiology **46** (2005), no. 4, 633–637.

[49] Vignon-Clementel IE Kim HJ Xiao N Ellwein LM Chan FP Feinstein JA Taylor CA LaDisa JF Jr, Alberto Figueroa C, *Computational simulations for aortic coarctation: representative results from a sampling of patients.*, J Biomech Eng **133** (2011), no. 9.

[50] J. Lantz, J. Renner, and M. Karlsson, *Wall shear stress in a subject specific human aorta. influence of fluid-structure interaction*, Internal Journal of Applied Mechanics **4** (2011), no. 3, 759–778.

[51] Engvall J Karlsson M Lantz J, Ebbers T, *Numerical and experimental assessment of turbulent kinetic energy in an aortic coarctation.*, J Biomech **46** (2013), no. 11, 1851–1858.

[52] Kevin D. Lau and Alberto Figueroa Alvarez, *Simulation of short-term pressure regulation during the tilt test in a coupled 3dŰ0d closed-loop model of the circulation*, BIOMECHANICS AND MODELING IN MECHANOBIOLOGY **14** (2015), no. 4, 915–929.

[53] Steinman DA Lee SW, Antiga L, *Correlations among indicators of disturbed flow at the normal carotid bifurcation.*, J. Biomech. Eng. **131** (2009).

[54] J. Lotz, *Flow measurements in cardiac mri*, Radiologe. Apr; **47** (2007), no. 4, 333–41.

[55] Joanna K Lovett and Peter M Rothwell, *Site of carotid plaque ulceration in relation to direction of blood flow: an angiographic and pathological study*, Cerebrovascular Diseases **16** (2003), no. 4, 369–375.

[56] Michael W. Gee Mahmoud Ismail, Wolfgang A. Wall, *Adjoint-based inverse analysis of windkessel parameters for patient-specific vascular models*, Journal of Computational Physics **244** (2013), 113Ű130.

[57] Adelmo Cristiano Innocenza Malossi, *Partitioned solution of geometrical multiscale problems for the cardiovascular system: Models, algorithms, and applications.*, Master's thesis, École Polytechnique Fédérale de Lausanne, 2012.

[58] M. Markl, W. Wallis, and A. Harloff, *Reproducibility of flow and wall shear stress analysis using flow-sensitive four-dimensional mri*, Journal Magn Reson Imaging **33** (2011), 988–94.

[59] Michael Markl, Mary T Draney, Michael D Hope, Jonathan M Levin, Frandics P Chan, Marcus T Alley, Norbert J Pelc, and Robert J Herfkens, *Time-resolved 3-dimensional velocity mapping in the thoracic aorta: visualization of 3-directional blood flow patterns in healthy volunteers and patients*, Journal of computer assisted tomography **28** (2004), no. 4, 459–468.

[60] Strecker C Gladstone BP Vach W Harloff A. Markl M, Wallis W, *Analysis of pulse wave velocity in the thoracic aorta by flow-sensitive four-dimensional mri: reproducibility and correlation with characteristics in patients with aortic atherosclerosis.*, J Magn Reson Imaging. **35** (2012), no. 5, 1162–8.

[61] KS Matthys, J Alastruey, J Peiro, AW Khir, P Segers, PR Verdonck, KH Parker, and SJ Sherwin, *Pulse wave propagation in a model human arterial network: Assessment of 1-d numerical simulations against in vitro measurements*, JOURNAL OF BIOMECHANICS **40** (2007), 3476–3486.

[62] Arjun Menon, Thomas J Eddinger, Hongfeng Wang, David C Wendell, Jeffrey M Toth, and John F LaDisa, *Altered hemodynamics, endothelial function, and protein expression occur with aortic coarctation and persist after repair*, American Journal of Physiology - Heart and Circulatory Physiology **303** (2012), no. 11, H1304–H1318.

[63] James K Min, Jonathon Leipsic, Michael J Pencina, Daniel S Berman, Bon-Kwon Koo, Carlos van Mieghem, Andrejs Erglis, Fay Y Lin, Allison M Dunning, Patricia Apruzzese, et al., *Diagnostic accuracy of fractional flow reserve from anatomic ct angiography*, Jama **308** (2012), no. 12, 1237–1245.

[64] Umberto Morbiducci, Raffaele Ponzini, Giovanna Rizzo, Marcello Cadioli, Antonio Esposito, FrancoMaria Montevecchi, and Alberto Redaelli, *Mechanistic insight into the physiological relevance of helical blood flow in the human aorta: an in vivo study*, Biomechanics and Modeling in Mechanobiology **10** (2011), no. 3, 339–355 (English).

[65] Wouter V. Potters & Henk A. Marquering & Ed VanBavel & Aart J. Nederveen, *Measuring wall shear stress using velocity-encoded mri*, Curr Cardiovasc Imaging Rep **7** (2014), 9257.

[66] Christoph A Nienaber and Rachel E Clough, *Management of acute aortic dissection*, The Lancet **385** (2015), no. 9970, 800–811.

[67] U.S Government Printing Office., *Centers for disease control and prevention healthy, united states, 2010: With special feature of death and dying*, 2011.

[68] Fabrèges B. Gerbeau J.-F. Pant, S. and Vignon-Clementel I., *A methodological paradigm for patient-specific multi-scale cfd simulations: From clinical measurements to parameter estimates for individual analysis.*, International Journal for Numerical Methods in Biomedical Engineering **30** (2014), 1614–1648.

[69] Weinberg PD. Peiffer V, Sherwin SJ, *Does low and oscillatory wall shear stress correlate spatially with early atherosclerosis? a systematic review*, Cardiovasc Res. **99** (2103), no. 2, 242–50.

[70] Perktold, *Pulsatile non-newtonian blood flow in three-dimensional carotid bifurcation models: A numerical study of flow phenomena under different bifurcation angles.*, J. Biomed. Eng **13** (1991), 507–515.

[71] Dyverfeldt P. Sigfridsson A.-Lantz J. Carlhäll C.-J. Petersson, S. and T. Ebbers, *Quantification of turbulence and velocity in stenotic flow using spiral three-dimensional phase-contrast mri.*, Magn Reson Med. (2015).

[72] Sven Petersson, Petter Dyverfeldt, and Tino Ebbers, *Assessment of the accuracy of mri wall shear stress estimation using numerical simulations*, Journal of Magnetic Resonance Imaging **36** (2012), 128–138.

[73] Nico HJ Pijls and Jan-Willem EM Sels, *Functional measurement of coronary stenosis*, Journal of the American College of Cardiology **59** (2012), no. 12, 1045–1057.

[74] Marquering H vanBavel E Nederveen AJ. Potters WV, van Ooij P, *Volumetric arterial wall shear stress calculation based on cine phase contrast mri.*, J Magn Reson Imaging. **41** (2015), no. 2, 505–16.

[75] L. Quartapelle, *Numerical solution of the incompressible navier-stokes equations*, 1993.

[76] A. Quarteroni and L. Formaggia, *Mathematical modelling and numerical simulation of the cardiovascular system*, 2002.

[77] A. Quarteroni and R. Sacco, *Matematica numerica*, 2000.

[78] A. Quarteroni and A. Valli, *Domain decomposition methods for partial differential equation*, 1999.

[79] Shum J Finol EA. Raut SS1, Chandra S, *The role of geometric and biomechanical factors in abdominal aortic aneurysm rupture risk assessment.*, Ann Biomed Eng. **41** (2013), no. 7, 1459–77.

[80] The OpenFOAM Foundation. All Rights Reserved., *Free open source cfd. openfoam*.

[81] Amy Gallo MD Michael A. Coady MD MPH George Tellides MD PhD Donald M. Botta MD Brendan Burke BS Marcus P. Coe BA Gary S. Kopf MD John A. Elefteriades MD Ryan R. Davies, MD, *Novel measurement of relative aortic size predicts rupture of thoracic aortic aneurysms*, The Annals of Thoracic Surgery **81** (2006), no. 1, 169–177.

[82] Judy Shum Christopher B. Washington Satish C. Muluk Ender A. Finol Samarth S. Raut, Santanu Chandra and José F. Rodríguez, *Biological, geometric and biomechanical factors influencing abdominal aortic aneurysm rupture risk: A comprehensive review*, Recent Patents on Medical Imaging **3** (2013), 44–59.

[83] Will Schroeder, Ken Martin, and Bill Lorensen, *The visualization toolkit, third edition*, Kitware Inc.

[84] ShawnC. Shadden and Sahar Hendabadi, *Potential fluid mechanic pathways of platelet activation*, Biomechanics and Modeling in Mechanobiology **12** (2013), no. 3, 467–474 (English).

[85] Maria Siebes and Yiannis Ventikos, *The role of biofluid mechanics in the assessment of clinical and pathological observations*, Annals of biomedical engineering **38** (2010), no. 3, 1216–1224.

[86] CJ Slager, JJ Wentzel, FJH Gijsen, JCH Schuurbiers, AC Van der Wal, AFW Van der Steen, and PW Serruys, *The role of shear stress in the generation of rupture-prone vulnerable plaques*, Nature Clinical Practice Cardiovascular Medicine **2** (2005), no. 8, 401–407.

[87] E. Soudah, Eyk Ng, Loong Th., and M. Bordone, *Cfd modelling of abdominal aortic aneurysm on hemodynamic loads using a realistic geometry with ct*, Computational and Mathematical Methods in Medicine **2564** (2013), 9.

[88] M. B. Srichai, R. P. Lim, S. Wong, and Lee Vs., *Cardiovascular applications of phase-contrast mri*, AJR Am Journal Roentgenol. **192** (2009), no. 3, 662–75.

[89] A. F. Stalder, A. Frydrychowicz, M. F. Russe, J. G. Korvink, J. Hennig, K. Li, and M. Markl, *Assessment of flow instabilities in the healthy aorta using flow-sensitive mri*, Journal of Magnetic Resonance Imaging, 2011.

[90] Nakayama T Shimizu H Endo H Inoue T Fujimura M Ohta M Takahashi A Tominaga T. Sugiyama S, Niizuma K, *Relative residence time prolongation in intracranial aneurysms: a possible association with atherosclerosis.*, Neurosurgery **73** (2013), no. 5, 767–76.

[91] Tenforde AS et al. Suh G-Y, Les AS, *Quantification of particle residence time in abdominal aortic aneurysms using magnetic resonance imaging and computational fluid dynamics.*, Annals of biomedical engineering. **39** (2011), no. 2, 864–883.

[92] Bruno Tayllamin, Ramiro Moreno, Franck Nicoud, Ming Chau, and Hervé Rousseau, *Cfd-based functional imaging for arteries: in vitro validation*, (2011).

[93] C. A. Taylor and C. A. Figueroa, *Patient-specific modeling of cardiovascular mechanics*, Annual Review of Biomedical Engineering **11** (2009), no. 1, 109–134.

[94] Ca. Taylor, A. Timothy, and K. Min James, *Computational fluid dynamics applied to cardiac computed tomography for noninvasive quantification of fractional flow reserve*, Journal of the American College of Cardiology **61** (2013), 22.

[95] E. Y. K. Ng Tejas Canchi, S. D. Kumar and Sriram Narayanan, *A review of computational methods to predict the risk of rupture of abdominal aortic aneurysms*, BioMed Research International **2015** (2015), 12.

[96] K. Thompson, *Time dependent boundary conditions for hyperbolic systems*, Journal Comp. Physics (**68** (1987), 1–24.

[97] G.J. Tortora and B. Derrickson, *Principios de anatomía y fisiología*, Médica Panamericana, 2006.

[98] Shengxian Tu, Emanuele Barbato, Zsolt Köszegi, Junqing Yang, Zhonghua Sun, Niels R. Holm, Balázs Tar, Yingguang Li, Dan Rusinaru, William Wijns, and Johan H.C. Reiber, *Fractional flow reserve calculation from 3-dimensional quantitative coronary angiographyăand timi frame counta fast computer model to quantify the functional significance of moderately obstructed coronary arteries*, JACC: Cardiovascular Interventions **7** (2014), no. 7, 768–777.

[99] Stergiopulos N. van de Vosse F, *Pulse wave propagation in the arterial tree.*, Annual Review of Fluid Mechanics **43** (2011), 467–499.

[100] Jeroen PHM van den Wijngaard, Janina CV Schwarz, Pepijn van Horssen, Monique GJTB van Lier, Johannes GG Dobbe, Jos AE Spaan, and Maria Siebes, *3d imaging of vascular networks for biophysical modeling of perfusion distribution within the heart*, Journal of biomechanics **46** (2013), no. 2, 229–239.

[101] J. J. Wang and K. H. Parker, *Wave propagation in a model of the arterial circulation*, Journal Biomech (**37** (2004), 457–470.

[102] S. M. Wasserman and J. N. Topper., *Adaptation of the endothelium to fluid flow: in vitro analyses of gene expression and in vivo implications*, Vascular Medicine **9** (2004), no. 1, 35–45.

[103] Jolanda J. Wentzel, Yiannis S. Chatzizisis, Frank J.H. Gijsen, George D. Giannoglou, Charles L. Feldman, and Peter H. Stone, *Endothelial shear stress in the evolution of coronary atherosclerotic plaque and vascular remodelling: current understanding and remaining questions*, Cardiovascular Research **96** (2012), no. 2, 234–243.

[104] M. Haidekker et al. White, C. R., *Temporal gradients in shear, but not spatial gradients, stimulate endothelial cell proliferation.*, Circulation **103** (2001), no. 20, 2508–2513.

[105] William Wijns, *The one-stop shop offering both coronary anatomy and myocardial perfusion: May well be opening soon, around the corner??*, JACC: Cardiovascular Imaging **5** (2012), no. 11, 1112–1114.

[106] Wikipedia, *Circulatory system — Wikipedia, the free encyclopedia*, 2004, [Online; accessed 22-July-2015].

[107] J. R. Womersley., *Method for the calculation of velocity, rate of flow and viscous drag in arteries when the pressure gradient is known.*, J. Physiology **127** (1955), 553Ű563.

[108] Tremmel M Ma D Mocco J Hopkins LN Siddiqui AH Levy EI Meng H. Xiang J, Natarajan SK, *Hemodynamic-morphologic discriminants for intracranial aneurysm rupture*, Stroke **42** (2011), no. 1, 144–52.

[109] Paul A. Yushkevich, Joseph Piven, Heather Cody Hazlett, Rachel Gimpel Smith, Sean Ho, James C. Gee, and Guido Gerig, *User-guided 3D active contour segmentation of anatomical structures: Significantly improved efficiency and reliability*, Neuroimage **31** (2006), no. 3, 1116–1128.

[110] Bharadvaj BK Sottiurai VS Mabon RF Glagov S Zarins CK, Giddens DP, *Carotid bifurcation atherosclerosis: Quantitative correlation of plaque localization with flow velocity profiles and wall shear stress.*, Circulation Research **53** (1985), 502–514.